INVESTIGATION OF ASYMMETRIC GEAR TOOTH BENDING STRESS FORMULATION

A THESIS SUBMITTED TO
THE GRADUATE SCHOOL OF NATURAL AND APPLIED SCIENCES
OF
MIDDLE EAST TECHNICAL UNIVERSITY

BY

MAHİR GÖKHAN ORAK

IN PARTIAL FULFILLMENT OF THE REQUIREMENTS
FOR
THE DEGREE OF MASTER OF SCIENCE
IN
MECHANICAL ENGINEERING

MARCH 2018

Approval of the thesis:

INVESTIGATION OF ASYMMETRIC GEAR TOOTH BENDING STRESS FORMULATION

Submitted by **MAHİR GÖKHAN ORAK** in partial fulfillment of the requirements for the degree of **Master of Science in Mechanical Engineering Department, Middle East Technical University** by,

Prof. Dr. Halil Kalıpçılar
Dean, Graduate School of **Natural and Applied Sciences** _____

Prof. Dr. M. A. Sahir Arıkan
Head of Department, **Mechanical Engineering** _____

Prof. Dr. Metin Akkök
Supervisor, **Mechanical Engineering Dept., METU** _____

Examining Committee Members:

Prof. Dr. F.Suat Kadıoğlu
Mechanical Engineering Dept., METU _____

Prof. Dr. Metin Akkök
Mechanical Engineering Dept., METU _____

Prof. Dr. Orhan Yıldırım
Mechanical Engineering Dept., METU _____

Prof. Dr. Ömer Anlağan
Mechanical Engineering Dept., Bilkent University _____

Assist. Prof. Dr. Orkun Özşahin
Mechanical Engineering Dept., METU _____

Date: 16.03.2018

I hereby declare that all information in this document has been obtained and presented in accordance with academic rules and ethical conduct. I also declare that, as required by these rules and conduct, I have fully cited and referenced all material and results that are not original to this work.

Name, Last name : Mahir Gökhan ORAK

Signature:

ABSTRACT

INVESTIGATION OF ASYMMETRIC GEAR TOOTH BENDING STRESS FORMULATION

Orak, Mahir Gökhan
M.S., Department of Mechanical Engineering
Supervisor: Prof. Dr. Metin Akkök
March 2018, 183 pages

An asymmetric gear has different pressure angle and base radius for the drive and coast side tooth flanks. A standard is not available to determine the bending stresses of external and internal asymmetric spur gears, although there are international standards to determine the bending stresses of external and internal symmetric spur gears. The main objective of this thesis is to determine the bending stresses of the external and internal asymmetric spur gears. The tooth thickness of a gear tooth at the critical bending stress section is summation of both drive and coast side tooth thicknesses. These thicknesses are not same for an asymmetric gear tooth contrary to a symmetric gear tooth. Then, the bending stress of an asymmetric gear tooth cannot be calculated same with a symmetric gear tooth. Therefore, the bending stresses of external and internal asymmetric spur gears shall be formulated.

In this thesis, ISO B methodology is modified to determine both external and internal asymmetric spur gear bending stresses. In this method, although the drive side tangent angle at the critical section is equal to 30° and 60° for external and internal asymmetric spur gears, respectively, the coast side tangent angles at their critical sections are calculated by using the kinematics of the generations of the gear coast

side root fillets. In this thesis, the analytical results of the modified ISO method are verified by FEA works. In order to do FEA works and determine the critical bending stress sections, detailed geometry studies of both of external and internal asymmetric spur gears are carried out. In these studies, an asymmetric rack-cutter and pinion type shaper cutter are used to generate the external and internal asymmetric spur gears, respectively.

For the external asymmetric spur gears, the calculated bending stress decreases with an increase in drive side pressure angle. This enables to enhance the bending strength of the gear tooth. The maximum bending stress calculated in analytical method is %5 lower than FEA results for low number of teeth and that increases to %10 for high number of teeth.

For the internal asymmetric spur gears, the calculated bending stress decreases with an increase in drive side pressure angle only for low coast side pressure angle smaller than 20°. The bending stresses of the modified ISO method are about % 5 different than the results of the FEA for drive and coast side pressure angles larger than 20°, but the percentage difference increases to % 15 for low drive and coast side pressure angles smaller than 20° (for example for 16°).

As a result, the modified ISO methods for external and internal asymmetric spur gears give as accurate results as the standard ISO methods for external and internal symmetric spur gears.

Keywords: External asymmetric spur gear bending stress, internal asymmetric spur gear bending stress, asymmetric rack-cutter, asymmetric pinion type shaper cutter

ÖZ

ASİMETRİK DİŞLİNİN EĞİLME GERİLMESİ FORMÜLASYONUNUN İNCELENMESİ

Orak, Mahir Gökhan
M.S., Makina Mühendisliği Bölümü
Tez Yöneticisi: Prof. Dr. Metin Akkök
Mart 2018, 183 sayfa

Asimetrik dişli, bir dişin sağ ve sol yanağında farklı basınç açısına ve temel dairesine sahip olan dişlidir. İç ve dış simetrik düz dişlilerin eğilme gerilimlerini hesaplayan uluslararası standartlar olmasına rağmen, iç ve dış asimetrik düz dişlilerin eğilme gerilmelerini hesaplayan bir standart bulunmamaktadır. Bu tezin ana gayesi, iç ve dış asimetrik düz dişlilerin eğilme gerilmelerini belirlemektir. Bir dişin kritik eğilme gerilmesi kesitindeki et kalınlığı hem süren hem de diğer yanağın bu kesitteki et kalınlıkları toplamına eşittir ve bu et kalınlıkları simetrik bir dişin aksine asimetrik bir dişte eşit değildir. Öyleyse, asimetrik bir dişlinin eğilme gerilmesi simetrik bir dişlinin eğilme gerilmesi ile aynı hesaplanamaz. Bu yüzden iç ve dış asimetrik düz dişlilerin eğilme gerilmeleri formüle edilmelidir.

Bu tezde, hem iç hem de dış asimetrik düz dişlilerin eğilme gerilmelerini belirlemek için ISO B metodu modifiye edilir. Bu metoda göre dişlinin çalışan yanakların kritik eğilme kesitindeki tanjant açısı iç ve dış dişliler için sırasıyla 30° ve 60° iken, çalışmayan yanakların kritik eğilme kesitindeki tanjant açıları bu yanakların diş dibi radyuslarının elde edilme kinematikleri kullanılarak hesaplanır. Bu tezde, modifiye edilmiş ISO metodunun analitik sonuçları sonlu eleman analizleri ile doğrulanır.

Sonlu eleman analizleri yapabilmek ve kritik eğilme gerilmesi kesitlerini belirleyebilmek için, hem iç hem dış dişlilerin detaylı geometri çalışmaları gerçekleştirilir. Bu çalışmalarda, sırasıyla iç ve dış asimetrik düz dişlileri elde etmek için kremayer ve pinyon şekilli planya kesicileri kullanılır.

Dış asimetrik düz dişliler için hesaplanan eğilme gerilimleri yük altında çalışan yanağın basınç açısı arttıkça artmaktadır. Bu dişlinin eğilme gerilimine karşı mukavemetini artırır. Düşük diş sayılarında analitik metodda hesaplanan maksimum eğilme gerilimleri, sonlu elaman analizlerine göre %5 az gelmektedir. Yüksek diş sayılarında ise bu fark %10 civarına çıkmaktadır.

İç asimetrik dişliler için hesaplanan eğilme gerilimleri, yük altında çalışan yanağın basınç açısı arttıkça sadece yük altında çalışmayan yanağın 20°'den düşük basınç açısına sahip olması durumunda azalmaktadır. Hem yük altında çalışan hem de yüke maruz kalmayan yanaklarda 20°'den daha yüksek basınç açıları için, modifiye ISO metoduna göre hesap edilen eğilme gerilimleri, sonlu elaman analizlerine göre %5 farrklılık göstermektedir. Ama her iki yanak için de 20°'den daha düşük basınç açıları için, bu fark %15 civarına çıkmaktadır.

Sonuç olarak, iç ve dış asimetrik düz dişliler için modifiye edilen ISO metodları, iç ve dış simetrik düz dişliler için var olan standart ISO metodları kadar iyi sonuçlar vermektedir.

Keywords: İç asimetirk dişli eğilme gerilmesi, dış asimetrik dişli eğilme gerilmesi, asimetirk kremayer kesici, asimetrik pinyon şekilli planya kesici

To My Wife,

Merve

&

To My Son

Hamza

ACKNOWLEDGEMENTS

I would like to thank my supervisor Prof. Dr. Metin Akkök for his supervision, help and guidance from the beginning to end of this dissertation.

I want to thank my wife Merve for her endless support and encouragement throughout this study.

I would like to express my thanks to my son Hamza for his patience when I was studying instead of playing together.

TABLE OF CONTENTS

LIST OF TABLES

TABLES

LIST OF FIGURES

FIGURES

LIST OF SYMBOLS

a	addendum coefficient
A	radius of rack cutter round
b	dedendum coefficient
C_o	operating center distance
C_r	contact ratio
E_c	center distance of external and internal gear mesh
E_s	center distance of shaper cutter and internal gear
f	facewidth direction
f_w	face width
F_n	normal force applied on external gear
F_r	radial component of the applied force
F_t	tangential component of the applied force
h_r	critical section tooth height
I	instantaneous center of rotation
m	module
M_{f1}	translation matrix between S_1&S_f
M_{2f}	rotation matric between S_f&S_2
M_{fs1}	rotation matrix between S_s&S_f
M_{fs2}	translation matrix between S_s&S_f
M_{if}	rotation matrix between S_f&S_i
M_{rot}	rotation matrix for the desired internal gear position
N	normal vector
p_b	base pitch
P	the point where critical section occurs on drive side
P_x	x component of point P

P_y	y component of point *P*
r_a	external gear tip radius
r_b	external gear base circle
r_{bf}	instantaneous base radius of external gear root fillet
r_{bsr}	instantaneous base radius of the shaper round surface
r_F	radius of the applied force
r_{gp}	generating pitch radius
r_h	radius of highest point single tooth contact
r_i	vector representation of $\Sigma_{\phi i}$
r_{if}	vector representation of $\Sigma_{\phi fi}$
r_l	lowest point of single tooth contact for internal spur gear
r_o	operating pitch radius
r_p	external gear pitch radius
r_r	radius of shaper round start point
r_s	position vector of a shaper involute surface
r_{sr}	position vector of a shaper round surface
r_t	pointed tip radius of external gear
r_1	position vector of a rack cutter inclined surface
r_2	vector representation of Σ_{ϕ}
r_{1r}	position vector of a rack cutter round surface
r_{2f}	vector representation of $\Sigma_{\phi f}$
s	amount of translation of a rack cutter
S_f	coordinate system of frame (gear housing)
S_i	coordinate system of internal gear
S_s	coordinate system of pinion type shaper cutter
S_1	coordinate system of rack cutter
S_2	coordinate system of external gear
t	tooth thickness of a rack cutter at generating pitch line

t_g	tooth thickness at generating pitch circle
t_f	rack cutter fillet center thickness
t_o	gear tooth thickness at operating pitch circle
t_{ow}	gear tooth space width at operating pitch circle
t_r	critical section tooth thickness
t_{ref}	tooth thickness of an external gear at pitch circle
T	the point where critical section occurs on coast side
T_x	x component of point *T*
T_y	y component of point *T*
u	inclination direction of the rack cutter
u_e	end point of rack cutter inclined surface generating Σ_2
u_r	start point of rack cutter inclined surface generating Σ_2
v	velocity of a rack cutter
v_g	velocity of external gear at instantaneous point of contact
v_{gi}	internal gear instantaneous velocity
v_{gin}	normal velocity component of internal gear instantaneous velocity
v_{gn}	normal velocity component of v_g
v_{gt}	tangential velocity component of v_g
v_n	normal velocity component of rack cutter
v_s	shaper instantaneous velocity
v_{sl}	sliding velocity
v_{sn}	normal velocity component of shaper instantaneous velocity
v_t	tangential velocity component of rack cutter
ω	angular velocity of a gear
x	profile shift
x_C	x component of shaper round center
x_s	the amount of vertical shift of shaper
y_C	y component of shaper round center
Y_F	tooth form factor

Y_S	stress correction factor
Z	number of teeth
Z_g	number of teeth of gear
Z_p	number of teeth of pinion
α	pressure angle of a rack cutter
α_a	tip radius pressure angle
α_b	pressure angle of a base radius according to the other side base radius
α_F	angle of the force
α_g	generating pressure angle
α_{gt}	the internal gear drive side generating pitch tooth thickness angle
α_h	pressure angle of HPSTC
α_j	pressure angle of external gear at instantaneous point of contact
α_l	pressure angle of r_l
α_o	operating pressure angle
α_ρ	angle of trochoid center line
α_r	pressure angle of r_r
α_t	pressure angle of r_t
β	critical section tangent angle
δ	shaper topland angle
δ_i	internal gear virtual topland angle
δ_s	angle of shaper round start point
ϕ	rotation angle of external gear
ϕ_{rot}	rotation angle for the desired internal gear position
ρ_F	radius of curvature of gear root fillet
σ	bending stress
Σ_i	internal gear involute surface
Σ_{id}	internal gear dedendum circle surface
Σ_{if}	internal gear root fillet surface
Σ_{ifrot}	desired internal gear root fillet surface

Σ_{irot}	desired internal gear involute flank surface
Σ_s	shaper involute surface
Σ_{sd}	shaper addendum circle surface
Σ_{sr}	shaper round surface
Σ_1	inclined surface of a rack cutter
Σ_2	involute flank surface of an external gear
Σ_{1r}	round surface of a rack cutter
Σ_{1d}	horizontal straight surface of a rack cutter
Σ_{2d}	dedendum circle surface of an external gear
Σ_{2f}	external gear root fillet surface
Σ_ϕ	family of surfaces generated by Σ_1
$\Sigma_{\phi f}$	family of surfaces generated by Σ_{1r}
$\Sigma_{\phi fi}$	family of surfaces generated by r_{sr}
$\Sigma_{\phi i}$	family of surfaces generated by r_s
θ	instantaneous angle of rack cutter round
θ_a	shaper round end topland angle
θ_C	angle between the shaper tooth axis and shaper round center
θ_e	end angle of the rack cutter round
θ_{sce}	shaper coast side round end angle
θ_{scs}	shaper coast side round start angle
θ_{sde}	shaper drive side round end angle
θ_{sds}	shaper drive side round start angle
ξ	critical section angle with respect to the frame vertical center line
ζ	angle between the internal gear tooth axis and vertical center line

Subscripts

c	coast side
d	drive side
i	internal gear
s	shaper

CHAPTER 1

INTRODUCTION AND LITERATURE SURVEY

1.1 Introduction

In gear design, there are possible failure forms that shall be considered. These are mainly bending, pitting and scuffing failures. In order to avoid these failures many solutions can be applied on gears such as shot peening, heat treatment, using a better material and tooth macro and micro geometry modifications. One of the tooth macro geometry modifications is the asymmetric gear tooth form.

A symmetric involute spur gear tooth has the same pressure angle and base radius for the left and right flanks of the tooth. On the other hand, an asymmetric gear tooth has different pressure angle and base radius for the flanks.

In most of the applications where gears are used in, the system mainly works by rotating in the same direction during the operation life. In such an application, a gear tooth is mainly and highly loaded on one of its sides which is called drive side. On the contrary, the other side of the gear tooth is unloaded or lightly loaded and called coast side. And the design purpose of an asymmetric gear tooth is to improve the performance of the drive side.

In order to be able to design an asymmetric gear tooth, the bending and contact stresses shall be calculated. Since the contact stress of a gear tooth is directly related to the drive side, an asymmetric gear tooth contact stress can be calculated same with a symmetric gear tooth having the same pressure angle with the drive side of the

asymmetric gear tooth. However, the bending stress of a gear tooth is dependent on not only the drive side but also the coast side. Because the tooth thickness of a gear tooth at the critical bending stress section is summation of both drive and coast side tooth thicknesses which are not same for an asymmetric gear tooth. Then, the bending stress of an asymmetric gear tooth cannot be calculated same with a symmetric gear tooth. Therefore the bending stress of an asymmetric gear tooth shall be formulated.

The main objective of this thesis is to determine the external and internal asymmetric spur gears bending stresses. In this thesis, ISO B methodology has been modified to determine both of the asymmetric external and internal gear tooth bending stresses. Also, a detailed study to obtain the geometry of both of the asymmetric external and internal gears have been done such that a FEA work can be carried out to compare the results with modified ISO B methodology.

1.2 Literature Survey

The first bending stress formulation is given by Wilfred Lewis (1893). In his model, the tooth, which was substituted by a parabola of uniform strength, was handled as a beam clamped at one end, i.e., a cantilever, and the loading force was assumed to be an evenly distributed force along the tooth length and applied on the tip of the tooth as the worst load case. For bending, the most dangerous section of the tooth is pointed by the point of the parabola which is tangent to the tooth root curve. The introduction of the notion of the tooth form factor is linked to Lewis [1]. Later Hofer refined Lewis' model. He marked out the dangerous section of the tooth root by straight lines angled 30° with the tooth center line [1]. After that, in 1950's, research works were published at both national and international levels on the gear strength scaling. The design recommendations of the American Gear Manufacturers Association (AGMA) have been published. Ten years later, in 1970, the national standard DIN3990 – in West Germany – and the international standard ISO 6336

were issued. Nowadays, the main regulations governing the calculation of the tooth root stress are summarized in ANSI/AGMA 2101-D04 (2004), DIN 3990-3 (1987), ISO 6336- 3:2006 [1].

The traditional Lewis bending stress and form factor equations of a symmetric gear tooth is defined in the paper [2] where the unknowns are the critical tooth thickness and height. In bending stress formulations of international standards, beside the form factor, there is also a stress correction factor which is based on the work [3] and this factor is also dependent on the critical tooth thickness and height. There are analytical ways of calculating these unknowns for symmetric gears in AGMA [4] which uses the Lewis model and in ISO-6336 [5] which uses the Hofer model. Examination of run-in teeth reveals that when a single tooth carries the full load and the load is applied at the highest point of single tooth contact (HPSTC), the maximum bending stress occurs [6]. So when doing the bending stresses analysis, contrary to application of the load at the tip of the gear tooth in traditional Lewis model, the load is applied at the HPSTC in both AGMA and ISO standards.

Although the gear geometry and design of asymmetric tooth gears are not covered by modern national and international gear design and rating standards, they are known and described in a number of technical articles and books.

In terms of the asymmetric spur gear geometry, a method is developed for the geometry and design of external spur gears with asymmetric involute teeth in paper [7]. This is a direct gear design method and independent on the traditional cutter parameters. Then, a mathematical model of a helical gear with asymmetric involute teeth is developed by using rack cutter in paper [8]. In the paper [9], a double envelope concept is used to determine the basic profile of an internal spur gear with asymmetric involute teeth. Based on this concept, the required cutter to generate the internal asymmetric gear can be obtained by the envelope to the family of a rack cutter surfaces. This generated cutter is like a pinion type shaper cutter. However by using this method, the tip of the shaper cutter cannot be rounded but can be obtained

with a trochoidal tip. Then, the internal gear is the envelope for the family of this generated shaper cutter surfaces and the generated internal gear has a different root fillet than the generated internal gear by a rounded pinion type shaper cutter. Through this proposed method, the profile of an internal gear with asymmetric involute teeth can be easily obtained. In paper [10], a pinion-type shaper cutter with rounded tip is considered as the generating tool for the generation of the external asymmetric gear, and a mathematical model of spur gears with asymmetric involute teeth is given according to the gearing theory. The equations of the profile of the cutter, the principle of coordinate transformation, the theory of differential geometry, and the theory of gearing are applied for describing generating and generated surfaces.

In terms of the asymmetric spur bending stress, in paper [7], it is found that external asymmetric spur gear tooth geometry (with larger pressure angle on drive tooth side) allow for an increase in load capacity while reducing weight and dimensions for same types of gears. In the paper [11], an adaptation of the standard ISO C methodology to determine bending stress calculations for external spur gears with asymmetric teeth is used and the results are compared with the results obtained using modern finite element methods**.** In another paper [12], the effect of bending stress of an external spur gear at the critical section for different pressure angle on the drive side along with the profile shift is studied by finite element analysis. Due to positive profile shift, the thickness of tooth at the root increases, resulting in greater load carrying capacity of the teeth. Profile shift varied from 0 to 0.5 and found lowest bending strength at critical section with profile shift value of 0.5; drive side pressure angle is also varied from 20 to 30 degree and found lowest bending strength at critical section with 30 degree pressure angle. It has been found that implementation of positive profile shift and pressure angle modification reduces bending stress considerably. In the paper [13], the Lewis factor of an external spur gear tooth for different coefficient of asymmetry is calculated for different number of teeth and it is found that Lewis factor increases with coefficient of asymmetry and number of teeth.

Then, in the paper [14]**,** the single-tooth bending fatigue strength and scuffing resistance of asymmetric and symmetric tooth gear are determined experimentally by designing, fabricating and testing specimens. Test results demonstrated higher bending fatigue strength for both the asymmetric tooth form and optimized fillet form compared to symmetric designs. Scuffing resistance was significantly increased for the asymmetric tooth form compared to a conventional symmetric involute tooth design. As an analytical study to determine the maximum bending stress, in the paper [2], a developed analytical method based on a previous trial graphical method has been introduced to find the solution of bending stress equation for symmetric and external asymmetric spur gear teeth with and without profile correction and for different gear design parameters. In order to achieve this analytical solution, certain geometrical properties for gear tooth shape of tooth loading angle, tooth critical section thickness, the load height from this section and Lewis form factor which are imperative to formulate the final form of the tooth bending stress equation must be determined analytically step-by-step. As a result of this work, the trial graphical method has been avoided by establishing a simple analytical expression which can be easily solved and it gives a higher accuracy and requires a shorter time. In another analytical method in paper [15], in order to estimate the tooth thickness and height at the gear tooth critical bending stress section for external asymmetric spur gear tooth, the standard ISO B methodology has been adapted suitably such that at the critical section 30 degrees is used for the drive side tangent angle and for the coast side tangent angle, coast side pressure angle minus drive side pressure angle is added to 30 degrees. Then, the critical tooth thickness and height and the parameters depending on them such as root fillet radius of curvature and tooth form factor for asymmetric spur gear tooth with several sets of drive side and coast side pressure angles are determined through an adapted ISO method and a comparative study with FEM is also carried out. An optimum design for an internal gear pair for the desired values of input parameters has been attempted through a direct gear design approach in paper [16]. By synthesizing several sets of asymmetric pinion cutters for specific values of input parameters, the respective internal gear and external pinion generated

by them have been analyzed by FEA for a balanced and lowest possible maximum fillet stress to decide the optimum one. A conventional gear design process has also been suggested with stub tooth concept in this regard.

A simple and effective approach to rating asymmetric tooth gears is outlined in paper [17]. The maximum bending stress is calculated by either using 2-D or 3D FEA for both asymmetric and comparable symmetric gear teeth and a bending stress conversion coefficient is defined by using FEA results of these gears. Then a standard stress analysis for the comparable symmetric gear tooth is done and the bending safety factor is found. Finally the bending safety factor for the asymmetric gear tooth is obtained by using the symmetric gear tooth bending safety factor and the bending stress conversion coefficient. The Direct Gear Design approach to asymmetric epicyclic gear stages with the singular and compound planet gears is outlined in paper [18]. Methods of optimization of the tooth flank asymmetry factor and root fillet profile are considered. This allows for a considerable increase in power transmission density, increase in load capacity, and reduction in the size and weight of asymmetric epicyclic gear drives. And an example implementation of asymmetric epicyclic gears has been demonstrated**.** This example is two stage planetary gearbox of the TV7-117S turboprop engine is demonstrated. This engine has been used in the Russian airplane IL-114 for several years and is going to be used in IL-112, MIG-110, TU-136 airplanes which resulted in extremely low weight to output torque ratio [19].

CHAPTER 2

EXTERNAL ASYMMETRIC SPUR GEAR TOOTH GEOMETRY AND ANALYTICAL BENDING STRESS INVESTIGATION

2.1 Generation of External Involute Spur Gear Tooth by a Rack Cutter

The generation of an external involute spur gear by a rack-cutter is shown in Fig. 2.1. The gear to be cut rotates with angular velocity ω about O, and the rack-cutter moves with velocity v.

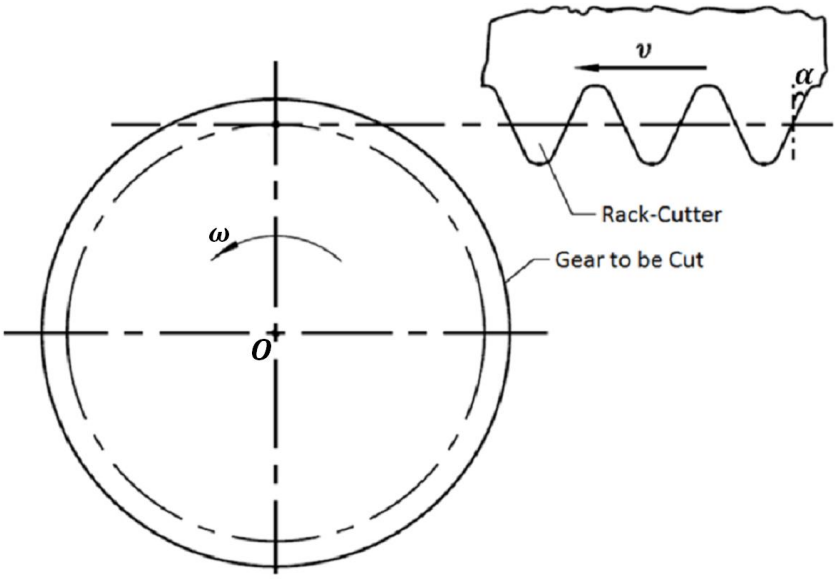

Fig. 2.1 Basic visualization of external spur gear generation by a rack-cutter

The rack-cutter and the external involute gear tooth are both composed of three parts as seen in Fig. 2.2. The inclined surface Σ_1 generates the involute flank surface Σ_2.

The round surface Σ_{1r} generates the root fillet surface Σ_{2f}. And the straight surface Σ_{1d} generates the dedendum circle surface Σ_{2d}.

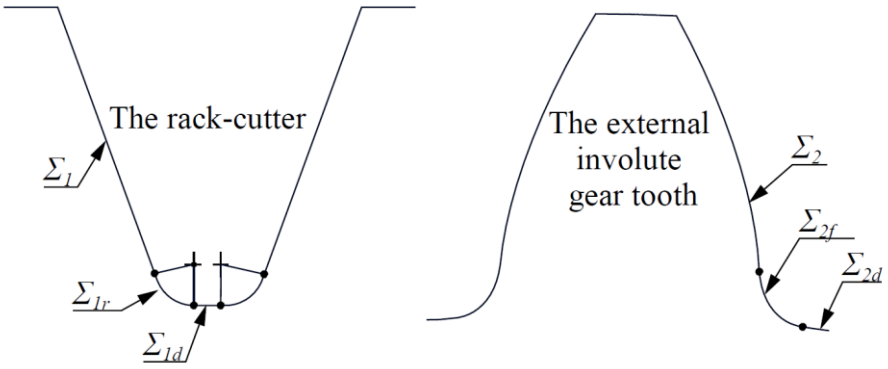

Fig. 2.2 Generating parts of rack-cutter and the corresponding generated parts of external spur gear tooth

2.1.1 The Generation of the Gear Involute Flank Surface

The rack-cutter inclined surface Σ_1 generates the involute flank surface Σ_2 as mentioned above. The basic kinematic relations of the generation and how to obtain gear involute flank surface are discussed below.

2.1.1.1 Basic Kinematic Relations

A rack-cutter having a constant linear velocity, v, have a constant normal angle, α, and normal velocity component, $v\cos(\alpha)$, on all points along the inclined surface, Σ_1. In order for two bodies to remain in contact their normal velocities on contact points must be equal as stated in [20]. Thus for conjugate action during the generation of involute flank surface, the gear to be cut must have the same constant normal angle and velocity with the rack-cutter inclined surface on all contact points. As it is illustrated in Fig. 2.3 by regarding constant angular velocity of the gear to be cut, ω, constant normal velocity $v\cos(\alpha)$ is only possible when the common normal

lines on all contact points are always tangent to the same circle, called base circle, with radius r_b.

$$\omega r_b = v\cos(\alpha) \tag{2.1}$$

By also knowing that these normal lines have the same angle, α, they result in a single line, called line of action, which includes all contact points.

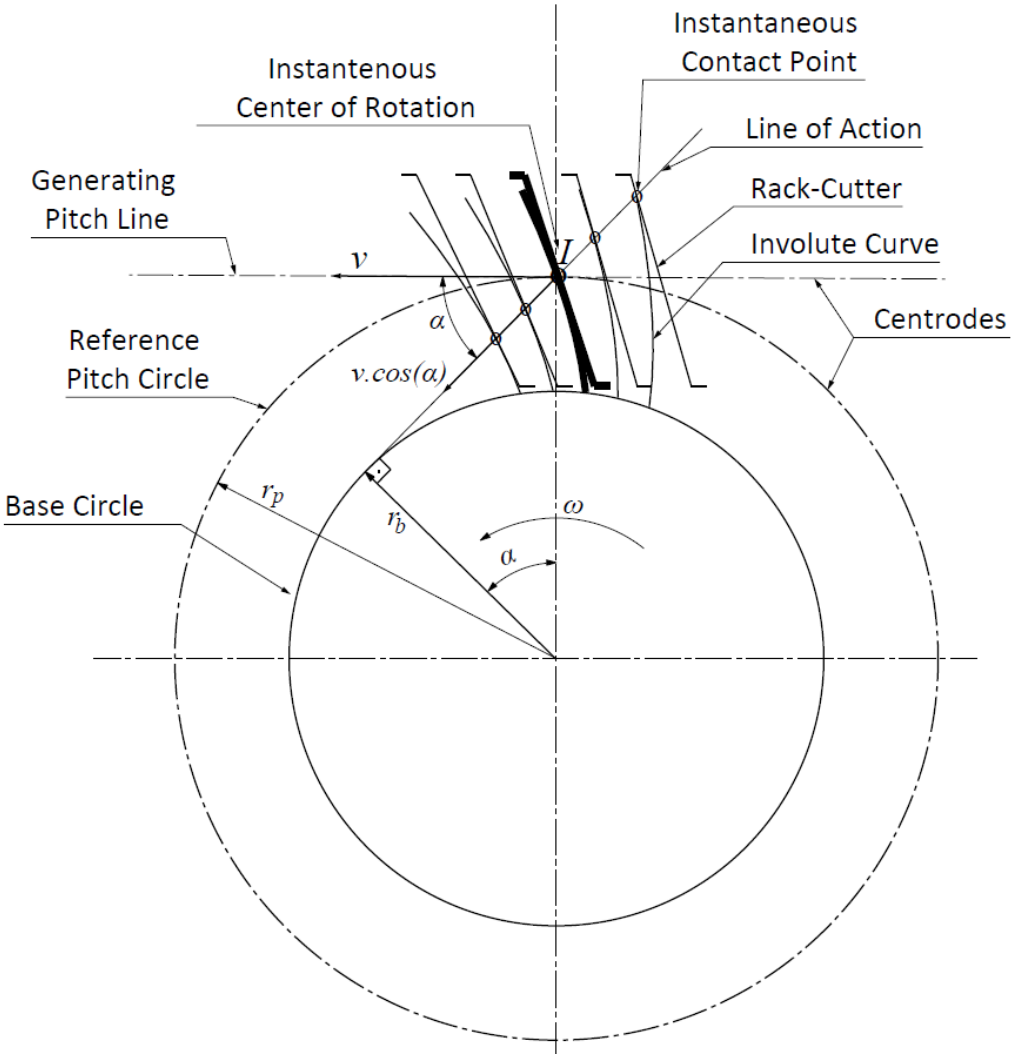

Fig. 2.3 Generation of external gear involute flank surface by the inclined surface of the rack-cutter

According to Lewis theorem any point of the rack-cutter inclined surface Σ_1, generates the corresponding point of the gear involute flank surface Σ_2 in a position that their common normal intersects the gear vertical center line at a point I called instantaneous center of rotation. At point I, the velocity of the gear to be cut is ωr_p that is parallel to the rack-cutter velocity, v and has the angle α with the line of action. And for this point, the normal velocity component of the gear to be cut is $\omega r_p \cos(\alpha)$ which must be equal to the constant normal velocity $v \cos(\alpha)$ of the rack-cutter inclined surface for the conjugate action. Then,

$$\omega r_p \cos(\alpha) = v \cos(\alpha) \tag{2.2}$$

$$\omega r_p = v \tag{2.3}$$

As seen in Equation (2.3) the velocities of the gear to be cut and the rack-cutter are equal to each other at the instantaneous center of rotation, I.

Also, use Equations (2.1) and (2.2):

$$\omega r_p \cos(\alpha) = \omega r_b \tag{2.4}$$

$$r_b = r_p \cos(\alpha) \tag{2.5}$$

2.1.1.1.1 Sliding Velocity

The conjugate surfaces have equal velocities along the common normal at contact point as it is mentioned above. In general the tangential velocity components differ in magnitude as it is illustrated in Fig. 2.4. This results in a relative velocity or sliding velocity v_{sl} between two centroids.

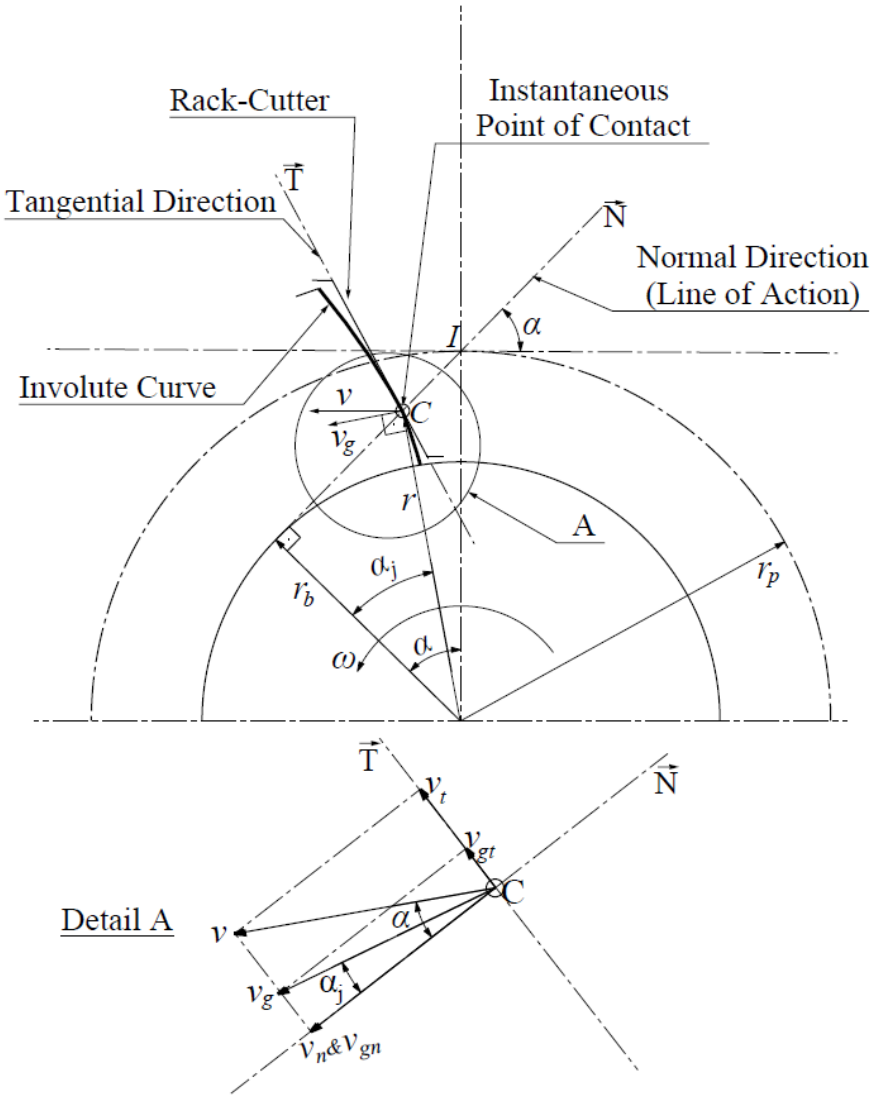

Fig. 2.4 Instantaneous point of contact during generation of external gear involute flank surface

$$v_{gn} = v_g \cos(\alpha_j) \tag{2.6}$$

$$v_n = v \cos(\alpha) \tag{2.7}$$

Use the equality of normal velocities at contact point:

$$v_{gn} = v_n \tag{2.8}$$

$$v_g = \frac{v \cos(\alpha)}{\cos(\alpha_j)} \tag{2.9}$$

$$v_t = v \sin(\alpha) \tag{2.10}$$

$$v_{gt} = v_g \sin(\alpha_j) \tag{2.11}$$

$$v_{sl} = v_t - v_{gt} \tag{2.12}$$

$$v_{sl} = v \sin(\alpha) - v_g \sin(\alpha_j) \tag{2.13}$$

$$v_{sl} = v \sin(\alpha) - \frac{v \cos(\alpha)}{\cos(\alpha_j)} \sin(\alpha_j) \tag{2.14}$$

$$v_{sl} = v\big(sin(\alpha) - cos(\alpha)\, tan\big(\alpha_j\big)\big) \tag{2.15}$$

Here, v and α are constant and α_j, the instantaneous pressure angle of the involute flank surface, varies by rotation for any contact point. Thus v_{sl} is a function of angle rotation. And the sliding or relative velocity is only zero at point I, instantaneous center of rotation where α_j and v_g is equal to α and v, respectively, so that v_{gt} is equal to v_t.

2.1.1.2 Parametric Representation of the Family of Surfaces

The coordinate systems, $S_1(x_1, y_1, z_1)$, $S_2(x_2, y_2, z_2)$ and $S_f(x_f, y_f, z_f)$ that are rigidly connected to rack-cutter, external gear to be cut and reference frame, respectively, as illustrated in Fig. 2.5.

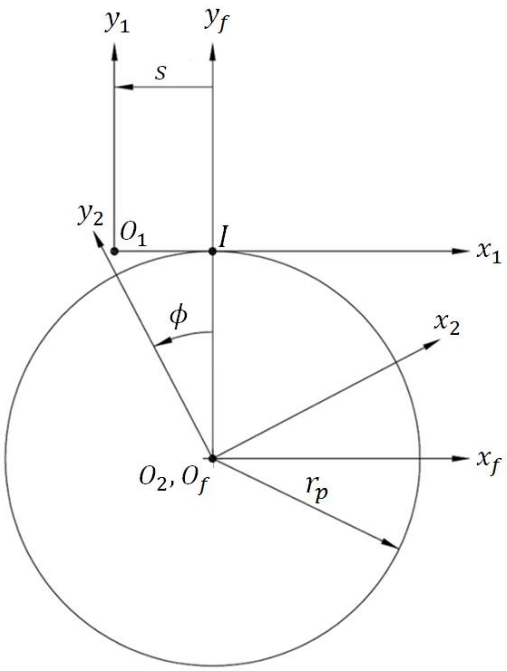

Fig. 2.5 Coordinate Systems of rack-cutter, external gear and reference frame

For any point on the rack-cutter inclined surface, r_1 represents the position vector of that point in S_1. As illustrated in Fig. 2.6, u and f are the rack-cutter inclination direction and face width direction, respectively. And in terms of all u and f components, $r_1(u, f)$ represents the rack-cutter inclined surface Σ_1, in S_1.

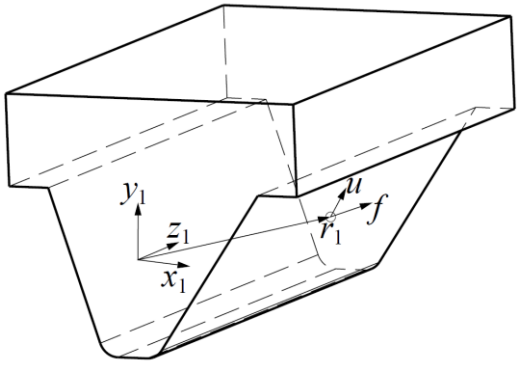

Fig. 2.6 Position vector of rack-cutter inclined surface

During the generation motion, the rack-cutter inclined surface, Σ_1, can be represented by a corresponding surface in S_2 at any instant. For the whole generation motion these corresponding surfaces are called as the family of surfaces, Σ_ϕ, illustrated in Fig. 2.7.

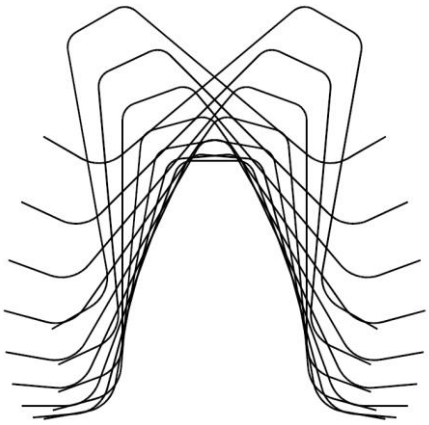

Fig. 2.7 The family of surfaces during external spur gear generation by a rack-cutter

In order to obtain parametric representation of the family of surfaces, Σ_ϕ, firstly, a translation matrix, M_{f1}, between S_1&S_f and secondly, a rotation matrix, M_{2f}, between S_f&S_2 should be applied on the rack-cutter inclined surface, $r_1(u, f)$. Then the following matrix equation is obtained:

$$r_2 = M_{2f} M_{f1} r_1 \tag{2.16}$$

The counter-clockwise rotation matrix in x-y plane around z axis has the following form,

$$R(\phi) = \begin{bmatrix} cos\,\phi & -sin\,\phi & 0 \\ sin\,\phi & cos\,\phi & 0 \\ 0 & 0 & 1 \end{bmatrix} \tag{2.17}$$

The direction of a vector rotation is counter-clockwise if ϕ is positive and the direction of a vector rotation is clockwise if ϕ is negative. According to the Fig. 2.5 during the generation motion, the direction of gear rotation is counter-clockwise so the direction of the rotation matrix, M_{2f}, which is opposite to the direction of the gear rotation, is clockwise and ϕ is negative. Then the rotation matrix M_{2f} can be written as:

$$M_{2f} = R(-\phi) = \begin{bmatrix} cos\,\phi & sin\,\phi & 0 \\ -sin\,\phi & cos\,\phi & 0 \\ 0 & 0 & 1 \end{bmatrix} \tag{2.18}$$

The translation matrix, M_{f1}, is related with r_p and s as seen in Fig. 2.5. The translation matrix components can be added to fourth column and written as:

$$M_{f1} = \begin{bmatrix} 1 & 0 & 0 & -s \\ 0 & 1 & 0 & r_p \\ 0 & 0 & 1 & 0 \\ 0 & 0 & 0 & 1 \end{bmatrix} \tag{2.19}$$

During the generation motion for a given time interval, t, the gear rotates amount of ϕ about O_2 with an angular velocity, ω, and the rack-cutter translates amount of s with a velocity, v. Then s can be found as follows:

For gear:

$$\phi = \omega t \tag{2.20}$$

For rack-cutter:

$$s = vt \tag{2.21}$$

Use Equation (2.3) in Equation (2.21):

$$s = \omega r_p t \tag{2.22}$$

Use Equation (2.3) in Equation (2.21):

$$s = r_p \phi \tag{2.23}$$

Thus M_{f1} can be rewritten as:

$$M_{f1} = \begin{bmatrix} 1 & 0 & 0 & -r_p\phi \\ 0 & 1 & 0 & r_p \\ 0 & 0 & 1 & 0 \\ 0 & 0 & 0 & 1 \end{bmatrix} \tag{2.24}$$

The rotation matrix M_{2f} is modified for matrix multiplication convenience and written as:

$$M_{2f} = \begin{bmatrix} cos\,\phi & sin\,\phi & 0 & 0 \\ -sin\,\phi & cos\,\phi & 0 & 0 \\ 0 & 0 & 1 & 0 \\ 0 & 0 & 0 & 1 \end{bmatrix} \tag{2.25}$$

According to the position of the rack-cutter in S_1, coordinates of r_1 change and in Chapter 2.2.3.1, r_1 matrix is defined accordingly desired rack-cutter position in S_1. However as being independent on the rack-cutter position in S_1 the coordinates of r_1 are function of u and f as mentioned above. And the elements of both matrices M_{f1} and M_{2f} are functions of ϕ as seen in Equations (2.24) and (2.25). Thus r_2 is a function of u, f and ϕ and $r_2(u, f, \phi)$ represents the family of surfaces, Σ_ϕ.

2.1.1.3 The Determination of the Envelope to the Family of Surfaces

The envelope of a family of surfaces is tangent to each surfaces of the family along the characteristic curve. As seen in Fig. 2.3, at any instant during the generation motion, the gear to be cut is in contact (tangency) with the rack-cutter inclined surface (an instantaneous surface of the family, Σ_ϕ, in S_f) along the line of action (characteristic curve). Thus, the generated external involute flank surface of the gear, Σ_2, is determined as the envelope to the family of surfaces, Σ_ϕ.

The partial derivatives $\partial r_2/\partial u$ and $\partial r_2/\partial f$ represent the tangents to each point on the rack-cutter inclined surface in S_2 at each instant. And the cross product of these tangents gives the normal vectors to these points and represented as follows:

$$N = \frac{\partial r_2}{\partial u} \times \frac{\partial r_2}{\partial f} \tag{2.26}$$

As illustrated in Fig. 2.4, the sliding velocity vector v_s is in the tangential direction at any contact point. Thus, at any point where one of the surfaces of the family and the involute tooth surface of the gear, Σ_2, are in tangency, the normal vector of that surface of the family and v_{sl} must be perpendicular to each other. So, the dot product of these two vectors is zero at any tangency point and if the dot product of these vectors is not zero, then, there is no tangency. This is the engineering approach

method to determine the involute flank surface of the external gear, Σ_2, as being envelope to the family of surfaces, Σ_ϕ, in gear theory [21].

$$\left(\frac{\partial r_2}{\partial u} \times \frac{\partial r_2}{\partial f}\right) \cdot v_{sl} = 0 \tag{2.27}$$

As shown in Fig. 2.4, at any point where one of the surfaces of the family and the involute flank surface of the gear, Σ_2, are in tangency:

$$r_2 \omega = v_g \tag{2.28}$$

$$r_2 \omega = v_{gn}\, \hat{n} + v_{gt}\, \hat{t} \tag{2.29}$$

$$\frac{\partial (r_2 \omega)}{\partial \phi} = \frac{\partial \left(v_{gn}\, \hat{n} + v_{gt}\, \hat{t}\right)}{\partial \phi} \tag{2.30}$$

$$\omega \frac{\partial r_2}{\partial \phi} = \frac{\partial (v_{gn})}{\partial \phi} \hat{n} + \frac{\partial (v_{gt})}{\partial \phi} \hat{t} \tag{2.31}$$

During the generation motion, the normal velocity of the contact point is constant as mentioned in Chapter 2.1.1.1, so its partial derivative with respect to ϕ is zero. Then Equation (2.31) reduces to:

$$\omega \frac{\partial r_2}{\partial \phi} = \frac{\partial (v_{gt})}{\partial \phi} \hat{t} \tag{2.32}$$

$$\frac{\partial r_2}{\partial \phi} = \frac{1}{\omega} \cdot \frac{\partial (v_{gt})}{\partial \phi} \hat{t} \tag{2.33}$$

Equation (2.33) shows that the partial derivative $\partial r_2 / \partial \phi$ is in the tangential direction at any contact point. This is also the direction of v_{sl}. So, in Equation (2.27), $\partial r_2 / \partial \phi$

can be used instead of v_{sl}. This is the classical or differential approach method to determine the involute tooth surface of the gear, Σ_2, as being envelope to the family of surfaces, Σ_ϕ, in gear theory [21].

$$\left(\frac{\partial r_2}{\partial u} \times \frac{\partial r_2}{\partial f}\right) \cdot \frac{\partial r_2}{\partial \phi} = 0 \tag{2.34}$$

These Equations (2.27) and (2.34) are called as equation of meshing. In this thesis the differential approach method with equation (2.34) is used in order to obtain gear geometry.

2.1.2 The Generation of the Gear Root Fillet Surface

The generation of the gear root fillet is illustrated in Fig. 2.8 by considering coordinate systems illustrated in Fig. 2.5. As defined in introduction of Chapter 2, the rack-cutter round surface Σ_{1r} generates the gear root fillet surface Σ_{2f}.

2.1.2.1 Basic Kinematic Relations

During the conjugate action the normal velocities must be equal and this equality can be written as:

$$v \sin(\theta) = \omega r_{bf} \tag{2.35}$$

Here, θ defines the point on the rack-cutter round surface between m_1 and m_2 and changes with respect to the contact point at any instant, so does the normal velocity as seen in Fig. 2.8. Thus, r_{bf} is not constant and is a function of θ. Then Equation (2.35) can be rewritten as:

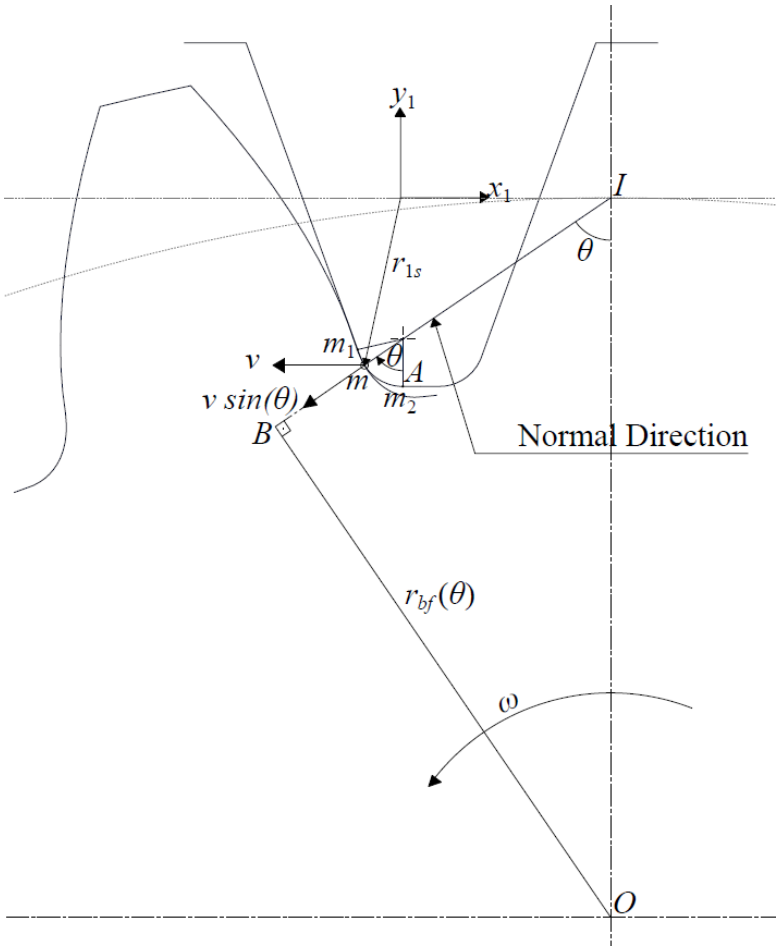

Fig. 2.8 Generation of external gear root fillet surface by the rounded surface of the rack-cutter

$$v\sin(\theta) = \omega r_{bf}(\theta) \tag{2.36}$$

$$\frac{v}{\omega} sin(\theta) = r_{bf}(\theta) \tag{2.37}$$

Use Equation (2.3) in Equation (2.37):

$$r_p sin(\theta) = r_{bf}(\theta) \tag{2.38}$$

As seen in Fig. 2.8, $\widehat{OIB}$ is equal to θ and by using OIB right triangle:

$$OI\ sin(\theta) = OB \tag{2.39}$$

$$OI\ sin(\theta) = r_{bf}(\theta) \tag{2.40}$$

Use Equation (2.38) in Equation (2.40):

$$OI \sin(\theta) = r_p \sin(\theta) \tag{2.41}$$

$$OI = r_p \tag{2.42}$$

The equation above shows that OI is equal to the reference pitch radius as being independent on θ. This can be explained according to Lewis theorem that a point of the rack-cutter round surface generates the respective point of the gear root fillet surface at a position where their common normal at the point of contact passes through the instantaneous center of rotation, I.

2.1.2.2 The Determination of the Envelope to the Family of Surfaces

For any point on the rack-cutter round surface, r_{1r} represents the position vector of that point in S_1. The vector r_{1r} is dependent on f, face width direction, and θ. And in terms of all f and θ components, $r_{1r}(\theta, f)$ represents the surface Σ_{1r}, rack-cutter round surface, in S_1. The r_{1r} matrix is defined in Chapter 2.2.3.2 because of the same reason for r_1 mentioned in Chapter 2.1.1.2.

Since the generation motions are same for both gear involute tooth and root fillet surfaces, the rotation and the translation matrices are also same for these two generations. Then, r_{1r} is represented in S_2 as:

$$r_{2f} = M_{2f} M_{f1} r_{1r} \tag{2.43}$$

Here r_{2f} is a function of θ, f and ϕ and $r_{2f}(\theta, f, \phi)$ representing the family of surfaces $\Sigma_{\phi f}$, generated in S_2 by surface Σ_{1r}, and illustrated in Fig. 2.7 together with $\Sigma_{\phi f}$.

Because of the conjugate action during the generation, the gear root fillet surface, Σ_{2f}, is determined as the envelope to the family of surfaces, $\Sigma_{\phi f}$. And as mentioned in Section 2.1.1.3, the equation of meshing is used to find the envelope. Then modify Equation (2.34) for the gear root fillet surface and obtain:

$$\left(\frac{\partial r_{2f}}{\partial \theta} \times \frac{\partial r_{2f}}{\partial f}\right) \cdot \frac{\partial r_{2f}}{\partial \phi} = 0 \tag{2.44}$$

2.2 Details of Asymmetric Rack Cutter and External Asymmetric Spur Gear Tooth

In order to generate an external asymmetric spur gear tooth, an asymmetric rack-cutter is used. The details of an asymmetric rack-cutter and external asymmetric spur gear tooth are discussed in the following sections.

2.2.1 Details of an Asymmetric Rack Cutter

Fig. 2.9 shows a representative transverse cross sectional shape of basic asymmetric rack-cutter, which is used to generate the respective asymmetric tooth profiles. The rack tooth thickness and space width at the tool reference line are $\pi m/2$. If the direction of the profile shift coefficient, x, is downward, it is negative and if the direction of x is upward, it is positive. With reference to Fig. 2.9 the rack tooth thickness and space width at the generating pitch line, t and t_{ref}, are defined by:

$$t = \pi m/2 + x_d + x_c \tag{2.45}$$

$$x_d = -xm \tan \alpha_d \tag{2.46}$$

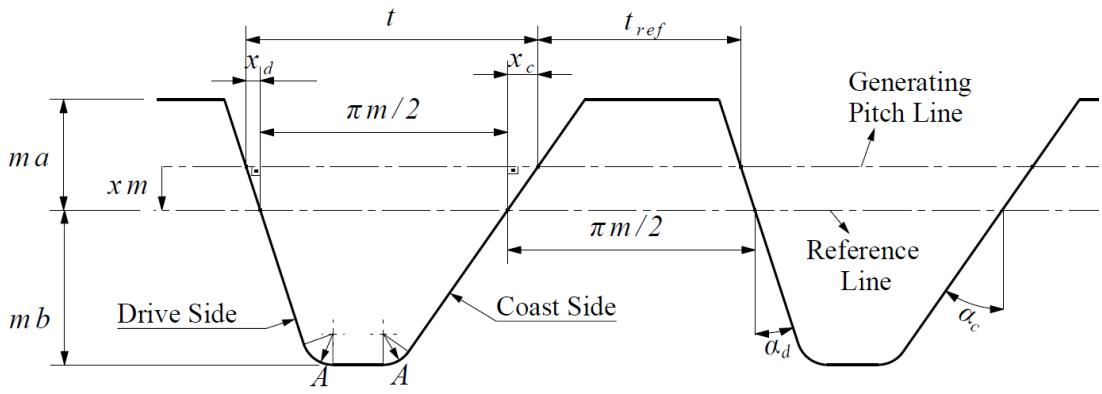

Fig. 2.9 Asymmetric rack-cutter details

$$x_c = -xm \tan \alpha_c \tag{2.47}$$

$$t = \pi m/2 - xm(\tan \alpha_d + \tan \alpha_c) \tag{2.48}$$

$$t_{ref} = \pi m - t \tag{2.49}$$

$$t_{ref} = \pi m/2 + xm(\tan \alpha_d + \tan \alpha_c) \tag{2.50}$$

The rack-cutter may be full-rounded with a radius A_{max}. The detailed derivation for calculating A_{max} is given in Appendix A.1 and is expressed by:

$$A_{max} = \frac{\pi m/2 - mb(tan\, \alpha_d + tan\, \alpha_c)}{\frac{1}{cos\, \alpha_d} + \frac{1}{cos\, \alpha_c} - (tan\, \alpha_d + tan\, \alpha_c)} \tag{2.51}$$

2.2.2 Details of an External Asymmetric Spur Gear Tooth

Fig. 2.10 shows a representative transverse cross sectional shape of basic external asymmetric spur gear tooth. Gear tooth axis is defined as the line passing through the gear center and the point where tooth tip is pointed. Here r_t is the pointed tooth tip radius and can be found as defined in Appendix B.1.

Pitch circle is the reference pitch circle with radius:

$$r_p = \frac{mZ}{2} \tag{2.52}$$

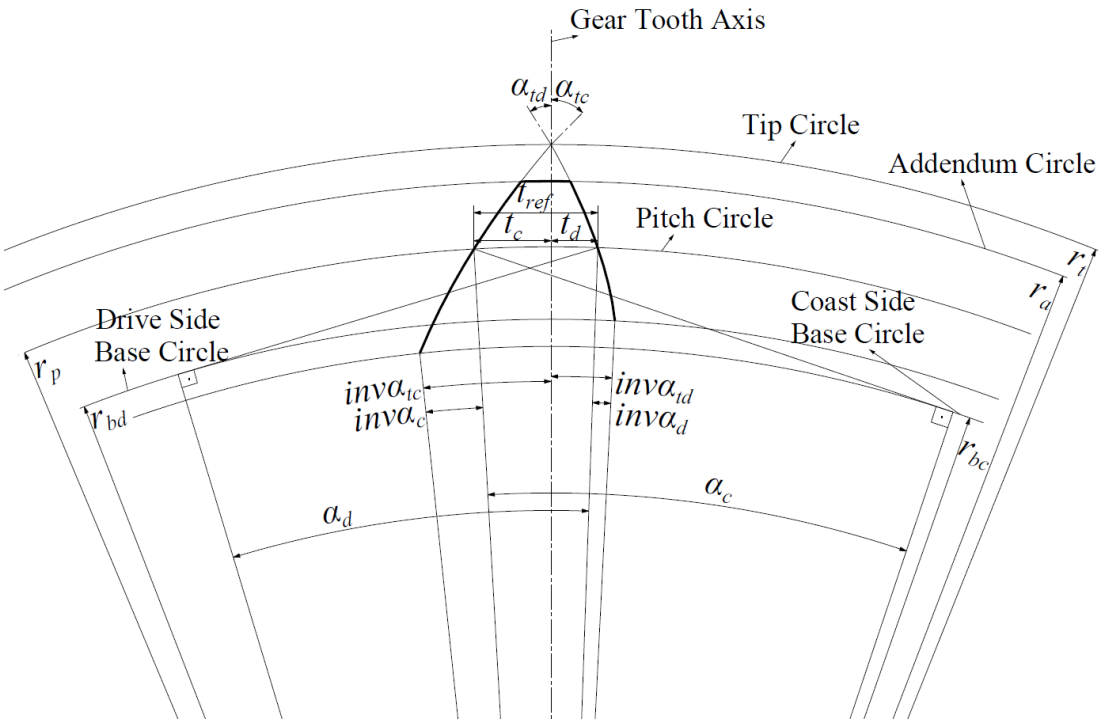

Fig. 2.10 External asymmetric spur gear details

Regarding Equation (2.5) drive and coast sides base circles can be respectively defined as:

$$r_{bd} = r_p \cos \alpha_d \tag{2.53}$$

$$r_{bc} = r_p \cos \alpha_c \tag{2.54}$$

The gear tooth thickness at reference pitch circle is equal to the tooth space width of the rack-cutter at generating pitch line which is t_{ref}. And the detailed derivation for calculating the drive and coast sides tooth thicknesses is given in Appendix B.1 and is expressed by:

$$t_d = \frac{mN}{2}\left(tan\left(cos^{-1}\left(\frac{r_{bd}}{r_t}\right)\right) - cos^{-1}\left(\frac{r_{bd}}{r_t}\right) - inv\alpha_d \right) \tag{2.55}$$

$$t_c = \frac{mN}{2}\left(tan\left(cos^{-1}\left(\frac{r_{bc}}{r_t}\right)\right) - cos^{-1}\left(\frac{r_{bc}}{r_t}\right) - inv\alpha_c \right) \tag{2.56}$$

2.2.3 Determination of the Position Vector Matrices for the Surfaces of the Asymmetric Rack Cutter

The position of the rack-cutter in S_1 gives us the desired external gear tooth position in S_2. In FEA for bending stress an external gear tooth is analyzed as its tooth axis being coincide with the vertical axis. Thus the rack-cutter should be positioned in S_1 so that the obtained gear tooth axis coincides with the vertical axis.

Fig. 2.11 illustrates that the dark colored inclined and rounded surfaces of drive and coast sides of the asymmetric rack-cutter generates the asymmetric external gear dark colored flank and root fillet surfaces which represent the tooth space. By complete

circular patterning as the number of the gear tooth, the asymmetric gear having the desired tooth position is obtained.

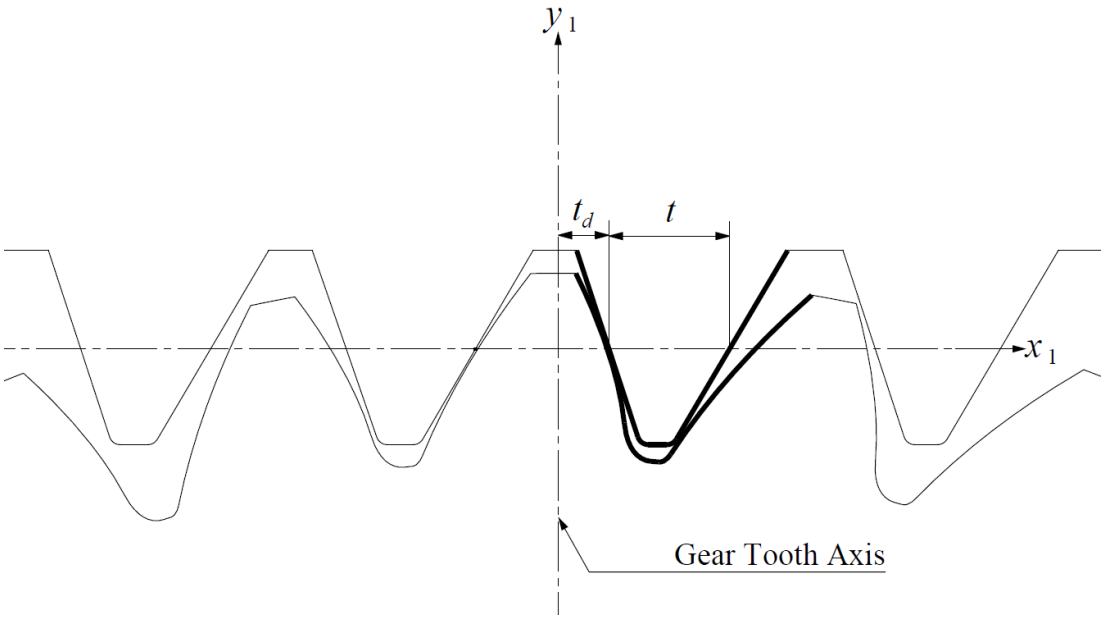

Fig. 2.11 The desired position of the external asymmetric gear tooth

2.2.3.1 Determination of the Position Vector Matrices for the Inclined Surfaces of the Asymmetric Rack Cutter Coast and Drive Sides

With reference to Fig. 2.12 and Fig. 2.13, the asymmetric rack-cutter drive and coast side inclined surfaces are defined as:

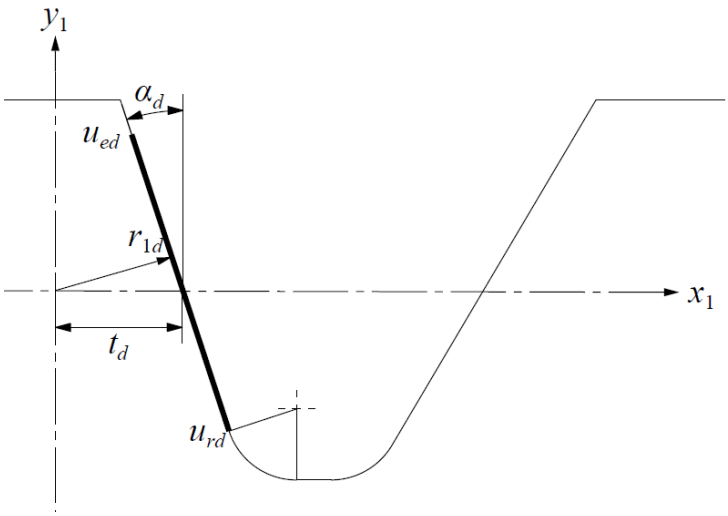

Fig. 2.12 The position vector of asymmetric rack-cutter drive side inclined surface

$$r_{1d} = \begin{bmatrix} t_d - u_d \sin\alpha_d \\ u_d \cos\alpha_d \\ f \\ 1 \end{bmatrix} \quad u_{rd} \le u_d \le u_{ed} \ , \ 0 \le f \le f_w \tag{2.57}$$

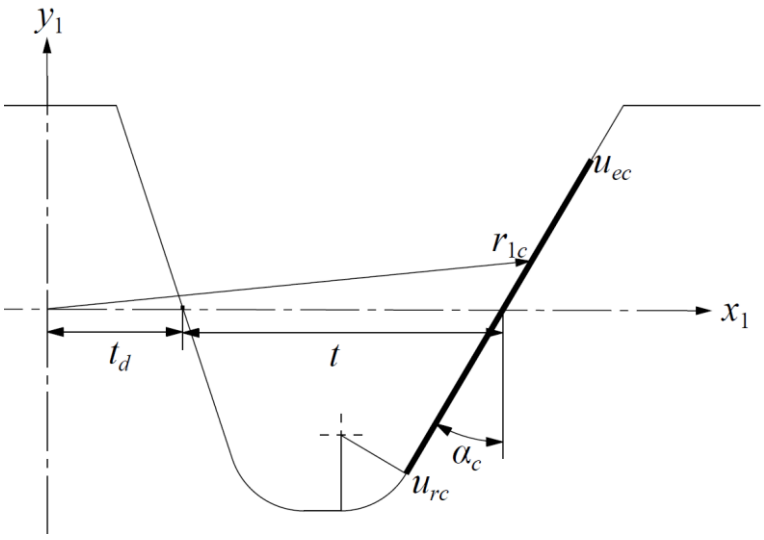

Fig. 2.13 The position vector of asymmetric rack-cutter coast side inclined surface

$$r_{1c} = \begin{bmatrix} t_d + t + u_c \sin\alpha_c \\ u_c \cos\alpha_c \\ f \\ 1 \end{bmatrix} \quad u_{rc} \le u_c \le u_{ec} \ , \ 0 \le f \le f_w \tag{2.58}$$

In Equations (2.57) and (2.58) the first and second rows are x and y components. The detailed derivations of u_{ed}, u_{rd}, u_{ec}, u_{rc} are in Appendices A.2 and A.3 and expressed by:

$$u_{ed} = \left(r_a.\sin\left(\cos^{-1}\left(\frac{r_{bd}}{r_a}\right)\right) - r_p.\sin\alpha_d\right).\tan\alpha_d \tag{2.59}$$

$$u_{rd} = -\frac{mb - A + A\sin\alpha_d}{\cos\alpha_d} \tag{2.60}$$

$$u_{ed} = (r_a.\sin\left(\cos^{-1}\left(\frac{r_{bc}}{r_a}\right)\right) - r_p.\sin\alpha_c).\tan\alpha_c \tag{2.61}$$

$$u_{rc} = -\frac{mb - A + A\sin\alpha_c}{\cos\alpha_c} \tag{2.62}$$

The third row is face-width component. For a spur gear the involute gear tooth sections are all same through the face-width direction. Finally the fourth row is added for appropriate matrix multiplication in Equations (2.57) and (2.58).

2.2.3.2 Determination of the Position Vector Matrices for the Rounded Surfaces of the Asymmetric Rack Cutter Coast and Drive Sides

With reference to Fig. 2.14 and Fig. 2.15, the asymmetric rack-cutter drive and coast side rounded surfaces are defined as:

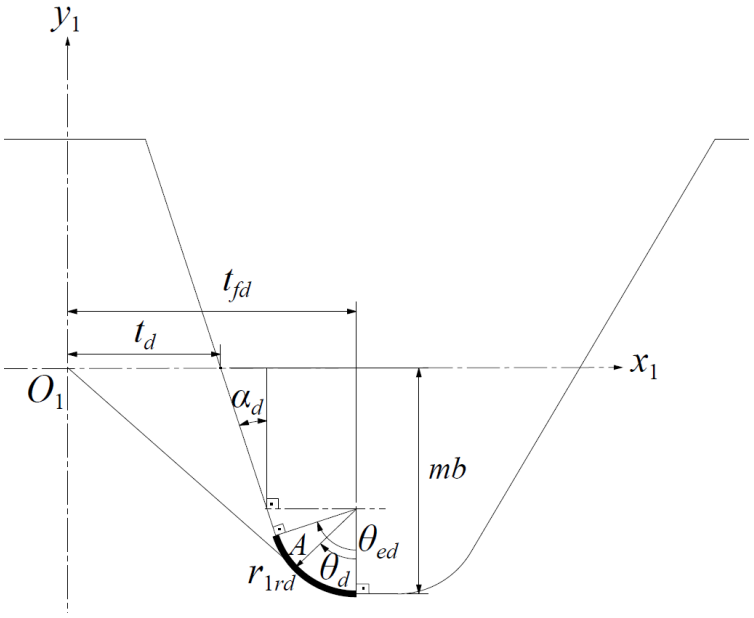

Fig. 2.14 The position vector of asymmetric rack-cutter drive side rounded surface

$$r_{1rd} = \begin{bmatrix} t_{fd} - A\sin\theta_d \\ -mb + A - A\cos\theta_d \\ f \\ 1 \end{bmatrix} \quad 0 \le \theta_d \le \theta_{ed} \ , \ \ 0 \le f \le f_w \tag{2.63}$$

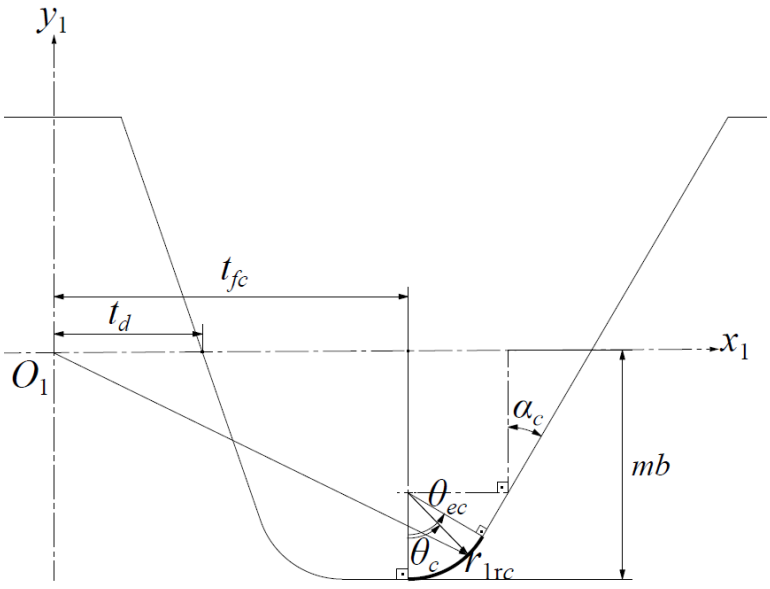

Fig. 2.15 The position vector of asymmetric rack-cutter coast side rounded surface

$$r_{1rc} = \begin{bmatrix} t_{fc} + A\sin\theta_c \\ -mb + A - A\cos\theta_c \\ f \\ 1 \end{bmatrix} \quad 0 \le \theta_c \le \theta_{ec} \ , \ \ 0 \le f \le f_w \tag{2.64}$$

With reference to Fig. 2.14 and Fig. 2.15:

$$\theta_{ed} = \frac{\pi}{2} - \alpha_d \tag{2.65}$$

$$\theta_{ec} = \frac{\pi}{2} - \alpha_c \tag{2.66}$$

The detailed derivations of t_{fd}, t_{fc} are in Appendix A.4 and expressed by:

$$t_{fd} = t_d + (mb - A)\tan\alpha_d + \frac{A}{\cos\alpha_d} \tag{2.67}$$

$$t_{fc} = t_d + t - (mb - A)\tan\alpha_c - \frac{A}{\cos\alpha_c} \tag{2.68}$$

2.3 Analytical Method to Determine the Critical Bending Stress Section and Related Parameters for an External Asymmetric Spur Gear Tooth

In this section a modified ISO B method which is very similar to the method in [15] mentioned in Chapter 1.2, is used in order to determine the critical tooth thickness and tooth height for an asymmetric external spur gear. In this method, as illustrated in Fig. 2.16, the drive side tangent angle at the critical section β_d is equal to 30°, same with [15] but the coast side tangent angle at the critical section β_c is not same with [15] and calculated by using the generation of the external gear coast side root fillet.

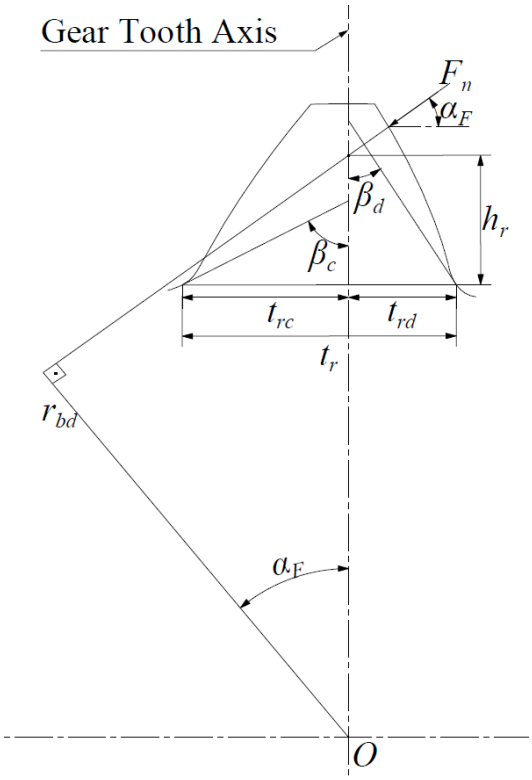

Fig. 2.16 The basic visualization of external asymmetric spur gear tooth bending stress critical section

2.3.1 Determination of the Angle and Radius of the Applied Force

The maximum bending stress on the external gear root occurs when the force is applied on the gear tooth at the highest point single tooth contact according to [6] as mentioned in Chapter 1.2. In order to verify the critical tooth thickness and tooth height, firstly radius of the applied force, r_F, and angle, α_F, as illustrated in Fig. 2.17 shall be determined. For this, radius of the highest point single tooth contact point, r_h, must be known. The detailed derivation of r_h is in Appendix B.3.

$$\alpha_h = \cos^{-1}\left(\frac{r_{bd}}{r_h}\right) \tag{2.69}$$

$$inv\alpha_h = \tan\alpha_h - \alpha_h \tag{2.70}$$

$$\alpha_F = \alpha_h - (inv\alpha_{td} - inv\alpha_h) \tag{2.71}$$

$$r_F = \frac{r_{bd}}{\cos(\alpha_F)} \tag{2.72}$$

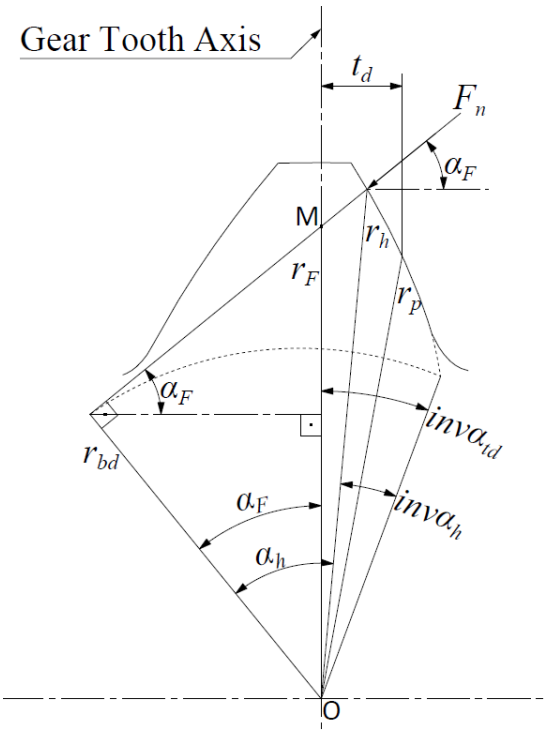

Fig. 2.17 The applied force at hpstc and the related parameters

2.3.2 Determination of the Critical Tooth Thickness and Height

The critical tooth thickness and tooth height can be determined by using the generation of the gear root fillet with a rack-cutter. Firstly, the drive side critical tooth thickness and the critical tooth height are obtained. Then with respect to the critical section, the coast side critical tooth thickness is obtained. Finally, the summation of the drive and coast side critical tooth thicknesses gives the critical tooth thickness.

2.3.2.1 Determination of the Drive Side Critical Tooth Thickness and Height

The drive side critical tooth thickness and tooth height are obtained by using the generation of the external asymmetric spur gear drive side root fillet surface with the asymmetric rack-cutter drive side rounded surface. Fig. 2.18 shows the generation of the gear drive side root fillet at point P where the critical section occurs.

The rack-cutter translates amount of s_d and with reference to Equation (2.23), s_d is equal to:

$$s_d = r_p \phi_d \tag{2.73}$$

$$PH = s_d - P_x \tag{2.74}$$

P_x: Absolute value of x component of r_{1rd}, Fig. 2.14, Equation (2.63)

$$PH = r_p \phi_d - (t_{fd} - A \sin \theta_d) \tag{2.75}$$

PH is also equal to:

$$PH = IH \tan \theta_d \tag{2.76}$$

IH: Absolute value of y component of r_{1rd}, Fig. 2.14, Equation (2.63)

$$PH = (mb - A + A \cos \theta_d) \tan \theta_d \tag{2.77}$$

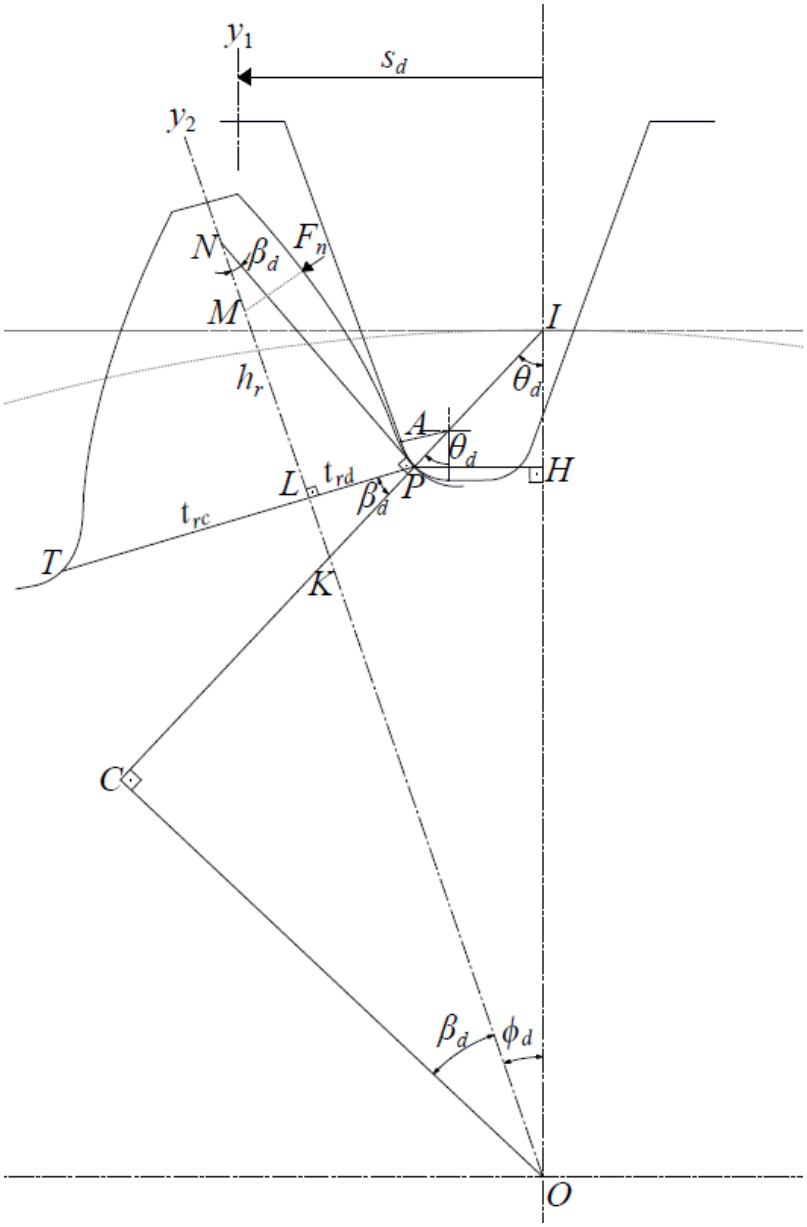

Fig. 2.18 The generation of the external asymmetric spur gear drive side root fillet at the location where the critical section occurs

By using Equations (2.75) and (2.77), obtain ϕ_d in terms of θ_d:

$$\phi_d = \frac{(mb - A + A\cos\theta_d)\tan\theta_d + (t_{fd} - A\sin\theta_d)}{r_p} \tag{2.78}$$

As seen in $\widehat{OCI}$ triangle:

$$\theta_d + \beta_d + \phi_d = \frac{\pi}{2} \tag{2.79}$$

Note that:

$$\beta_d = \frac{\pi}{6} \tag{2.80}$$

And put Equations (2.78) and (2.79) in equation (2.80) and solve for θ_d. Then,

$$PI = \frac{IH}{\cos\theta_d} \tag{2.81}$$

$$PI = \frac{(mb - A + A\cos\theta_d)}{\cos\theta_d} \tag{2.82}$$

$$CI = OI\cos\theta_d \tag{2.83}$$

$$CI = r_p\cos\theta_d \tag{2.84}$$

$$OC = OI\sin\theta_d \tag{2.85}$$

$$OC = r_p\sin\theta_d \tag{2.86}$$

$$CK = OC\ tan\ \beta_d \tag{2.87}$$

$$CK = r_p\ sin\ \theta_d\ tan\ \beta_d \tag{2.88}$$

$$KP = CI - PI - CK \tag{2.89}$$

$$KP = r_p\ cos\ \theta_d - \frac{(mb - A + A\ cos\ \theta_d)}{cos\ \theta_d} - \left(r_p\ sin\ \theta_d\ tan\ \beta_d\right) \tag{2.90}$$

$$t_{rd} = KP\ cos\ \beta_d \tag{2.91}$$

$$t_{rd} = \left(r_p\ cos\ \theta_d - \frac{(mb - A + A\ cos\ \theta_d)}{cos\ \theta_d} - \left(r_p\ sin\ \theta_d\ tan\ \beta_d\right)\right) cos\ \beta_d \tag{2.92}$$

$$OK = \frac{OC}{cos\ \beta_d} \tag{2.93}$$

$$OK = \frac{r_p\ sin\ \theta_d}{cos\ \beta_d} \tag{2.94}$$

$$KL = KP\ sin\ \beta_d \tag{2.95}$$

$$KL = \left(r_p\ cos\ \theta_d - \frac{(mb - A + A\ cos\ \theta_d)}{cos\ \theta_d} - \left(r_p\ sin\ \theta_d\ tan\ \beta_d\right)\right) sin\ \beta_d \tag{2.96}$$

$$h_r = OM - (OK + KL) \tag{2.97}$$

Note that OM is r_F, Fig. 2.17, then:

$$h_r = r_F - \left(\frac{r_p \sin\theta_d}{\cos\beta_d} + \left(r_p \cos\theta_d - \frac{(mb - A + A\cos\theta_d)}{\cos\theta_d}\cdots - \left(r_p \sin\theta_d \tan\beta_d\right)\right)\sin\beta_d\right) \tag{2.98}$$

2.3.2.2 Determination of the Coast Side Critical Tooth Thickness and Height

The coast side critical tooth thickness is obtained by using the generation of the external asymmetric spur gear coast side root fillet surface with the asymmetric rack-cutter coast side rounded surface. Fig. 2.19 shows the generation of the gear coast side root fillet at point T where the critical section occurs.

The rack-cutter translates amount of s_c and with reference to Equation (2.23), s_c is equal to:

$$s_c = r_p \phi_c \tag{2.99}$$

$$FT = s_c - T_x \tag{2.100}$$

T_x: $\pi m -$ (Absolute value of x component of r_{1rc}) , Fig. 2.15, Equation (2.64)

$$FT = r_p \phi_c - \left(\pi m - \left(t_{fc} + A\sin\theta_c\right)\right) \tag{2.101}$$

FT is also equal to:

$$FT = IF\tan\theta_c \tag{2.102}$$

IF: Absolute value of y component of r_{1rc}, Fig. 2.15, Equation (2.64)

$$FT = (mb - A + A\cos\theta_c)\tan\theta_c \tag{2.103}$$

By using Equations (2.101) and (2.103), obtain ϕ_c in terms of θ_c:

$$\phi_c = \frac{(mb - A + A\cos\theta_c)\tan\theta_c + \left(\pi m - \left(t_{fc} + A\sin\theta_c\right)\right)}{r_p} \tag{2.104}$$

As seen in $\widehat{ORI}$ triangle:

$$\theta_c + \beta_c + \phi_c = \frac{\pi}{2} \tag{2.105}$$

Put Equation (2.103) in Equation (2.104) and obtain β_c in terms of θ_c. Then,

$$\beta_c = \frac{\pi}{2} - \theta_c - \frac{(mb - A + A\cos\theta_c)\tan\theta_c + \left(\pi m - \left(t_{fc} + A\sin\theta_c\right)\right)}{r_p} \tag{2.106}$$

$$TI = \frac{IF}{\cos\theta_c} \tag{2.107}$$

$$TI = \frac{(mb - A + A\cos\theta_c)}{\cos\theta_c} \tag{2.108}$$

$$RI = OI\cos\theta_c \tag{2.109}$$

$$RI = r_p\cos\theta_c \tag{2.110}$$

$$OR = OI\sin\theta_c \tag{2.111}$$

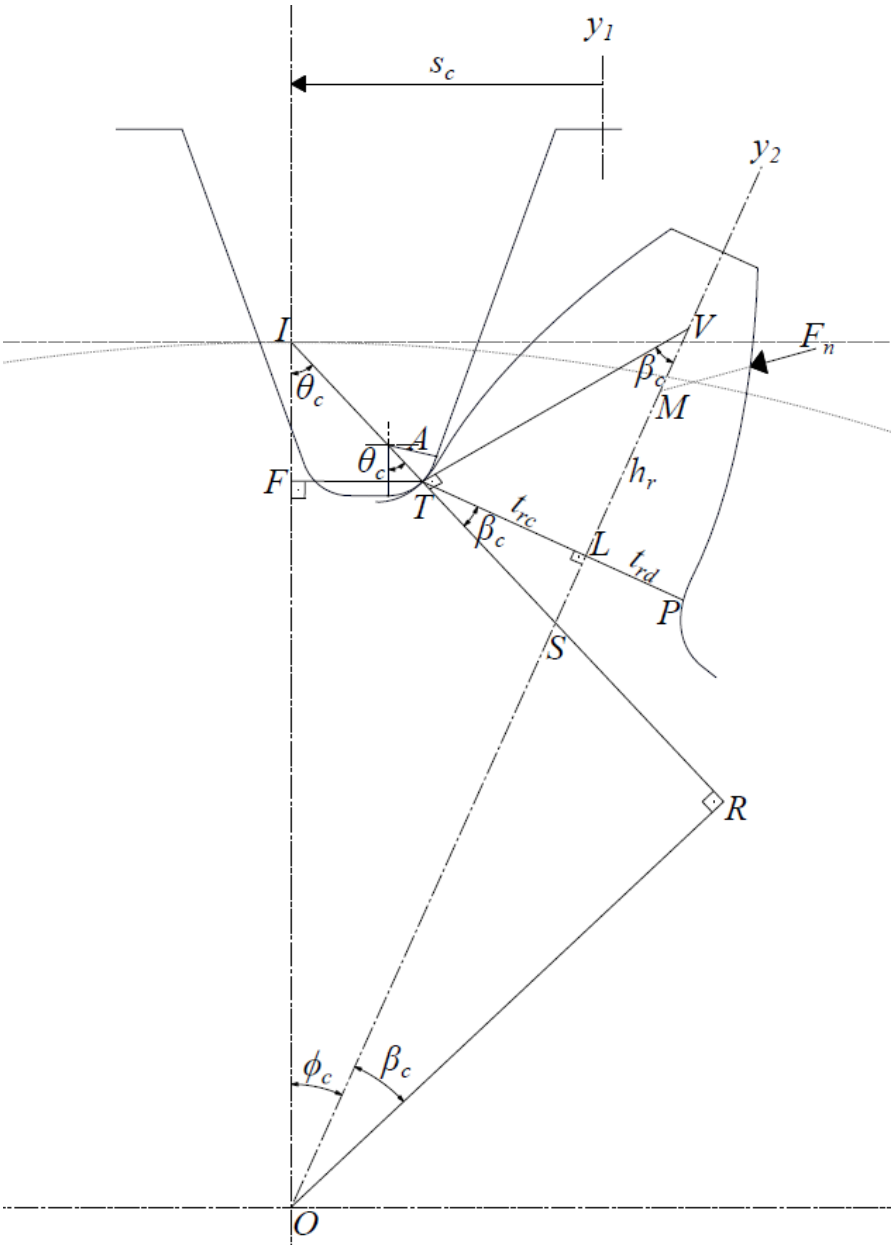

Fig. 2.19 The generation of the external asymmetric spur gear coast side root fillet at the location where the critical section occurs

$$OR = r_p \sin\theta_c \tag{2.112}$$

$$RS = OR \tan\beta_c \tag{2.113}$$

$$RS = r_p \sin\theta_c \tan\beta_c \tag{2.114}$$

$$ST = RI - TI - RS \tag{2.115}$$

$$ST = r_p \cos\theta_c - \frac{(mb - A + A\cos\theta_c)}{\cos\theta_c} - \left(r_p \sin\theta_c \tan\beta_c\right) \tag{2.116}$$

$$OS = \frac{OR}{\cos\beta_c} \tag{2.117}$$

$$OS = \frac{r_p \sin\theta_c}{\cos\beta_c} \tag{2.118}$$

$$SL = ST \sin\beta_c \tag{2.119}$$

$$SL = \left(r_p \cos\theta_c - \frac{(mb - A + A\cos\theta_c)}{\cos\theta_c} - \left(r_p \sin\theta_c \tan\beta_c\right)\right)\sin\beta_c \tag{2.120}$$

$$h_r = OM - (OS + SL) \tag{2.121}$$

$$h_r = r_F - \left(\frac{r_p \sin\theta_c}{\cos\beta_c} + \left(r_p \cos\theta_c - \frac{(mb - A + A\cos\theta_c)}{\cos\theta_c}\cdots - \left(r_p \sin\theta_c \tan\beta_c\right)\right)\sin\beta_c\right) \tag{2.122}$$

Note that β_c is already obtained in terms of θ_c, in Equation (2.106). If Equation (2.106) is put into the Equation (2.122), then h_r is only a function of θ_c. And remember that h_r is already found in Equation (2.98). Then if the Equation (2.98) is equated to Equation (2.122), θ_c at point T is found. After that put θ_c in Equation (2.106) and obtain β_c. Now, the coast side critical tooth thickness can be obtained as below:

$$t_{rc} = ST \cos \beta_c \tag{2.123}$$

$$t_{rc} = \left(r_p \cos \theta_c - \frac{(mb - A + A \cos \theta_c)}{\cos \theta_c} - \left(r_p \sin \theta_c \tan \beta_c \right) \right) \cos \beta_c \tag{2.124}$$

2.4 Determination of Tooth Form Factor, Stress Correction Factor and Maximum Bending Stress for an External Asymmetric Spur Gear Tooth through Modified ISO and FEA

The maximum bending stress at the external spur gear tooth root may be expressed through the following known relation:

$$\sigma = \frac{F_n}{fm} Y_F Y_S \tag{2.125}$$

where, F_n is normal load, Y_F is tooth form factor and Y_S is stress correction factor. In addition to the bending stress formulations of AGMA and ISO standards, the compressive stress produced by the radial load F_r is also taken in to account in this thesis so that the normal force F_n is used instead of F_t in Equation (2.125).

Y_F and Y_S are determined for an external asymmetric gear tooth with both modified ISO and FEA methods in the following Chapters.

2.4.1 Modified ISO Method for Bending Stress Parameters

The tooth form factor Y_F is also affected by the radial load F_r. The detailed derivation of Y_F can be found in Appendix of [15] and defined as:

$$(Y_F)_{ISO} = \frac{6mh_r \cos \alpha_F}{{t_r}^2} - \frac{m \sin \alpha_F}{t_r} \tag{2.126}$$

where,

$$t_r = t_{rc} + t_{rd} \tag{2.127}$$

The stress correction factor Y_S is defined in [5] as:

$$(Y_S)_{ISO} = (1.2 + 0.13L){q_s}^{\left[\frac{1}{1.21+\frac{2.3}{L}}\right]} \tag{2.128}$$

where,

$$L = \frac{t_r}{h_r} \tag{2.129}$$

$$q_s = \frac{t_r}{2\rho_F} \tag{2.130}$$

Here, ρ_F is the root fillet radius of curvature of the drive side root fillet trochoid at the critical section and can be found with the help of the Fig. 2.20:

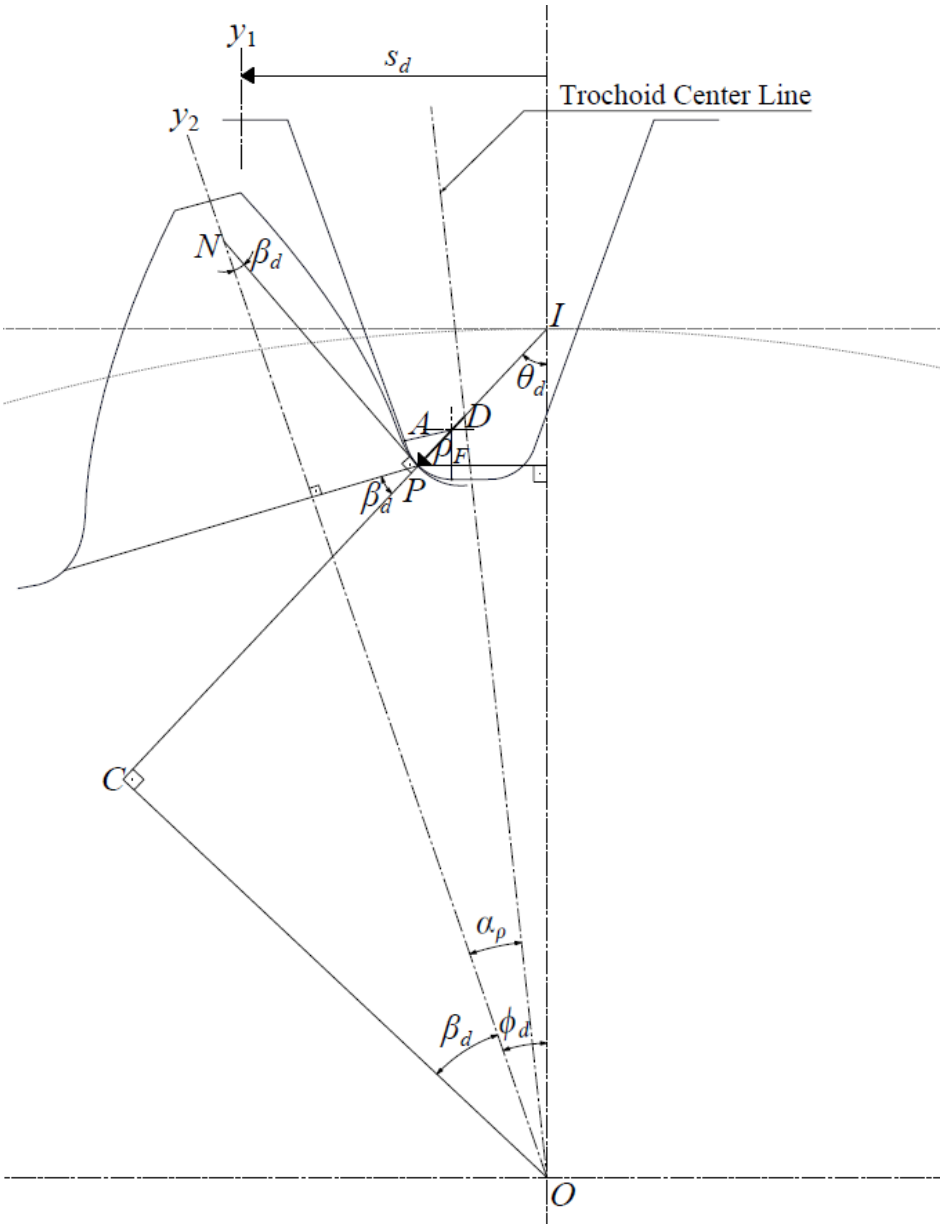

Fig. 2.20 The root fillet radius of curvature at the drive side critical section of the external asymmetric spur gear

$$\rho_F = PI - (CI - CD) \tag{2.131}$$

Here, PI and CI are already defined by Equations (2.82), (2.84) and CD is defined as:

$$CD = OC \tan(\beta_d + \alpha_\rho) \tag{2.132}$$

Here, β_d and OC are already defined by Equations (2.80), (2.86) and the angle α_ρ can be defined by the help of Fig. 2.21:

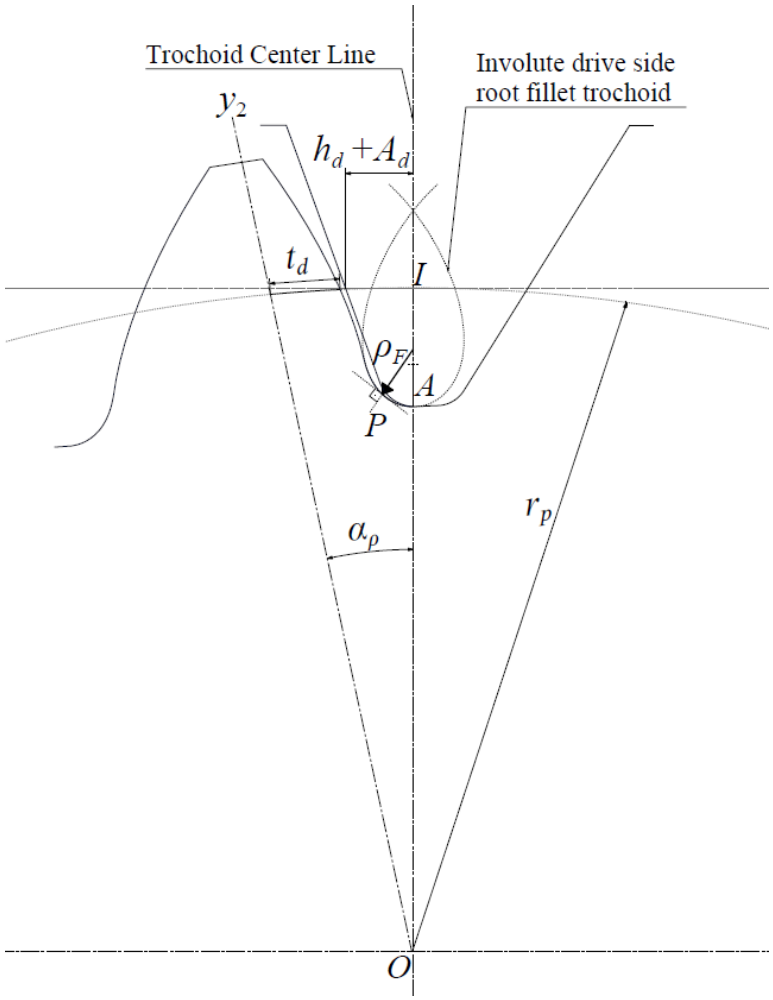

Fig. 2.21 The angle of the root fillet radius of curvature at the drive side critical section of the external asymmetric spur gear

$$r_p \alpha_\rho = t_d + h_d + A_d \tag{2.133}$$

The parameters h_d and A_d are found by using Equations (A.1), (A.2) and (A.4).

$$\alpha_\rho = \frac{t_d + h_d + A_d}{r_p} \tag{2.134}$$

Finally, the stress correction factor, $(Y_S)_{ISO}$, can be estimated, too. Then, the maximum bending stress of an asymmetric gear tooth root can be calculated by:

$$(\sigma)_{ISO} = \frac{F_n}{f_w m} (Y_F)_{ISO} (Y_S)_{ISO} \tag{2.135}$$

2.4.2 FEA Method for Bending Stress Parameters

Tensile stresses cause crack initiations and propagations. Thus, in terms of the bending failure of a gear tooth, the maximum tensile stress on the root fillet can be defined as the maximum bending stress. Additionally the maximum tensile stress is determined as the maximum principle stress which is normal to the surface where shear stresses are zero. Therefore the maximum principle stress on the root fillet gives the maximum bending stress through FEA.

$$(\sigma)_{FEA} = \frac{F_n}{f_w m} (Y_F)_{FEA} (Y_S)_{FEA} \tag{2.136}$$

The form factor $(Y_F)_{FEA}$ is calculated with Equation (2.126) by using FEA based values of t_r and h_r. Then $(Y_S)_{FEA}$ can be defined as:

$$(Y_S)_{FEA} = \frac{(\sigma)_{FEA}}{\frac{F_n}{f_w m} (Y_F)_{FEA}} \tag{2.137}$$

The FEA based ρ_F at the critical section is obtained by using Equation (2.131) with the FEA based critical section parameters which are defined in Chapter 2.4.2.2.1.

In order to use this method, 2D FEA is carried out in this thesis and the asymmetric external spur gear 2D FE model is the need for FEA. In order to create a 2D FE model, firstly, a 3D cat model of the asymmetric internal spur gear is created in this thesis and 2D gear geometry is obtained by using this cat model. Then 2D FE model can be created by using this 2D gear geometry.

2.4.2.1 External Asymmetric Spur Gear 3D Model

The external asymmetric spur gear as shown in Fig. 2.23 is obtained by using a Matlab code, written according to the theory explained in this thesis, and illustrated in Fig. 2.22. Here, the profile is consist of points and represents the tooth space surface. Also the profile is 3D and the points continue through the face width direction. Since this is a spur gear, the profile at each section is same.

Fig. 2.22 External asymmetric spur gear tooth space profile

In order to obtain 3D model of the external asymmetric spur gear, firstly, the points obtained in Matlab are put in an excel file, a macro of CATIA V5 R22. This macro has the spline option inside itself. By choosing this spline option the involute flank and trochoidal root profiles are generated in CATIA from these points. Later in

generative shape design of CATIA the generated flank and root profiles are joined and the gear tooth space surface is obtained from the jointed profiles being at different sections of the face width by using multi-section surface command. Then, a complete circular patterning as number of the gear tooth is done and the whole tooth space surfaces are obtained. After that, the whole tooth space surfaces are splitted from the 3D model of the gear to be cut which is a cylinder with a radius, r_a and a height, f_w. Finally, 3D model of the external asymmetric spur gear is obtained.

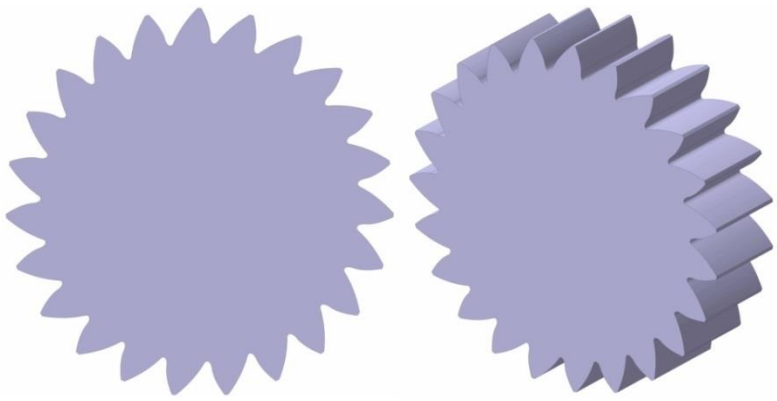

Fig. 2.23 External asymmetric spur gear 3D cat model

Later, by creating sketch on one of the faces of the gear and using the project 3D elements option in CATIA a 2D geometry of the external asymmetric spur gear can be obtained.

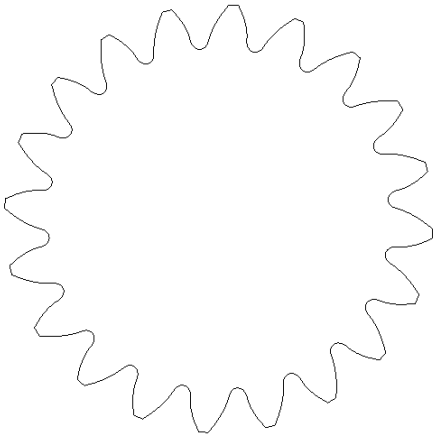

Fig. 2.24 External asymmetric spur gear 2D geometry

2.4.2.2 FE Model of the External Asymmetric Spur Gear

In this thesis FE modeling and analysis are done in ABAQUS 6.14. A sample 2D FE model of the external asymmetric spur gear is shown in Fig. 2.25. The FE model is consist of three tooth and have enough rim thickness to provide a rim thickness factor of 1 according to [5].

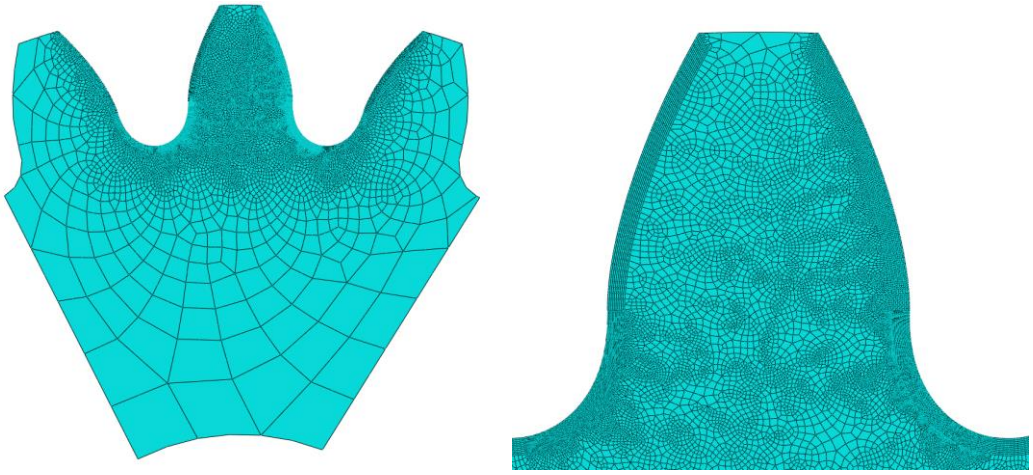

Fig. 2.25 External asymmetric spur gear tooth 2D FE model

FE model properties:

1) 2D FE analysis with plane strain condition is done by assuming a uniform load distribution along face width of the gear tooth.

2) The material is a linear elastic isotropic and homogeneous one with an elastic constant of E = 210 GPa and Poisson's ratio= 0.3.

3) The load is applied at RP-1 (reference point) which is HPSTC point. The reference point is coupled to the nodes at that diameter with continuum distributing and the FE model is fixed from the inner round and side lines as shown in Fig. 2.26.

4) The gear tooth profiles for this analysis have been generated using a full rounded rack cutter.

5) The 2-D 8-nodded quadratic elements are used to mesh the gear model. The loaded gear tooth flanks and root fillets and the next unloaded tooth flanks and root fillets are meshed sensitively by using partition regions, which are offset from the original profile around 0.1 times module. There are 350x10 elements in the loaded tooth drive side root fillet and 150x10 elements in the loaded tooth drive side flank and coast side root fillet and 50x10 elements in the loaded tooth coast side involute flank. There are also 50x5 elements in the next unloaded tooth flanks and root fillets. For the other regions suitable global size elements are used.

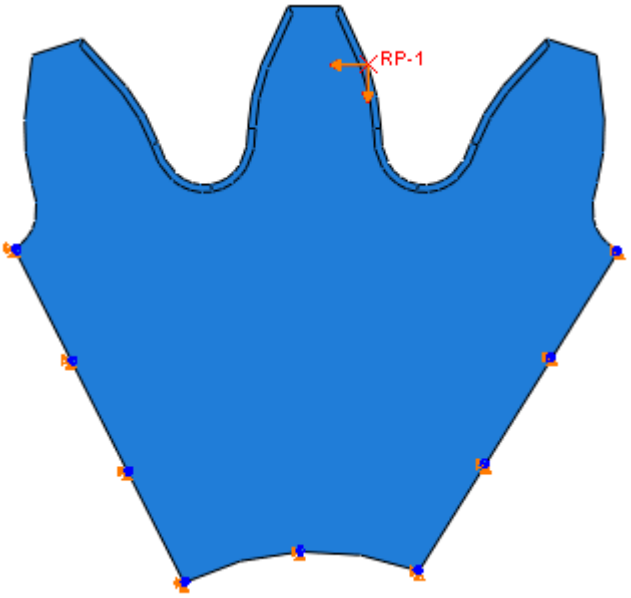

Fig. 2.26 External asymmetric spur gear tooth 2D FE model boundary condition and force application point

2.4.2.2.1 External Asymmetric Spur Gear FE Model Critical Section Parameters

In the FEA the maximum principle stress location which is the point P illustrated in Fig. 2.27, is found and defines the critical section. The x and y components of point P are read in Abaqus. Here, P_x and P_y are defined as:

$$P_x = t_{rd} \tag{2.138}$$

$$P_y = OL \tag{2.139}$$

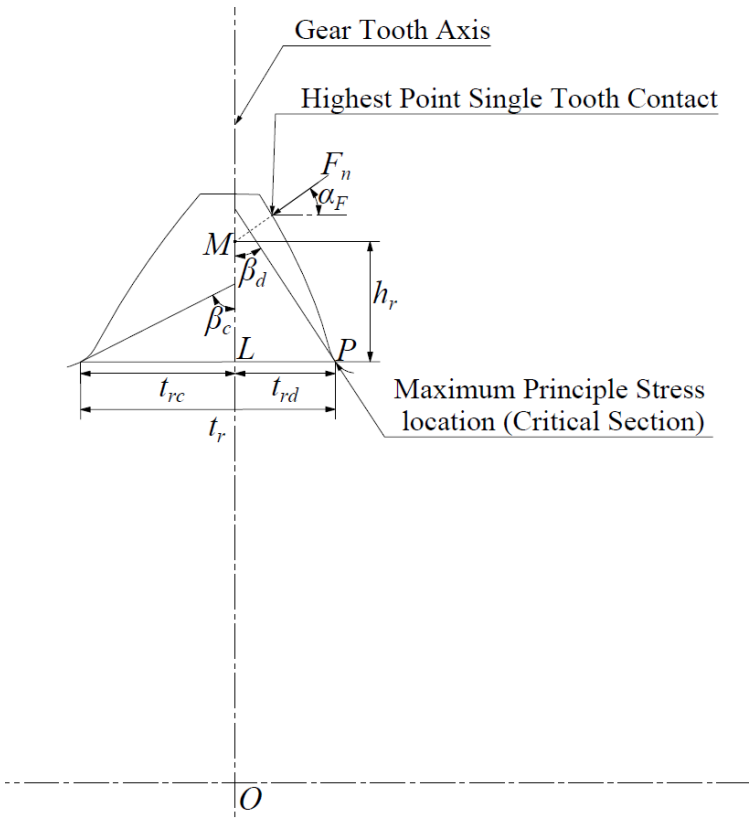

Fig. 2.27 External asymmetric spur gear tooth 2D FE model critical section

The critical tooth height is found as:

$$h_r = OM - (OL) \tag{2.140}$$

Remember that OM is r_F, Fig. 2.17, then:

$$h_r = r_F - P_y \tag{2.141}$$

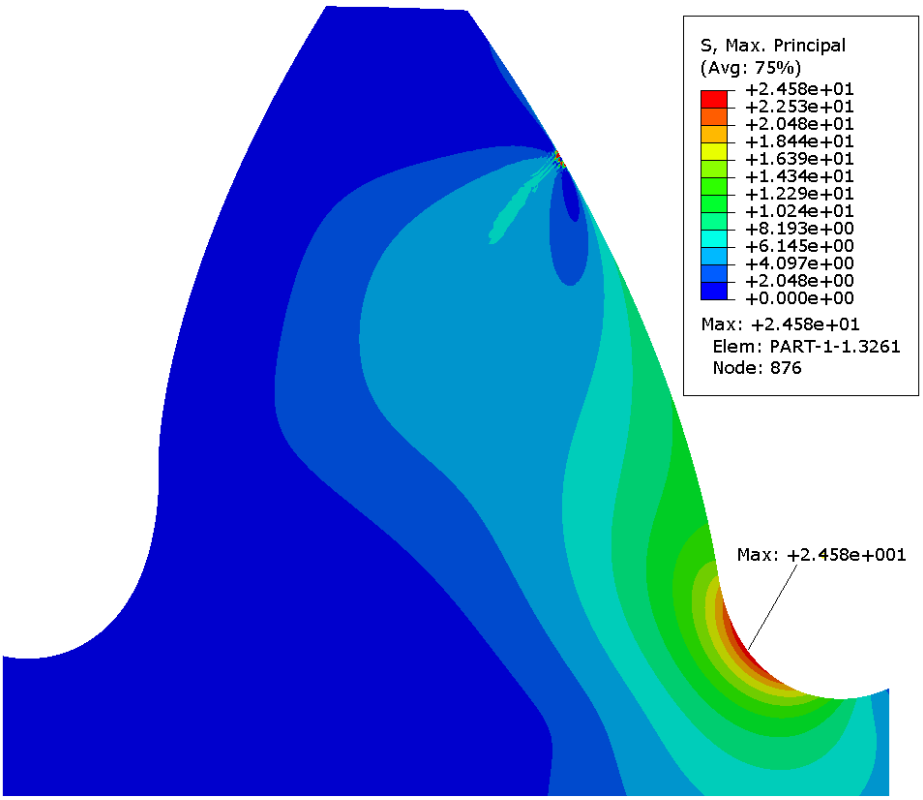

Fig. 2.28 An example of the FEA bending stress results for the external asymmetric spur gear with 20 teeth, α_{id}/α_{ic}=30°/20°

Since the critical tooth height is known and the critical section tangent angle is not known for the gear tooth drive side in FEA, the same method with the analytical method used in the coast side parameters derivation is used to obtain the drive side parameters in FEA method. According to this method the drive side critical tooth height is calculated by using Equation (2.98) and equated with Equation (2.141) so

that unknown parameters can be found. Although there are two unknowns θ_d and β_d in Equation (2.98) the drive side tangent angle β_d can be obtained in terms of θ_d by using Equations (2.78) and (2.79). Then θ_d becomes the only unknown and is found by equating Equations (2.98) and (2.141).

$$\beta_d = \frac{\pi}{2} - \theta_d - \frac{(mb - A + A\cos\theta_d)\tan\theta_d + (t_{fd} - A\sin\theta_d)}{r_p} \qquad (2.142)$$

The drive side critical section tooth thickness, t_{rd}, can also be found by using Equation (2.92) for FE model. The results of Equations (2.92) and (2.138) shall be equal such that the correctness of the analytical method is proven.

The coast side critical section parameters for FE model are found by using totally same equations and method mentioned in Chapter 2.3.2.2. The only difference is that the input parameter, the critical tooth height, is not obtained by analytical method but it comes from FEA. The coast side tangent angle and critical tooth thickness are found by using Equations (2.106) and (2.124), respectively.

CHAPTER 3

INTERNAL ASYMMETRIC SPUR GEAR TOOTH GEOMETRY AND ANALYTICAL BENDING STRESS INVESTIGATION

3.1 Generation of Internal Involute Spur Gear Tooth by a Pinion Type Shaper Cutter

The generation of an internal involute spur gear by a pinion type shaper cutter is shown in Fig. 3.1. The internal gear to be cut rotates with angular velocity ω_i about O_i, and the pinion type shaper-cutter rotates with angular velocity ω_s about O_s.

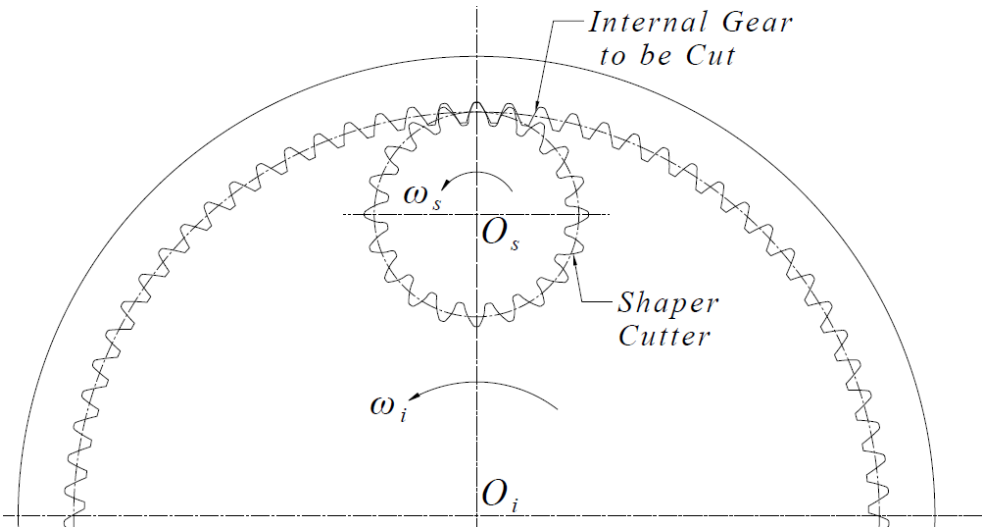

Fig. 3.1 Basic visualization of internal spur gear generation by a shaper cutter

The pinion type shaper cutter and the internal gear tooth are both composed of three parts as seen in Fig. 3.2. The shaper involute flank surface Σ_s generates the internal gear involute flank surface Σ_i. The shaper round surface Σ_{sr} generates the internal

gear root fillet surface Σ_{if}. And the shaper addendum surface Σ_{sd} generates the internal gear dedendum surface Σ_{id}.

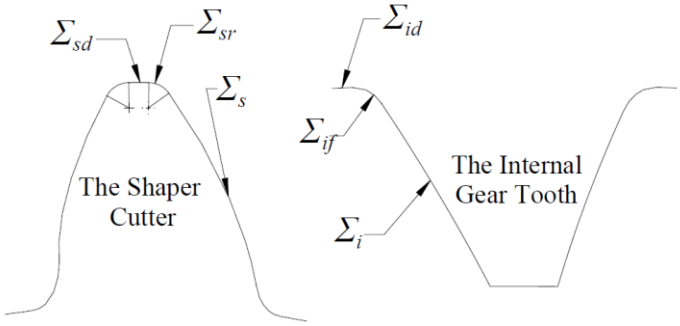

Fig. 3.2 Generating parts of pinon type shaper cutter and the corresponding generated parts of internal spur gear tooth

3.1.1 The Generation of the Gear Involute Flank Surface

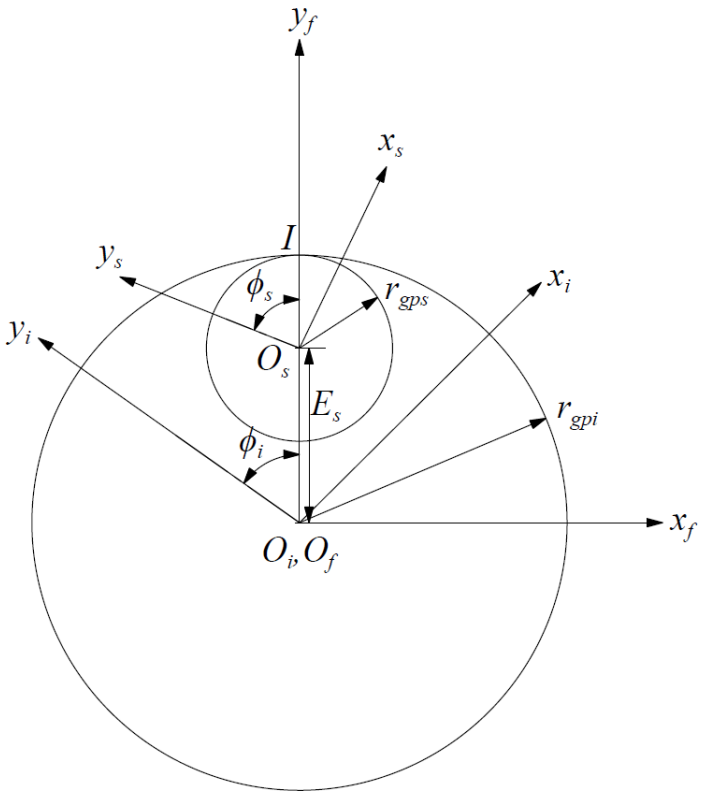

Fig. 3.3 Coordinate Systems of shaper, internal gear to be cut and gear housing

The shaper cutter involute flank surface Σ_s generates the internal gear involute flank surface Σ_i as mentioned above. The coordinate systems illustrated in Fig. 3.3, S_s, S_i and S_f that are rigidly connected to shaper-cutter, internal gear to be cut and frame (gear housing), respectively. By using these coordinate systems the basic kinematic relations of the generation and how to obtain internal gear involute flank surface are discussed below.

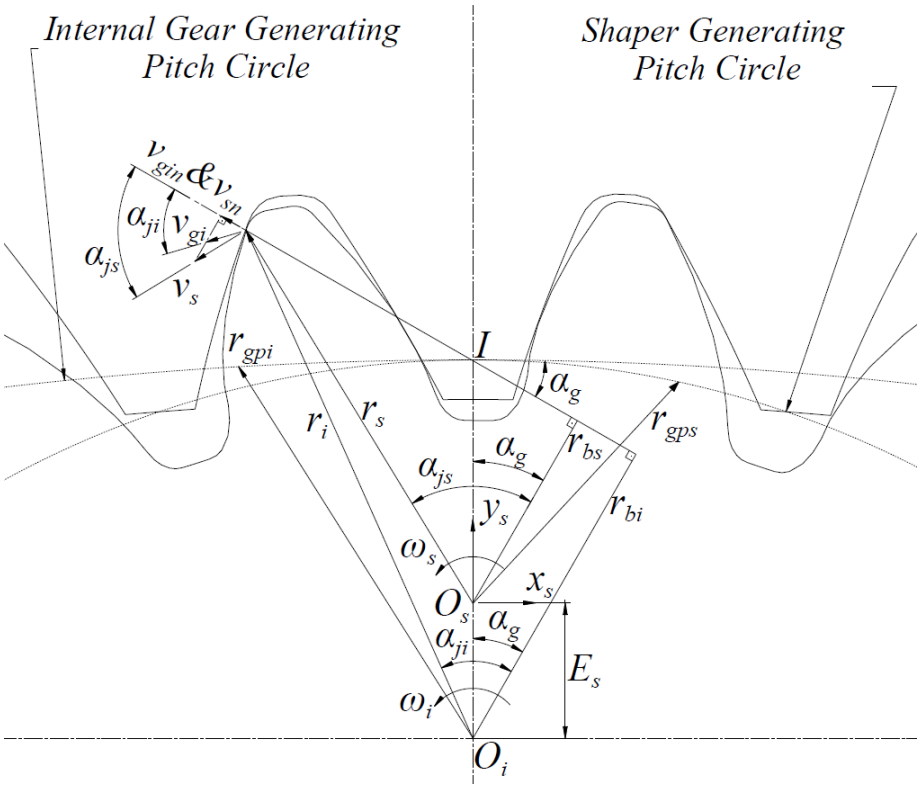

Fig. 3.4 Generation of internal gear involute flank surface by the involute surface of the shaper cutter

3.1.1.1 Basic Kinematic Relations

The kinematics of a shaper cutter is same with an external involute gear since it is essentially an external involute gear. Therefore, the involute flank surface of a shaper cutter has a line of action passing through the instantaneous center of rotation and a

constant normal velocity at all contact points during any conjugate action. Then an internal gear to be cut must also have the same line of action and constant normal velocity at all contact points during the generation motion with the involute flank surface of the shaper cutter.

$$v_{gin} = v_{sn} \tag{3.1}$$

$$v_{gi} \cos \alpha_{ji} = v_s \cos \alpha_{js} \tag{3.2}$$

$$r_i \omega_i \cos \alpha_{ji} = r_s \omega_s \cos \alpha_{js} \tag{3.3}$$

$$\omega_i r_{bi} = \omega_s r_{bs} \tag{3.4}$$

Here ω_s, r_{bs} and ω_i are constant parameters, then r_{bi} is also constant. Then the generated surface of the internal gear by the involute flank surface of the shaper cutter must also be involute.

The velocities of the shaper and internal gear must be equal at point I:

$$v_{gi} = v_s \tag{3.5}$$

$$r_{gpi} \omega_i = r_{gps} \omega_s \tag{3.6}$$

$$r_{gpi} = r_{gps} \frac{\omega_s}{\omega_i} \tag{3.7}$$

$$r_{gpi} = r_{gps} + E_s \tag{3.8}$$

Use Equations (3.4) and (3.8) in (3.7):

$$r_{gps} + E_s = r_{gps}\frac{r_{bi}}{r_{bs}} \tag{3.9}$$

$$r_{gps} = \frac{E_s}{\frac{r_{bi}}{r_{bs}} - 1} \tag{3.10}$$

For zero profile shift:

$$r_{gps} = r_{ps} = m\frac{Z_s}{2} \tag{3.11}$$

$$\alpha_g = \alpha_s \tag{3.12}$$

$$r_{bs} = r_{ps}\cos\alpha_s \tag{3.13}$$

$$r_{bs} = m\frac{Z_s}{2}\cos\alpha_s \tag{3.14}$$

$$r_{gpi} = r_{pi} = m\frac{Z_i}{2} \tag{3.15}$$

$$r_{bi} = r_{pi}\cos\alpha_s \tag{3.16}$$

$$r_{bi} = m\frac{Z_i}{2}\cos\alpha_s \tag{3.17}$$

Then use Equations (3.14) and (3.17) in Equation (3.10):

$$r_{gps} = \frac{E_s}{\frac{Z_i}{Z_s} - 1} \tag{3.18}$$

$$E_s = r_{pi} - r_{ps} + x_s \tag{3.19}$$

Here x_s is the amount of the vertical shift of the shaper cutter. If the shift is upward it is positive and if the shift is downward it is negative. By defining an input value for x_s, r_{gps} can be found with Equation (3.18).

Then the α_g can be found as:

$$r_{bs} = r_{gps} \cos \alpha_g \tag{3.20}$$

$$\alpha_g = \cos^{-1}\left(\frac{r_{bs}}{r_{gps}}\right) \tag{3.21}$$

3.1.1.2 The Determination of the Envelope to the Family of Surfaces

For any point on the shaper cutter involute flank surface, r_s represents the position vector of that point in S_s. The vector r_s is dependent on f, face width direction, and α_{js}. In terms of all f and α_{js} components, $r_s(\alpha_{js}, f)$ represents the surface Σ_s, shaper-cutter involute flank surface, in S_s.

In order to obtain parametric representation of the family of surfaces, $\Sigma_{\phi i}$, firstly, a rotation matrix, M_{fs1}, and translation matrix , M_{fs2}, between S_s&S_f and secondly, a second rotation matrix, M_{if}, between S_f&S_i should be applied on the shaper-cutter flank surface, $r_s(\alpha_{js}, f)$. Then the following matrix equation is obtained:

$$r_i = M_{if} M_{fs2} M_{fs1} r_s \tag{3.22}$$

According to the Fig. 3.3 during the generation motion, the direction of shaper rotation is counter-clockwise so the direction of the rotation matrix, M_{fs2}, which is same with the direction of the shaper rotation, is also counter-clockwise and ϕ_s is positive. Then the rotation matrix, M_{fs1} can be written as:

$$M_{fs1} = \begin{bmatrix} cos\,\phi_s & -sin\,\phi_s & 0 \\ sin\,\phi_s & cos\,\phi_s & 0 \\ 0 & 0 & 1 \end{bmatrix} \tag{3.23}$$

The translation matrix, M_{fs2}, between S_s&S_f is simply:

$$M_{fs2} = \begin{bmatrix} 1 & 0 & 0 & 0 \\ 0 & 1 & 0 & E_s \\ 0 & 0 & 1 & 0 \\ 0 & 0 & 0 & 1 \end{bmatrix} \tag{3.24}$$

According to the Fig. 3.3 during the generation motion, the direction of internal gear to be cut is counter-clockwise so the direction of the rotation matrix, M_{if}, which is opposite to the direction of the internal gear rotation, is clockwise and ϕ_i is negative. Then the rotation matrix, M_{if} can be written as:

$$M_{if} = \begin{bmatrix} cos\,\phi_i & sin\,\phi_i & 0 \\ -sin\,\phi_i & cos\,\phi_i & 0 \\ 0 & 0 & 1 \end{bmatrix} \tag{3.25}$$

Here ϕ_i is dependent on ϕ_s. By using Equations (3.4), (3.14) and (3.17):

$$\frac{\omega_s}{\omega_i} = \frac{Z_i}{Z_s} \tag{3.26}$$

Then,

$$\frac{\phi_s}{\phi_i} = \frac{\omega_s}{\omega_i} = \frac{Z_i}{Z_s} \tag{3.27}$$

$$\phi_i = \phi_s \frac{Z_s}{Z_i} \tag{3.28}$$

According to the position of the shaper-cutter in S_s, coordinates of r_s change and in Chapter 3.2.3.1, r_s matrix is defined accordingly desired shaper cutter position in S_s. However as being independent on the shaper-cutter position in S_s the coordinates of r_s are function of α_{js} and f as mentioned above. And the elements of both matrices M_{fs1} and M_{if} are functions of ϕ_s. Thus r_i is a function of α_{js}, f and ϕ_s and $r_i(\alpha_{js}, f, \phi_s)$ representing the family of surfaces $\Sigma_{\phi i}$, generated in S_i by surface Σ_s. Because of the conjugate action during the generation, the internal gear flank surface, Σ_i, is determined as the envelope to the family of surfaces, $\Sigma_{\phi i}$. And as mentioned in Chapter 2.1.1.3, the equation of meshing is used to find the envelope. Then modify Equation (2.34) for the internal gear flank surface and obtain:

$$\left(\frac{\partial r_i}{\partial \alpha_{js}} \times \frac{\partial r_i}{\partial f}\right) \cdot \frac{\partial r_i}{\partial \phi_s} = 0 \tag{3.29}$$

3.1.2 The Generation of the Gear Root Fillet Surface

The shaper cutter round surface Σ_{sr} generates the internal gear root fillet surface Σ_{if} as mentioned in Chapter 3.1. By using the coordinate systems in Fig. 3.3 the basic kinematic relations of the generation and how to obtain internal gear root fillet surface are discussed below.

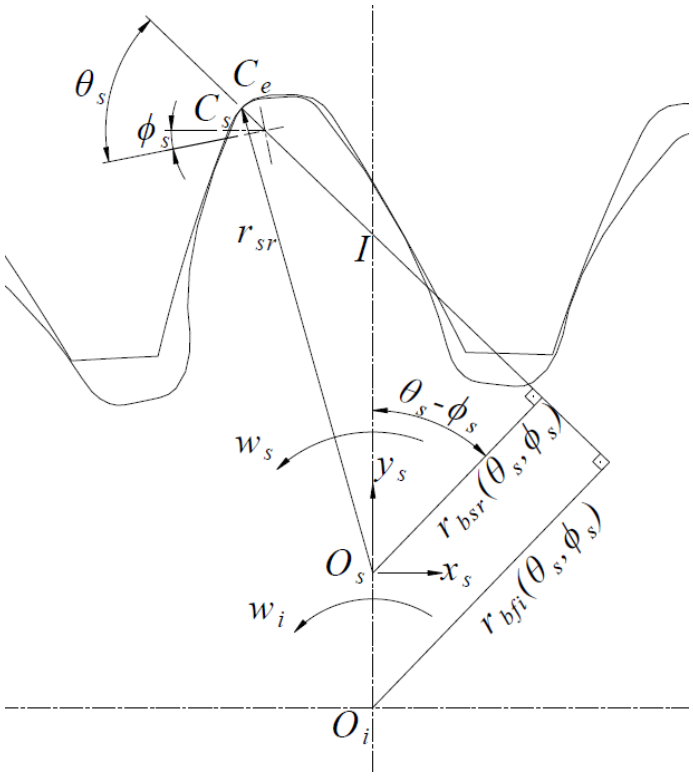

Fig. 3.5 Generation of internal gear root fillet surface by the rounded surface of the shaper cutter

3.1.2.1 Basic Kinematic Relations

During the conjugate action the normal velocities must be equal and this equality can be written as:

$$\omega_s \, r_{bsr}(\theta_s, \phi_s) = \omega_i \, r_{bfi}(\theta_s, \phi_s) \tag{3.30}$$

Here, θ_s defines the point on the shaper-cutter round between C_s and C_e and changes with respect to the contact point at any instant as seen in Fig. 3.5. Also r_{bsr} and r_{bfi} are functions of θ_s and ϕ_s.

$$\frac{r_{bsr}(\theta_s, \phi_s)}{r_{bfi}(\theta_s, \phi_s)} = \frac{\omega_i}{\omega_s} \tag{3.31}$$

By using the similarity between triangles in Fig. 3.5 and also putting Equation (3.26) in to Equation (3.31).

$$\frac{IO_s}{IO_i} = \frac{Z_s}{Z_i} \tag{3.32}$$

$$\frac{IO_s}{IO_s + E_s} = \frac{Z_s}{Z_i} \tag{3.33}$$

$$IO_s\, Z_i = IO_s\, Z_s + E_s\, Z_s \tag{3.34}$$

$$IO_s\, Z_i - IO_s\, Z_s = E_s\, Z_s \tag{3.35}$$

$$IO_s(\, Z_i - Z_s) = E_s\, Z_s \tag{3.36}$$

$$IO_s = \frac{E_s\, Z_s}{(\, Z_i - Z_s)} \tag{3.37}$$

$$IO_s = \frac{E_s}{\frac{Z_i}{Z_s} - 1} \tag{3.38}$$

The Equation (3.38) is same with Equation (3.18) which means IO_s is equal to the generating pitch radius as being independent on θ. This can be explained according to Lewis theorem that a point of the shaper-cutter round generates the respective point of the internal gear root fillet at a position where their common normal at the point of contact passes through the instantaneous center of rotation, I.

3.1.2.2 The Determination of the Envelope to the Family of Surfaces

For any point on the shaper-cutter round, r_{sr} represents the position vector of that point in S_s. The vector r_{sr} is dependent on f, face width direction, and θ_s. And in terms of all f and θ_s components, $r_{sr}(\theta_s, f)$ represents the surface Σ_{sr}, shaper-cutter round surface, in S_s. The r_{sr} matrix is defined in Chapter 3.2.3.2 because of the same reason for r_{1r} mentioned in Chapter 3.1.1.2.

Since the generation motions are same for both internal gear involute tooth and root fillet surfaces, the rotation and the translation matrices are also same for these two generations. Then, r_{sr} is represented in S_i as:

$$r_{if} = M_{if} M_{fs2} M_{fs1} r_{sr} \tag{3.39}$$

Here r_{if} is a function of θ_s, f and ϕ_s and $r_{if}(\theta_s, f, \phi_s)$ representing the family of surfaces $\Sigma_{\phi fi}$, generated in S_i by surface Σ_{sr}. Because of the conjugate action during the generation, the internal gear root fillet surface, Σ_{if}, is determined as the envelope to the family of surfaces, $\Sigma_{\phi fi}$. And as mentioned in Chapter 2.1.1.3, the equation of meshing is used to find the envelope. Then modify Equation (2.34) for the internal gear root fillet surface and obtain:

$$\left(\frac{\partial r_{if}}{\partial \theta_s} \times \frac{\partial r_{if}}{\partial f}\right) \cdot \frac{\partial r_{if}}{\partial \phi_s} = 0 \tag{3.40}$$

3.2 Details of Asymmetric Shaper Cutter and Internal Asymmetric Spur Gear Tooth

In order to generate an asymmetric internal gear tooth, an asymmetric shaper-cutter is used. The details of an asymmetric shaper-cutter and internal gear tooth are discussed in the following chapters.

3.2.1 Details of an Asymmetric Shaper Cutter

Fig. 3.6 shows a representative transverse cross sectional shape of basic asymmetric pinion type shaper cutter, which is used to generate the respective asymmetric internal tooth profiles. Some basic properties of an asymmetric shaper cutter are defined below:

$$r_{ps} = \frac{mZ_s}{2} \tag{3.41}$$

$$r_{bsd} = r_{ps} \cos \alpha_{sd} \tag{3.42}$$

$$r_{bsc} = r_{ps} \cos \alpha_{sc} \tag{3.43}$$

$$\alpha_{asd} = \cos^{-1}\left(\frac{r_{bsd}}{r_{as}}\right) \tag{3.44}$$

$$\alpha_{asc} = \cos^{-1}\left(\frac{r_{bsc}}{r_{as}}\right) \tag{3.45}$$

The shaper tooth thickness and space width at the tool reference pitch circle are $\pi m/2$.

$$t_{refs} = \pi m/2 \tag{3.46}$$

The shaper cutter tooth axis is defined as the line passing through the middle of the tooth tip thickness.

$$\delta = \frac{t_{refs}}{r_{ps}} - (inv\alpha_{asd} - inv\alpha_{sd}) - (inv\alpha_{asc} - inv\alpha_{sc}) \tag{3.47}$$

As mentioned in Chapter 3.1.1.1 with respect to vertical shift amount, x_s, of the shaper cutter the generating pitch circle changes and the generating pitch radius of the shaper cutter r_{gps} and the generating pressure angle α_g are already defined. Then α_{gsc} and α_g can be found as:

$$\alpha_{gsc} = \cos^{-1}\left(\frac{r_{bsc}}{r_{gps}}\right) \tag{3.48}$$

$$\alpha_g = \cos^{-1}\left(\frac{r_{bsd}}{r_{gps}}\right) \tag{3.49}$$

And the drive and coast sides tooth thicknesses are defined as:

$$t_{gsc} = r_{gps}\left(inv\alpha_{asc} - inv\alpha_{gsc} + \delta/2\right) \tag{3.50}$$

$$t_{gsd} = r_{gps}\left(inv\alpha_{asd} - inv\alpha_{gsd} + \delta/2\right) \tag{3.51}$$

$$t_{gs} = t_{gsc} + t_{gsd} \tag{3.52}$$

The details of points C_{cs}, C_{ce}, C_c, C_{ds}, C_{de} and C_d are defined with respect to the radius A_s in Appendix C.1. Also the shaper-cutter may be full-rounded with a radius A_{maxs}. The detailed derivation for calculating A_{maxs} is given in Appendix C.2.

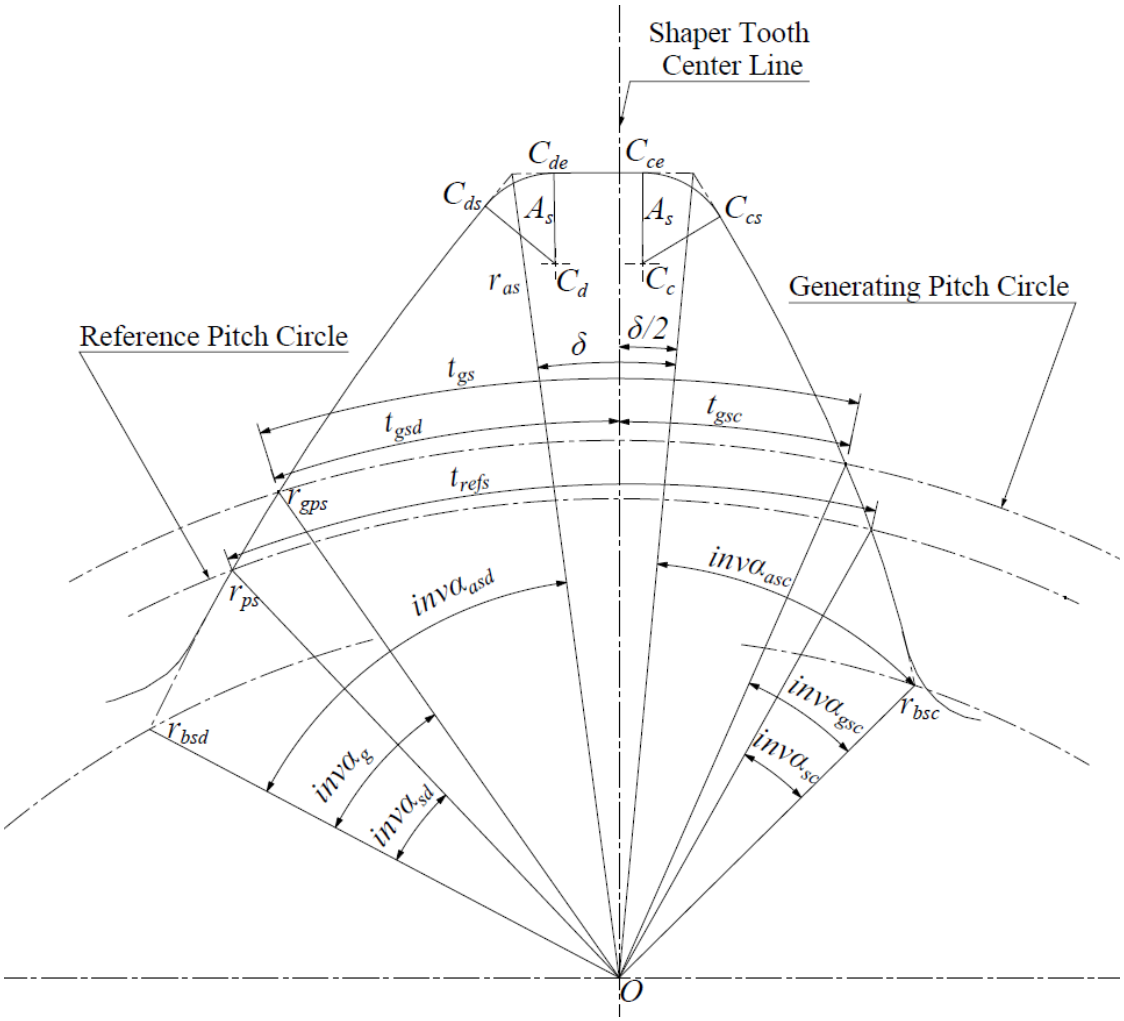

Fig. 3.6 Asymmetric shaper cutter details

3.2.2 Details of an Internal Asymmetric Gear Tooth

Fig. 3.7 shows a representative transverse cross sectional shape of basic asymmetric internal gear tooth. In an asymmetric internal gear, the base radiuses of the coast and drive side flanks may intersect or may not intersect each other. However in general they do not intersect each other as represented in Fig. 3.7. For this case the larger base radius is accepted as the imaginary tip radius of the internal gear tooth and the gear tooth axis is defined as the line passing through the middle of the imaginary tip tooth thickness.

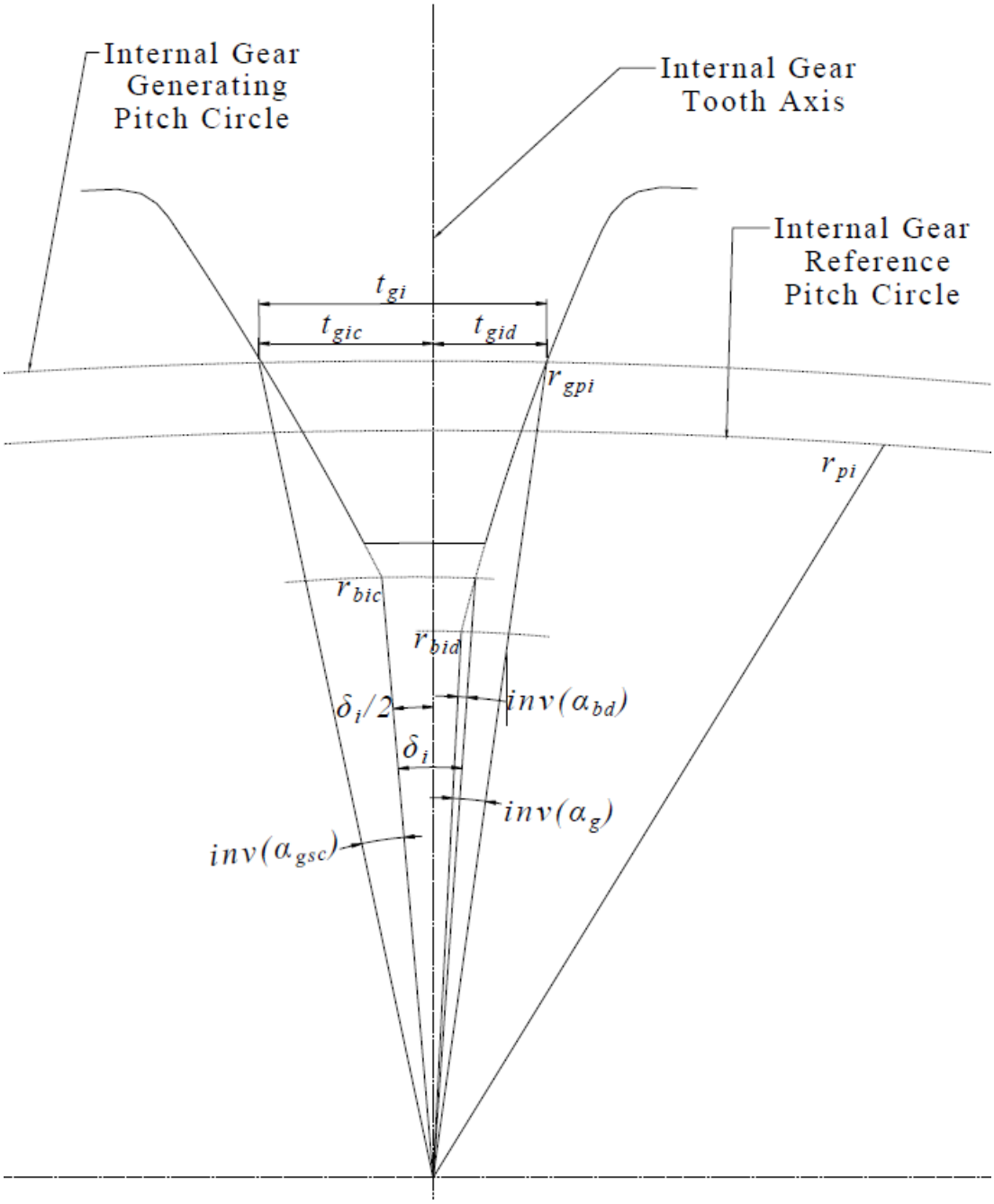

Fig. 3.7 Internal asymmetric gear tooth details

Some basic properties of an asymmetric internal gear tooth are defined below:

$$r_{pi} = \frac{mZ_i}{2} \tag{3.53}$$

$$r_{bid} = r_{pi} \cos \alpha_{sd} \tag{3.54}$$

$$r_{bic} = r_{pi} \cos \alpha_{sc} \tag{3.55}$$

$$t_{gi} = \frac{2\pi r_{gpi}}{Z_i} - t_{gs} \tag{3.56}$$

The internal gear tooth axis angle δ_i and respective generating pitch circle coast and drive side tooth thicknesses are defined according to Fig. 3.7 as below:

$$\delta_i = \frac{t_{gi}}{r_{gpi}} - inv\alpha_{gsc} - \left(inv\alpha_{gsd} - inv\alpha_{bd}\right) \tag{3.57}$$

$$\alpha_{bd} = \cos^{-1}\left(\frac{r_{bid}}{r_{bic}}\right) \tag{3.58}$$

$$t_{gic} = r_{gpi}\left(inv\alpha_{gsc} + \delta_i/2\right) \tag{3.59}$$

$$t_{gid} = r_{gpi}\left(inv\alpha_{gsd} - inv\alpha_{bd} + \delta_i/2\right) \tag{3.60}$$

In contrast to Fig. 3.7, if the drive side base radius is larger than the coast side base radius and they do not intersect each other, then Equations (3.57), (3.59) and (3.60) can be modified as:

$$\delta_i = \frac{t_{gi}}{r_{gpi}} - inv\alpha_{gsd} - \left(inv\alpha_{gsc} - inv\alpha_{bc}\right) \tag{3.61}$$

$$\alpha_{bc} = \cos^{-1}\left(\frac{r_{bic}}{r_{bid}}\right) \tag{3.62}$$

$$t_{gid} = r_{gpi}\left(inv\alpha_{gsd} + \delta_i/2\right) \tag{3.63}$$

$$t_{gic} = r_{gpi}\left(inv\alpha_{gsc} - inv\alpha_{bc} + \delta_i/2\right) \tag{3.64}$$

If the base radiuses intersect each other, then the gear tooth axis is defined as the line passing through this intersection point. The radius of this intersection point r_{ti} can be found as defined in Appendix D.1. The generating pitch line coast and drive side tooth thicknesses according to this case are also defined in Appendix D.1 and expressed by:

$$t_{gid} = r_{gpi}\left(inv\alpha_{gsd} - inv\alpha_{tid}\right) \tag{3.65}$$

$$t_{gic} = r_{gpi}\left(inv\alpha_{gsc} - inv\alpha_{tic}\right) \tag{3.66}$$

3.2.3 Determination of the Position Vector Matrices for the Surfaces of the Asymmetric Shaper Cutter

The position of the shaper cutter in S_s gives us the desired internal gear tooth position in S_i. In FEA for bending stress an internal gear tooth is analyzed as its tooth axis being coincide with the vertical axis. Thus the obtained internal gear tooth axis must coincide with the vertical axis.

Fig. 3.8 illustrates that the dark colored involute flanks and rounds of drive and coast sides of the asymmetric shaper-cutter generates the asymmetric internal gear dark colored flanks and roots which represent the tooth space. Also in order to obtain the desired tooth position the obtained tooth space must be rotated as the angle ϕ_{rot}.

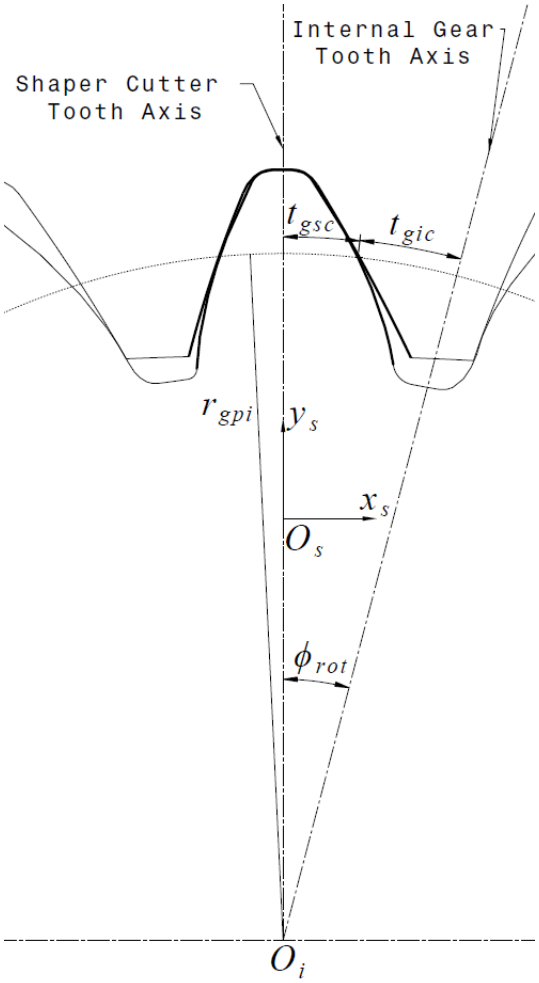

Fig. 3.8 The desired position of the internal asymmetric gear tooth

Then by complete circular patterning as the number of the gear tooth the asymmetric gear having the desired tooth position is obtained.

$$\phi_{rot} = \frac{t_{gsc} + t_{gic}}{r_{gpi}} \tag{3.67}$$

$$M_{rot} = \begin{bmatrix} cos\,\phi_{rot} & -sin\,\phi_{rot} & 0 \\ sin\,\phi_{rot} & cos\,\phi_{rot} & 0 \\ 0 & 0 & 1 \end{bmatrix} \tag{3.68}$$

$$\Sigma_{irot} = M_{rot}\,\Sigma_i \tag{3.69}$$

$$\Sigma_{ifrot} = M_{rot}\,\Sigma_{if} \tag{3.70}$$

3.2.3.1 Determination of the Position Vector Matrices for the Involute Flank Surfaces of the Asymmetric Shaper Cutter Coast and Drive Sides

With reference to Fig. 3.9, the asymmetric shaper-cutter flank drive and coast side surfaces are defined as:

$$r_{sc} = \begin{bmatrix} r_{sc}\,sin\left(\delta_{sc} + inv\alpha_{rc} - inv\alpha_{jsc}\right) \\ r_{sc}\,cos\left(\delta_{sc} + inv\alpha_{rc} - inv\alpha_{jsc}\right) \\ f \\ 1 \end{bmatrix} \quad 0 \le \alpha_{jsc} \le \alpha_{rc}\,, \;\; 0 \le f \le f_w \tag{3.71}$$

$$r_{sd} = \begin{bmatrix} -\,r_{sd}\,sin\left(\delta_{sd} + inv\alpha_{rs} - inv\alpha_{jsd}\right) \\ r_{sd}\,cos\left(\delta_{sd} + inv\alpha_{rs} - inv\alpha_{jsd}\right) \\ f \\ 1 \end{bmatrix} 0 \le \alpha_{jsd} \le \alpha_{rd}, \;\; 0 \le f \le f_w \tag{3.72}$$

Here δ_{sd}, δ_{sc}, α_{rc} and α_{rd} are defined in Appendix C.1. Also r_{sd} and r_{sc} can be defined as:

$$r_{sd} = \frac{r_{bsd}}{\cos\left(\alpha_{jsd}\right)} \tag{3.73}$$

$$r_{sc} = \frac{r_{bsc}}{\cos(\alpha_{jsc})} \tag{3.74}$$

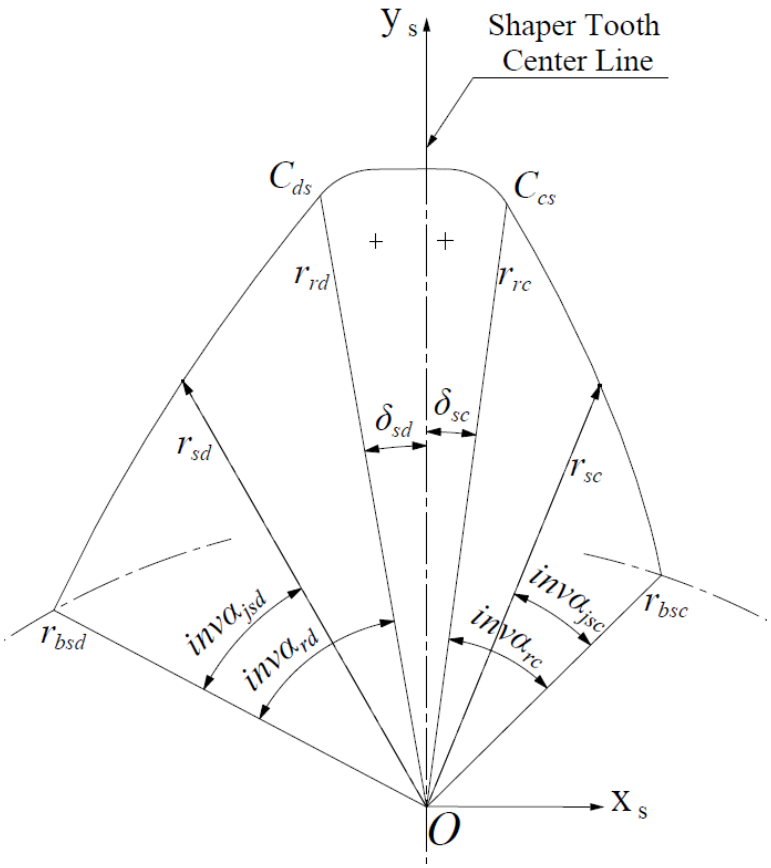

Fig. 3.9 The position vectors of asymmetric shaper cutter drive and coast sides involute flank surfaces

Then Equation (3.71) and (3.72) becomes:

$$r_{sc} = \begin{bmatrix} \frac{r_{bsc}}{\cos(\alpha_{jsc})} sin(\delta_{sc} + inv\alpha_{rc} - inv\alpha_{jsc}) \\ \frac{r_{bsc}}{\cos(\alpha_{jsc})} cos(\delta_{sc} + inv\alpha_{rc} - inv\alpha_{jsc}) \\ f \\ 1 \end{bmatrix} \tag{3.75}$$

$$0 \leq \alpha_{jsc} \leq \alpha_{rc}$$

$$0 \leq f \leq f_w$$

$$r_{sd} = \begin{bmatrix} -\dfrac{r_{bsd}}{\cos(\alpha_{jsd})} sin(\delta_{sd} + inv\alpha_{rd} - inv\alpha_{jsd}) \\ \dfrac{r_{bsd}}{\cos(\alpha_{jsd})} cos(\delta_{sd} + inv\alpha_{rd} - inv\alpha_{jsd}) \\ f \\ 1 \end{bmatrix} \tag{3.76}$$

$$0 \leq \alpha_{jsd} \leq \alpha_{rd}$$

$$0 \leq f \leq f_w$$

3.2.3.2 Determination of the Position Vector Matrices for the Rounded Surfaces of the Asymmetric Shaper Cutter Coast and Drive Sides

With reference to Fig. 3.10 the asymmetric shaper-cutter round drive and coast side surfaces are defined as:

$$r_{src} = \begin{bmatrix} x_{Cc} + A_s\, cos(\theta_{sc}) \\ y_{Cc} + A_s\, sin(\theta_{sc}) \\ f \\ 1 \end{bmatrix} \quad \theta_{scs} \leq \theta_{sc} \leq \theta_{sce} \ , \ 0 \leq f \leq f_w \tag{3.77}$$

$$r_{srd} = \begin{bmatrix} x_{Cd} - A_s\, cos(\theta_{sd}) \\ y_{Cd} + A_s\, sin(\theta_{sd}) \\ f \\ 1 \end{bmatrix} \quad \theta_{sds} \leq \theta_{sd} \leq \theta_{sde} \ , \ 0 \leq f \leq f_w \tag{3.78}$$

Here x_{Cc}, y_{Cc}, θ_{scs}, θ_{sce}, x_{Cd}, y_{Cd}, θ_{sds} and θ_{sde} are defined in Appendix C.1.

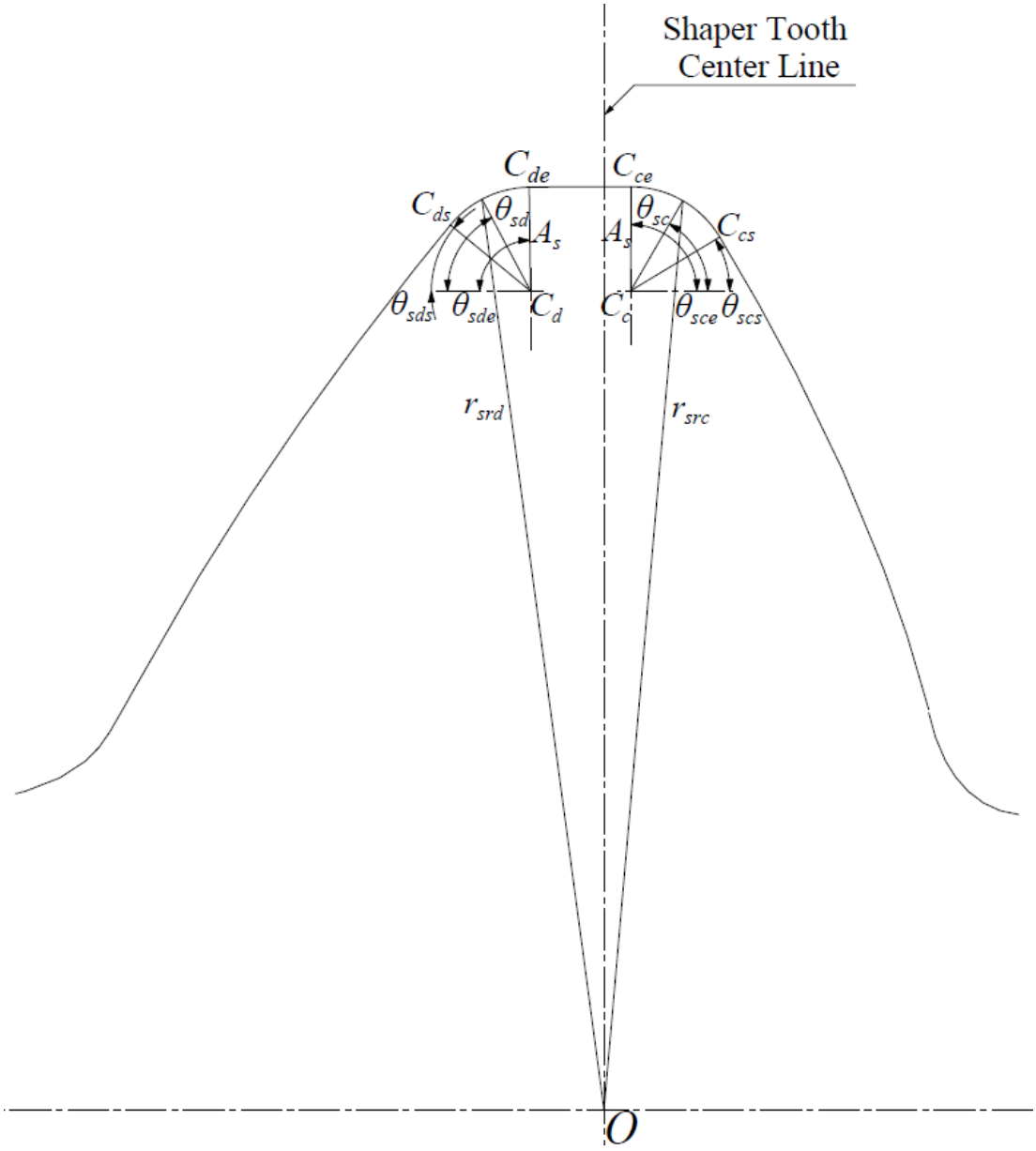

Fig. 3.10 The position vectors of asymmetric shaper cutter drive and coast sides rounded surfaces

3.3 Analytical Method to Determine the Critical Bending Stress Section and Related Parameters for an Internal Asymmetric Spur Gear Tooth

In Fig. 3.11, the basic visualization of asymmetric internal spur gear tooth bending stress critical section is illustrated.

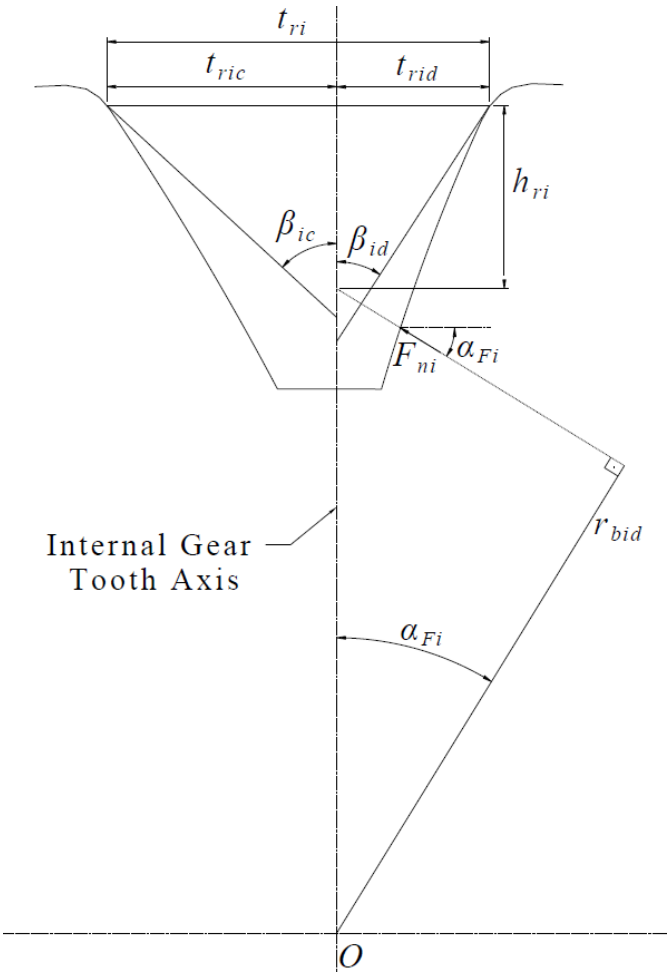

Fig. 3.11 The basic visualization of asymmetric internal spur gear tooth bending stress critical section

In this chapter the same modified ISO B method which is used for the external asymmetric spur gears mentioned in Chapter 2.3, is used for internal asymmetric gears in order to determine the critical tooth thickness and tooth height. In this

method, the drive side tangent angle at the critical section β_{id} is equal to 60°, the coast side tangent angle at the critical section β_{ic} is calculated by using the generation of the internal gear coast side root fillet.

3.3.1 Determination of the Angle and Radius of the Applied Force

The maximum bending stress on the internal gear root occurs when the force is applied at the lowest point single tooth contact point. In order to verify the critical tooth thickness and tooth height, firstly radius of the applied force, r_{Fi}, and angle, α_{Fi}, as illustrated in Fig. 3.12, shall be determined.

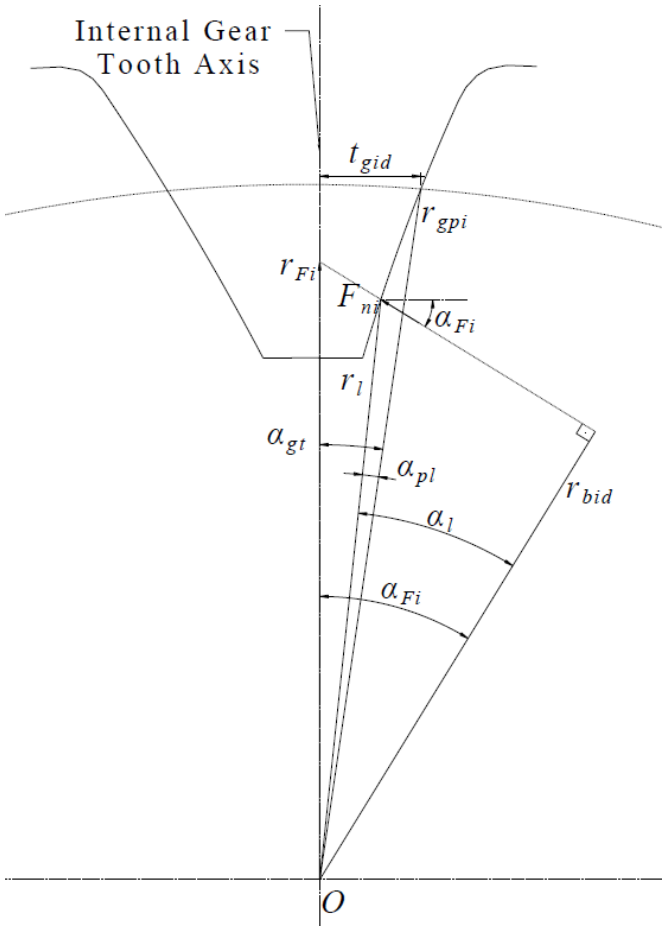

Fig. 3.12 The applied force at LPSTC and the related parameters

For this, radius of the lowest point single tooth contact point, r_l, must be known. The detailed derivation of r_l is in Appendix D.2.

$$\alpha_{Fi} = \alpha_l - \alpha_{pl} + \alpha_{gt} \tag{3.79}$$

$$\alpha_l = \cos^{-1}\left(\frac{r_{bid}}{r_l}\right) \tag{3.80}$$

$$\alpha_{pl} = inv(\alpha_g) - inv(\alpha_l) \tag{3.81}$$

$$\alpha_{gt} = \frac{t_{gid}}{r_{gpi}} \tag{3.82}$$

$$r_{Fi} = \frac{r_{bid}}{\cos(\alpha_{Fi})} \tag{3.83}$$

3.3.2 Determination of the Critical Tooth Thickness and Height

The critical tooth thickness and tooth height can be determined by using the generation of the internal gear root fillet with a shaper cutter. Firstly, the drive side critical tooth thickness and the critical tooth height are obtained. Then with respect to the critical section, the coast side critical tooth thickness is obtained. Finally, the summation of the drive and coast side critical tooth thicknesses gives the critical tooth thickness.

3.3.2.1 Determination of the Drive Side Critical Tooth Thickness and Height

The drive side critical tooth thickness and tooth height are obtained by using the generation of the internal gear drive side root fillet surface with the shaper cutter

drive side round surface. Fig. 3.13 shows the generation of the gear drive side root fillet at point *P* where the critical section occurs.

$$\zeta_d = \frac{t_{gid} + t_{gsd}}{r_{gpi}} \tag{3.84}$$

$$\beta_{id} = \zeta_d + \phi_i + \theta_{sd} - \phi_s \tag{3.85}$$

$$\beta_{id} = \frac{\pi}{3} \tag{3.86}$$

$$\phi_i = \phi_s \frac{Z_s}{Z_i} \tag{3.87}$$

$$\theta_{sd} = \beta_{id} - \zeta_d - \phi_i + \phi_s \tag{3.88}$$

$$\theta_{sd} = \frac{\pi}{3} - \frac{t_{gid} + t_{gsd}}{r_{gpi}} - \phi_s \frac{Z_s}{Z_i} + \phi_s \tag{3.89}$$

$$O_s C_d = \sqrt{(x_{Cd})^2 + (y_{Cd})^2} \tag{3.90}$$

$$\theta_{Cd} = \tan^{-1}\left(\frac{|x_{Cd}|}{y_{Cd}}\right) \tag{3.91}$$

$$C_d G = O_s C_d \sin(\theta_{Cd} + \phi_s) \tag{3.92}$$

$$IG = O_s G - O_s I \tag{3.93}$$

$$IG = O_s C_d \cos(\theta_{Cd} + \phi_s) - r_{gps} \tag{3.94}$$

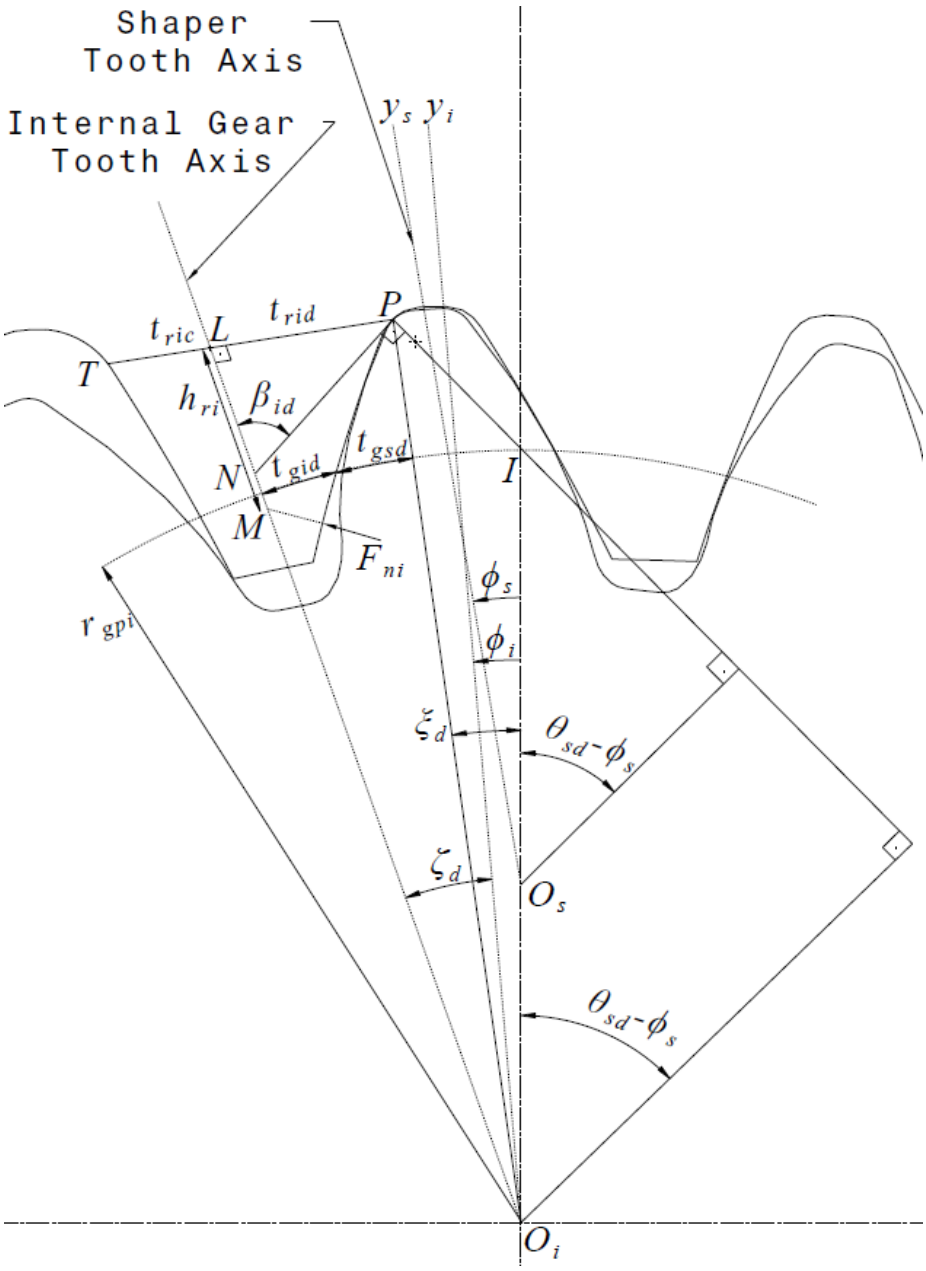

Fig. 3.13 The generation of the internal asymmetric spur gear drive side root fillet at the location where the critical section occurs

$$\tan(\theta_{sd} - \phi_s) = \frac{IG}{C_d G} \tag{3.95}$$

$$\theta_{sd} - \phi_s = \tan^{-1}\left(\frac{IG}{C_d G}\right) \tag{3.96}$$

$$\theta_{sd} = \tan^{-1}\left(\frac{IG}{C_d G}\right) + \phi_s \tag{3.97}$$

In Equations (3.97) and (3.89), the only variable is ϕ_s and by equating them obtain ϕ_s. Then by using Equation (3.89) obtain θ_{sd}. Some of the details of the shaper cutter are given in Fig. 3.14.

$$P_{xs} = O_s C_d \sin(\theta_{Cd} + \phi_s) + A_s \cos(\theta_{sd} - \phi_s) \tag{3.98}$$

$$P_{ys} = O_s C_d \cos(\theta_{Cd} + \phi_s) + A_s \sin(\theta_{sd} - \phi_s) \tag{3.99}$$

$$P_{xi} = P_{xs} \tag{3.100}$$

$$P_{yi} = P_{ys} + E_s \tag{3.101}$$

$$\tan(\xi_d) = \frac{P_{xi}}{P_{yi}} \tag{3.102}$$

$$\xi_d = \tan^{-1}\left(\frac{P_{xi}}{P_{yi}}\right) \tag{3.103}$$

$$t_{rid} = O_i P \sin\big(\zeta_d - (\xi_d - \phi_i)\big) \tag{3.104}$$

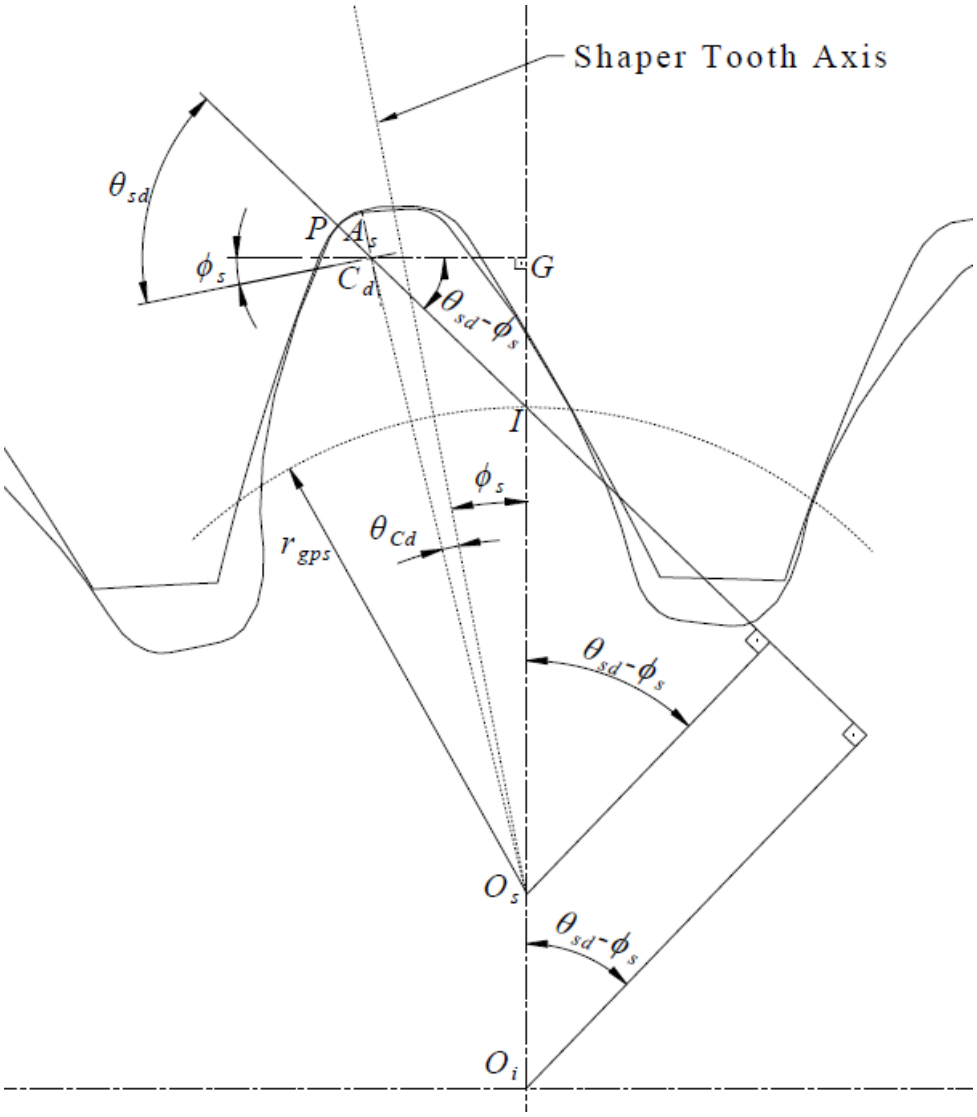

Fig. 3.14 The details of the asymmetric shaper cutter during the generation of the internal asymmetric spur gear drive side root fillet at the location where the critical section occurs

$$t_{rid} = \sqrt{(P_{xi})^2 + \left(P_{yi}\right)^2} \sin\left(\zeta_d - \left(\xi_d - \phi_s \frac{Z_s}{Z_i}\right)\right) \tag{3.105}$$

$$h_{ri} = O_i P \cos\left(\zeta_d - (\xi_d - \phi_i)\right) - O_i M \tag{3.106}$$

$$h_{ri} = \sqrt{(P_{xi})^2 + \left(P_{yi}\right)^2} \cos\left(\zeta_d - \left(\xi_d - \phi_s \frac{Z_s}{Z_i}\right)\right) - r_{Fi} \tag{3.107}$$

3.3.2.2 Determination of the Coast Side Critical Tooth Thickness and Height

The coast side critical tooth thickness and tooth height are obtained by using the generation of the internal gear coast side root fillet surface with the shaper cutter coast side rounded surface. Fig. 3.16 shows the generation of the internal gear coast side root fillet at point T where the critical section occurs. Some of the details of the shaper cutter are given in Fig. 3.15.

$$O_s C_c = \sqrt{(x_{Cc})^2 + (y_{Cc})^2} \tag{3.108}$$

$$\theta_{Cc} = \tan^{-1}\left(\frac{|x_{Cc}|}{y_{Cc}}\right) \tag{3.109}$$

$$C_c Z = O_s C_c \sin(\theta_{Cc} + \phi_s) \tag{3.110}$$

$$IZ = O_s Z - O_s I \tag{3.111}$$

$$IZ = O_s C_c \cos(\theta_{Cc} + \phi_s) - r_{gps} \tag{3.112}$$

$$\tan(\theta_{sc} - \phi_s) = \frac{IZ}{C_c Z} \tag{3.113}$$

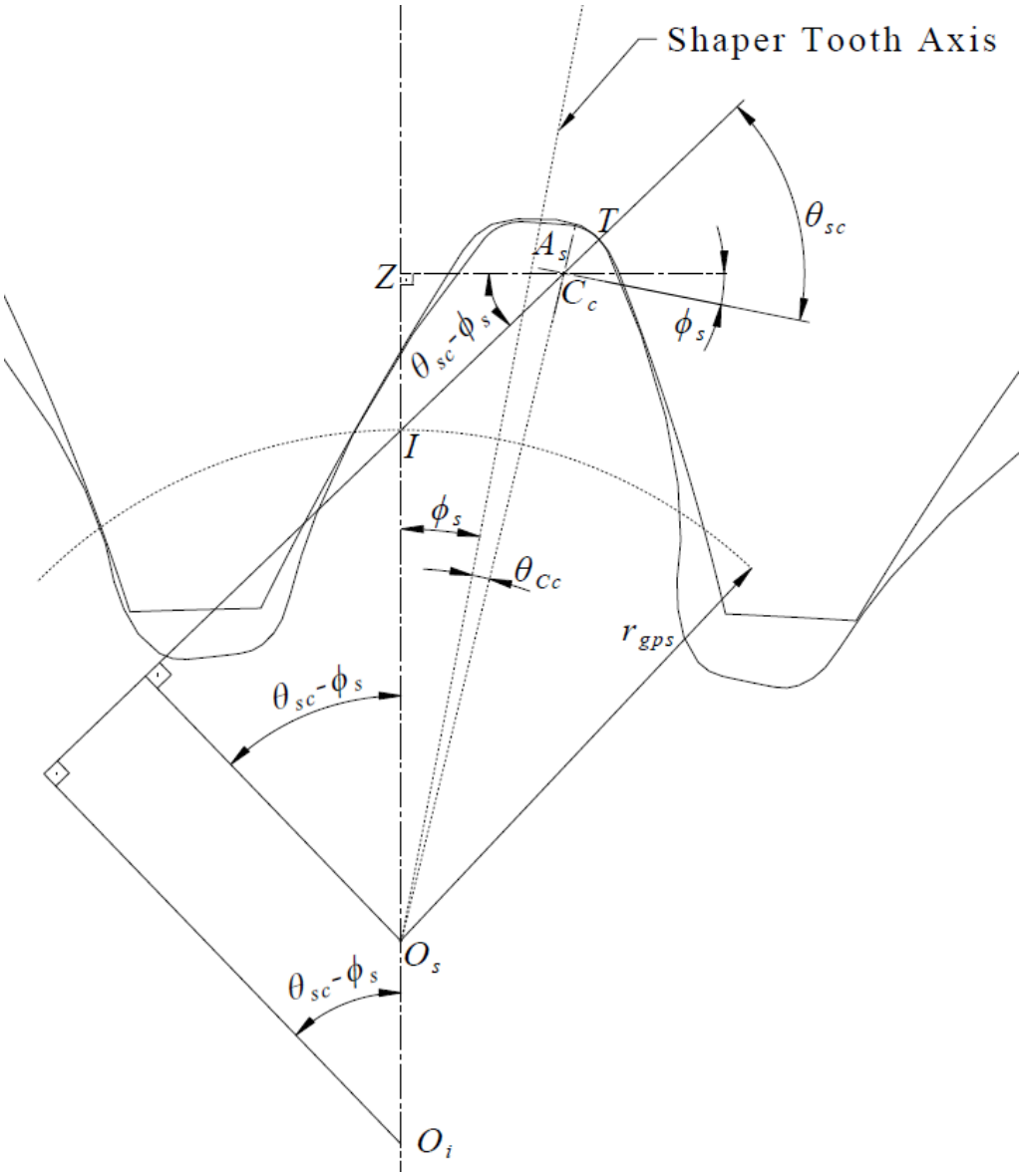

Fig. 3.15 The details of the asymmetric shaper cutter during the generation of the internal asymmetric spur gear coast side root fillet at the location where the critical section occurs

$$\theta_{sc} - \phi_s = \tan^{-1}\left(\frac{IZ}{C_c Z}\right) \tag{3.114}$$

$$\theta_{sc} = \tan^{-1}\left(\frac{IZ}{C_c Z}\right) + \phi_s \tag{3.115}$$

$$\theta_{sc} = \tan^{-1}\left(\frac{\sqrt{(x_{Cc})^2 + (y_{Cc})^2}\cos(\theta_{Cc} + \phi_s) - r_{gps}}{\sqrt{(x_{Cc})^2 + (y_{Cc})^2}\sin(\theta_{Cc} + \phi_s)}\right) + \phi_s \tag{3.116}$$

$$T_{xs} = O_s C_c \sin(\theta_{Cc} + \phi_s) + A_s \cos(\theta_{sc} - \phi_s) \tag{3.117}$$

$$T_{ys} = O_s C_c \cos(\theta_{Cc} + \phi_s) + A_s \sin(\theta_{sc} - \phi_s) \tag{3.118}$$

$$T_{xi} = T_{xs} \tag{3.119}$$

$$T_{yi} = T_{ys} + E_s \tag{3.120}$$

$$\tan(\xi_c) = \frac{T_{xi}}{T_{yi}} \tag{3.121}$$

$$\xi_c = \tan^{-1}\left(\frac{T_{xi}}{T_{yi}}\right) \tag{3.122}$$

$$h_{ri} = O_i T \cos\big(\zeta_c - (\xi_c - \phi_i)\big) - O_i M \tag{3.123}$$

$$h_{ri} = \sqrt{(T_{xi})^2 + \left(T_{yi}\right)^2}\cos\left(\zeta_c - \left(\xi_c - \phi_s \frac{Z_s}{Z_i}\right)\right) - r_{Fi} \tag{3.124}$$

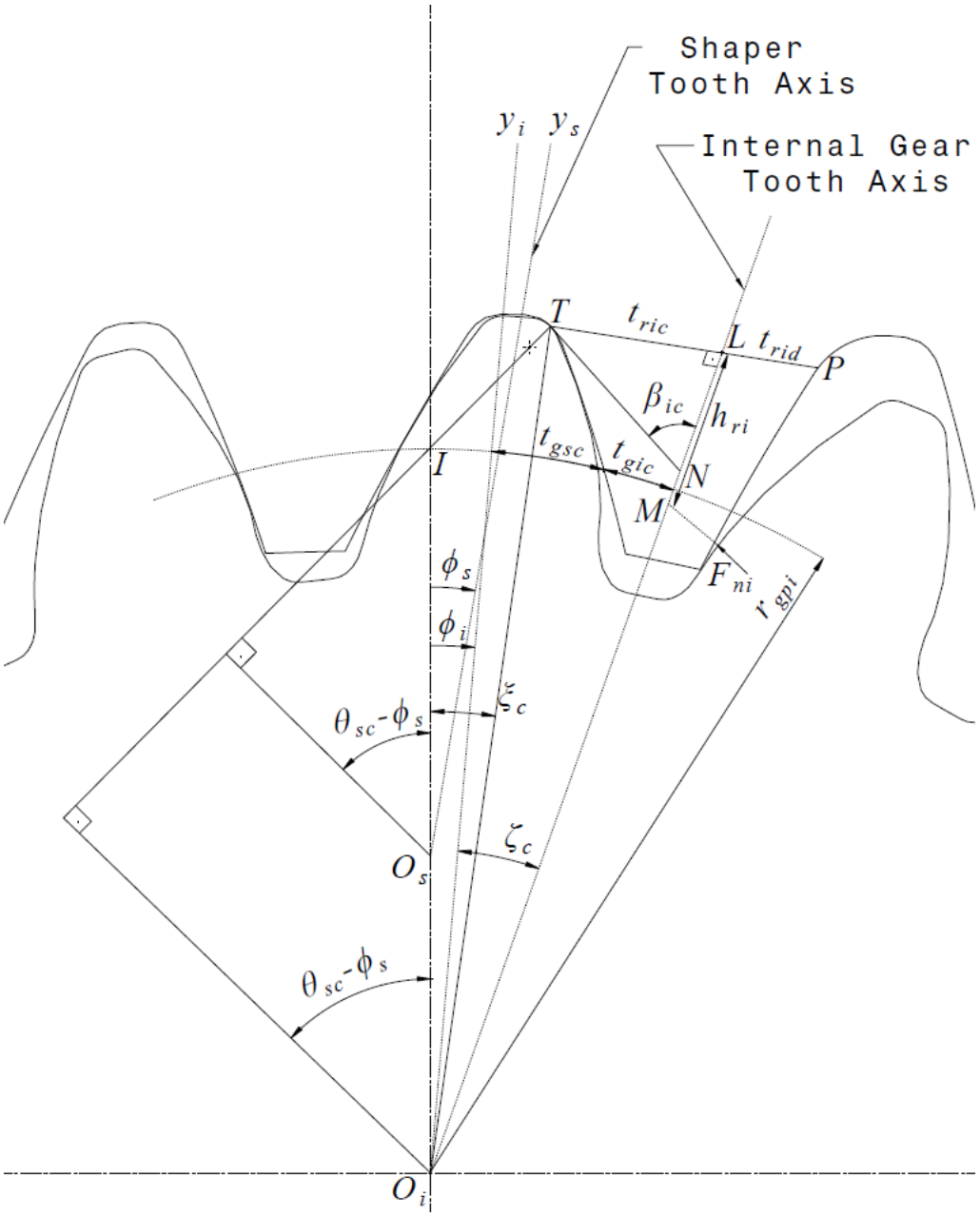

Fig. 3.16 The generation of the internal asymmetric spur gear coast side root fillet at the location where the critical section occurs

Put Equation (3.116) in Equations (3.117) and (3.118). Then Equation (3.124) is now only dependent on ϕ_s. Note that h_{ri} is already found in Equation (3.107) and by equating Equations (3.107) and (3.124) obtain ϕ_s.

$$t_{ric} = O_i T \sin\left(\zeta_c - (\xi_c - \phi_i)\right) \tag{3.125}$$

$$t_{ric} = \sqrt{(T_{xi})^2 + \left(T_{yi}\right)^2} \sin\left(\zeta_c - \left(\xi_c - \phi_s \frac{Z_s}{Z_i}\right)\right) \tag{3.126}$$

$$\zeta_c = \frac{t_{gic} + t_{gsc}}{r_{gpi}} \tag{3.127}$$

$$\beta_{ic} = \zeta_c + \phi_i + \theta_{sc} - \phi_s \tag{3.128}$$

$$\beta_{ic} = \zeta_c + \phi_s \frac{Z_s}{Z_i} + \theta_{sc} - \phi_s \tag{3.129}$$

Put Equation (3.116) in Equation (3.129). Then Equation (3.129) is only dependent on ϕ_s. Since ϕ_s is already found β_{ic} is found, too.

3.4 Estimation of Tooth Form Factor, Stress Correction Factor and Maximum Bending Stress for an Internal Asymmetric Spur Gear Tooth through Modified ISO and FEA Methods

The maximum bending stress formulation at the internal gear tooth root is same with the external gear tooth root and may be expressed as:

$$\sigma_i = \frac{F_{ni}}{fm} Y_{Fi} Y_{Si} \tag{3.130}$$

where, F_{ni} is normal load, Y_{Fi} is tooth form factor and Y_{Si} is stress correction factor. In addition to the bending stress formulations of international standards, the compressive stress produced by the radial load F_{ri} is also taken in to account in this thesis so that the normal force F_{ni} is used instead of F_{ti} in Equation (2.125). Y_{Fi} and Y_{Si} are determined for an internal asymmetric gear tooth with both ISO B and FEA methods in the following Chapters.

3.4.1 Modified ISO Method for Bending Stress Parameters

The tooth form factor Y_{Fi} is also affected by being taken in to account of the radial load F_{ri}. The detailed derivation of Y_{Fi} is same with Y_F of the external gear tooth which can be found in Appendix of [15] and defined as:

$$(Y_{Fi})_{ISO} = \frac{6mh_{ri}\cos\alpha_{Fi}}{{t_{ri}}^2} - \frac{m\sin\alpha_{Fi}}{t_{ri}} \tag{3.131}$$

$$t_{ri} = t_{ric} + t_{rid} \tag{3.132}$$

The stress correction factor Y_{Si} is same with Y_S of the external gear tooth and defined in [5] as:

$$(Y_{Si})_{ISO} = (1.2 + 0.13L_i)q_s^{\left[\frac{1}{1.21+\frac{2.3}{L_i}}\right]} \tag{3.133}$$

$$L_i = \frac{t_{ri}}{h_{ri}} \tag{3.134}$$

$$q_{si} = \frac{t_{ri}}{2\rho_{Fi}} \tag{3.135}$$

Here, ρ_{Fi} is root fillet radius of curvature of the internal gear drive side root fillet trochoid at the critical section and can be found with the help of the Fig. 3.17:

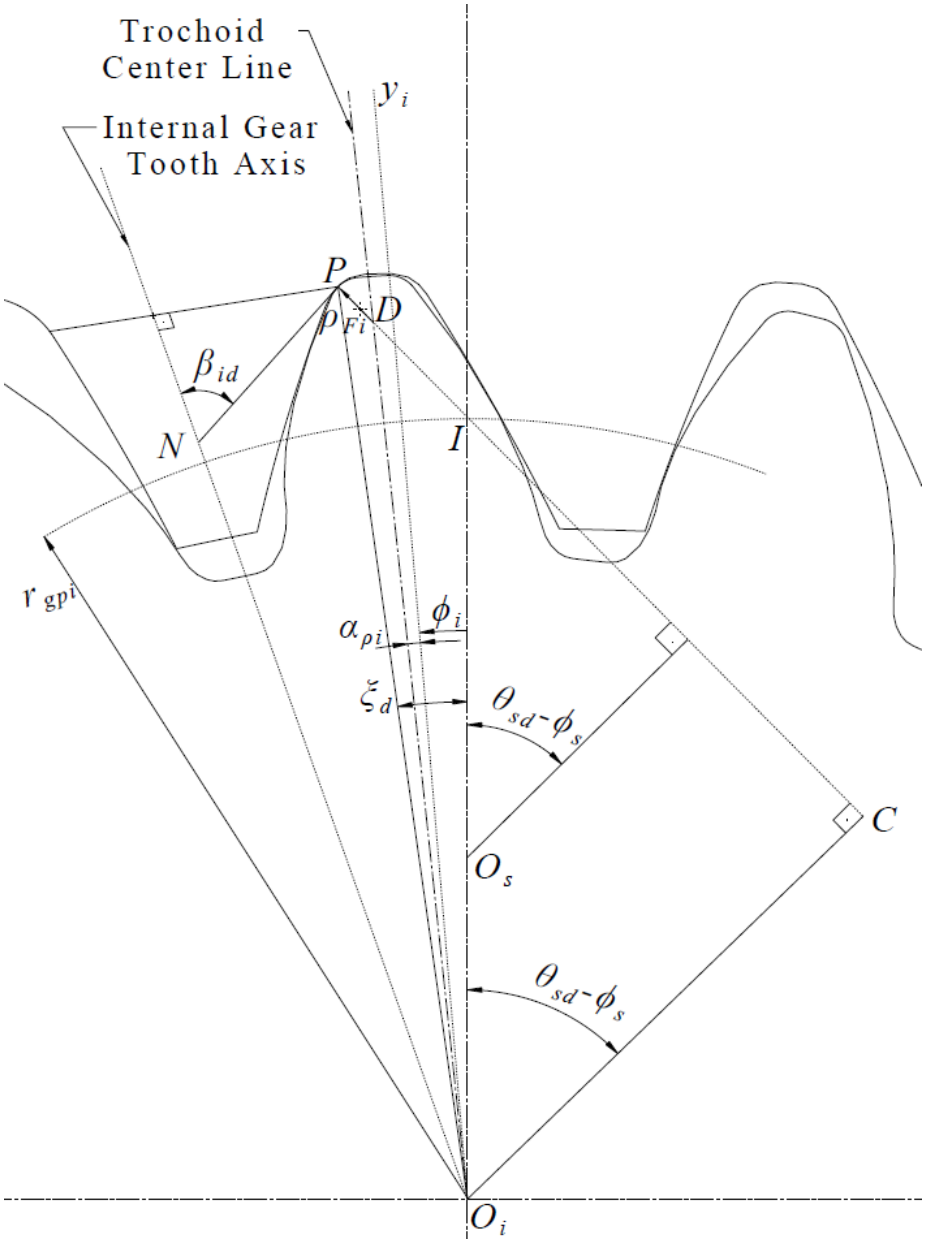

Fig. 3.17 The root fillet radius of curvature at the drive side critical section of the internal asymmetric spur gear

$$\rho_{Fi} = CP - CD \tag{3.136}$$

$$\rho_{Fi} = O_iC\tan(\theta_{ds} - \phi_s + \xi_d) - O_iC\tan\left(\theta_{ds} - \phi_s + \phi_{id} + \alpha_{\rho i}\right) \tag{3.137}$$

$$O_iC = O_iI\cos(\theta_{ds} - \phi_s) \tag{3.138}$$

$$O_iC = r_{gpi}\cos(\theta_{ds} - \phi_s) \tag{3.139}$$

Here all parameters of ρ_{Fi} are already found for the drive side critical section so that ρ_{Fi} can be found, too.

At the instant when the centerline of the trochoid coincides with the shaper drive side round center on the axis y_f, the angle $\alpha_{\rho i}$ between the trochoid center line and y_i, is equal to the angle θ_{Cd}, divided by the gear ratio.

$$\alpha_{\rho i} = \frac{\theta_{Cd}}{\frac{Z_i}{Z_s}} \tag{3.140}$$

The angle θ_{Cd} was already defined by Equation (3.91) as:

$$\theta_{Cd} = \tan^{-1}\left(\frac{|x_{Cd}|}{y_{Cd}}\right) \tag{3.141}$$

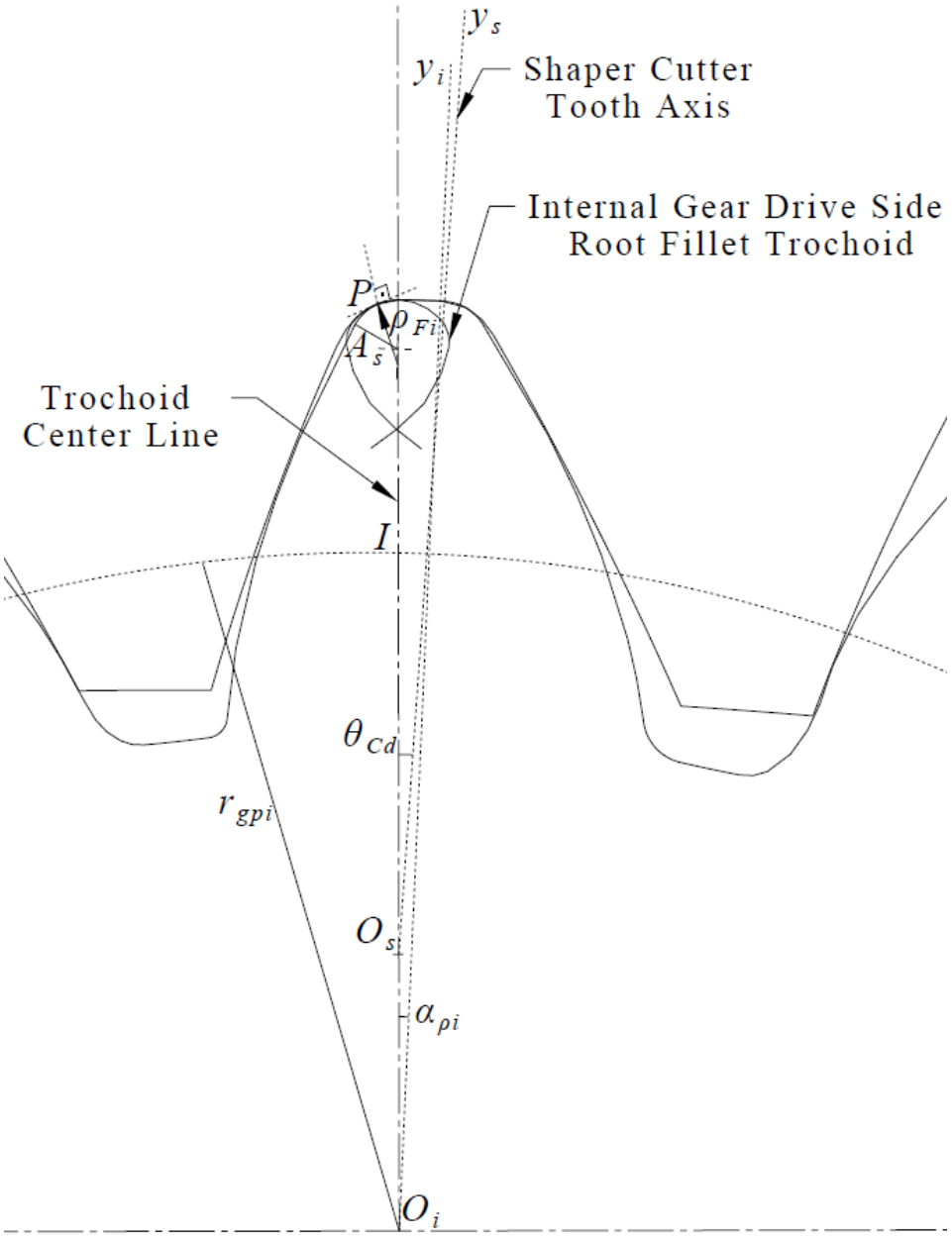

Fig. 3.18 The angle of the root fillet radius of curvature at the drive side critical section of the internal asymmetric spur gear

3.4.2 FEA Method for Bending Stress Parameters

The maximum principle stress on the internal gear root fillet gives the maximum bending stress through FEA as stated in Chapter 2.4.2 for the external gears.

$$(\sigma_i)_{FEA} = \frac{F_{ni}}{f_w m}(Y_{Fi})_{FEA}(Y_{Si})_{FEA} \tag{3.142}$$

The form factor $(Y_{Fi})_{FEA}$ is calculated with Equation (3.131) by using FEA based values of t_{ri} and h_{ri}. Then $(Y_{Si})_{FEA}$ can be defined as:

$$(Y_{Si})_{FEA} = \frac{(\sigma_i)_{FEA}}{\frac{F_{ni}}{fm}(Y_{Fi})_{FEA}} \tag{3.143}$$

The FEA based ρ_{Fi} at the critical section is obtained by using Equation (3.137) with the FEA based critical section parameters which are defined in Chapter 3.4.2.2.1.

In order to use this method, 2D FEA is carried out in this thesis and the asymmetric internal spur gear 2D FE model is the need for FEA. In order to create a 2D FE model, firstly, a 3D cat model of the asymmetric internal spur gear is created in this thesis and 2D internal gear geometry is obtained by using this cat model. Then 2D FE model can be created by using this 2D gear geometry.

3.4.2.1 Internal Asymmetric Spur Gear 3D Model

The asymmetric internal spur gear as shown in Fig. 3.20 is obtained by using a Matlab code, written according to the theory explained in this thesis, and illustrated in Fig. 3.19.

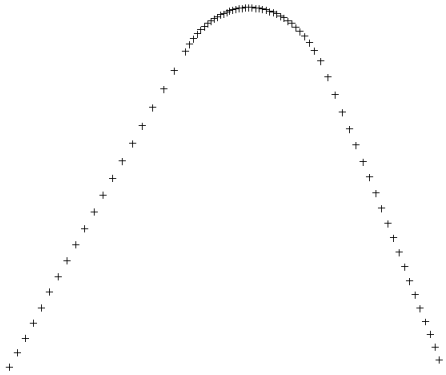

Fig. 3.19 Internal asymmetric spur gear tooth space profile

Here, the profile consists of points and represents the internal gear tooth space surface. Also the profile is 3D and the points continue through the face width direction. Since this is a spur gear, the profile at each section is same.

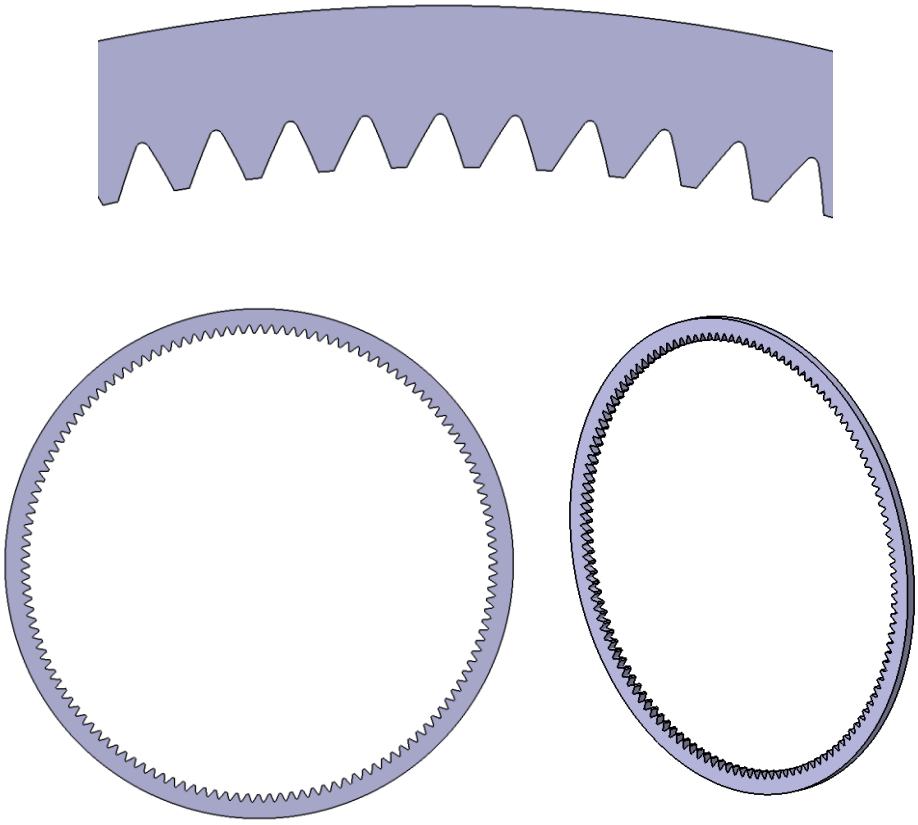

Fig. 3.20 Internal asymmetric spur gear 3D model

In order to obtain firstly 3D cat model and then 2D geometry of the internal asymmetric spur gear, the same method explained in Chapter 2.4.2.1 for the external asymmetric spur gear is used. Fig. 3.21 shows an example of 2D geometry of the internal asymmetric spur gear

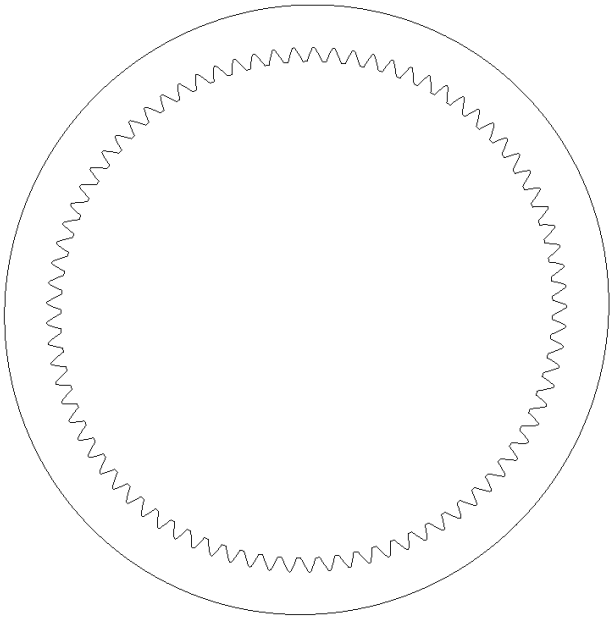

Fig. 3.21 Internal asymmetric spur gear 2D geometry

3.4.2.2 FE Model of the Internal Asymmetric Spur Gear

In this thesis FE modeling and analysis are done in ABAQUS 6.14. A sample 2D FE model of the asymmetric internal gear is shown in Fig. 3.22. The FE model is consist of three tooth and have enough rim thickness to provide a rim thickness factor of 1 according to [5].

FE model properties:

1) 2D FE analysis with plane strain condition is done by assuming a uniform load distribution along face width of the gear tooth.

2) The material is a linear elastic isotropic and homogeneous one with an elastic constant of E = 210 GPa and Poisson's ratio= 0.3.

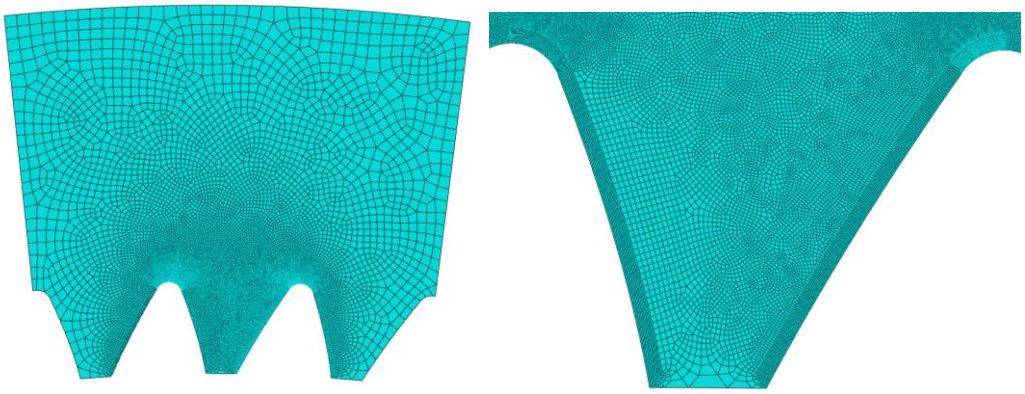

Fig. 3.22 Internal asymmetric spur gear tooth 2D FE model

3) The load is applied at RP-1 (reference point) which is ŞPSTC point. The reference point is coupled to the nodes at that diameter with continuum distributing and the FE model is fixed from the outer round and side lines as shown in Fig. 3.23.

4) The gear tooth profiles for this analysis have been generated using a full rounded shaper cutter.

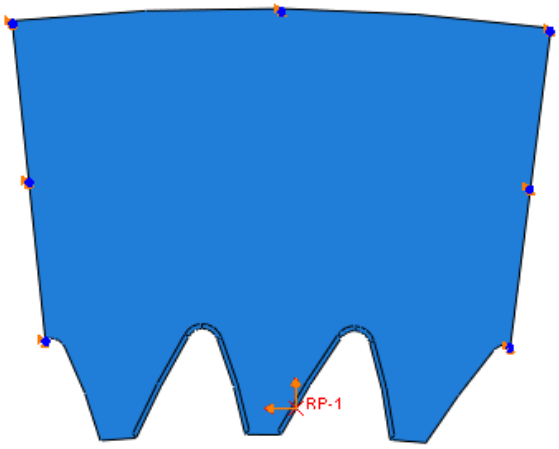

Fig. 3.23 Internal asymmetric spur gear tooth 3D FE model boundary condition and force application point

5) The 2-D 8-nodded quadratic elements are used to mesh the gear model. The loaded gear tooth flanks and root fillets and the next unloaded tooth flanks and root fillets are meshed sensitively by using partition regions, which are offset from the original profile around 0.1 times module. There are 350x10 elements in the loaded tooth drive side root fillet and 150x10 elements in the loaded tooth drive side flank and coast side root fillet and 50x10 elements in the loaded tooth coast side involute flank. There are also 50x5 elements in the next unloaded tooth flanks and root fillets. For the other regions suitable global size elements are used.

3.4.2.2.1 Internal Asymmetric Spur Gear FE Model Critical Section Parameters

In the FEA the maximum principle stress location which is the point P illustrated in Fig. 3.24, is found and defines the critical section. The x and y components of point P are read in Abaqus. Here, P_{xi} and P_{yi} are defined as:

$$P_{xfea} = t_{rid} \tag{3.144}$$

$$P_{yfea} = OL \tag{3.145}$$

The critical tooth height is found as:

$$h_{ri} = OL - (OM) \tag{3.146}$$

Remember that OM is r_{Fi}, Fig. 3.12, then:

$$h_{ri} = P_{yfea} - r_{Fi} \tag{3.147}$$

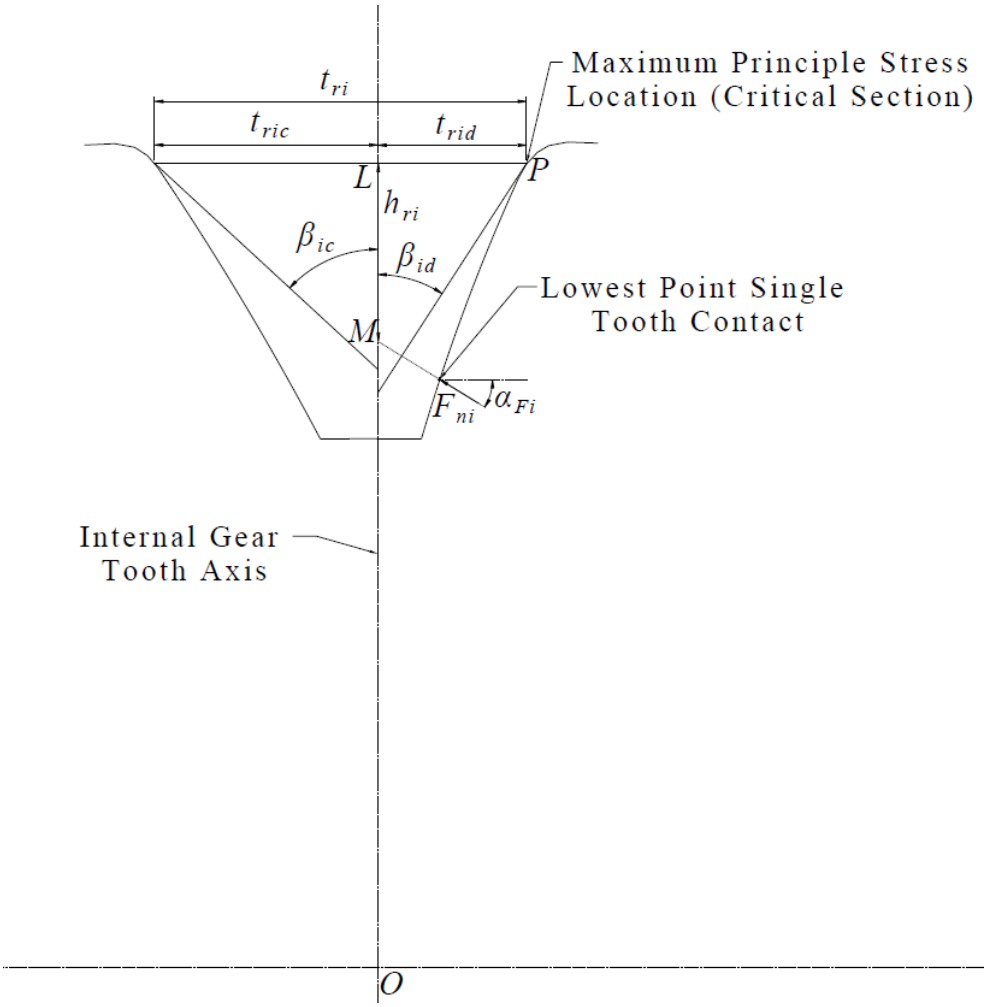

Fig. 3.24 Internal asymmetric spur gear tooth 2D FE model critical section

Since the critical tooth height is known and the critical section tangent angle is not known for the gear tooth drive side in FEA, the same method with the analytical method used in the coast side parameters derivation is used to obtain the drive side parameters in FEA method. According to this method put Equation (3.97) in Equation (3.107) such that the only parameter becomes ϕ_s in Equation (3.107). Since the drive side critical tooth height is also calculated by using Equation (3.107), ϕ_s is obtained by equating Equations (3.107) and (3.141). Then θ_{sd} is obtained by using Equation (3.97). Finally β_{id} can be found by modifying Equation (3.88):

$$\beta_{id} = \theta_{sd} + \zeta_d + \phi_i - \phi_s \tag{3.148}$$

$$\beta_{id} = \theta_{sd} + \frac{t_{gid} + t_{gsd}}{r_{gpi}} + \phi_s \frac{Z_s}{Z_i} - \phi_s \tag{3.149}$$

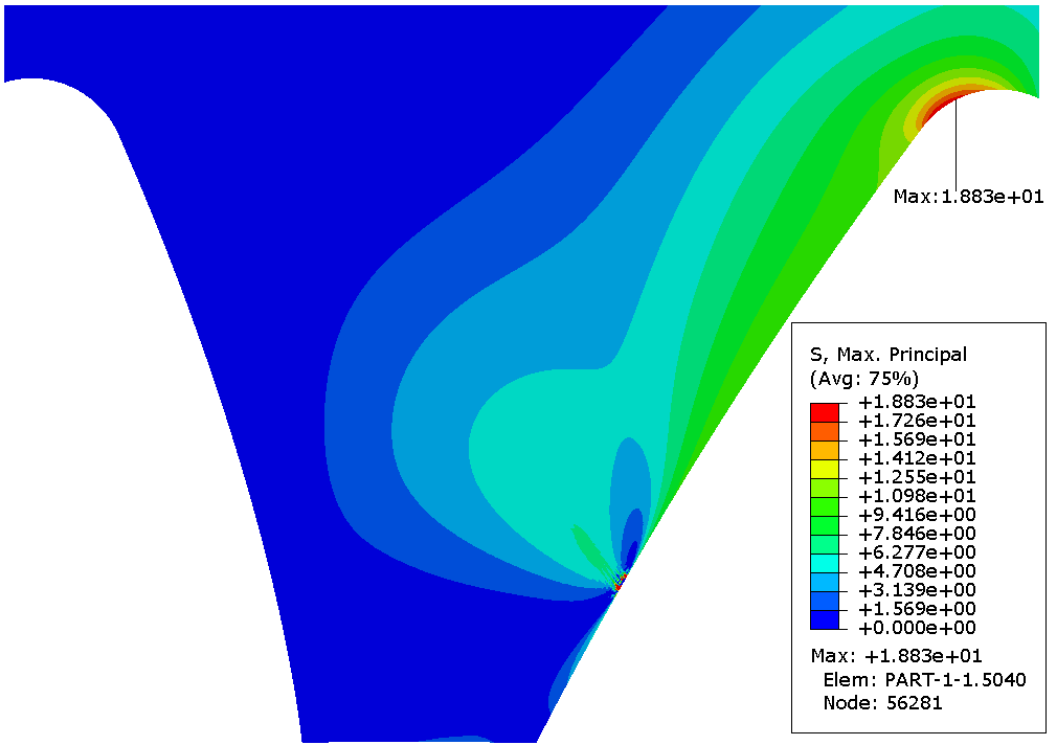

Fig. 3.25 An example of the FEA bending stress results for the internal asymmetric spur gear with 60 teeth, α_{id}/α_{ic}=30°/16°

The drive side critical section tooth thickness, t_{rid}, can also be found by using Equation (3.105) for FE model. The results of Equations (3.105) and (3.144) shall be equal such that the correctness of the analytical method is proven. The coast side critical section parameters for FE model are found by using totally same equations and method mentioned in Chapter 3.3.2.2. The only difference is that the input parameter, the critical tooth height, is not obtained by analytical method but it comes from FEA. The coast side tangent angle and critical tooth thickness are found by using Equations (3.126) and (3.129), respectively.

CHAPTER 4

RESULTS AND DISCUSSIONS FOR MODIFIED ISO AND FEA METHODS OF EXTERNAL AND INTERNAL ASYMMETRIC SPUR GEARS

4.1 Results and Discussions for Modified ISO and FEA Methods of External Asymmetric Spur Gear

The critical section and bending stress parameters (β_d, β_c, h_r, t_r, ρ_F, Y_F, Y_S, σ) are determined through FEA and modified ISO methods according to the different cases for the external asymmetric spur gears.

4.1.1 The Case of Lightly Loaded Gear with Small Module

In this chapter external asymmetric spur gears with 1 mm module, unit face width, standard tooth height (a=1, b=1.25), zero profile shift and 10 N applied force are studied with FEA and modified ISO methods. These studies are done in two cases. In first case the influence of drive side pressure angles are examined and in second case the influence of coast side pressure angles are examined. Then the results of these studies are compared with the previous work [15].

4.1.1.1 The Effect of Drive Side Pressure Angle

In previous work [15], the influence of drive side pressure angle on the critical section and bending stress parameters (β_d, β_c, h_r, t_r, ρ_F, Y_F, Y_S, σ) is plotted for

different pinion teeth numbers Z_p (from 20 to 100). On these plots the datas are given for only two teeth number 20 and 100. These datas are compared with this thesis works in Table 1 and Table 2. Here, PW means previous work and TH means this thesis work. It is seen that this thesis and previous work [15] data are very close to each other for these two teeth number for this case. In order to verify this thesis results more accurately, another teeth number from the previous work [15] can be selected. This teeth number is chosen as 40 since the data at this teeth number are the farthest ones to the line which starts from the data of 20 to 100 teeth numbers in the previous work [15] plots.

Table 1. Comparison of the FEA and modified ISO method results with previous work [15] for the bending stress parameters, α_c=20°, Z_p=Z_g=20

PARAMETERS										
	α_d/α_c		β_d (°)	β_c (°)	h_r (mm)	t_r (mm)	ρ_F (mm)	Y_F	Y_S	σ (MPa)
Z 20, m 1	20°/20°	PW-ISO	30	30	1.0507	1.9564	0.5507	1.3821	1.824	25.209
		PW-FEM	33	33	1.0784	1.9918	0.5473	1.37	1.918	26.276
		TH-ISO	30	30	1.0507	1.9575	0.5511	1.3805	1.8242	25.183
		TH-FEM	34.0285	34.0285	1.0875	2.0035	0.5469	1.3659	1.9196	26.22
	25°/20°	PW-ISO	30	35	1.1682	2.0666	0.4906	1.2734	1.924	24.5
		PW-FEM	37	39	1.2276	2.1492	0.4826	1.2393	2.0407	25.29
		TH-ISO	30	33.909	1.1672	2.0622	0.4912	1.278	1.9207	24.547
		TH-FEM	34.5448	38.826	1.2049	2.1137	0.4859	1.2572	2.0077	25.24
	30°/20°	PW-ISO	30	40	1.2896	2.1919	0.4181	1.1447	2.0695	23.69
		PW-FEM	39.75	51.2	1.3561	2.3074	0.4068	1.086	2.265	24.594
		TH-ISO	30	39.9043	1.2891	2.1915	0.4188	1.1447	2.0682	23.674
		TH-FEM	39.1719	51.7379	1.3528	2.3005	0.4077	1.09	2.2551	24.58

Table 2. Comparison of the FEA and modified ISO method results with previous work [15] for the bending stress parameters, α_c=20°, Z_p=Z_g=100

PARAMETERS										
	α_d/α_c		β_d (°)	β_c (°)	h_r (mm)	t_r (mm)	ρ_F (mm)	Y_F	Y_S	σ (MPa)
Z 100, m 1	20°/20°	PW-ISO	30	30	0.826	2.225	0.493	0.795	2.298	18.28
		PW-FEM	40.9	41	0.906	2.354	0.489	0.784	2.581	20.3
		TH-ISO	30	30	0.8257	2.2391	0.4934	0.7841	2.3117	18.126
		TH-FEM	43.502	43.502	0.9235	2.3848	0.4884	0.7801	2.5919	20.22
	25°/20°	PW-ISO	30	35	0.958	2.364	0.424	0.753	2.453	18.47
		PW-FEM	45.05	47.81	1.027	2.462	0.418	0.753	2.66	20.03
		TH-ISO	30	31.1754	0.9562	2.3598	0.4241	0.7584	2.4522	18.5963
		TH-FEM	45.1679	46.7417	1.0508	2.5084	0.4176	0.7432	2.7261	20.26
	30°/20°	PW-ISO	30	40	1.085	2.522	0.339	0.688	2.728	18.77
		PW-FEM	49.9	55.7	1.181	2.68	0.33	0.668	2.996	20.03
		TH-ISO	30	32.9042	1.0818	2.5065	0.3394	0.696	2.7164	18.9061
		TH-FEM	46.9293	51.1941	1.1672	2.6503	0.3311	0.6755	2.9948	20.23

Table 3. Comparison of the bending stress parameters for the FEA and modified ISO method results, α_c=20°, Z_p=Z_g=40

PARAMETERS										
	α_d/α_c		β_d (°)	β_c (°)	h_r (mm)	t_r (mm)	ρ_F (mm)	Y_F	Y_S	σ (MPa)
Z 40, m 1	20°/20°	TH-ISO	30	30	0.9249	2.126	0.5188	1.0072	2.0732	20.8824
		TH-FEM	37.9907	37.9907	0.9909	2.2149	0.5128	0.9984	2.2345	22.31
	25°/20°	TH-ISO	30	32.3793	1.0444	2.2395	0.4538	0.9477	2.1966	20.8164
		TH-FEM	39.435	42.3297	1.1133	2.3395	0.4458	0.9293	2.3534	21.87
	30°/20°	TH-ISO	30	35.9222	1.1658	2.3774	0.3748	0.8587	2.4005	20.6126
		TH-FEM	42.4855	50.6337	1.2414	2.5033	0.3632	0.827	2.5865	21.39

Table 4. Comparison of the bending stress of standard ISO method with FEA results for α_d=α_c=20°

		σ (MPa)	
α_d/α_c	Z_p/Z_g	ISO	FEA
20°/20°	20/20	27.54	26.22
	40/40	22.96	22.3
	100/100	20.72	20.22

Then this thesis works for 40 teeth are also compared with the previous work [15] by putting signs in its plots as shown in Fig. 4.1, Fig. 4.2, Fig. 4.3 and Fig. 4.4. In these figures some of the parameters have different symbols. Here, ψ is β, α_{od} is α_d, h_f is h_r and s_f is t_r according to this thesis work. It is clearly seen that for 40 teeth the results of this thesis and previous work [15] is also very close to each other. Thus this thesis work is verified by using the previous work [15] results. Then the similar discussions for this case with the previous work [15] can be done:

1- From Table 1, Table 2, Table 3 and with the help of Fig. 4.1 it is found that as α_d increases the angle of tangent at the drive and coast sides (β_d and β_c) increases and by increasing the number of teeth the amount of increase becomes larger and larger in the FEA study. However, the value of β_d is always equal to 30° and the respective β_c increases with an increase in α_d in the modified ISO method. Also contrary to the FEA study and previous work [15] modified ISO method by increasing the number of teeth, the coast side tangent angle β_c decreases in this thesis modified ISO method.

2- From Table 1, Table 2, Table 3 and with the help of Fig. 4.2, Fig. 4.3 and Fig. 4.4 it is found that as α_d increases the tooth form factor Y_F decreases which is mainly because of the corresponding increase in critical tooth thickness t_r, despite the increase in critical tooth height h_r. However the stress correction factor Y_s increases because of the corresponding decrease in root fillet radius of curvature ρ_f. The respective determined values of the bending stress σ decreases with an increase in α_d. This is because of the corresponding decrease in tooth form factor Y_F, which is more dominating than the increase in stress correction factor. This enables to enhance the bending strength of the gear tooth.

3- The present FEA results show higher values of σ than that of the modified ISO method, which is mainly because of higher critical tooth height h_r and lesser root fillet radius of curvature ρ_f. The bending stresses in FEA are %5 percentage higher than modified ISO method for low number of teeth and the percentage increases to %10 for high number of teeth. According to Table 4, for external symmetric spur gears with 20° pressure angle, the standard ISO method gives %3-5 larger bending stress results than FEA results. By increasing the number of tooth, the results get closer to each other.

4- By increasing the number of teeth the bending stress σ decreases. The bending stress in modified ISO method decreases more than FEA method since the stress correction factor Y_s increases less than FEA method for the modified ISO method while the number of teeth is increasing.

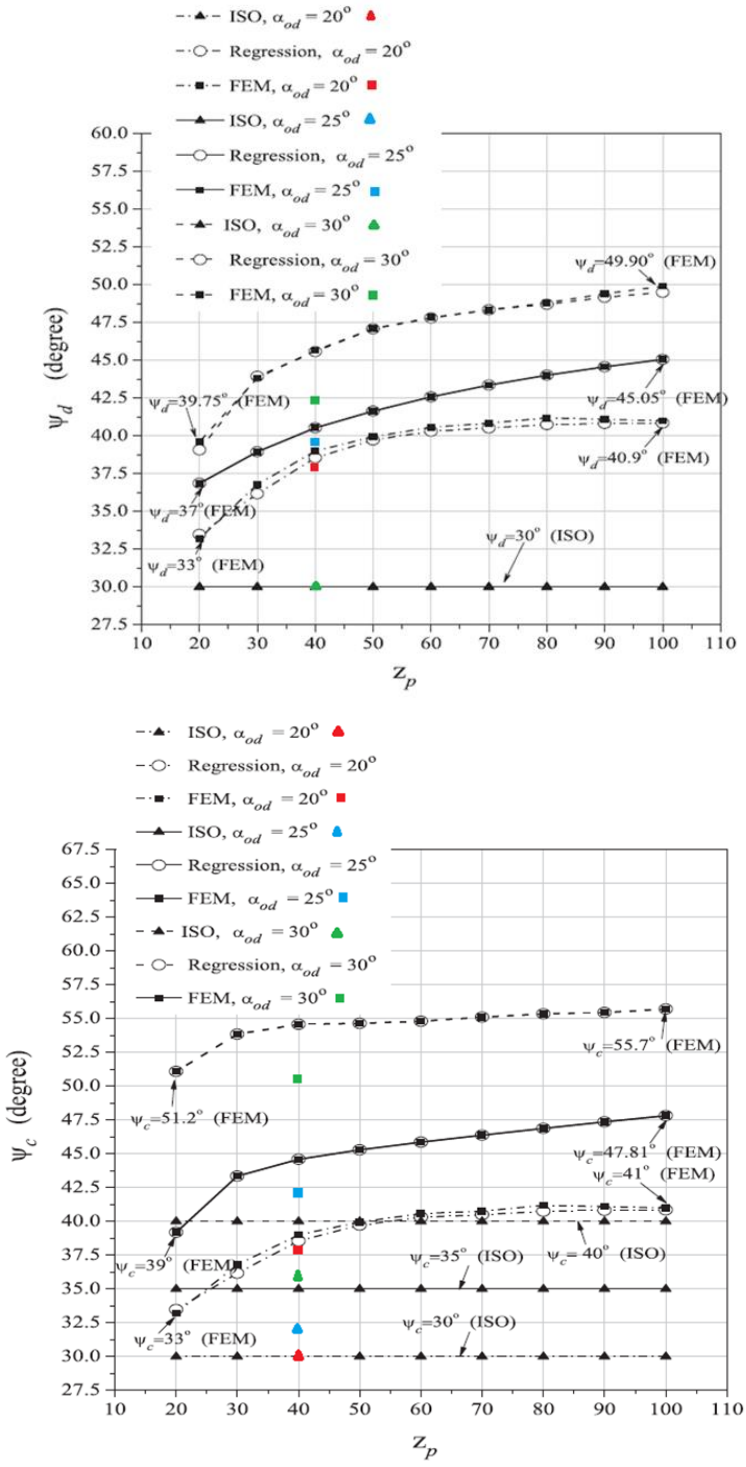

Fig. 4.1 Comparison of the drive and coast sides critical section tangent angles of this thesis and previous work [15] on the plots of [15] at Z_p=40 for different drive side pressure angles, α_c=20°

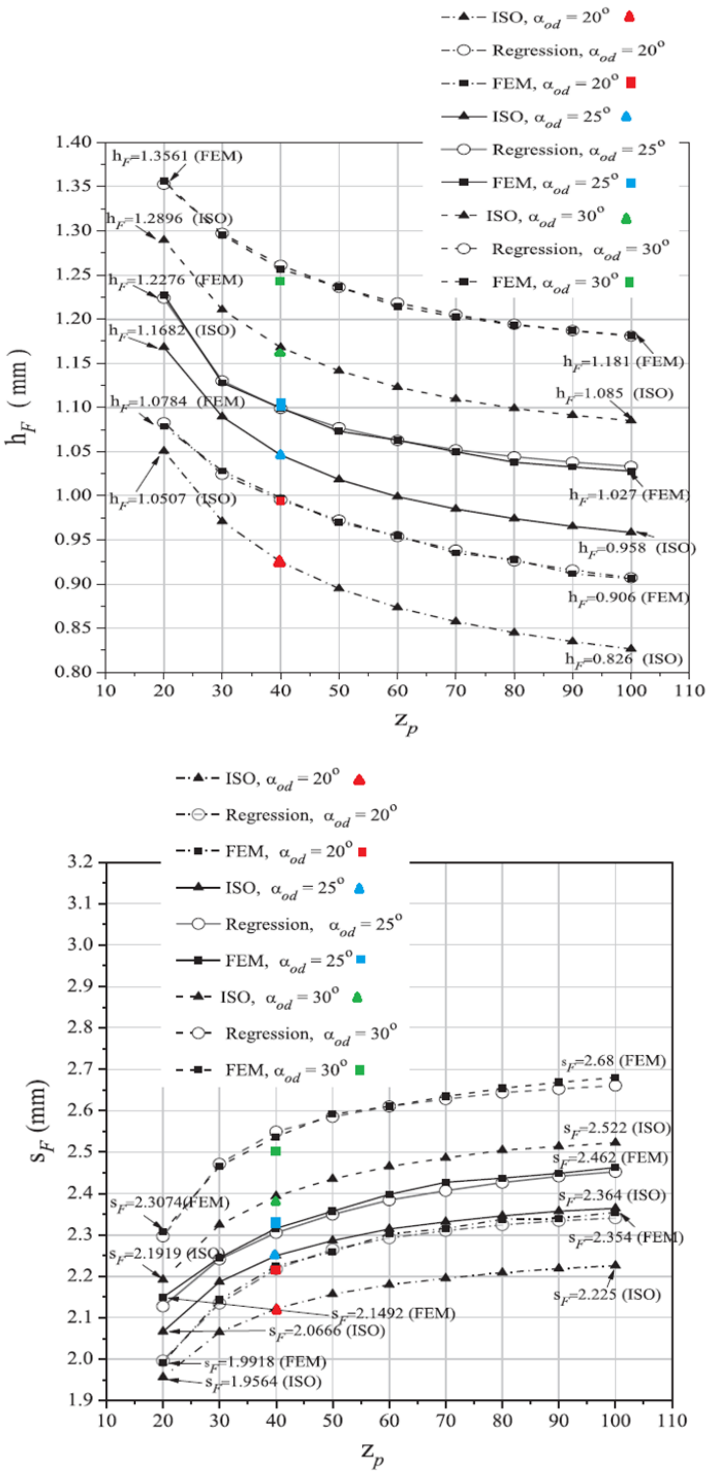

Fig. 4.2 Comparison of the critical section tooth height and thickness of this thesis and previous work [15] on the plots of [15] at Z_p=40 for different drive side pressure angles, α_c=20°

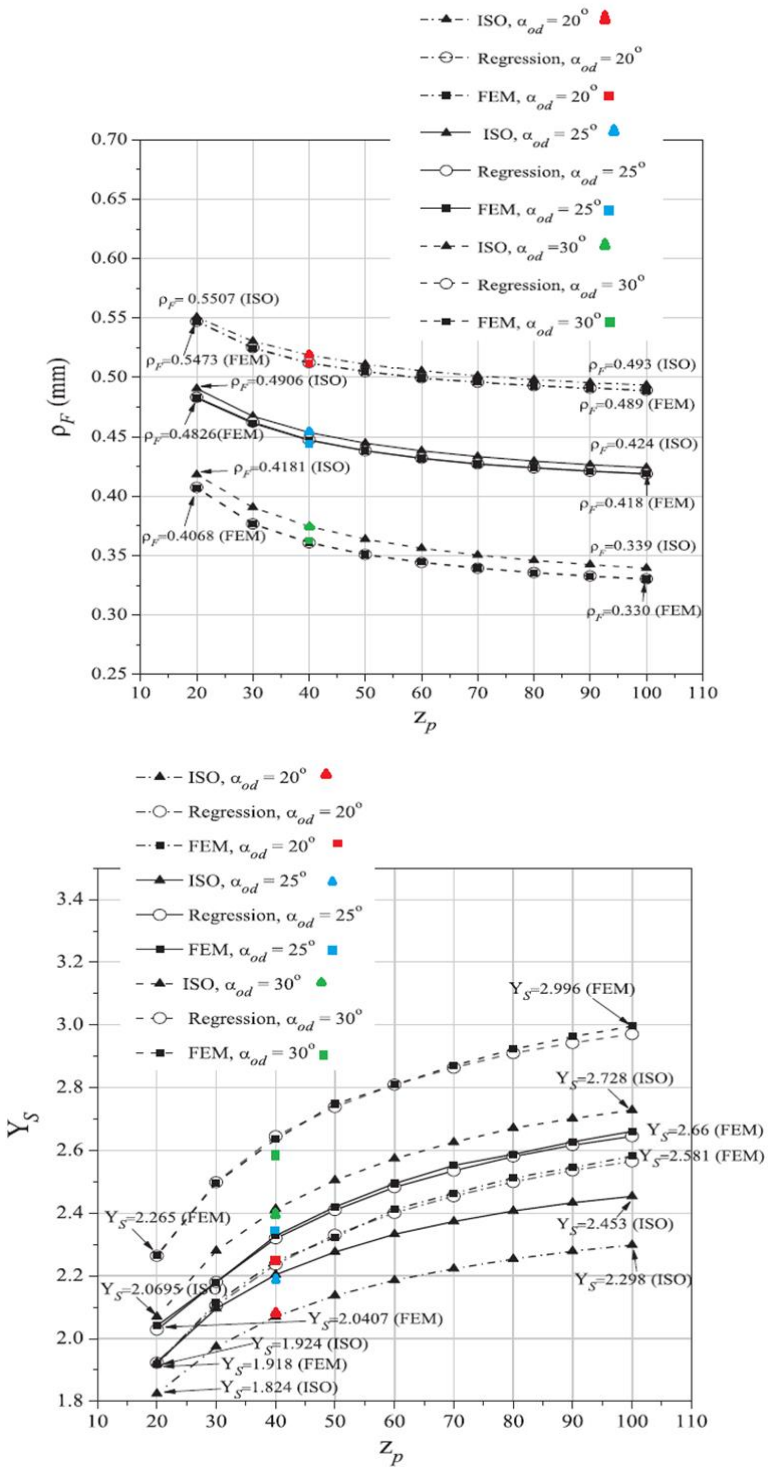

Fig. 4.3 Comparison of the critical section root fillet radius of curvature and stress correction factor of this thesis and previous work [15] on the plots of [15] at Z_p=40 for different drive side pressure angles, α_c=20°

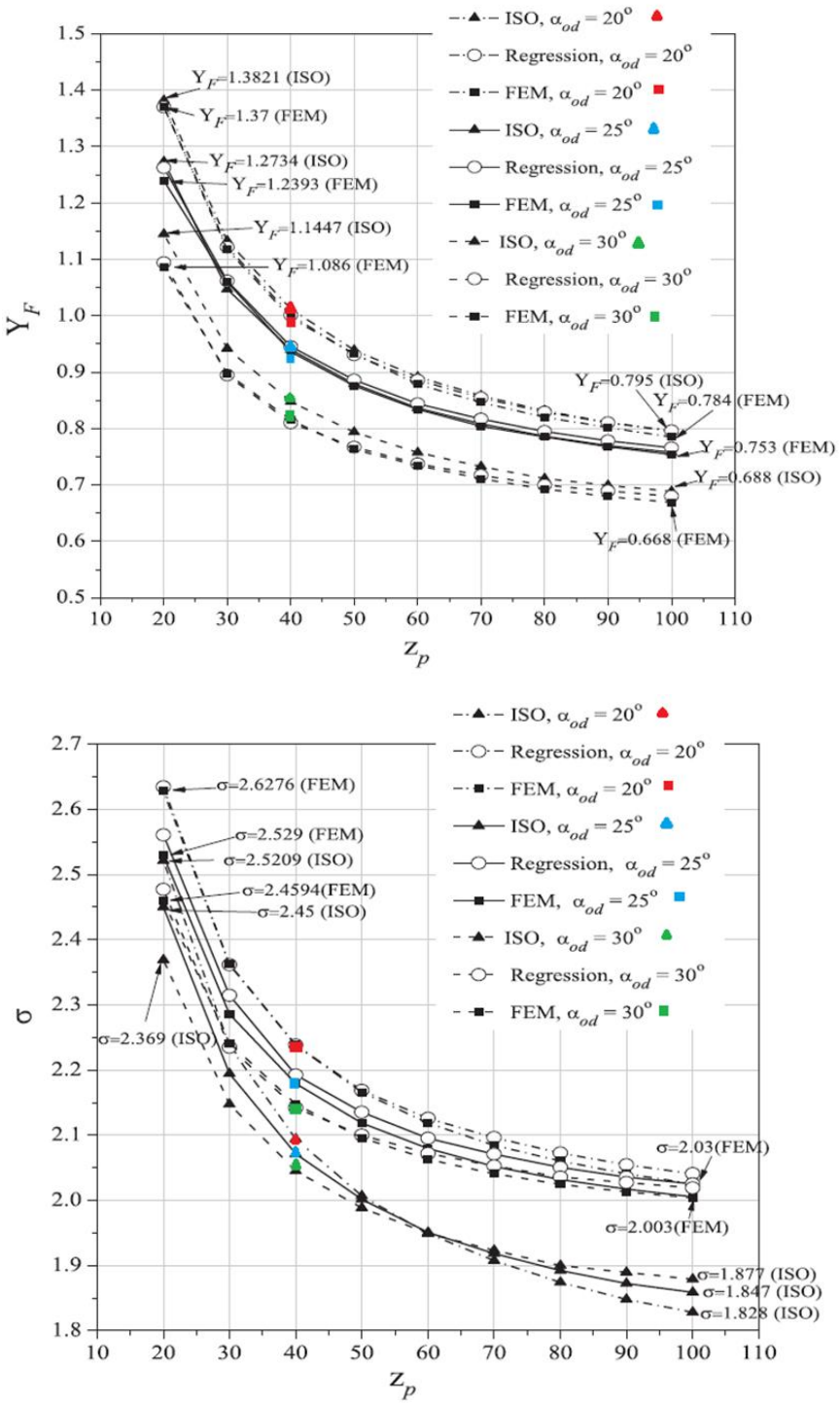

Fig. 4.4 Comparison of the critical section tooth form factor and bending stress of this thesis and previous work [15] on the plots of [15] at Z_p=40 for different drive side pressure angles, α_c=20°

4.1.1.2 The Effect of Coast Side Pressure Angle

In previous work [15] the influence of coast side pressure angle on the critical section and bending stress parameters (β_d, β_c, h_r, t_r, ρ_F, Y_F, Y_S, σ) is plotted for different pinion teeth numbers Z_p (from 20 to 100). On these plots the data are given for only two teeth number 20 and 100 similar to the drive side plots. These data are compared with this thesis works in Table 5 and Table 6. It is seen that this thesis and previous work [15] data are very close to each other for this case.

Table 5. Comparison of the FEA and modified ISO method results with previous work [15] for the bending stress parameters, α_d=30°, Z_p=Z_g=20

PARAMETERS										
	α_d/α_c		β_d (°)	β_c (°)	h_r (mm)	t_r (mm)	ρ_F (mm)	Y_F	Y_S	σ (MPa)
Z 20, m 1	30°/20°	PW-ISO	30	40	1.2896	2.1919	0.4181	1.1447	2.0695	23.69
		PW-FEM	39.75	51.2	1.3561	2.3074	0.4068	1.086	2.265	24.594
		TH-ISO	30	39.9043	1.2891	2.1915	0.4188	1.1447	2.0682	23.674
		TH-FEM	39.1719	51.7379	1.3528	2.3005	0.4077	1.09	2.2551	24.58
	30°/25°	PW-ISO	30	35	1.338	2.2635	0.3494	1.108	2.2434	24.858
		PW-FEM	41.15	49	1.4055	2.374	0.3345	1.056	2.324	24.594
		TH-ISO	30	35.6678	1.3385	2.2659	0.3502	1.1059	2.243	24.805
		TH-FEM	41.2497	48.998	1.4057	2.3745	0.3349	1.0581	2.291	24.24
	30°/30°	PW-ISO	30	30	1.3953	2.36	0.2675	1.056	2.5244	26.66
		PW-FEM	47.7	47.73	1.4759	2.4874	0.2424	1.0063	2.5244	25.399
		TH-ISO	30	30	1.3953	2.36	0.2686	1.056	2.5258	26.673
		TH-FEM	46.1429	46.1429	1.4704	2.4757	0.2446	1.0122	2.4827	25.13

Table 6. Comparison of the FEA and modified ISO method results with previous work [15] for the bending stress parameters, α_d=30°, Z_p=Z_g=100

PARAMETERS										
	α_d/α_c		β_d (°)	β_c (°)	h_r (mm)	t_r (mm)	ρ_F (mm)	Y_F	Y_S	σ (MPa)
Z 100, m 1	30°/20°	PW-ISO	30	40	1.085	2.522	0.339	0.688	2.728	18.77
		PW-FEM	49.9	55.7	1.181	2.68	0.33	0.668	2.996	20.03
		TH-ISO	30	32.9042	1.0818	2.5065	0.3394	0.696	2.7164	18.9061
		TH-FEM	46.9293	51.1941	1.1672	2.6503	0.3311	0.6755	2.9948	20.23
	30°/25°	PW-ISO	30	35	1.165	2.639	0.256	0.679	3.121	21.24
		PW-FEM	52.5	54.78	1.247	2.787	0.244	0.652	3.23	21.14
		TH-ISO	30	31.8007	1.164	2.6405	0.2562	0.6775	3.125	21.1721
		TH-FEM	48.5968	51.5478	1.2367	2.7632	0.2457	0.6601	3.2206	21.26
	30°/30°	PW-ISO	30	30	1.253	2.795	0.155	0.652	3.971	25.9
		PW-FEM	58	58.05	1.317	2.926	0.139	0.627	3.894	24.42
		TH-ISO	30	30	1.2523	2.8039	0.1553	0.6476	3.9866	25.8192
		TH-FEM	52.1206	52.1206	1.308	2.8979	0.1413	0.6351	3.8186	24.25

Table 7. Comparison of the bending stress parameters for the FEA and modified ISO method results, α_d=30°, Z_p=Z_g=40

PARAMETERS										
	α_d/α_c		β_d (°)	β_c (°)	h_r (mm)	t_r (mm)	ρ_F (mm)	Y_F	Y_S	σ (MPa)
Z 40, m 1	30°/20°	TH-ISO	30	35.9222	1.1658	2.3774	0.3748	0.8587	2.4005	20.6126
		TH-FEM	42.4855	50.6337	1.2414	2.5033	0.3632	0.827	2.5865	21.39
	30°/25°	TH-ISO	30	33.4942	1.232	2.4862	0.2982	0.8286	2.685	22.2483
		TH-FEM	46.9956	52.753	1.3139	2.6262	0.2811	0.7939	2.7937	22.18
	30°/30°	TH-ISO	30	30	1.3055	2.6196	0.2061	0.789	3.2026	25.2669
		TH-FEM	53.4706	53.4706	1.3843	2.7553	0.181	0.7577	3.1528	23.89

Table 8. Comparison of the bending stress of standard ISO method with FEA results for α_d=α_c=30°

		σ (MPa)	
α_d/α_c	Z_p/Z_g	ISO	FEA
30°/30°	20/20	28.44	25.13
	40/40	25.75	23.89
	100/100	26.76	24.25

Then similar to the previous case, this thesis works for 40 teeth are also compared with the previous work by putting signs in its plots as shown in Fig. 4.5, Fig. 4.6, Fig. 4.7 and Fig. 4.8. It is clearly seen that for 40 teeth the results of this thesis and

previous work is also very close to each other. Thus this thesis work is again verified by using the previous work [15] results. Then the similar discussions for this case with the previous work [15] can be done:

1- From Table 5, Table 6, Table 7 and with the help of Fig. 4.5 it is found that as α_c increases the angle of tangent at the drive side β_d increases in FEA study. It is also inferred that the angle of tangent at the coast side β_c decreases with an increase in α_c in modified ISO method. Also by increasing the number of teeth both of β_d and β_c increase in both of the FEA and modified ISO studies.

2- From Table 5, Table 6, Table 7 and with the help of Fig. 4.6, Fig. 4.7 and Fig. 4.8 it is found that as α_c increases the tooth form factor Y_f decreases which is mainly because of the corresponding increase in critical tooth thickness t_r, despite the increase in critical tooth height h_r. However the stress correction factor Y_s increases because of the corresponding decrease in root fillet radius of curvature ρ_f. The respective determined values of the bending stress σ increases with an increase in α_c. This is because of the corresponding increase in stress correction factor Y_s is more dominating than the increase in tooth form factor Y_F. Thus an increase in α_c is not a suitable way to enhance the bending strength of the gear tooth. Also by increasing the number of teeth the bending stress σ does not decrease for high α_c since the Y_s increases very much.

3- The present FEA results also show higher values of σ than that of the modified ISO method. The bending stresses in FEA are %5 higher than modified ISO method for low number of teeth and the percentage increases to %10 for high number of teeth. According to Table 8, the standard ISO method gives %8-12 larger bending stress results than FEA results for external symmetric gears with 30° pressure angle.

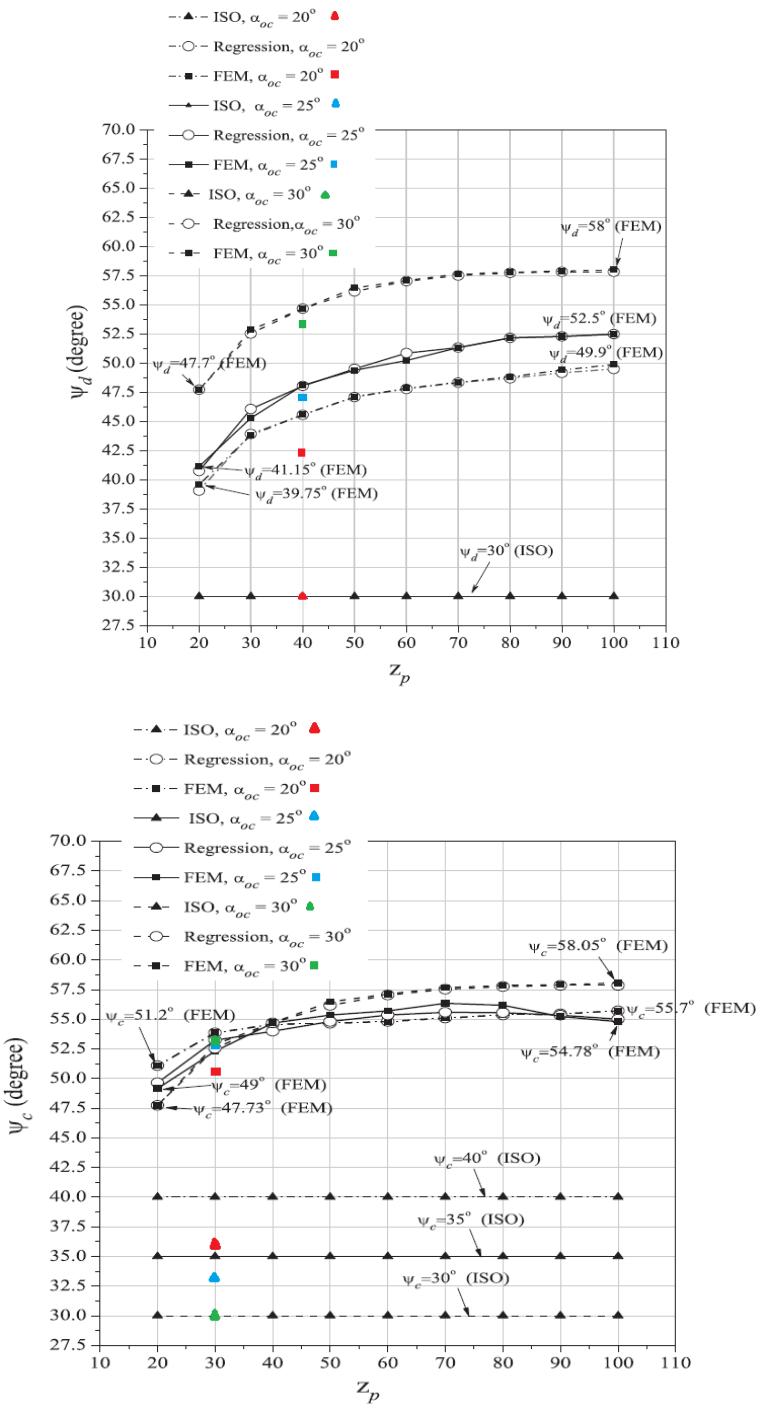

Fig. 4.5 Comparison of the drive and coast sides critical section tangent angles of this thesis and previous work [15] on the plots of [15] at Z_p=40 for different coast side pressure angles, α_d=30°

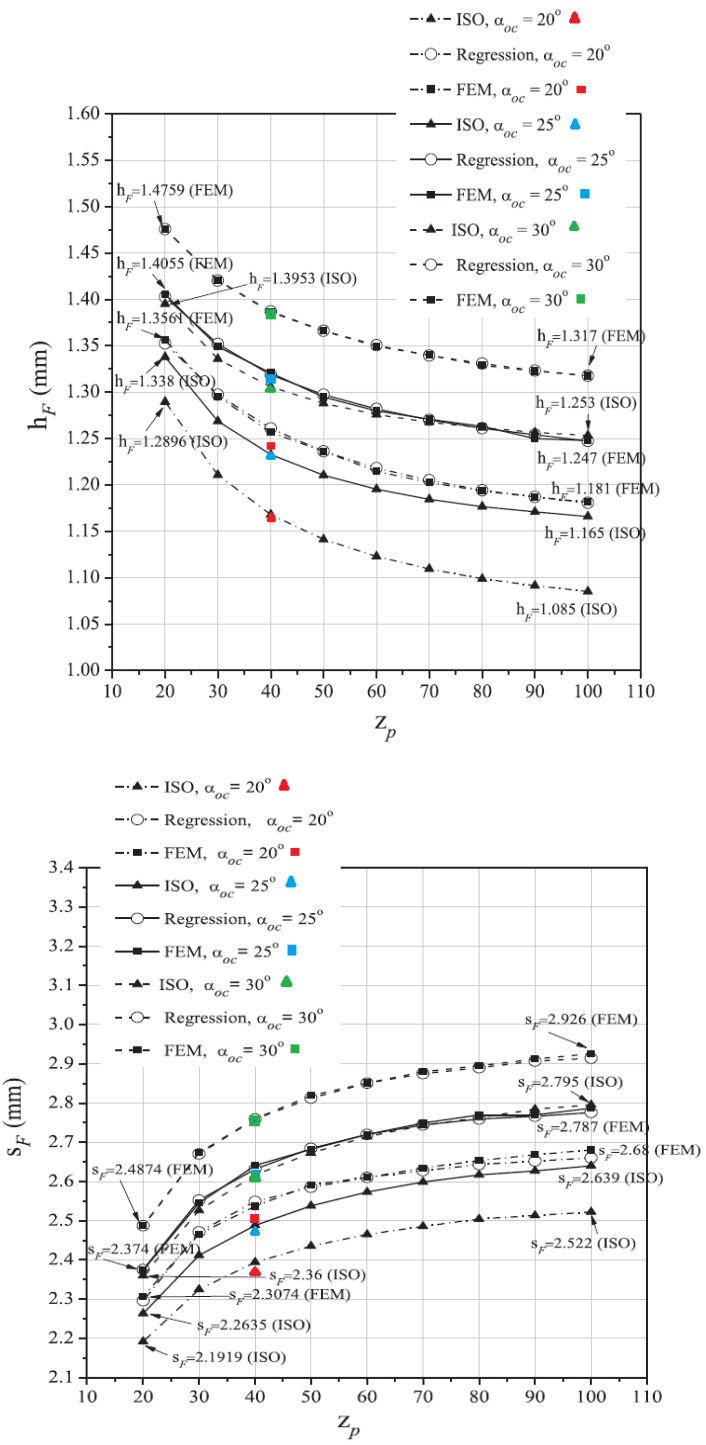

Fig. 4.6 Comparison of the critical section tooth height and thickness of this thesis and previous work [15] on the plots of [15] at Z_p=40 for different coast side pressure angles, α_d=30°

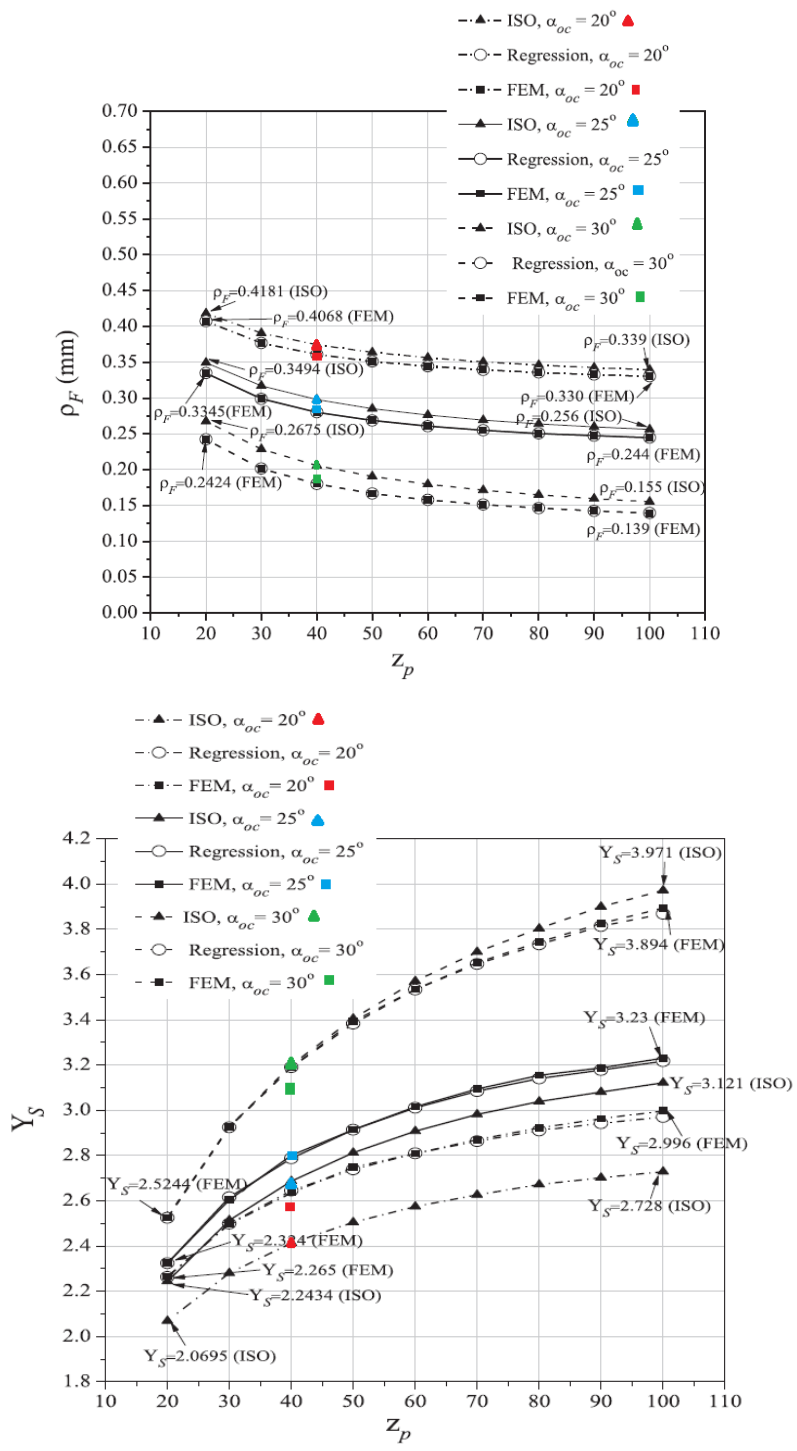

Fig. 4.7 Comparison of the critical section root fillet radius of curvature and stress correction factor of this thesis and previous work [15] on the plots of [15] at Z_p=40 for different coast side pressure angles, α_d=30°

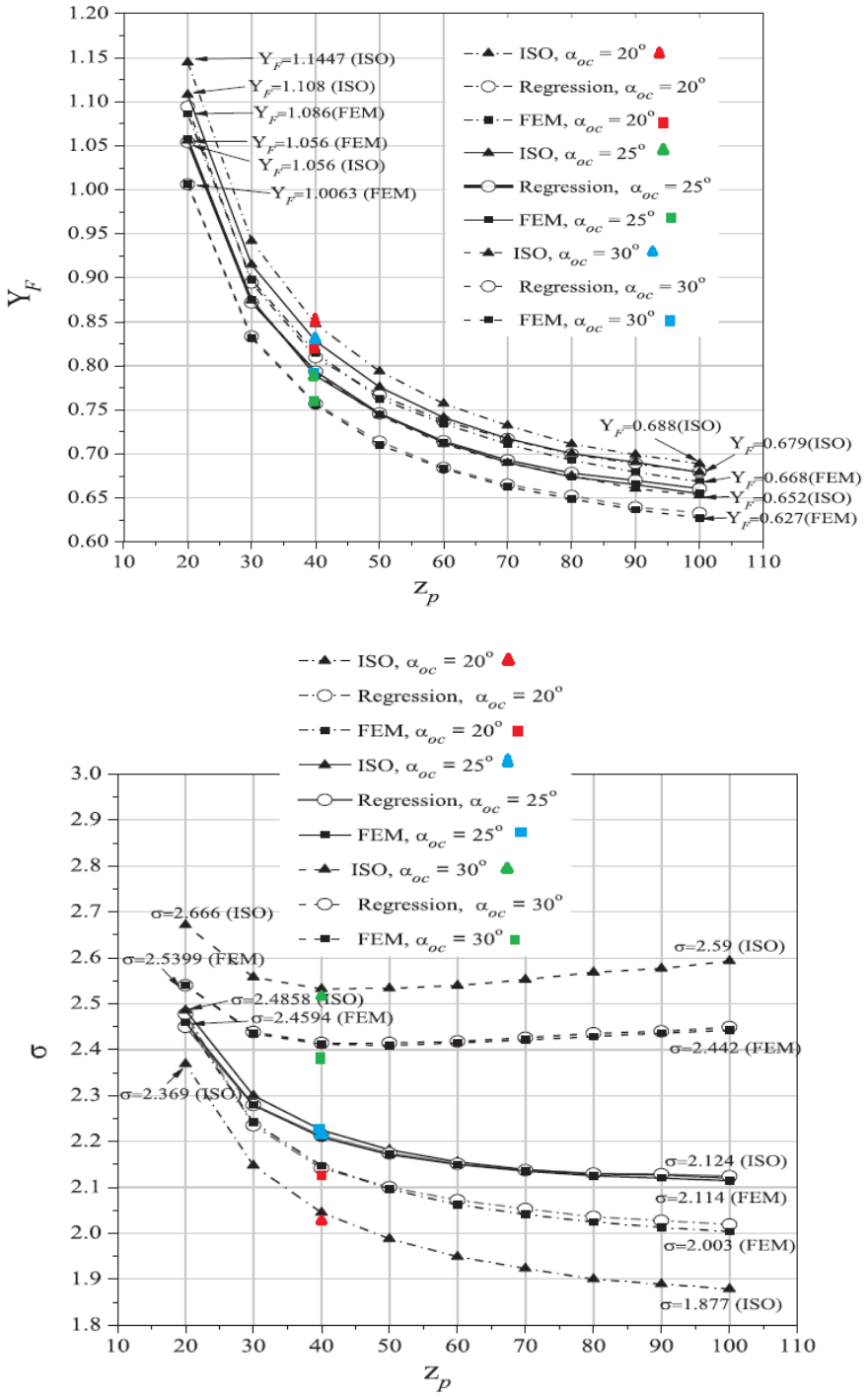

Fig. 4.8 Comparison of the critical section tooth form factor and bending stress of this thesis and previous work [15] on the plots of [15] at Z_p=40 for different coast side pressure angles, α_d=30°

4.1.2 The Case of Heavily Loaded Gear with Large Module

In this chapter external asymmetric spur gears with 4 mm module, unit face width, standard tooth height (a=1, b=1.25), zero profile shift and 500 N applied force are studied with FEA and modified ISO methods. These studies are done in two cases. In first case the influence of drive side pressure angles are examined and in second case the influence of coast side pressure angles are examined.

4.1.2.1 The Effect of Drive Side Pressure Angle

By the help of Fig. 4.9, Fig. 4.10, Fig. 4.11 and Fig. 4.12, the heavily loaded case analysis can be compared with lightly loaded case analysis according to the drive side pressure angle change. With respect to the lightly loaded case, the drive and coast side tangent angles β_d and β_c are almost same. The critical section tooth height h_r and thickness t_r and the root fillet radius of curvature ρ_f almost increased to four times of their values. Also the tooth form factor and stress correction factor are almost same. Finally, the maximum bending stress is almost 12.5 times larger for this case. Here the value, 12.5, comes from 50 divided by 4 where the load is 50 times larger and the module is 4 times larger for this case. All these results are the expected results.

The graphs of this case are very similar to the lightly loaded case so that the same discussions with the first analysis can be done. The main result is that the bending stress σ decreases with an increase in α_d. Also, the bending stresses in FEA are %5 higher than modified ISO method for low number of teeth and the percentage increases to %10 for high number of teeth. Also by increasing the number of teeth the bending stress σ decreases.

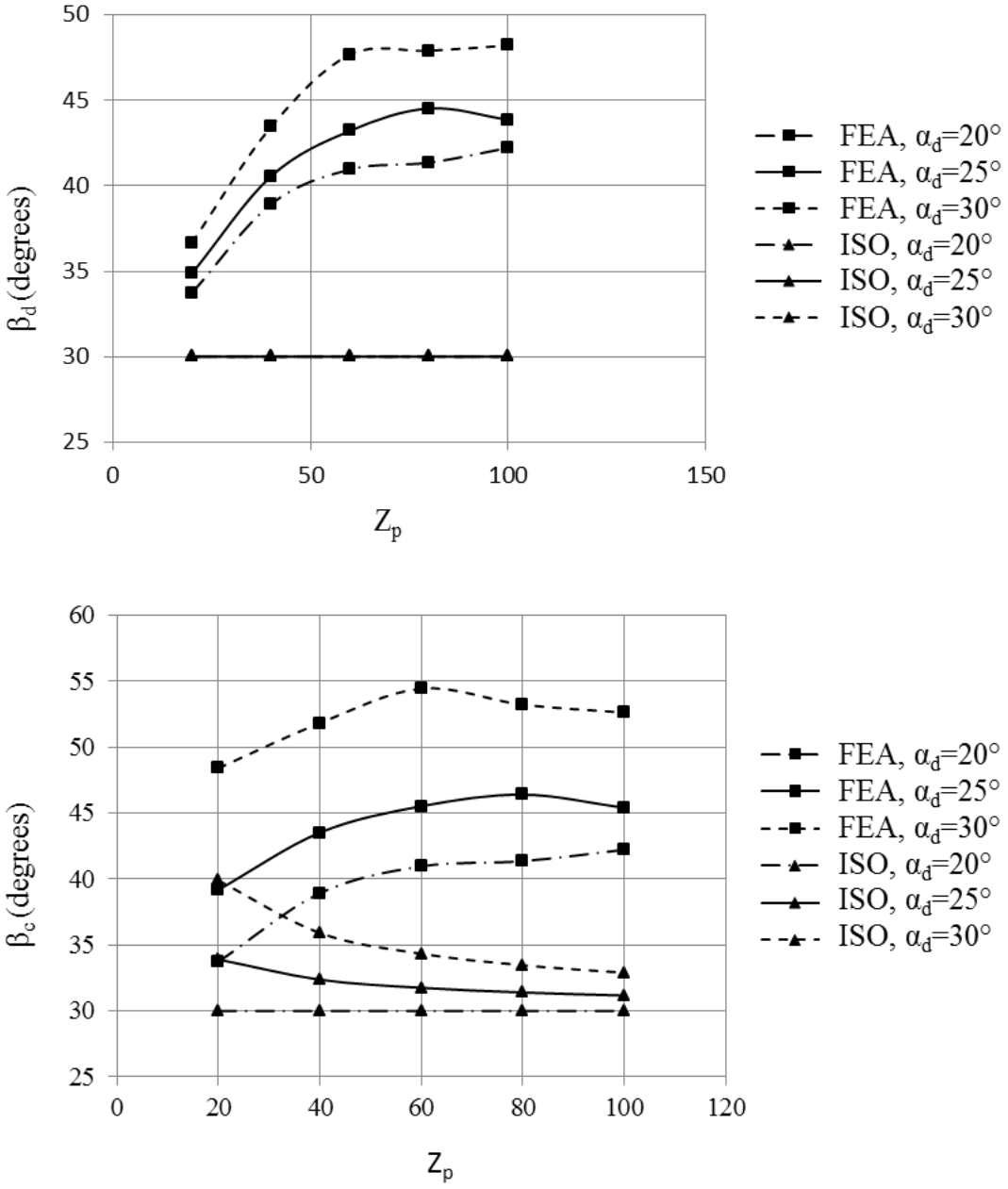

Fig. 4.9 Comparison of the drive and coast sides critical section tangent angles for different drive side pressure angles, α_c=20°

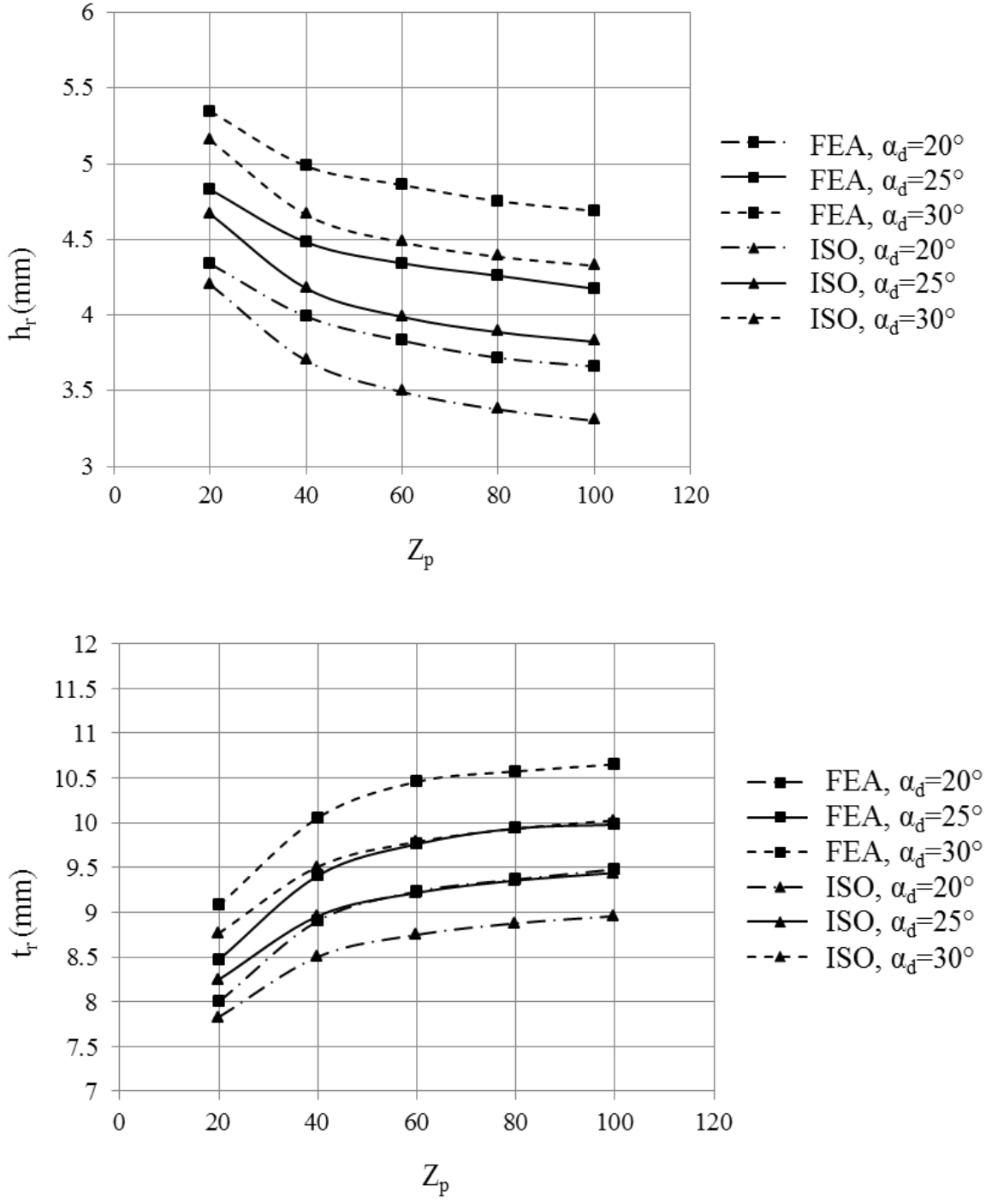

Fig. 4.10 Comparison of the critical section tooth height and thickness for different drive side pressure angles, α_c=20°

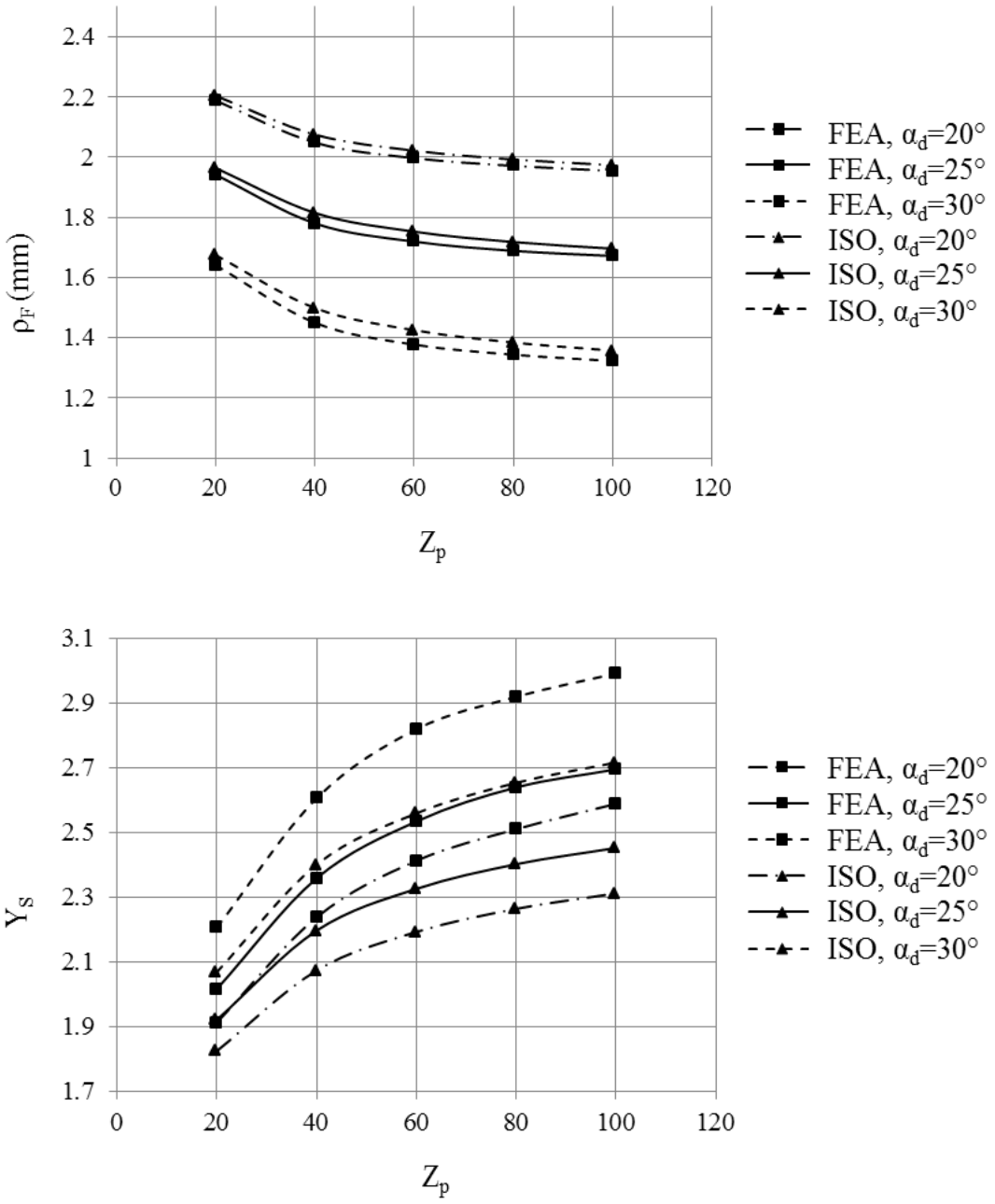

Fig. 4.11 Comparison of the critical section root fillet radius of curvature and stress correction factor for different drive side pressure angles, α_c=20°

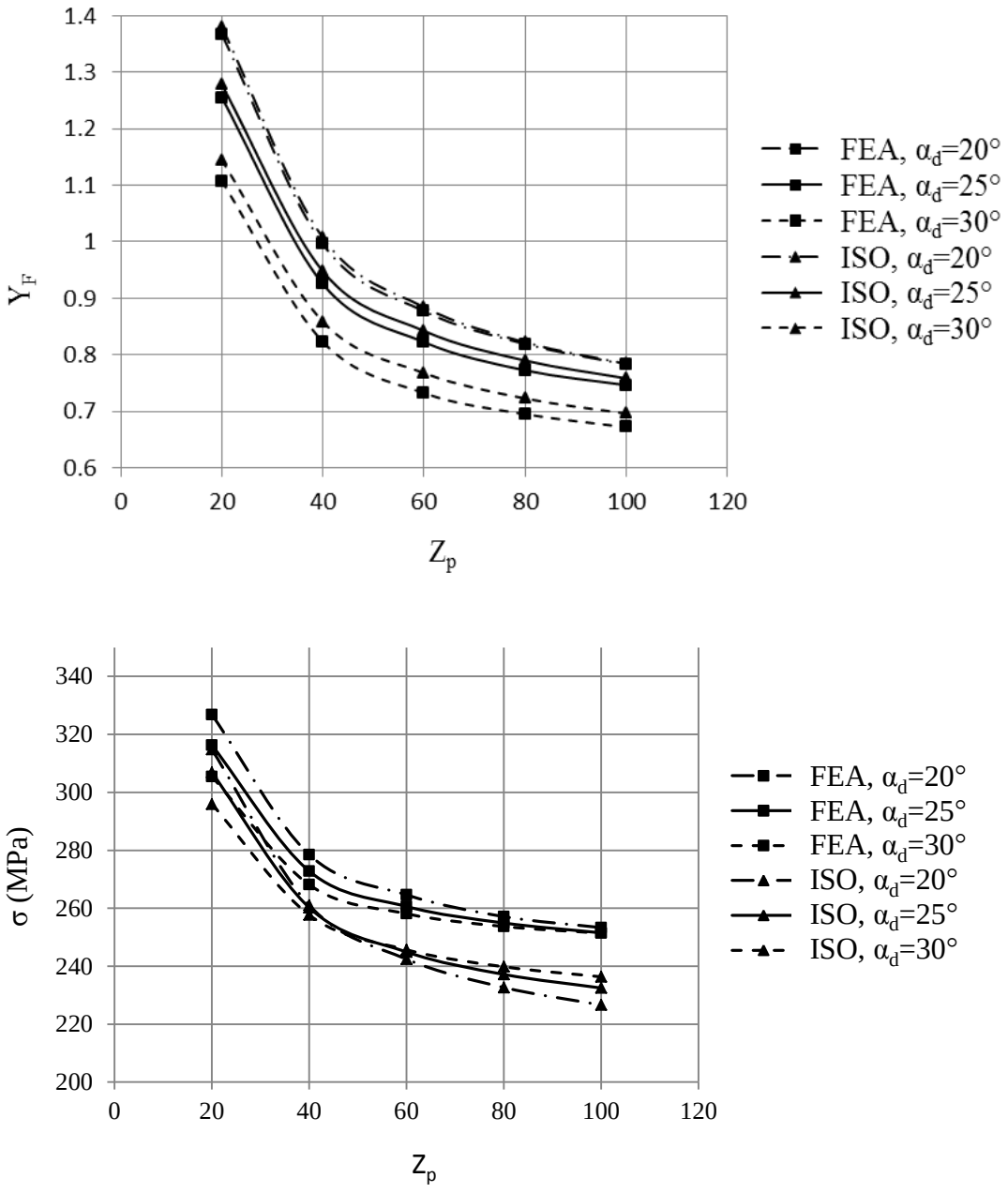

Fig. 4.12 Comparison of the critical section tooth form factor and bending stress for different drive side pressure angles, α_c=20°

4.1.2.2 The Effect of Coast Side Pressure Angle

By the help of Fig. 4.13, Fig. 4.14, Fig. 4.15 and Fig. 4.16, the heavily loaded case analysis can be compared with lightly loaded case analysis according to coast side pressure angle increase. With respect to the lightly loaded case, the drive and coast side tangent angles β_d and β_c are almost same. The critical section tooth height h_r and thickness t_r and the root fillet radius of curvature ρ_f almost increased to four times of their values. Also the tooth form factor and stress correction factor are almost same. Finally, the maximum bending stress is almost 12.5 times larger for this case. Here, the value, 12.5, comes from 50 divided by 4 where the load is 50 times larger and the module is 4 times larger for this case. All these results are the expected results.

The graphs of this case are very similar to the lightly loaded case so that the same discussions with the first analysis can be done. The main result is that the bending stress σ decreases with an increase in α_d. Also, the bending stresses in FEA are %5 higher than modified ISO method for low number of teeth and the percentage increases to %10 for high number of teeth. Also by increasing the number of teeth the bending stress σ decreases.

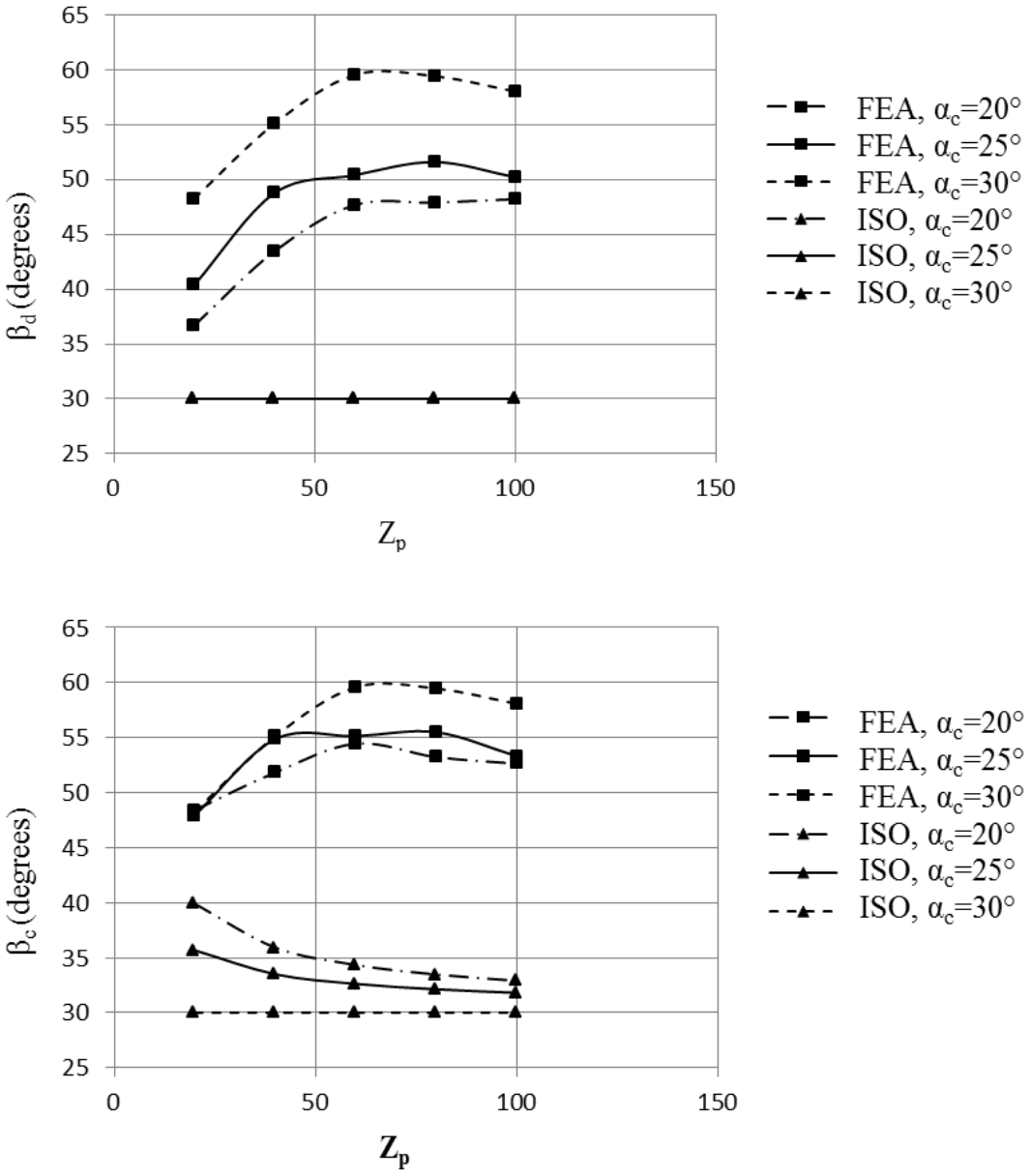

Fig. 4.13 Comparison of the drive and coast sides critical section tangent angles for different coast side pressure angles, α_d=30°

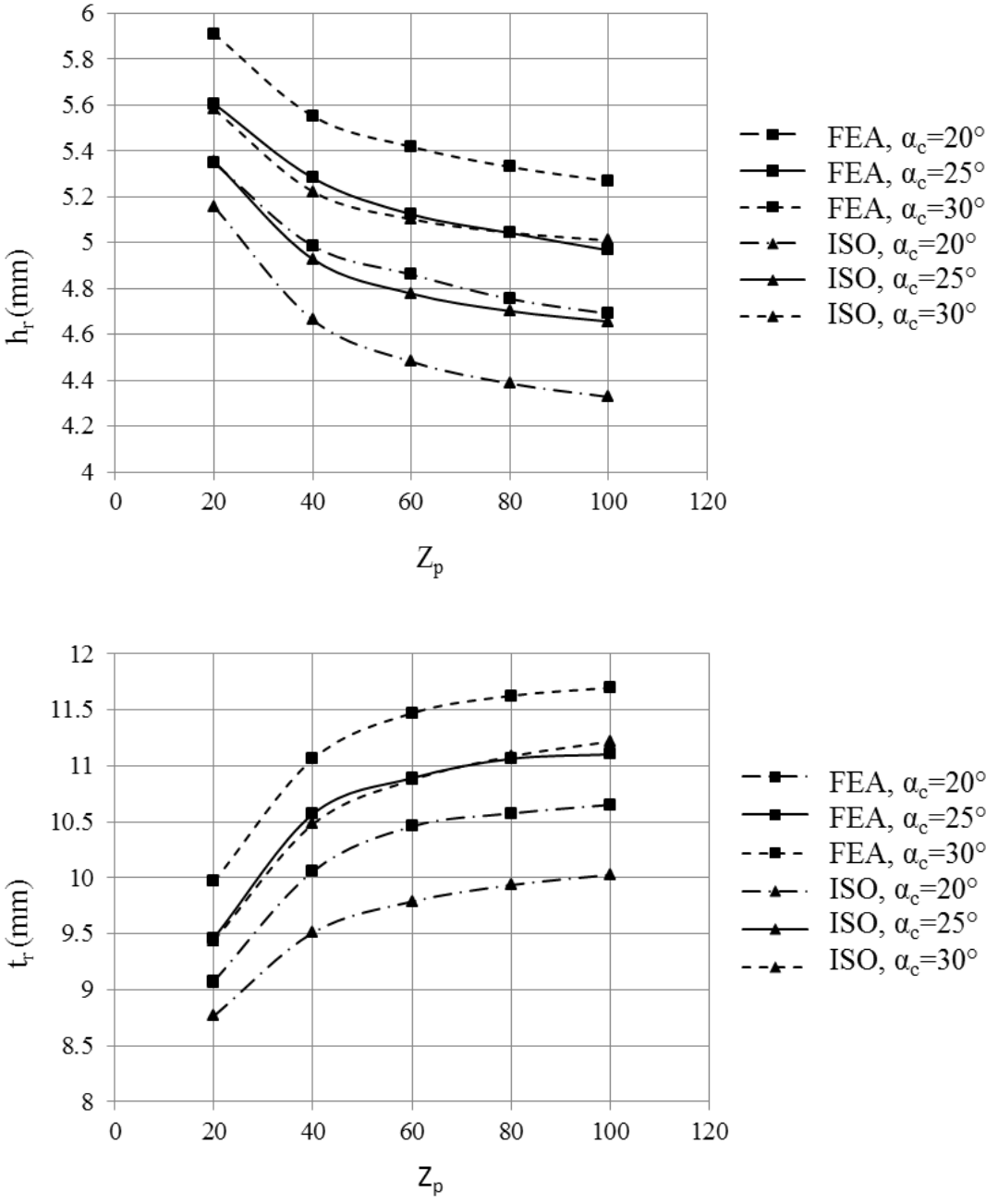

Fig. 4.14 The Comparison of the critical section tooth height and thickness for different coast side pressure angles, α_d=30°

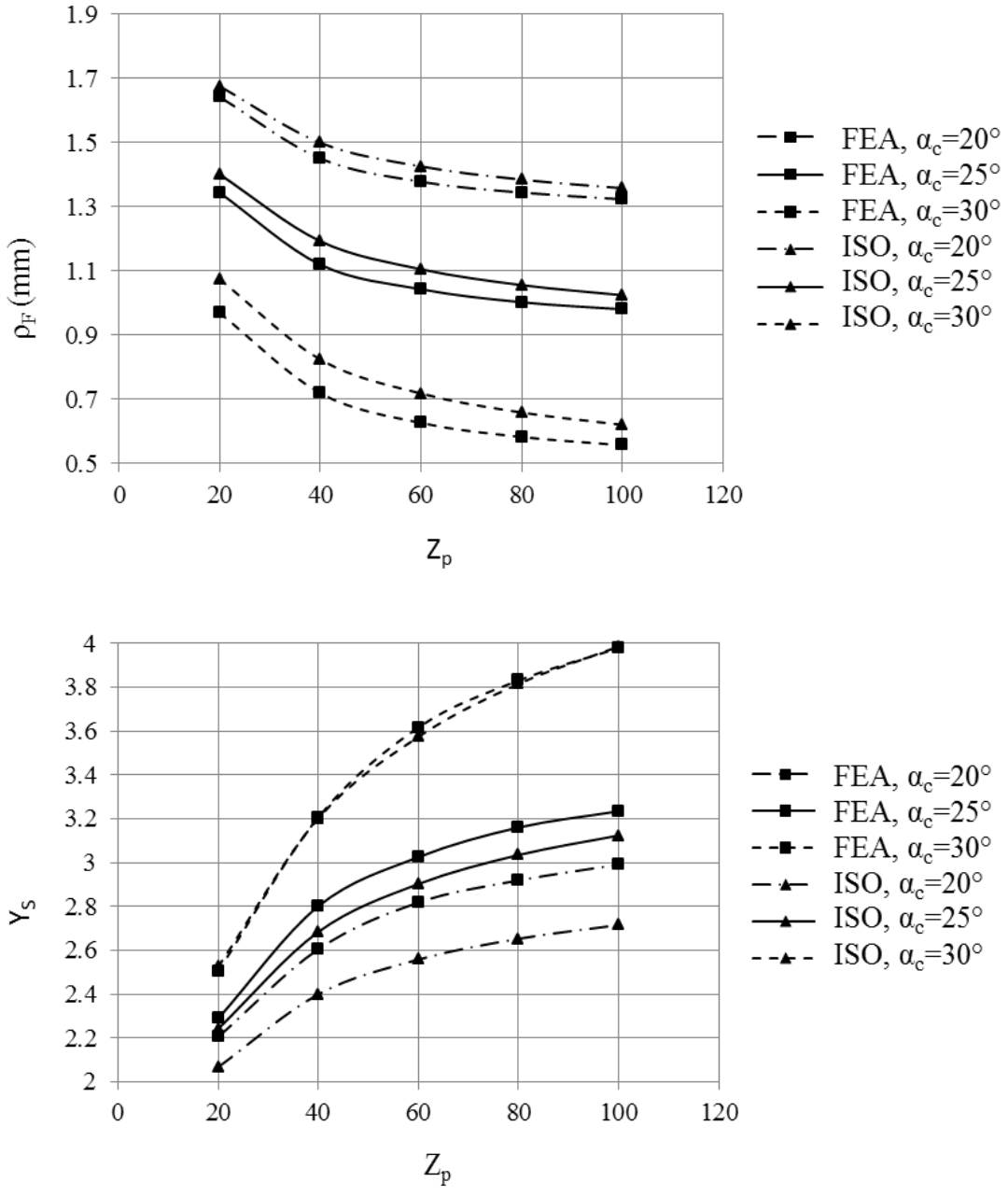

Fig. 4.15 Comparison of the critical section root fillet radius of curvature and stress correction factor for different coast side pressure angles, α_d=30°

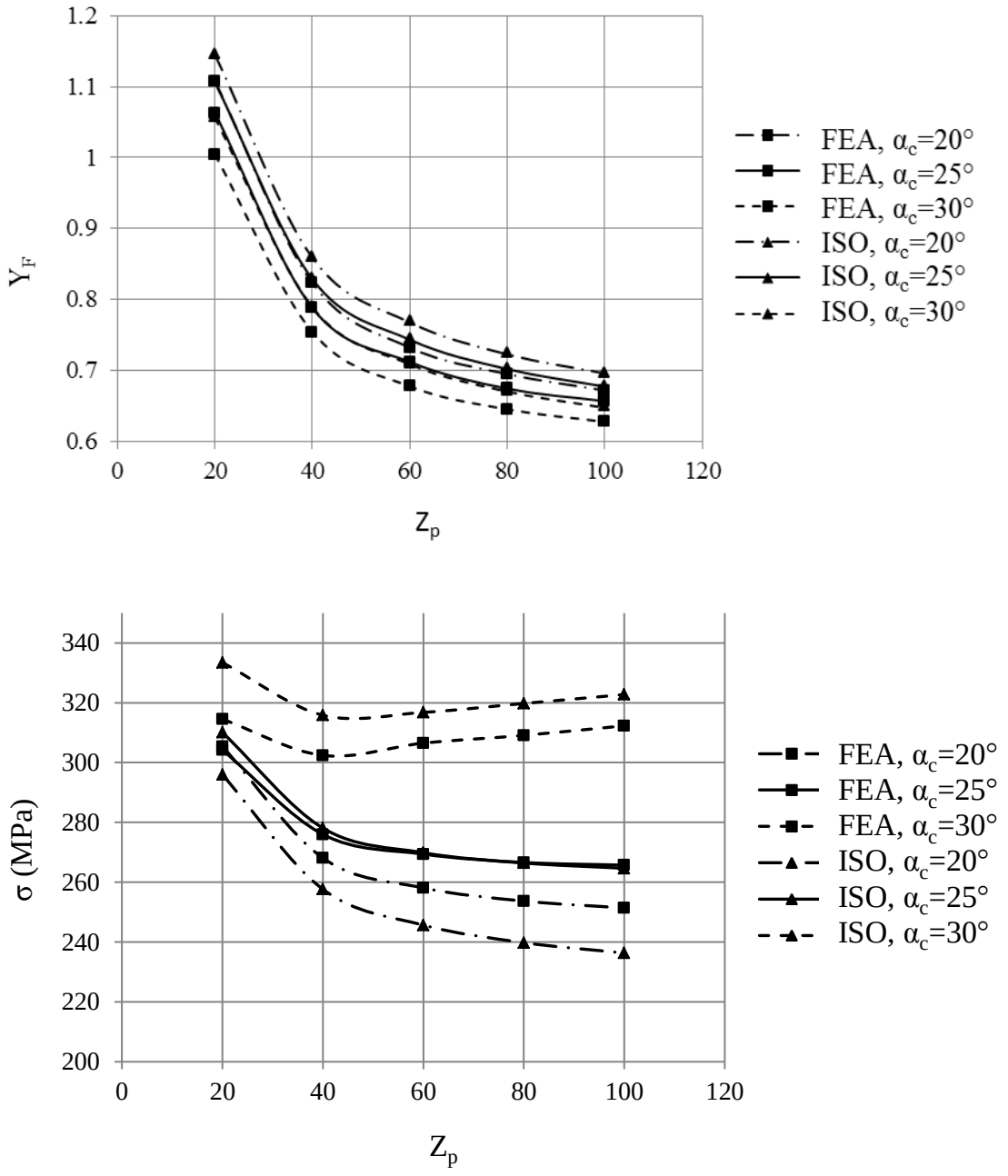

Fig. 4.16 Comparison of the critical section tooth form factor and bending stress for different coast side pressure angles, α_d=30°

4.2 Results and Discussions for Modified ISO and FEA Methods of Internal Asymmetric Spur Gear

The critical section and bending stress parameters (β_{id}, β_{ic}, h_{ri}, t_{ri}, ρ_{Fi}, Y_{Fi}, Y_{Si}, σ_i) are determined through FEA and modified ISO methods according to the different cases for the internal asymmetric spur gears.

4.2.1 The Case of Lightly Loaded Gear with Small Module

In this chapter internal asymmetric spur gears with 1 mm module, unit face width, zero profile shift and 10 N applied force are studied with FEA and ISO methods. These studies are done in two cases. In first case the analysis are done for internal gears having standard tooth height for different number of teeth. In this study, the effects of the coast and drive side pressure angles are reflected in a single figure for each parameter for a specified number of teeth. Moreover, the results of the standard and modified ISO methods are compared with FEA results for symmetric internal gears. In second case the analysis are done for internal gears having small tooth height for a specified number of teeth and only the effect of the drive side pressure angle is studied such that the results can be compared with [16].

4.2.1.1 The Effect of Drive and Coast Sides Pressure Angles for Internal Gears Having Standard Tooth Height

The first and second analyses are done with internal gears with 60 and 81 teeth, respectively. The addendum coefficient of the pinion type shaper cutter a_s (the dedendum coefficient of the internal gear at the same time) is 1.25 and the addendum coefficient of the internal gear a_i is 1. Then the internal gears in this study are typical standard (normal height) internal gears.

In terms of the first analysis, in the FEA according to Fig. 4.17 the drive side tangent angle β_{id} increases by the inrease of both of the drive and coast side pressure angles but the coast side tangent angle β_{ic} either slightly increases or decreases until 30° for coast side pressure angle. In the modified ISO method, the value of β_{id} is always equal to 60° and the respective β_{ic} increases with the increase of coast side pressure angle but decrease with the increase of drive side pressure angle and is generally higher than the FEA results. In the FEA according to Fig. 4.20 the tooth form factor Y_{Fi} decreases with increase in both drive and coast side pressure angles, which is mainly because of the corresponding increase in critical tooth thickness t_{ri}, despite the increase in critical tooth height h_{ri}. However the stress correction factor Y_{Si} increases with the increase in both drive and coast side pressure angles because of the corresponding decrease in root fillet radius of curvature ρ_{Fi}. In the FEA the respective determined values of the bending stress σ_i increases with the increase in coast side pressure angle and usually decreases with the decrease in coast side pressure angle. In terms of increase in drive side pressure angle the bending stress increases for the high coast side pressure angles and decreases only for very low coast side pressure angles α_{ci} (smaller than 20°). In case of a 16° coast side pressure angle, for instance, the bending stress decreases % 6 by the increase of the drive side pressure angle from 16° to 30°. The bending stress results of modified ISO method are % 5 lower than the results of the FEA except low drive and coast side pressure angles smaller than 20°. For example, for 16° drive and coast side pressure angles, modified ISO method gives % 10-15 lower bending stress than FEA method. Therefore, in the modified ISO method, the bending stress always increases with an increase in drive side pressure angle. For the low drive and coast side pressure angles, this is mainly because of the high differences in β_{id} and β_{ic} for FEA and ISO methods which causes increase in the amount of the differences in t_{ri} and Y_{fi} values for these methods.

Table 9. The analysis input parameters for Z_i=60, m=1

Analysis Input Parameters	
Z_e	20
a_s	1,25
a_i	1
a_e	1
F_{ni}	10 N

Table 10. Comparison of the bending stress of standard ISO method with FEA results for internal symmetric spur gears

		σ (MPa)	
Z_i	α_d/α_c	ISO	FEA
60	16°/16°	23	20
	20°/20°	20	19.76
	25°/25°	22.16	20.5
	30°/30°	28	38.5

According to Table 10, for internal symmetric spur gears, the standard ISO method generally gives %7-10 larger bending stress results than FEA results except 20° pressure angle. For low and high pressure angles the percentage increase to %15.

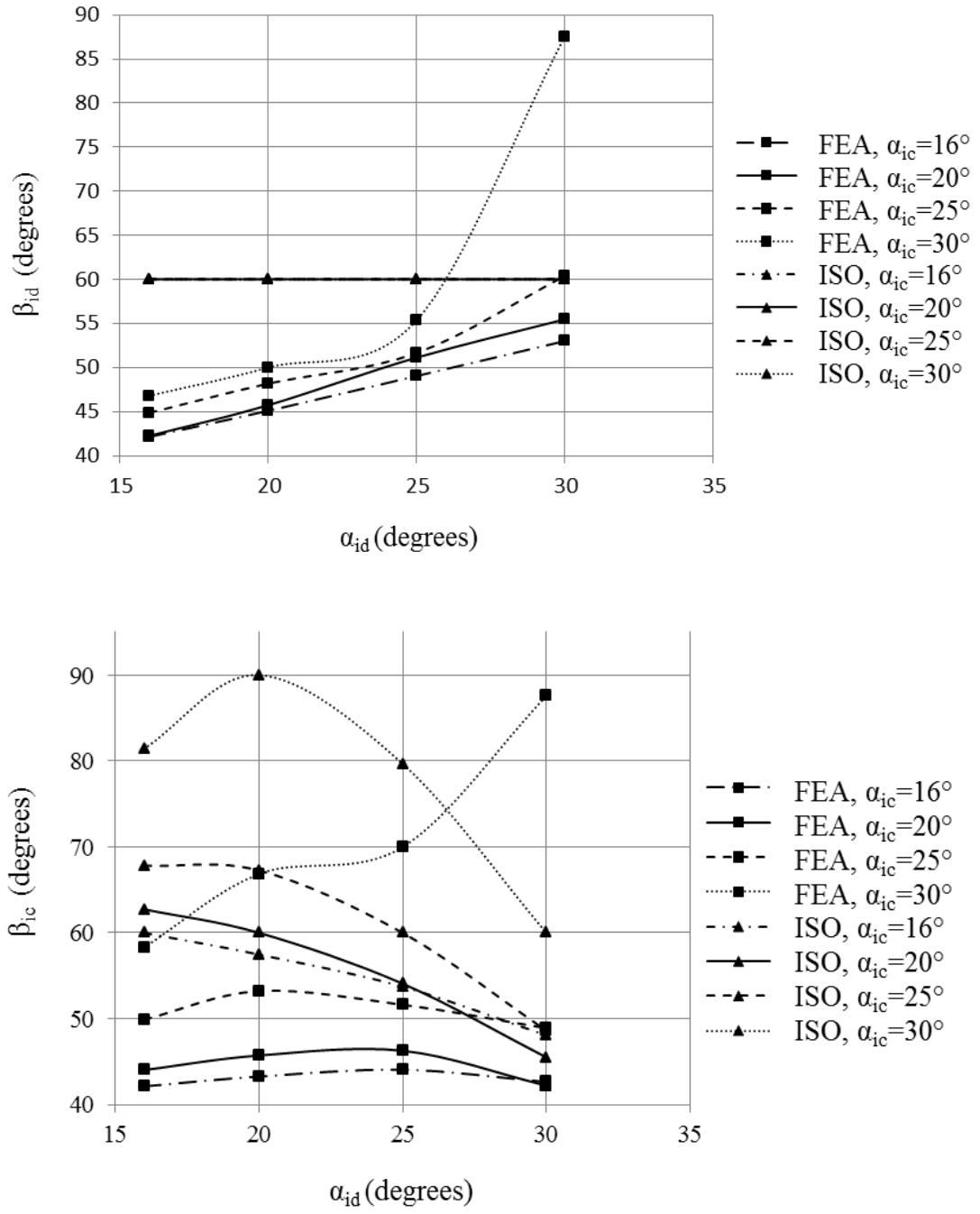

Fig. 4.17 Comparison of the drive and coast sides critical section tangent angles for different drive and coast side pressure angles at light load for $Z_i = 60$

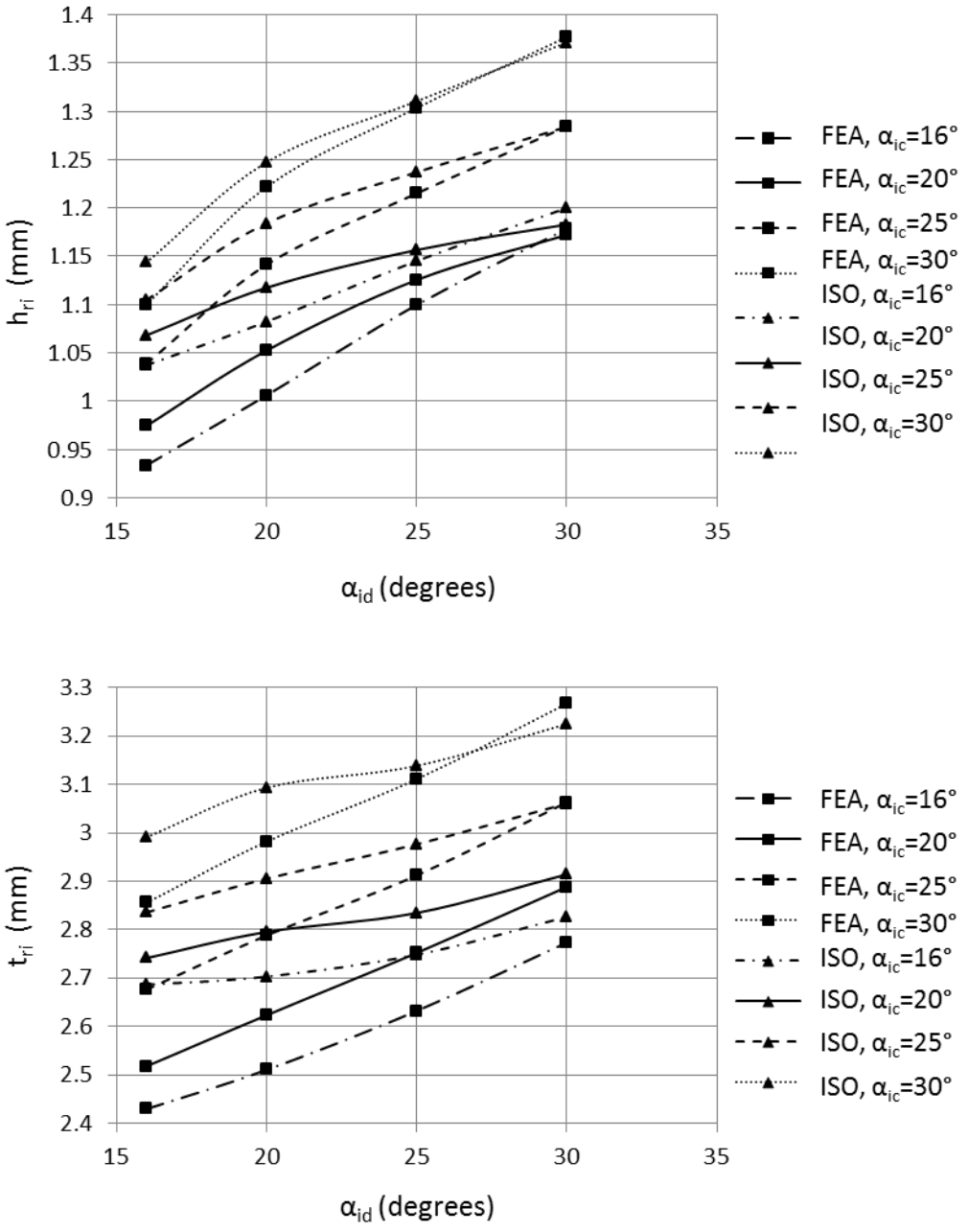

Fig. 4.18 Comparison of the critical section tooth height and thickness for different drive and coast side pressure angles at light load for $Z_i = 60$

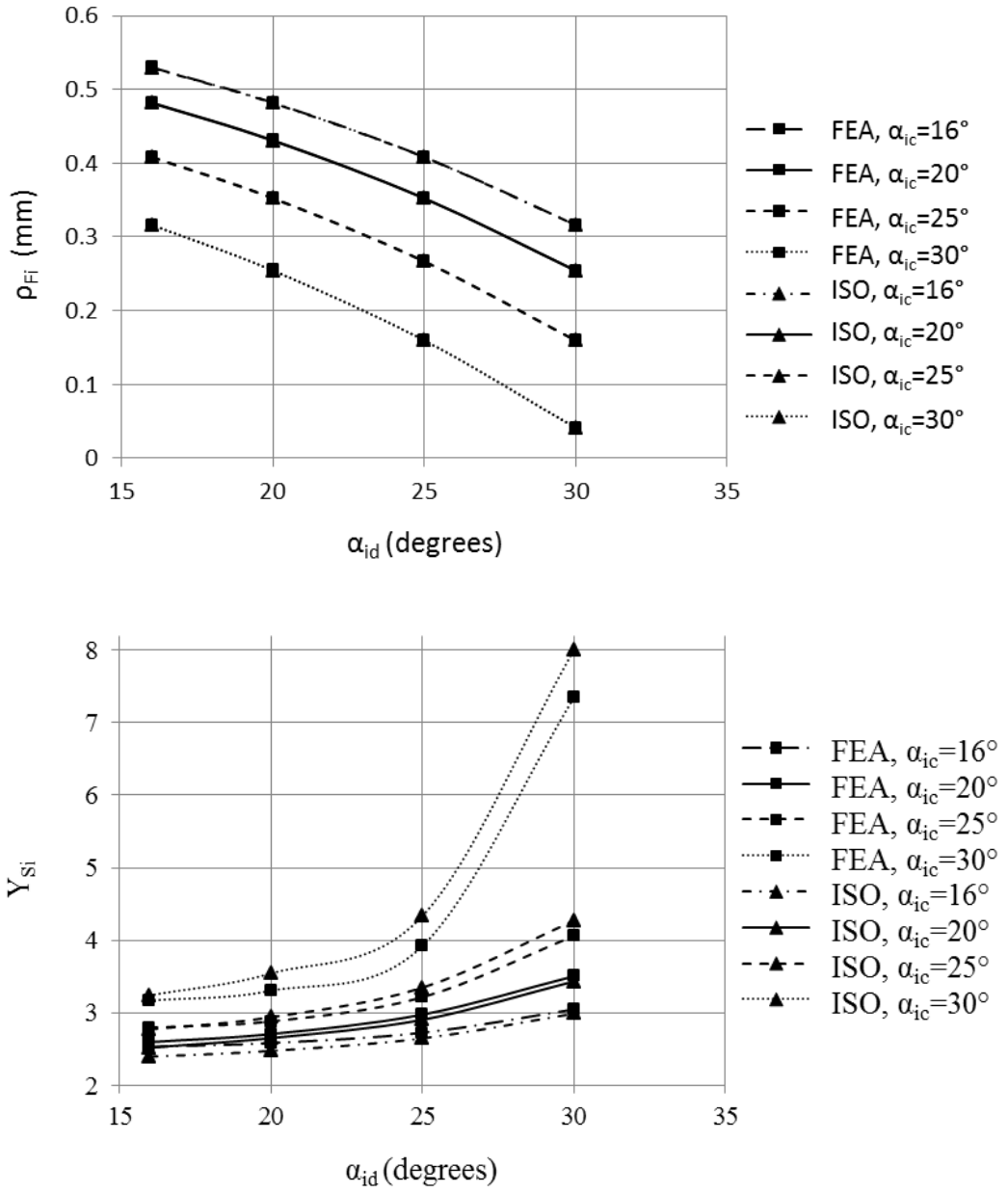

Fig. 4.19 Comparison of the critical section root fillet radius of curvature and stress correction factor for different drive and coast side pressure angles at light load for $Z_i = 60$

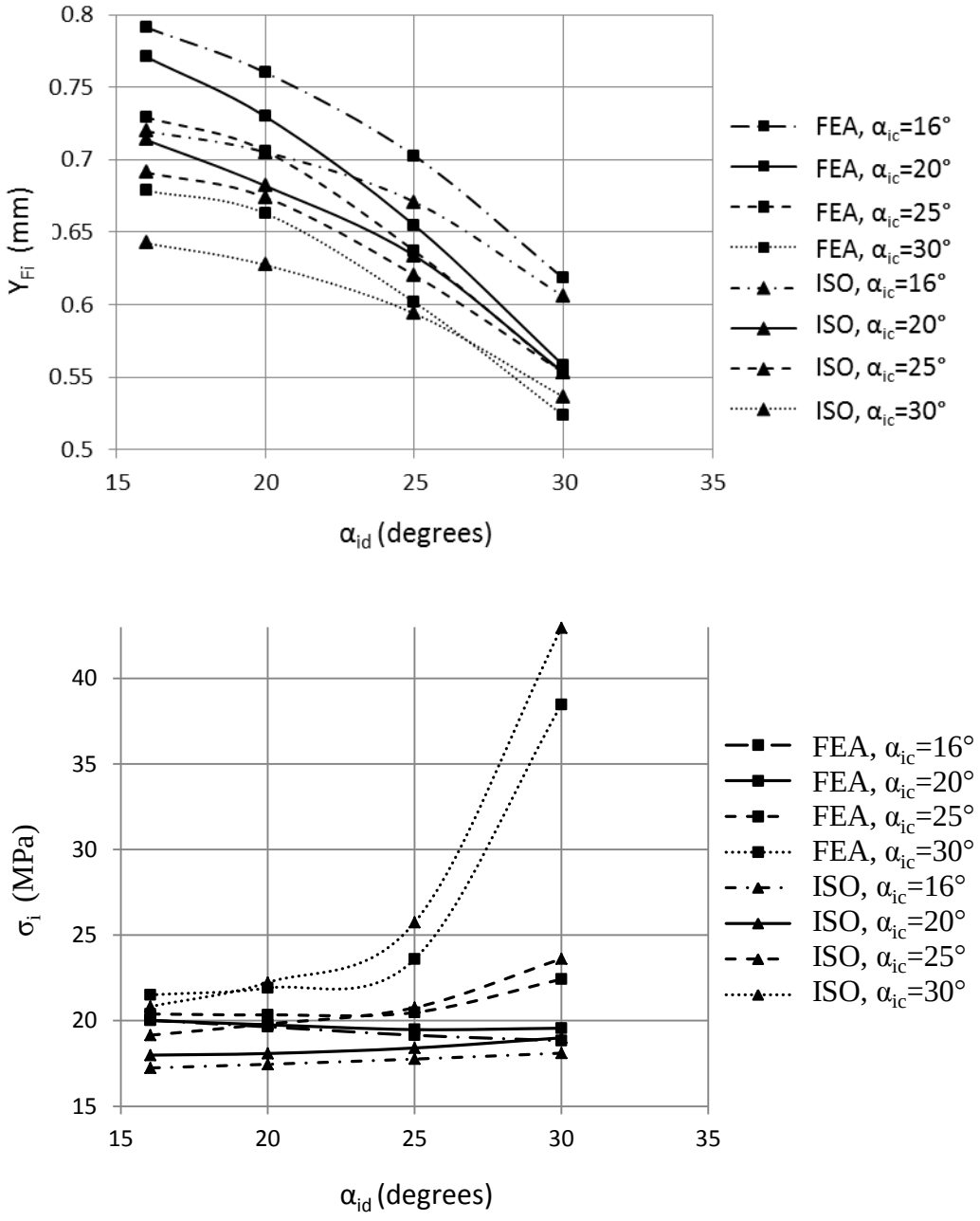

Fig. 4.20 Comparison of the critical section tooth form factor and bending stress for different drive and coast side pressure angles at light load for $Z_i = 60$

By the help of Fig. 4.21, Fig. 4.22, Fig. 4.23and Fig. 4.24, the second analysis, internal gear with 81 teeth, can be compared with the first analysis, internal gear with 60 teeth. With respect to the first analysis, the drive and coast side tangent angles β_{id} and β_{ic} are almost same. The critical section tooth height h_{ri} and thickness t_{ri} generally decreased but the root fillet radius of curvature ρ_{Fi} generally increased. Also the tooth form factor generally decreased and stress correction factor generally increased. Finally, the maximum bending stress decreased very less or remained same.

The graphs of the second analysis are very similar to the first analysis so that the same results with the first analysis can be obtained. The maximum bending stress σ_i increases with the increase in coast side pressure angle and almost always decreases with the decrease in coast side pressure angle. In terms of increase in drive side pressure angle the bending stress increases for the high coast side pressure angles and decreases only for very low coast side pressure angles α_{ci} (smaller than 20°). In case of a 16° coast side pressure angle, for instance, the bending stress decreases % 5 by the increase of the drive side pressure angle from 16° to 30°.

Table 11. The analysis input parameters for Z_i=81, m=1

Analysis Input Parameters	
Z_e	27
a_s	1,25
a_i	1
a_e	1
F_{ni}	10 N

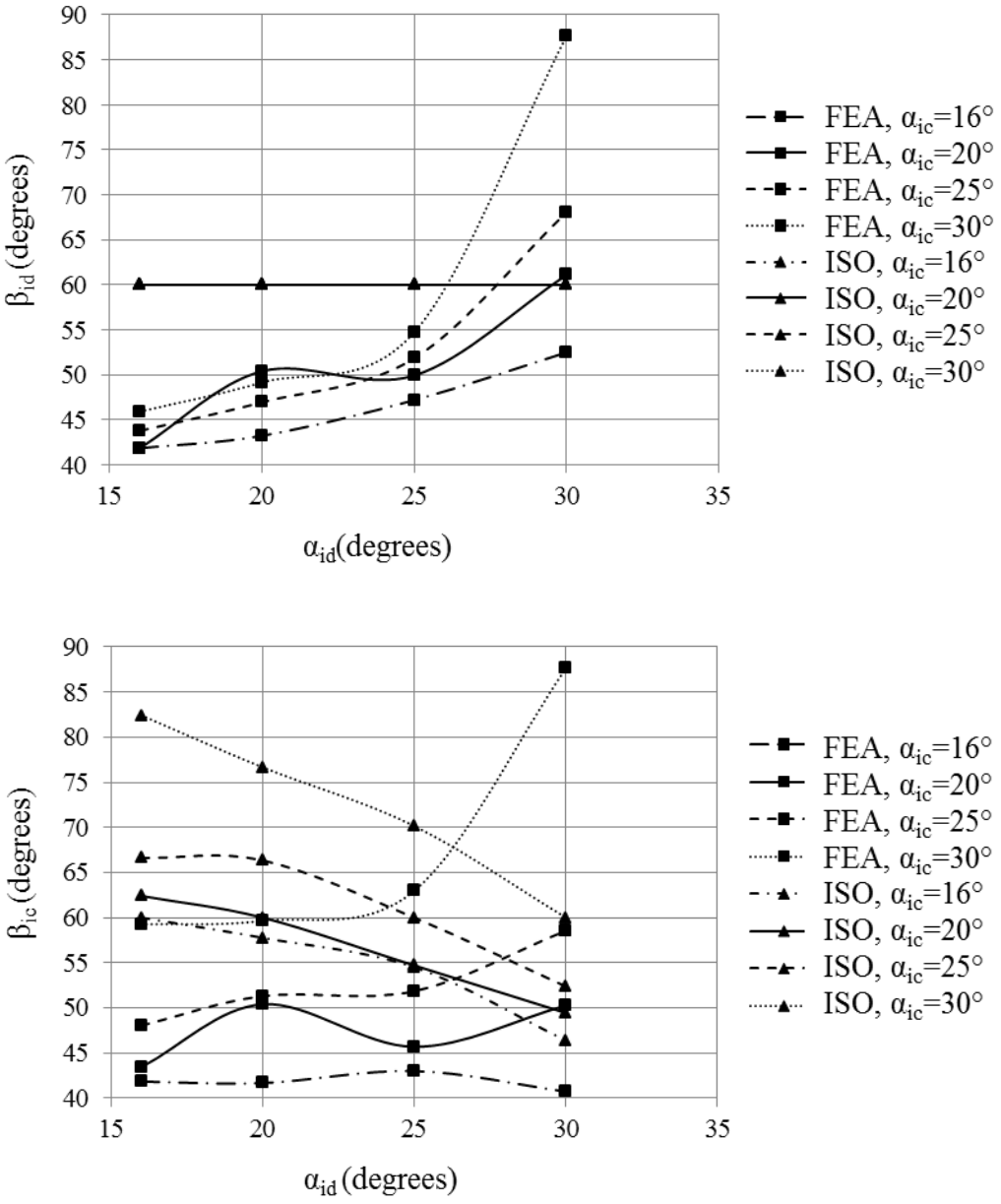

Fig. 4.21 Comparison of the drive and coast sides critical section tangent angles for different drive and coast side pressure angles at light load for $Z_i = 81$

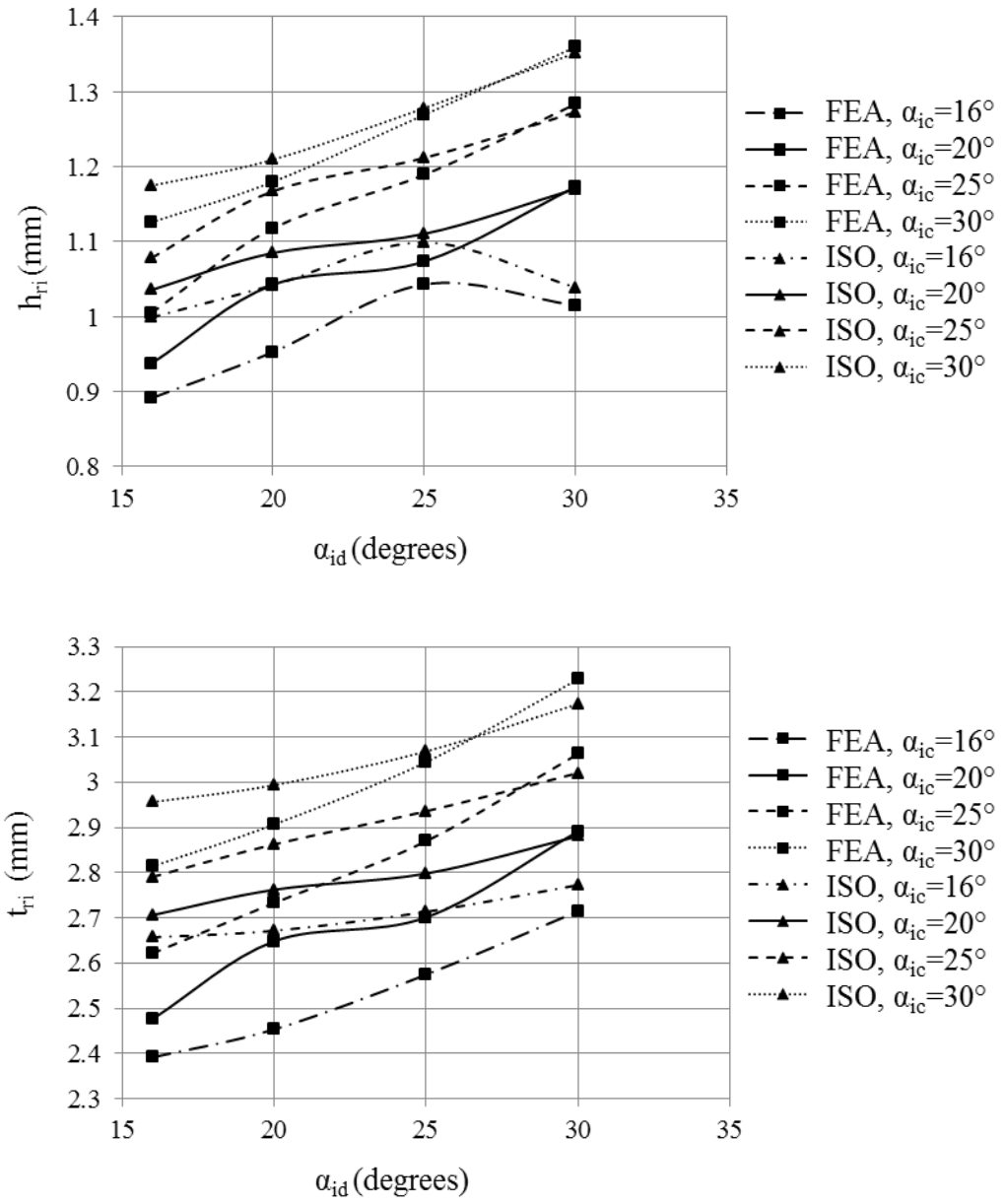

Fig. 4.22 Comparison of the critical section tooth height and thickness for different drive and coast side pressure angles at light load for $Z_i = 81$

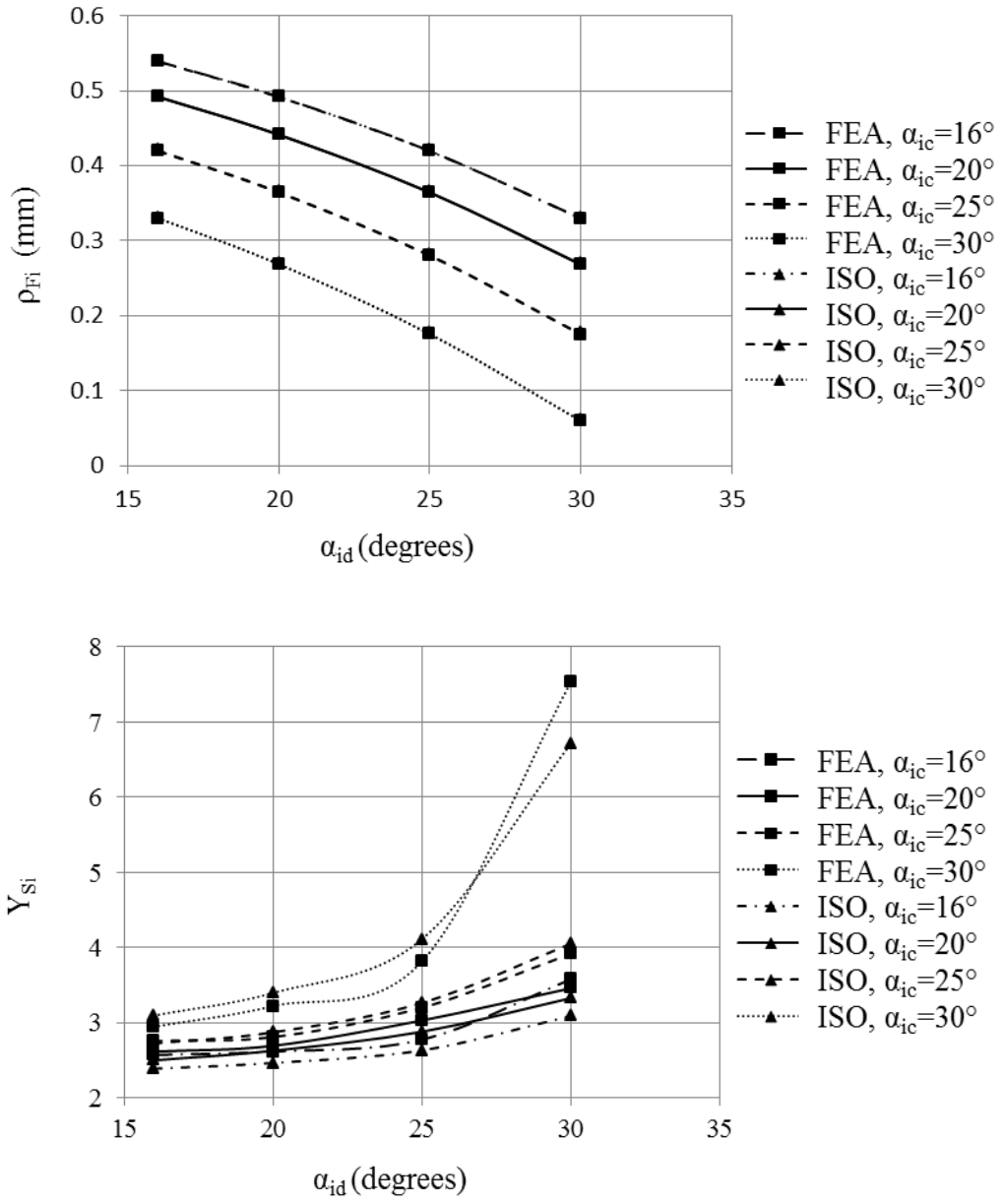

Fig. 4.23 Comparison of the critical section root fillet radius of curvature and stress correction factor for different drive and coast side pressure angles at light load for $Z_i = 81$

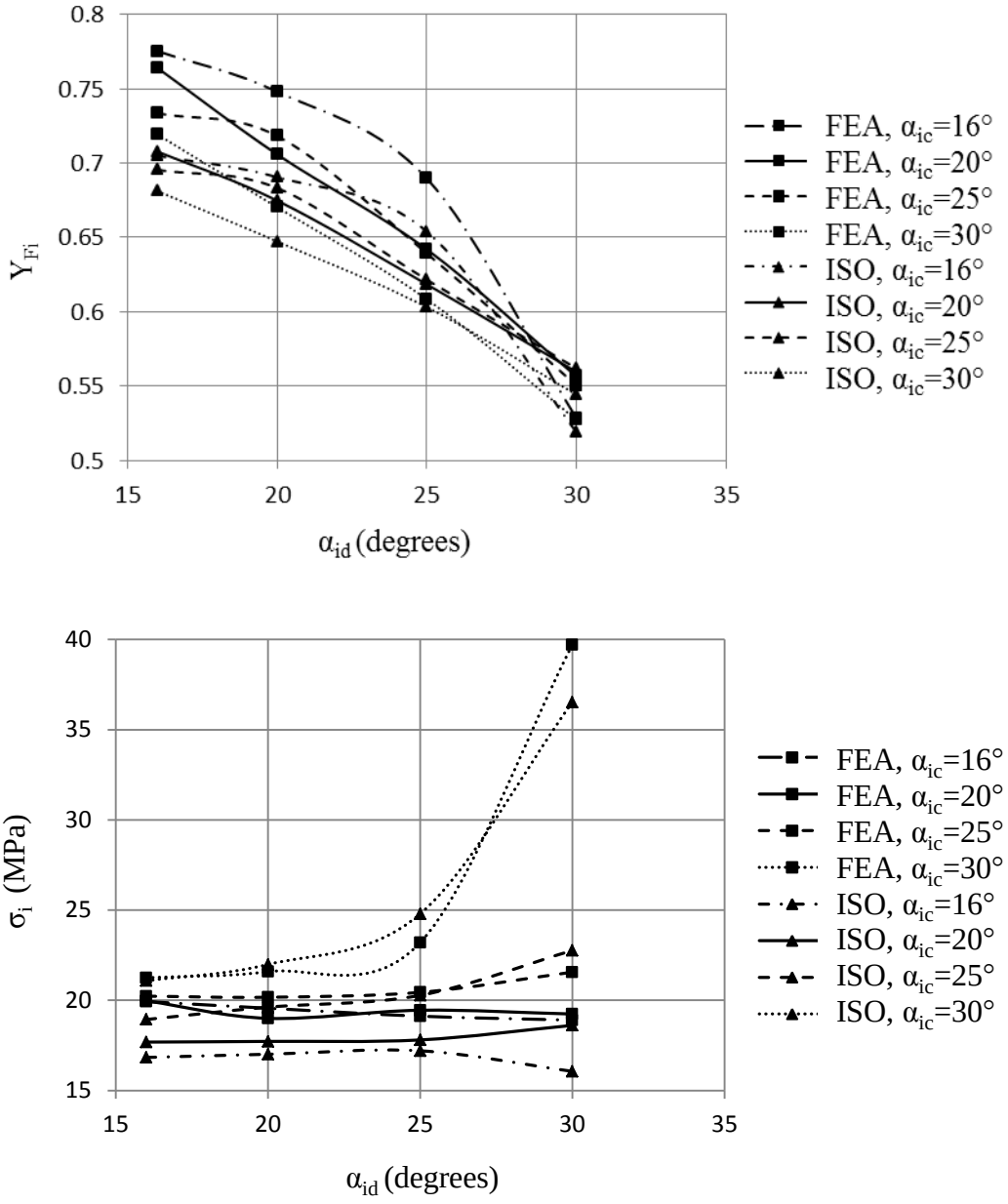

Fig. 4.24 Comparison of the critical section tooth form factor and bending stress for different drive and coast side pressure angles at light load for $Z_i = 81$

4.2.1.2 The Effect of Drive Side Pressure Angle for Internal Gears Having Different Tooth Heights

The results of the previous chapter shows that by the increase in drive side pressure angle the bending stress decreases for only low coast side pressure angles. In [16] it is stated that the desired trend that the fillet stresses decreased with the increasing drive side pressure angle has been achieved to a large extent by the consideration of stud tooth at the cost of contact ratio by keeping its values always above the required limit 1.1. The bending stress decreases with respect to decrease in the tooth height according to [16] and the minimum tooth height with an addendum coefficient, 0.8 is analyzed. In this study the same minimum tooth height with the same addendum coefficient is also analyzed with respect to the increase in drive side pressure angle and the results are discussed.

The addendum coefficient of the internal a_i gear does not affect its own bending stress but affects the bending stress of the external gear in the mesh since the HPSTC of the external gear is affected by the tip diameter of the internal gear. The addendum coefficient of the external gear a_e affects the bending stress of the internal gear since the LPSTC of the internal gear is affected by the tip diameter of the external gear. If the tip diameter of the external gear increases the LPSTC diameter increases and critical section tooth height decreases. Then the maximum bending stress also decreases. If the tip diameter of the external gear decreases the LPSTC diameter decreases and critical section tooth height increases. Then the maximum bending stress also increases. The addendum coefficient of the shaper cutter a_s (the dedendum coefficient of the internal gear) also affects the bending stress of the internal gear. If a_s increases, the critical section tooth height increases so that the bending stress increases and if a_s decreases, then the critical section tooth height decreases so that the bending stress decreases. After all these explanations if the a_s is decreased from 1.25 to 0.8 the bending stress must absolutely decrease. However a_e must also decrease since the dedendum of the internal gear is decreased. Then the

bending must increase again. Here, for instance, a_e can be maximum 0.6 because there must be also an enough clearance between the root of the internal gear tooth and tip of the external gear tooth. From Fig. 4.25 and Fig. 4.26 it is clearly seen that the bending stress for a_s (0.8) and a_e (0.6) case, either remains same or very slightly decreases with respect to increase in drive side pressure angle and it is also even more than the bending stress of the normal tooth height case, a_s (1.25) and a_e (1). Also this causes a very important decrease in the contact ratio. Then there is no advantage of stud tooth suggestion of [16] for the internal gears. Although a_e can be maximum 0.6 for a_s 0.8, assume that a_e is 0.8 in order to just make an analysis. Then, From Fig. 4.27 and Fig. 4.28 it is clearly seen that the bending stress for a_s (0.8) and a_e (0.8) case, decreases with the increase in drive side pressure angle. However, this causes a geometric interference during meshing and this solution is not practical.

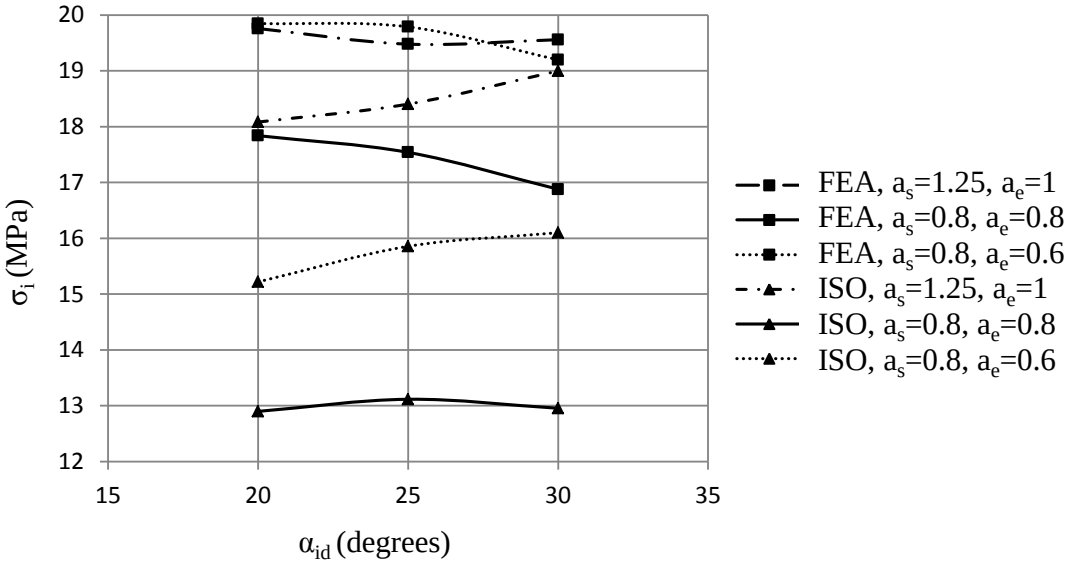

Fig. 4.25 Comparison of the critical section bending stress for different drive side pressure angles and tooth heights for $Z_i = 60$

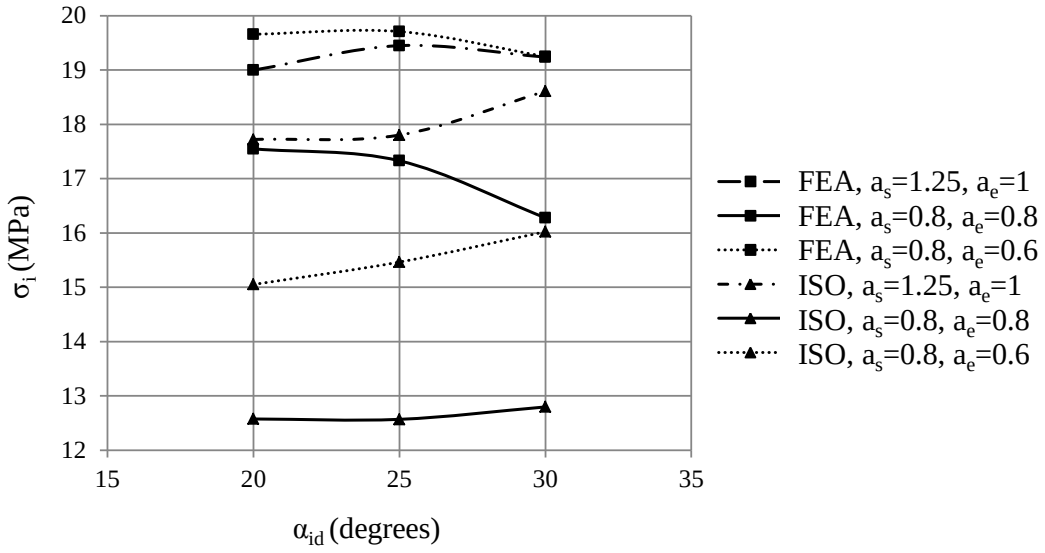

Fig. 4.26 Comparison of the critical section bending stress for different drive side pressure angles and tooth heights for $Z_i = 81$

4.2.2 The Case of Heavily Loaded Gear with Large Module

In this chapter internal asymmetric spur gears with 4 mm module, unit face width, standard tooth height (a_i=1, b=1.25), zero profile shift and 500 N applied force are studied with FEA and ISO methods. In this study the effects of the coast and drive side pressure angles are reflected in a single figure for each parameter for a specified number of teeth.

Table 12. The analysis input parameters for Z_i=60, m=4

Analysis Input Parameters	
Z_e	20
a_s	1,25
a_i	1
a_e	1
F_{ni}	500 N

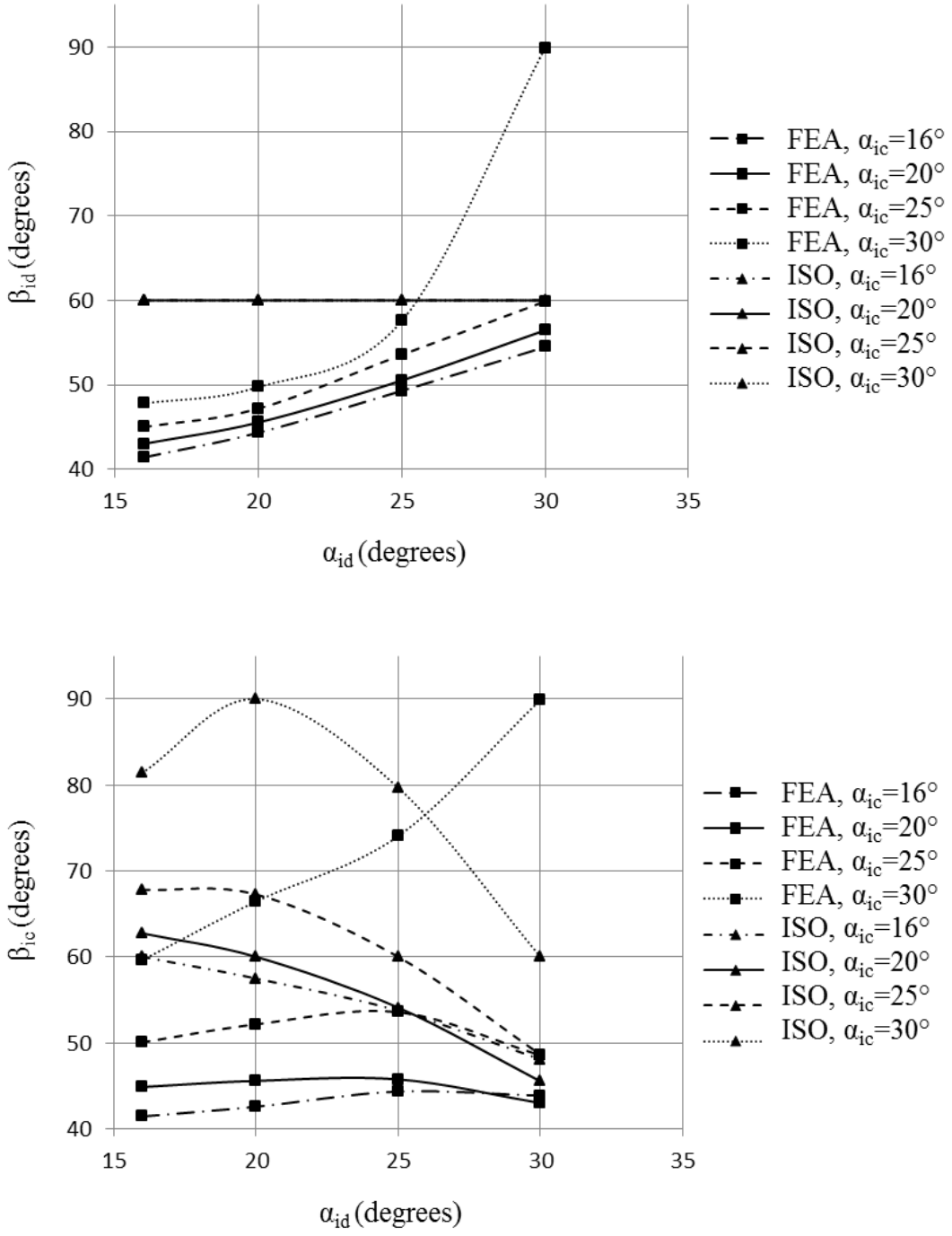

Fig. 4.27 Comparison of the drive and coast side critical section tangent angles for different drive and coast sides pressure angles at heavy load for $Z_i = 60$

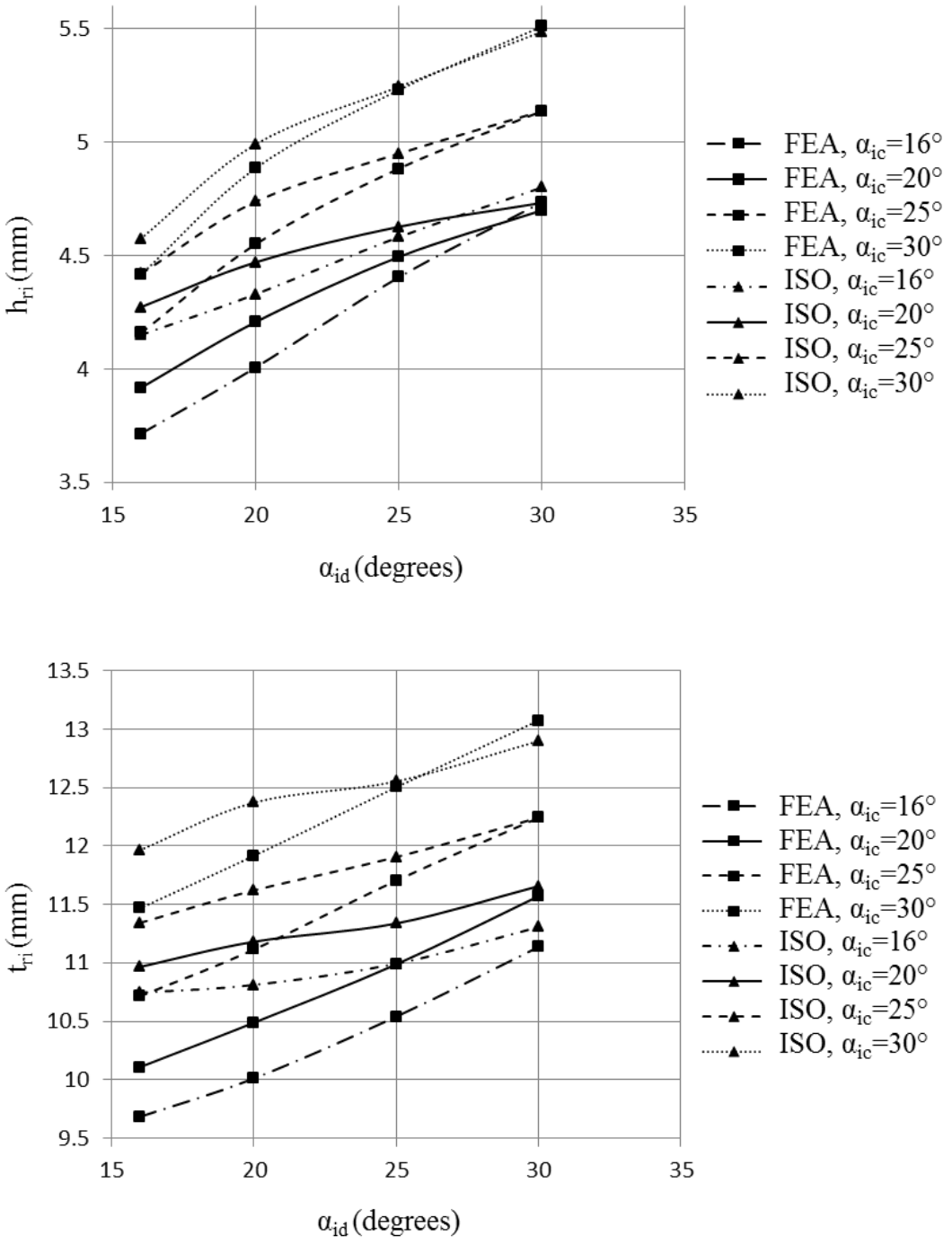

Fig. 4.28 Comparison of the critical section tooth height and thickness for different drive and coast sides pressure angles at heavy load for $Z_i = 60$

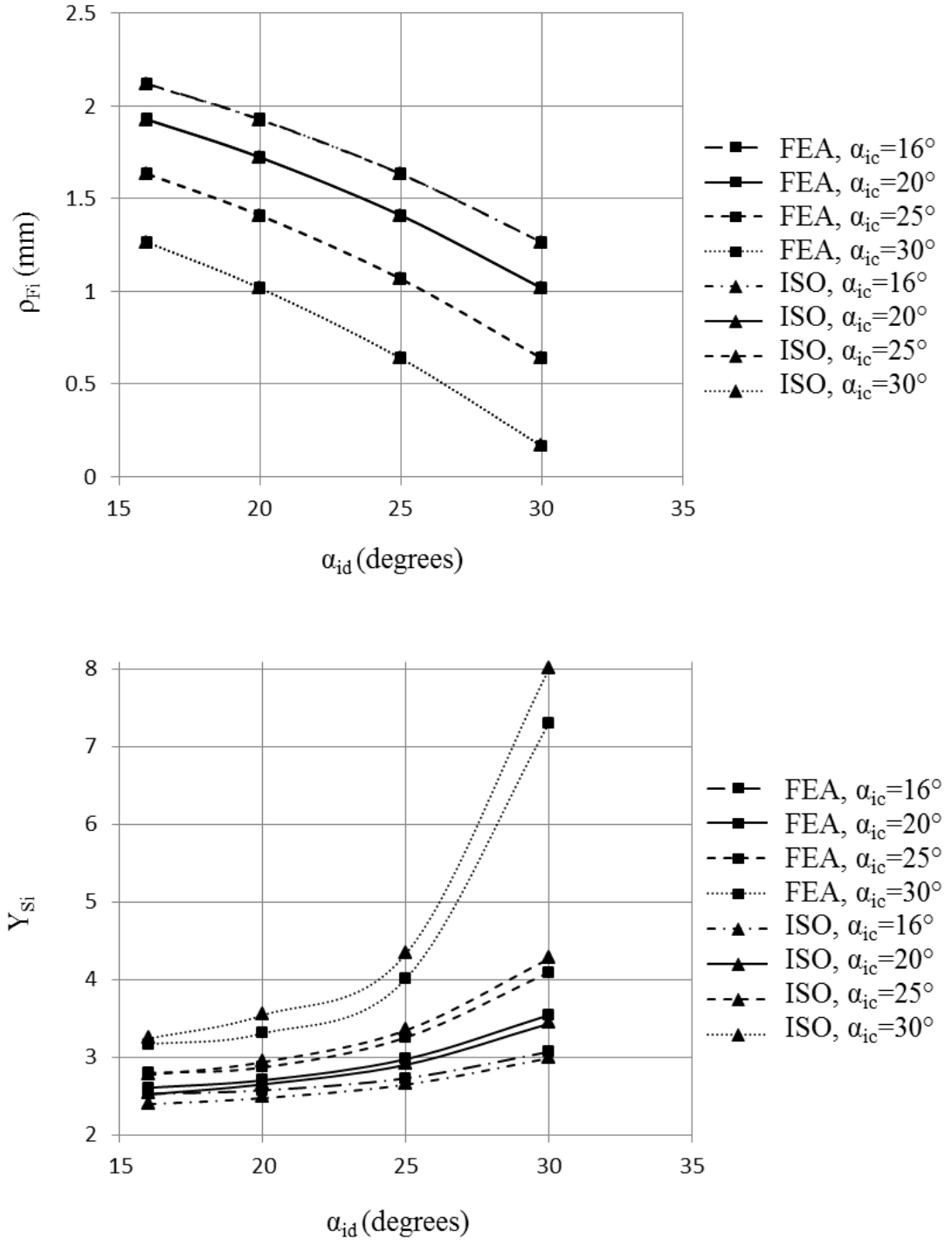

Fig. 4.29 Comparison of the critical section root fillet radius of curvature and stress correction factor for different drive and coast sides pressure angles at heavy load for $Z_i = 60$

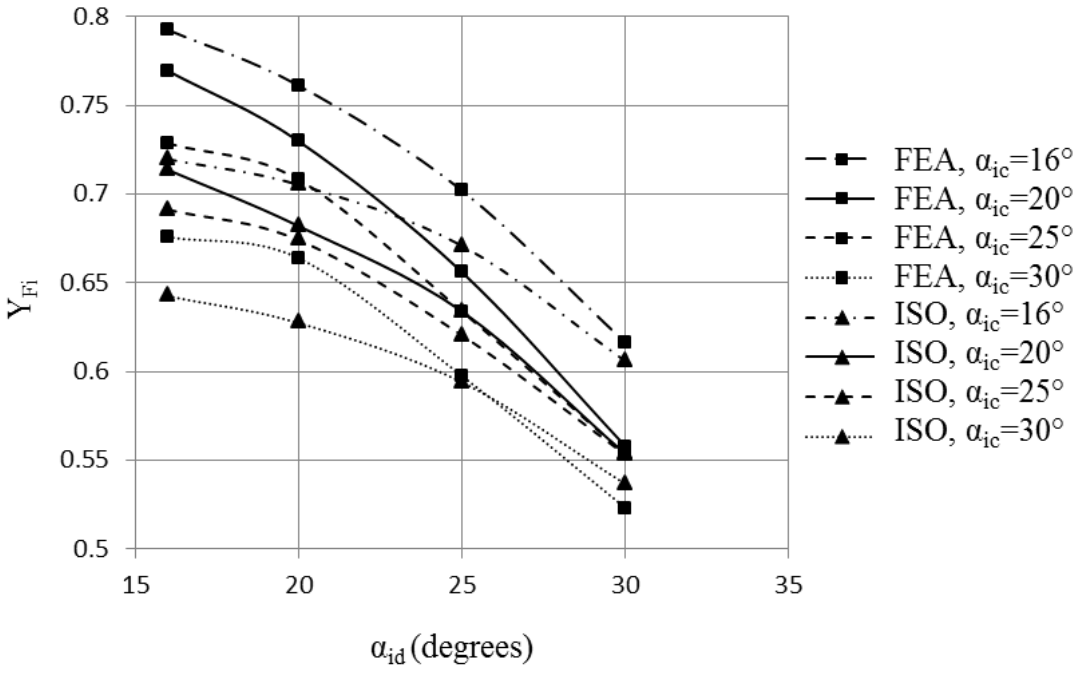

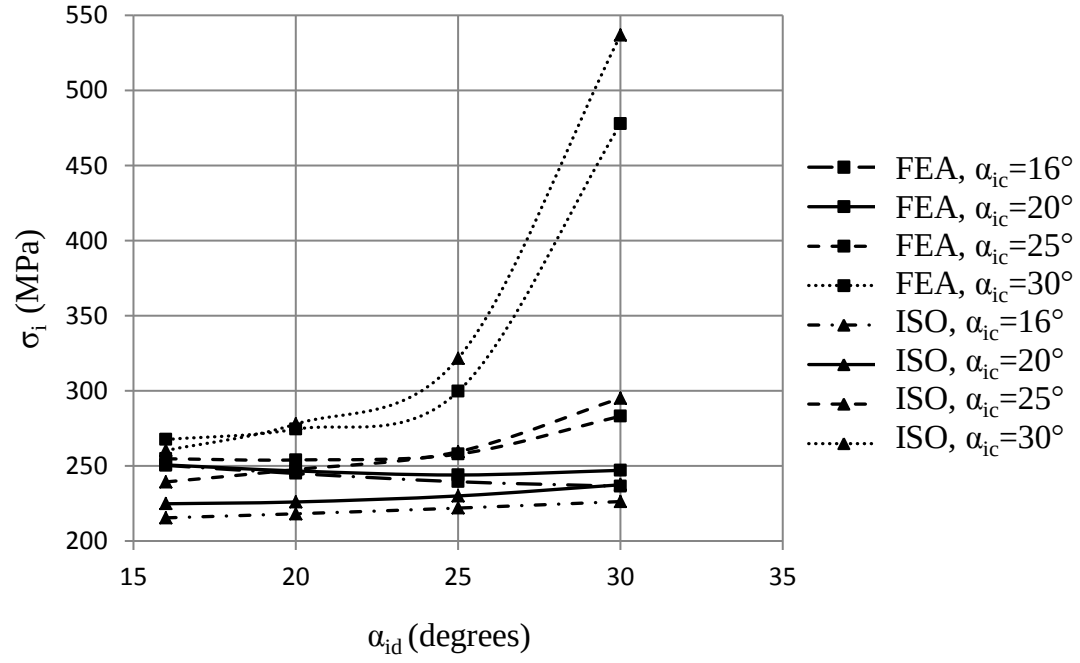

Fig. 4.30 Comparison of the critical section tooth form factor and bending stress for different drive and coast sides pressure angles at heavy load for $Z_i = 60$

Table 13. The analysis input parameters for Z_i=81, m=4

Analysis Input Parameters	
Z_e	27
a_s	1,25
a_i	1
a_e	1
F_{ni}	500 N

By the help of Fig. 4.27, Fig. 4.28, Fig. 4.29, Fig. 4.30, Fig. 4.31 ,Fig. 4.32 ,Fig. 4.33 and Fig. 4.34, the heavily loaded case analysis can be compared with lightly loaded case analysis of the internal gears (Z_i=60 and Z_i=81) according to the drive and coast sides pressure angle changes. With respect to the lightly loaded case, the drive and coast side tangent angles β_{id} and β_{ic} are almost same. The critical section tooth height h_{ri} and thickness t_{ri} and the root fillet radius of curvature ρ_{fi} almost increased to four times of their values. Also the tooth form factor and stress correction factor are almost same. Finally, the maximum bending stress is almost 12.5 times larger than its value. Here, similar to the external gear results, 12.5 comes from 50 divided by 4 where the load is 50 times larger and the module is 4 times larger than their values. All these results are the expected results.

The graphs of the second case are very similar to the first case so that the same results with the first case can be obtained. The maximum bending stress σ_i increases with the increase in coast side pressure angle and almost always decreases with the decrease in coast side pressure angle. In terms of increase in drive side pressure angle the bending stress increases for the high coast side pressure angles and decreases only for very low coast side pressure angles α_{ic} (smaller than 20°). In case of a 16° coast side pressure angle, for instance, the bending stress decreases % 5 by the increase of the drive side pressure angle from 16° to 30°.

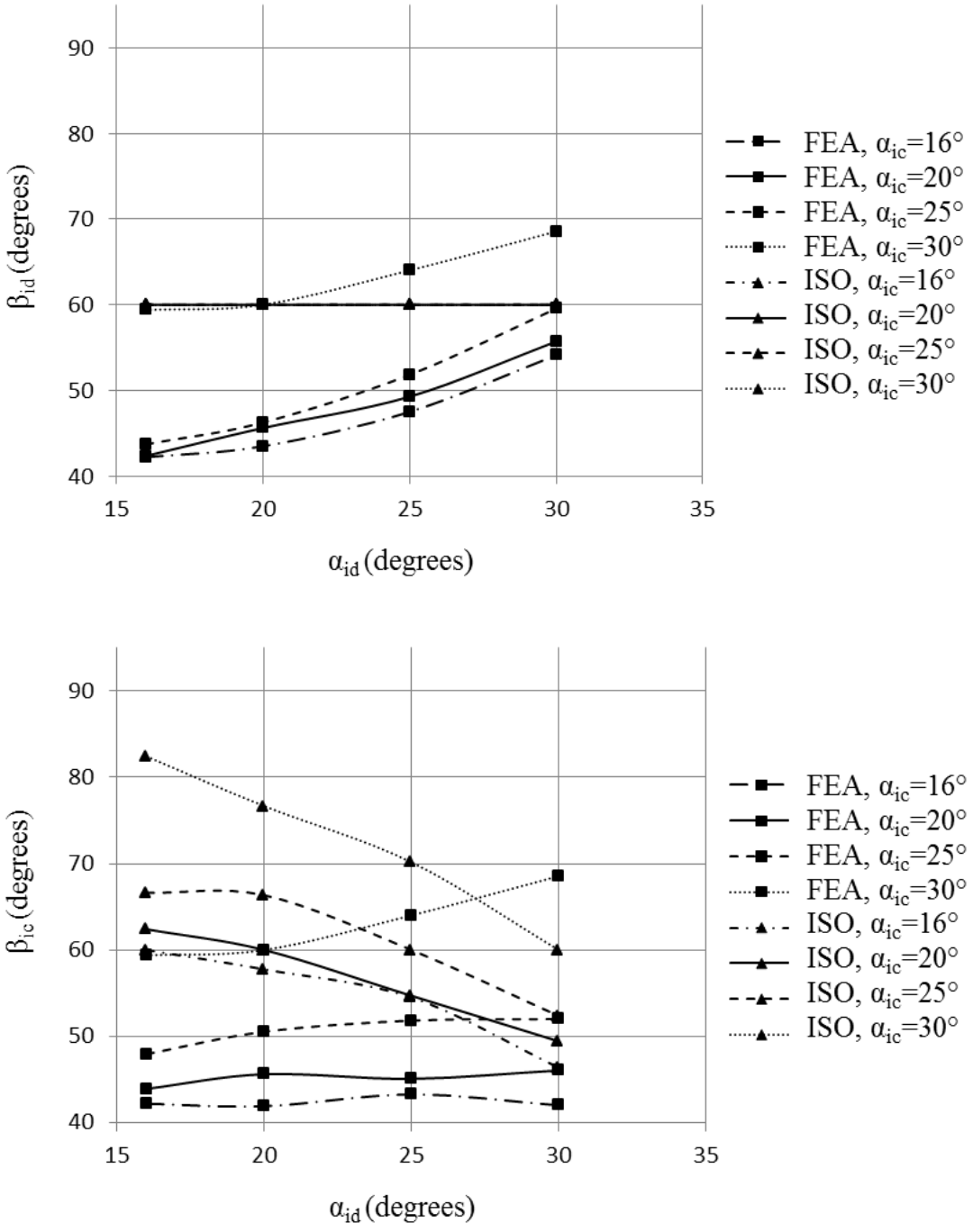

Fig. 4.31 Comparison of the drive and coast side critical section tangent angles for different drive and coast sides pressure angles at heavy load for $Z_i = 81$

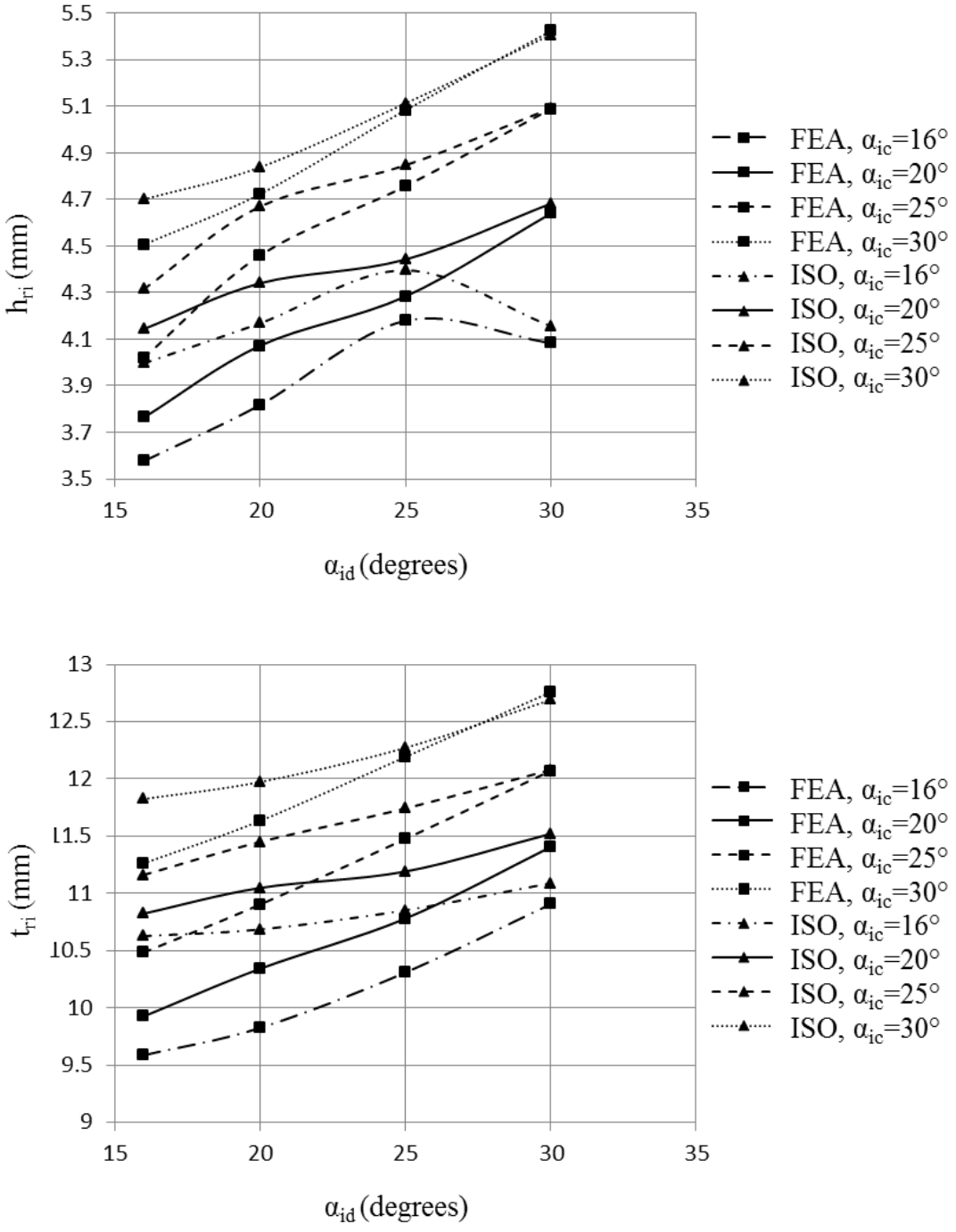

Fig. 4.32 Comparison of the critical section tooth height and thickness for different drive and coast sides pressure angles at heavy load for $Z_i = 81$

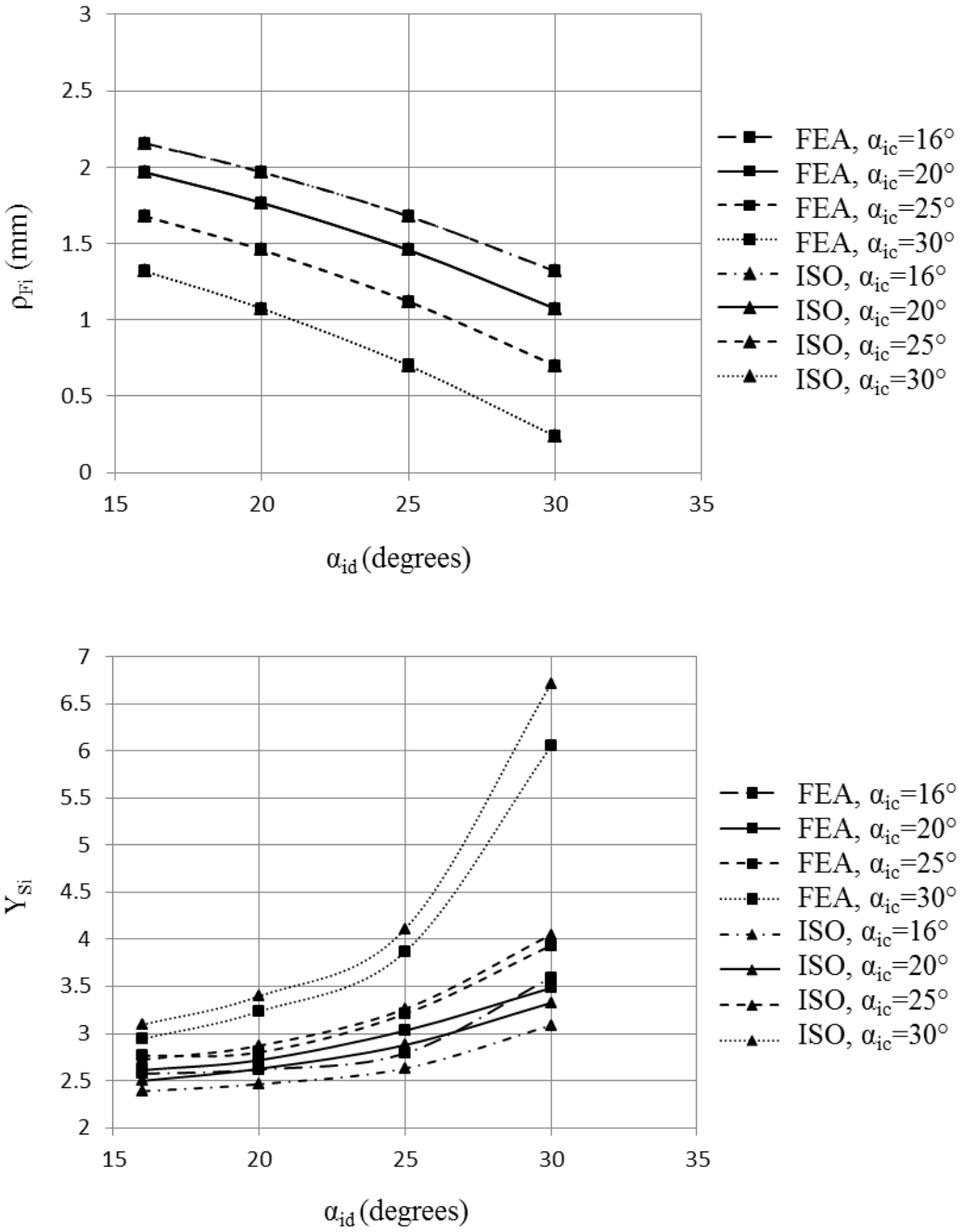

Fig. 4.33 Comparison of the critical section root fillet radius of curvature and stress correction factor for different drive and coast sides pressure angles at heavy load for $Z_i = 81$

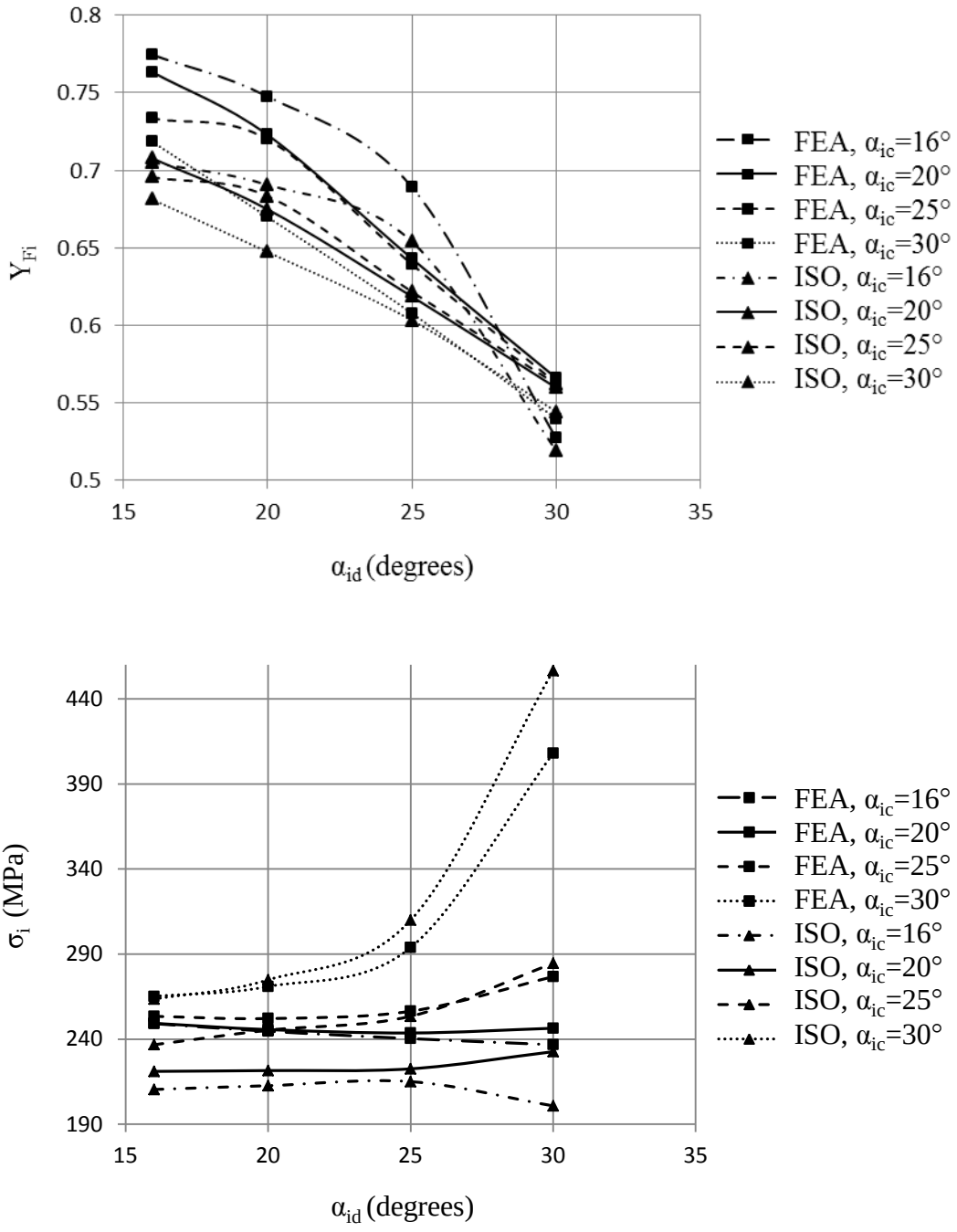

Fig. 4.34 Comparison of the critical section tooth form factor and bending stress for different drive and coast sides pressure angles at heavy load for $Z_i = 81$

CHAPTER 5

CONCLUSION AND FUTURE WORK

The external asymmetric spur gears are generated by using full rounded asymmetric rack-cutters and the internal asymmetric spur gears are generated by using full rounded asymmetric pinion type shaper cutters. In this thesis, considering the detailed geometries of the external and internal asymmetric gear teeth, the analytical methods are developed to find the maximum bending stress of both external and internal asymmetric spur gears by modifying ISO methods.

The method for external gear is very similar to previous work [15]. The critical section drive side tangent angle is 30° and all other critical section parameters including coast side tangent angle are derived by using the generation motion. There is no analytical method for internal asymmetric gears in the literature, but the analytical method developed for internal asymmetric gears in this thesis is similar to the external gears. In this method, the critical section drive side tangent angle is 60° and all other critical section parameters including coast side tangent angle are derived by using the generation motion. Then these results are compared with previous work [15] and FEA for external asymmetric gears and with FEA for internal asymmetric gears. The analyses are done for external and internal asymmetric gears with small and large modules and light and heavy applied forces, respectively.

For small module and light load case, the external gear analytical and FEA results are very similar to previous work [15] results. Therefore, almost the same results with previous work [15] are obtained for external asymmetric gears. The calculated values of the bending stress σ decreases with an increase in α_d. This is because of the

corresponding decrease in tooth form factor Y_F which is more dominating than the increase in stress correction factor Y_S. This enables to enhance the bending strength of the gear tooth. The maximum bending stress calculated in analytical method is %5 lower than FEA results for low number of teeth and that increases to %10 for high number of teeth. This is mainly caused by differences in the critical section tangent angles of the modified ISO and FEA methods. The results of standard ISO method with FEA results for external symmetric gears are also compared in this thesis. For 20° pressure angle the standard ISO method gives %3-5 larger bending stress results than FEA. For higher pressure angles like 30° this difference increases to %8-12.

For small module and light load case, the internal gear bending stress σ_i in FEA, increases with the increase in coast side pressure angle and usually decreases with the decrease in coast side pressure angle. For increase in drive side pressure angle the bending stress increases but decreases only for very low coast side pressure angles α_{ic} (smaller than 20°). In case of a 16° coast side pressure angle, for instance, the bending stress decreases % 6 by the increase of the drive side pressure angle from 16° to 30°. The bending stresses of ISO method are about % 5 different than the results of the FEA for drive and coast side pressure angles larger than 20°, but the percentage difference increases to % 15 for low drive and coast side pressure angles smaller than 20° (for example for 16°). This is mainly because of the higher differences in β_{id} and β_{ic} for FEA and ISO methods. In modified ISO method of the internal gears, the bending stress always increases with an increase in drive side pressure angle, even for very low coast side pressure angles because of the mentioned high bending stress difference % 15 with FEA results for low pressure angles. In order to decrease the bending stress of an internal asymmetric gear by increase in drive side pressure angle, the stub tooth is suggested in [16]. In this thesis, this suggestion is also analyzed and it is seen that the bending stress decreases for small tooth height if only the addendum coefficient of the external gear in mesh equal or greater than the dedendum coefficient of the internal gear. However, this causes a geometric interference during meshing and this solution is not practical. The

results of standard ISO method with FEA results for internal symmetric gears are also compared in this thesis. The standard ISO method generally gives %7-10 larger bending stress results than FEA results. For low and high pressure angles, this difference increases up to %15.

In both of external and internal asymmetric gears, for large module and high load case, the results of the geometry related parameters, the tooth form and stress correction factors, are almost independent of module and the same with small module case. This is an expected result because by increasing module, all geometric parameters of the gears increase with the same ratio. Therefore, the maximum bending stress changes with a ratio of the applied load to module.

As a result, the modified ISO method for external asymmetric gears gives as accurate results as the standard ISO method for external symmetric gears. As a future work, the optimization of drive side critical section tangent angle can be conducted especially for high number of teeth. Similarly, the modified ISO method for internal asymmetric gears gives as accurate results as standard ISO method for internal symmetric gears. As a future work, the optimization of drive side critical section tangent angle optimization can be conducted especially for low pressure angles.

Finally, an asymmetric planetary spur gear stage design optimization for sun, planet and ring gears can be investigated in terms of bending and contact stresses, top land thicknesses, contact ratios and some other important parameters. This optimized design can be verified by FEA and also experimental works.

REFERENCES

[1] Z. S. D. Rágár and L. Á. K. Amondi, "Change of Tooth Root Stress Calculation Model for Non-symmetric Tooth Shape," *Des. Mach. Struct.*, vol. 3, no. 1, pp. 19–24, 2013.

[2] M. Q. Abdullah, "Analytical Solution of Bending Stress Equation for Symmetric and Asymmetric Involute Gear Teeth Shapes with and without Profile Correction," *ISSN*, vol. 3, no. 6, pp. 19–34, 2012.

[3] T. J. Dolan and E. L. Brogmaher, "a Photoelastic Study of Stresses in Gear Tooth Fillets," *Eng. Exp. Stn. Bull. Ser. No. 335*, 1942.

[4] American Gear Manufacturers Association, "Geometry Factors for Determining the Pitting Resistance and Bending Strength of Spur, Helical and Herringbone Gear Teeth AGMA 908-B89," vol. 89, no. August, p. 79, 1989.

[5] S. Webport, "International Standard," *Program*, vol. 2006, 2011.

[6] M.-J. Wang, "A New Photoelastic Investigation of the Dynamic Bending Stress of Spur Gears," *J. Mech. Des.*, vol. 125, no. 2, p. 365, 2003.

[7] A. Kapelevich, "Geometry and design of involute spur gears with asymmetric teeth," *Mech. Mach. Theory*, vol. 35, no. 1, pp. 117–130, 2000.

[8] S. C. Yang, "Mathematical model of a helical gear with asymmetric involute teeth and its analysis," *Int. J. Adv. Manuf. Technol.*, vol. 26, no. 5–6, pp. 448–456, 2005.

[9] S. C. Yang, "Study on an internal gear with asymmetric involute teeth," *Mech. Mach. Theory*, vol. 42, no. 8, pp. 977–994, 2007.

[10] C. Fetvaci, "Generation Simulation of Involute Spur Gears Machined by Pinion-Type Shaper Cutters," vol. 56, pp. 644–652, 2010.

[11] G. Di Francesco and S. Marini, "Asymmetric Teeth : Bending Stress Calculation," no. April, pp. 52–55, 2007.

[12] G. Mallesh and V. B. Math, "Estimation of Critical Section and Bending

Stress Analysis for Asymmetric Spur Gear Tooth," pp. 107–112, 2009.

[13] J. L. Moya, J. A. Machado, R. Velasquex, and J. E. Fernández, "A Study in Asymmetric Plastic Spur Gears," no. April, 2010.

[14] B. F. W. Brown, S. R. Davidson, D. B. Hanes, D. J. Weires, F. W. Brown, S. R. Davidson, D. B. Hanes, D. J. Weires, T. B. Company, A. Kapelevich, and A. K. Gears, "Analysis and Testing of Gears with Asymmetric Involute Tooth Form and Optimized Fillet Form for Potential Application in Helicopter Main Drives Analysis and Testing of Gears with Asymmetric Involute Tooth Form and Optimized Fillet Form for Potential Appli," *AGMA Tech. Pap.*, 2010.

[15] R. Prabhu Sekar and G. Muthuveerappan, "Estimation of tooth form factor for normal contact ratio asymmetric spur gear tooth," *Mech. Mach. Theory*, vol. 90, pp. 187–218, 2015.

[16] D. V. Muni and G. Muthuveerappan, "A comprehensive study on the asymmetric internal spur gear drives through direct and conventional gear design," *Mech. Based Des. Struct. Mach.*, vol. 37, no. 4, pp. 431–461, 2009.

[17] A. L. Kapelevich and Y. V Shekhtman, "Rating of Asymmetric Tooth Gears," no. April, pp. 40–45, 2016.

[18] L. A. Kapalevich, "Analysis and Optimization of Asymmetric Epicyclic Gears," vol. 51, no. August, pp. 35–52, 2016.

[19] A. S. Novikov, A. G. Paikin, V. L. Dorofeyev, V. M. Ananiev, and A. L. Kapelevich, "Application of gears with asymmetric teeth in turboprop engine gearbox," *Geartechnology*. pp. 60–65, 2008.

[20] D. B. Dooner, *Kinematic Geometry of Gearing Second Edition*.

[21] F. L. Litvin and A. Fuentes, *Gear Geometry And Applied Theory*. 2004.

APPENDIX A

DETERMINATION OF ASYMMETRIC RACK CUTTER PARAMETERS

A.1. Determination of Maximum Asymmetric Rack Cutter Radius

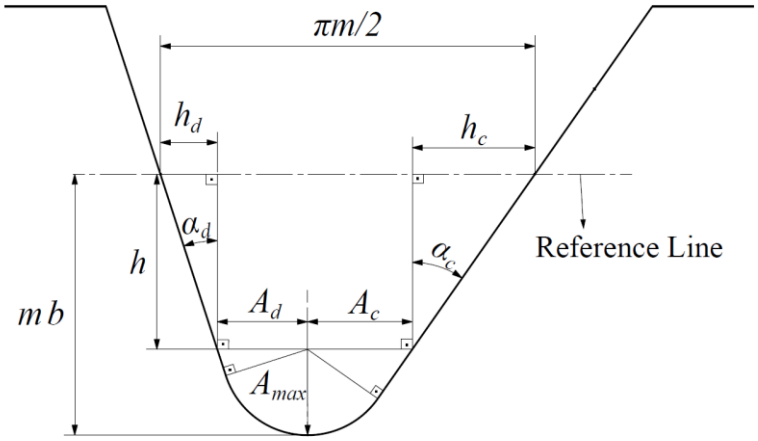

Fig. A.1 Maximum asymmetric rack-cutter radius

For any rack-cutter radius A, the parameters of the rack-cutter are given as:

$$h = mb - A \tag{A.1}$$

$$h_d = h\,tan\,\alpha_d \tag{A.2}$$

$$h_c = h\,tan\,\alpha_c \tag{A.3}$$

$$A_d = \frac{A}{\cos\alpha_d} \tag{A.4}$$

$$A_c = \frac{A}{\cos \alpha_c} \tag{A.5}$$

If the rack is full rounded as shown in Fig. A.1, use A_{max} in Equations (A.1) to (A.5). Then A_{max} can be found as:

$$\pi m/2 = h_d + h_c + A_d + A_c \tag{A.6}$$

$$\pi m/2 = (mb - A_{max}) \tan \alpha_d + (mb - A_{max}) \tan \alpha_c + \frac{A_{max}}{\cos \alpha_d} + \frac{A_{max}}{\cos \alpha_c} \tag{A.7}$$

$$\pi m/2 = mb\,(\tan \alpha_d + \tan \alpha_c) - A_{max}\,(\tan \alpha_d + \tan \alpha_c) \ldots + A_{max}\left(\frac{1}{\cos \alpha_d} + \frac{1}{\cos \alpha_c}\right) \tag{A.8}$$

$$\pi m/2 - mb\,(\tan \alpha_d + \tan \alpha_c) = A_{max}\left(\frac{1}{\cos \alpha_d} + \frac{1}{\cos \alpha_c} - (\tan \alpha_d + \tan \alpha_c)\right) \tag{A.9}$$

$$A_{max} = \frac{\pi m/2 - mb(\tan \alpha_d + \tan \alpha_c)}{\frac{1}{\cos \alpha_d} + \frac{1}{\cos \alpha_c} - (\tan \alpha_d + \tan \alpha_c)} \tag{A.10}$$

A.2. Determination of Lower Limits of Position Vectors of Asymmetric Rack Cutter Coast and Drive Sides Inclined Surfaces

$$A_{ud} = A \sin \alpha_d \tag{A.11}$$

$$h_{ud} = mb - A + A_{ud} \tag{A.12}$$

$$u_{rd} = -\frac{h_{ud}}{\cos \alpha_d} \tag{A.13}$$

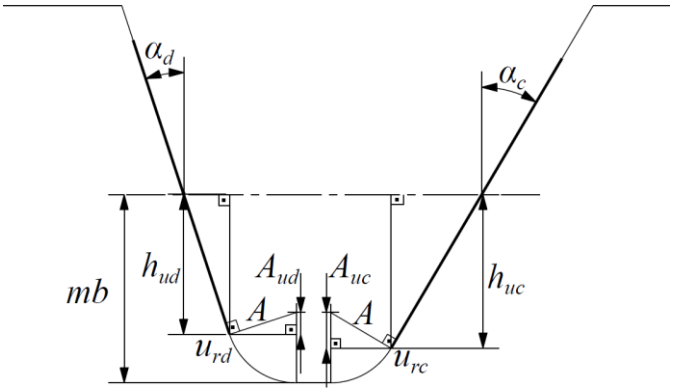

Fig. A.2 Lower limits of position vectors of asymmetric rack-cutter coast and drive side inclined surfaces

$$u_{rd} = -\frac{mb - A + A \sin \alpha_d}{\cos \alpha_d} \tag{A.14}$$

Modify the Equation (A.14) and obtain the coast side parameter, u_{rc}:

$$u_{rc} = -\frac{mb - A + A \sin \alpha_c}{\cos \alpha_c} \tag{A.15}$$

A.3. Determination of Upper Limits of Position Vectors of Asymmetric Rack Cutter Coast and Drives Sides Inclined Surfaces

During the generation motion of involute flank surface, any contact occurs on the intersection of line of action and the rack-cutter inclined surface. If the radius of the contact point is equal to tip radius, then tip radius point of the involute flank is generated. This is illustrated on the figure below.

$$r_a \cos \alpha_{ad} = r_{bd} \tag{A.16}$$

$$\alpha_{ad} = \cos^{-1}\left(\frac{r_{bd}}{r_a}\right) \tag{A.17}$$

$$CB = r_a . \sin \alpha_{ad} \tag{A.18}$$

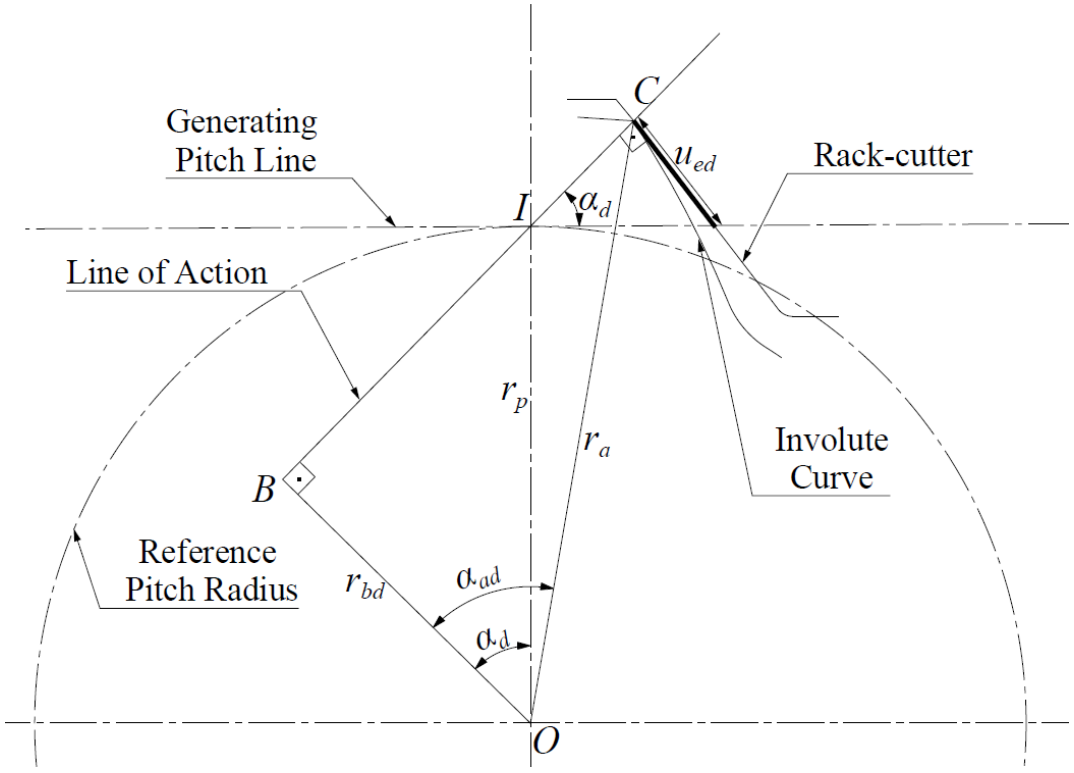

Fig. A.3 Upper limits of position vectors of asymmetric rack-cutter coast and drive side inclined surfaces

$$IB = r_p . \sin \alpha_d \tag{A.19}$$

$$u_{ed} = CI . \tan \alpha_d \tag{A.20}$$

$$u_{ed} = (CB - IB) . \tan \alpha_d \tag{A.21}$$

$$u_{ed} = (r_a.\sin\alpha_{ad} - r_p.\sin\alpha_d).\tan\alpha_d \tag{A.22}$$

$$u_{ed} = \left(r_a.\sin\left(\cos^{-1}\left(\frac{r_{bd}}{r_a}\right)\right) - r_p.\sin\alpha_d\right).\tan\alpha_d \tag{A.23}$$

Define α_{ac} and modify the Equations (A.22) and (A.23) and obtain the coast side parameter, u_{ce}:

$$\alpha_{ac} = \cos^{-1}\left(\frac{r_{bc}}{r_a}\right) \tag{A.24}$$

$$u_{ec} = (r_a.\sin\alpha_{ac} - r_p.\sin\alpha_c).\tan\alpha_c \tag{A.25}$$

$$u_{ec} = (r_a.\sin\left(\cos^{-1}\left(\frac{r_{bc}}{r_a}\right)\right) - r_p.\sin\alpha_c).\tan\alpha_c \tag{A.26}$$

A.4. Determination of X Component Limits of Position Vectors of Asymmetric Rack Cutter Coast and Drive Sides Rounded Surfaces

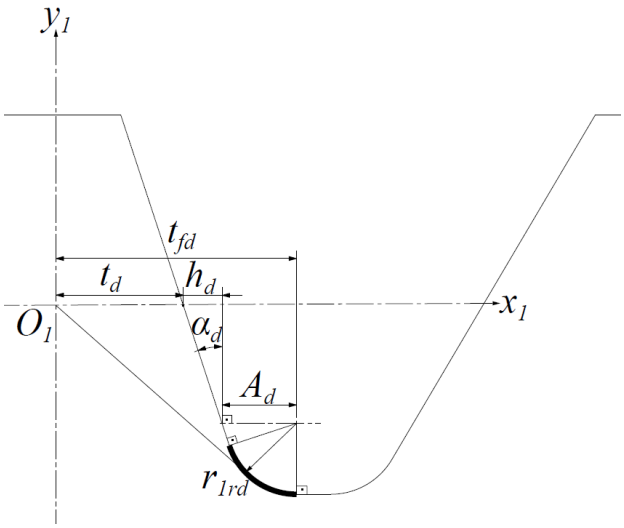

Fig. A.4 The x component limit of position vector of asymmetric rack-cutter drive side rounded surface

$$t_{fd} = t_d + h_d + A_d \tag{A.27}$$

Put Equations (A.1), (A.2) and (A.4) in Equation (A.27) and obtain:

$$t_{fd} = t_d + (mb - A)\tan\alpha_d + \frac{A}{\cos\alpha_d} \tag{A.28}$$

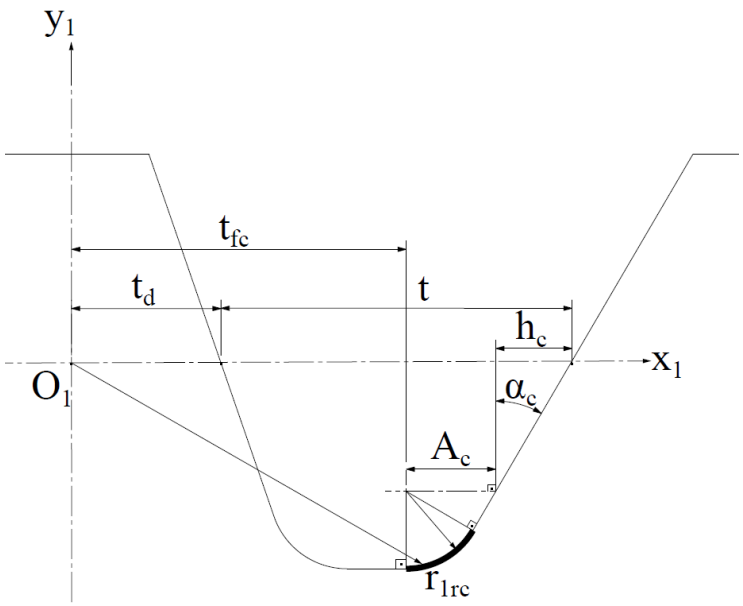

Fig. A.5 The x component limit of position vector of asymmetric rack-cutter coast side rounded surface

$$t_{fc} = t_d + t - h_c - A_c \tag{A.29}$$

Put Equations (A.1), (A.3) and (A.5) in Equation (A.29) and obtain:

$$t_{fc} = t_d + t - (mb - A)\tan\alpha_c - \frac{A}{\cos\alpha_c} \tag{A.30}$$

APPENDIX B

DETERMINATION OF EXTERNAL ASYMMETRIC INVOLUTE GEAR TOOTH AND GEAR PAIR MESH PARAMETERS

B.1. Determination of External Asymmetric Spur Gear Tooth Pointed Tip Radius, Drive and Coast Sides Tooth Thicknesses

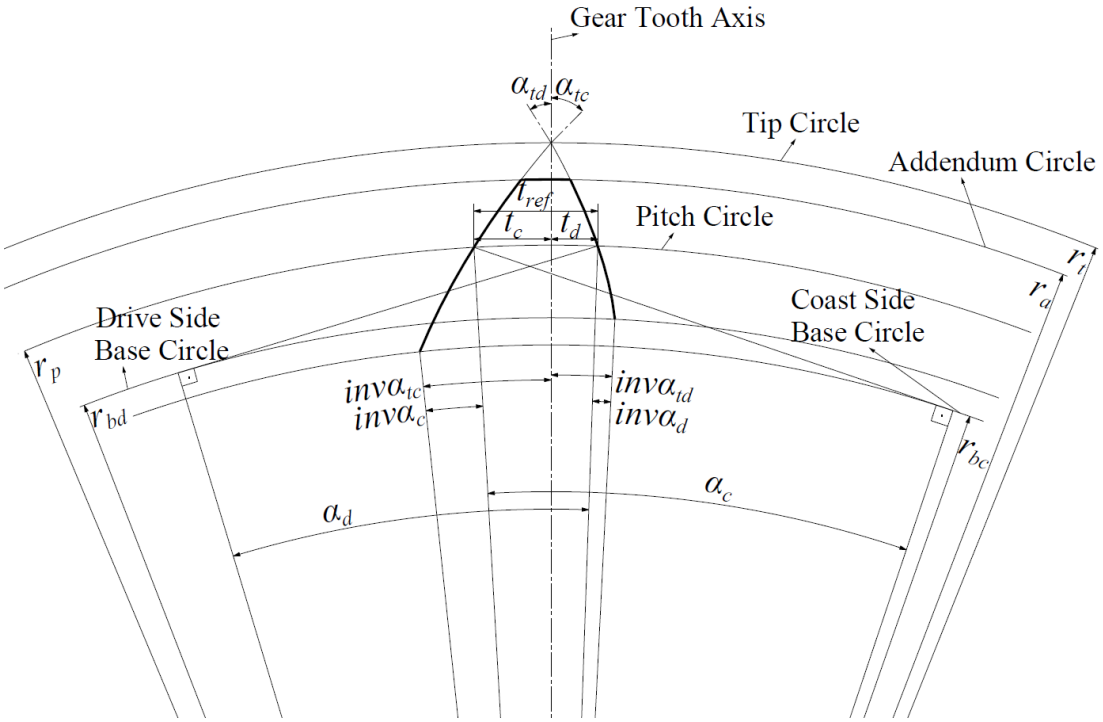

Fig. B.1 External asymmetric gear tooth pointed tip radius

$$t_{ref} = r_p\left(inv\alpha_{td} + inv\alpha_{tc} - (inv\alpha_d + inv\alpha_c)\right) \tag{B.1}$$

$$inv\alpha_d = \tan\alpha_d - \alpha_d \tag{B.2}$$

$$inv\alpha_c = \tan\alpha_c - \alpha_c \tag{B.3}$$

$$r_t \cos\alpha_{td} = r_{bd} \tag{B.4}$$

$$\alpha_{td} = \cos^{-1}\left(\frac{r_{bd}}{r_t}\right) \tag{B.5}$$

$$inv\alpha_{td} = \tan\alpha_{td} - \alpha_{td} \tag{B.6}$$

$$inv\alpha_{td} = \tan\left(\cos^{-1}\left(\frac{r_{bd}}{r_t}\right)\right) - \cos^{-1}\left(\frac{r_{bd}}{r_t}\right) \tag{B.7}$$

$$r_t \cos\alpha_{tc} = r_{bc} \tag{B.8}$$

$$\alpha_{tc} = \cos^{-1}\left(\frac{r_{bc}}{r_t}\right) \tag{B.9}$$

$$inv\alpha_{tc} = \tan\alpha_{tc} - \alpha_{tc} \tag{B.10}$$

$$inv\alpha_{tc} = \tan\left(\cos^{-1}\left(\frac{r_{bc}}{r_t}\right)\right) - \cos^{-1}\left(\frac{r_{bc}}{r_t}\right) \tag{B.11}$$

Use Equations (B.7) and (B.11) in Equation (B.1) and obtain:

$$t_{ref} = \frac{mN}{2}\left(\tan\left(\cos^{-1}\left(\frac{r_{bd}}{r_t}\right)\right) - \cos^{-1}\left(\frac{r_{bd}}{r_t}\right) + \tan\left(\cos^{-1}\left(\frac{r_{bc}}{r_t}\right)\right) \ldots - \cos^{-1}\left(\frac{r_{bc}}{r_t}\right) \quad - (inv\alpha_d + inv\alpha_c)\right) \tag{B.12}$$

In Equation (B.12) all parameters are known except r_t and in order to find r_t Newton-Raphson method is used to solve the Equation (B.12). In Matlab, fsolve function uses this method and can be used to find r_t. The drive and coast sides tooth thicknesses on pitch circle are defined as:

$$t_d = \frac{mN}{2}(\, inv\alpha_{td} - inv\alpha_d) \tag{B.13}$$

$$t_d = \frac{mN}{2}\left(\, tan\left(cos^{-1}\left(\frac{r_{bd}}{r_t}\right)\right) - cos^{-1}\left(\frac{r_{bd}}{r_t}\right) - inv\alpha_d\right) \tag{B.14}$$

$$t_c = \frac{mN}{2}(\, inv\alpha_{tc} - inv\alpha_c) \tag{B.15}$$

$$t_c = \frac{mN}{2}\left(\, tan\left(cos^{-1}\left(\frac{r_{bc}}{r_t}\right)\right) - cos^{-1}\left(\frac{r_{bc}}{r_t}\right) - inv\alpha_c\right) \tag{B.16}$$

B.2. Determination of an External Asymmetric Spur Gear Pair Mesh Properties

Here subscripts "p and g" represent the pinion and gear in mesh.

$$\alpha_o = \cos^{-1}\left(\frac{r_{bdp} + r_{bdg}}{O_1O_2}\right) \;\; where \;\; O_1O_2 = C_o \tag{B.17}$$

$$inv\alpha_o = \tan\alpha_o - \alpha_o \tag{B.18}$$

$$r_{op} = \frac{r_{bdp}}{\cos\alpha_o} \tag{B.19}$$

$$\alpha_{ocp} = \cos^{-1}\left(\frac{r_{bcp}}{r_{op}}\right) \tag{B.20}$$

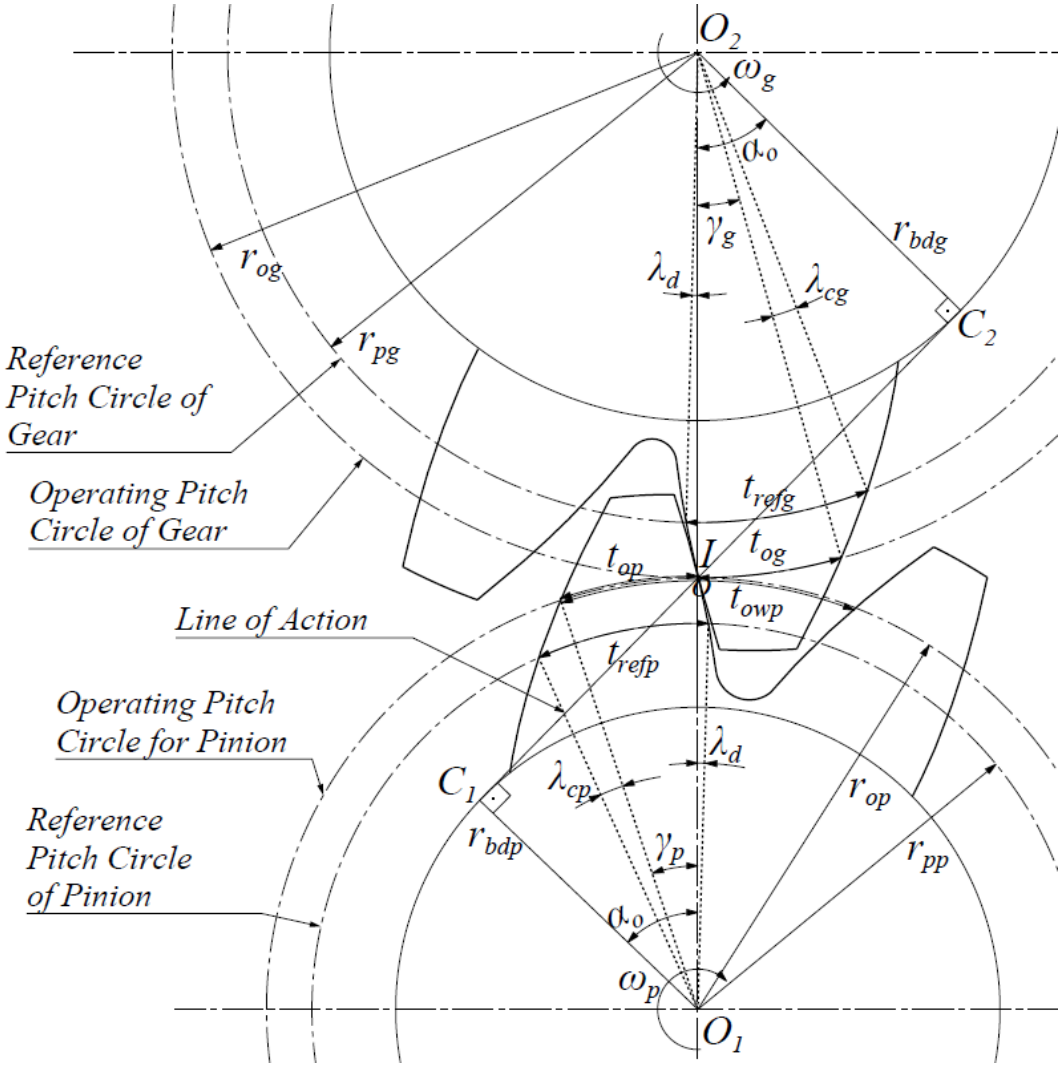

Fig. B.2 External asymmetric gear mesh

$$inv\alpha_{ocp} = \tan\alpha_{ocp} - \alpha_{ocp} \tag{B.21}$$

$$r_{og} = \frac{r_{bdg}}{\cos\alpha_o} \tag{B.22}$$

$$\alpha_{ocg} = \cos^{-1}\left(\frac{r_{bcg}}{r_{og}}\right) \tag{B.23}$$

$$inv\alpha_{ocg} = \tan\alpha_{ocg} - \alpha_{ocg} \tag{B.24}$$

$$\gamma_p = \frac{t_{refp}}{r_{pp}} \tag{B.25}$$

$$t_{refp} = \pi m/2 + x_p m\left(\tan\alpha_d + \tan\alpha_{cp}\right) \tag{B.26}$$

$$\gamma_p = \frac{\pi m/2 + x_p m\left(\tan\alpha_d + \tan\alpha_{cp}\right)}{r_{pp}} \tag{B.27}$$

$$\gamma_g = \frac{t_{refg}}{r_{pg}} \tag{B.28}$$

$$t_{refg} = \pi m/2 + x_g m\left(\tan\alpha_d + \tan\alpha_{cg}\right) \tag{B.29}$$

$$\gamma_g = \frac{\pi m/2 + x_g m\left(\tan\alpha_d + \tan\alpha_{cg}\right)}{r_{pg}} \tag{B.30}$$

$$\lambda_d = inv\alpha_o - inv\alpha_d \tag{B.31}$$

$$\lambda_{cp} = inv\alpha_{ocp} - inv\alpha_{cp} \tag{B.32}$$

$$\lambda_{cg} = inv\alpha_{ocg} - inv\alpha_{cg} \tag{B.33}$$

$$t_{op} = (\gamma_p - \lambda_d - \lambda_{cp}) r_{op} \tag{B.34}$$

$$t_{op} = \left(\frac{\pi m/2 + x_p m(\tan\alpha_d + \tan\alpha_{cp})}{r_{pp}} - (inv\alpha_o - inv\alpha_d) \ldots \right. \\ \left. - (inv\alpha_{ocp} - inv\alpha_{cp}) \right) r_{op} \tag{B.35}$$

$$t_{og} = \left(\frac{\pi m/2 + x_g m(\tan\alpha_d + \tan\alpha_{cg})}{r_{pg}} - (inv\alpha_o - inv\alpha_d) \ldots \right. \\ \left. - (inv\alpha_{ocg} - inv\alpha_{cg}) \right) r_{og} \tag{B.36}$$

$$t_{og} = (\gamma_g - \lambda_d - \lambda_{cg}) r_{og} \tag{B.37}$$

Here t_{op} and t_{og} are dependent on the unknowns x_p and x_g, respectively. And note that at operating pitch circle, the gear tooth thickness is equal to the pinion tooth space width for zero backlash condition. Then,

$$t_{og} = t_{owp} - t_{op} \tag{B.38}$$

$$t_{og} + t_{op} = \frac{2\pi r_{op}}{Z_p} \tag{B.39}$$

As seen in the Equations (B.35), (B.36) and (B.39**)** the profile shift coefficients of the pinion and gear x_p, x_g are dependent on each other. If one of them is given as

an input value, then the other one is found by using the Equations (B.35), (B.36) and (B.39**)**.

B.3. Determination of Highest Point Single Tooth Contact Radius

$$C_1B_1 = B_2B_1 - B_2C_1 \tag{B.40}$$

$$C_4B_1 = p_b + C_1B_1 \tag{B.41}$$

$$r_{hp} = \sqrt{(C_4B_1)^2 + \left(r_{bdp}\right)^2} \tag{B.42}$$

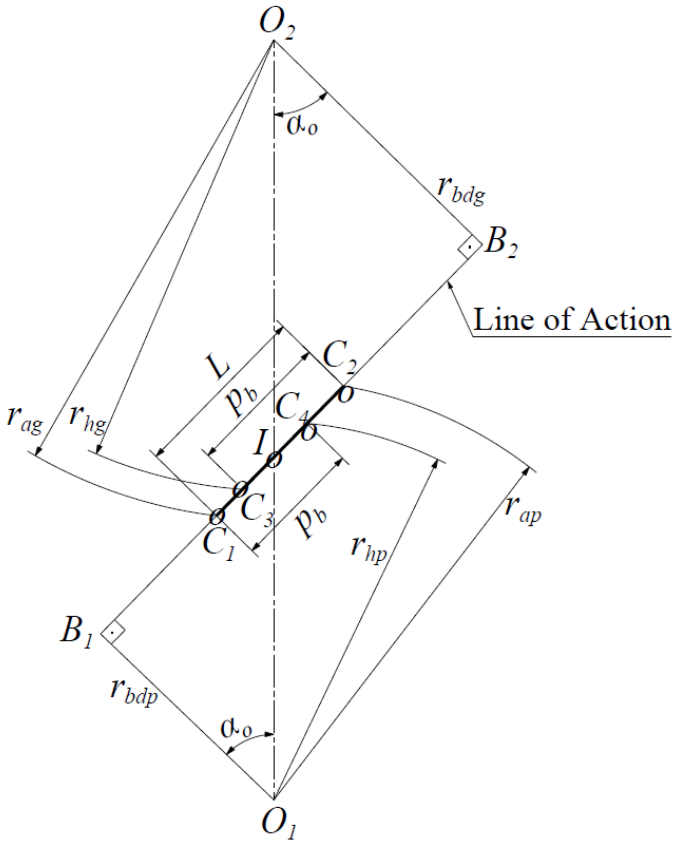

Fig. B.3 The line of action of external asymmetric gear mesh

$$C_2B_1 = \sqrt{\left(r_{ap}\right)^2 - \left(r_{bdp}\right)^2} \tag{B.43}$$

$$B_2C_2 = B_2B_1 - C_2B_1 \tag{B.44}$$

$$B_2C_3 = p_b + B_2C_2 \tag{B.45}$$

$$r_{hg} = \sqrt{(B_2C_3)^2 + \left(r_{bdg}\right)^2} \tag{B.46}$$

$$L = C_2B_1 - C_1B_1 \tag{B.47}$$

$$C_r = \frac{L}{p_b} \tag{B.48}$$

APPENDIX C

DETERMINATION OF THE PARAMETERS OF THE ASYMMETRIC PINION TYPE SHAPER CUTTER ROUNDED SURFACES

C.1. The Case of any Value for Shaper Cutter Tip Radius

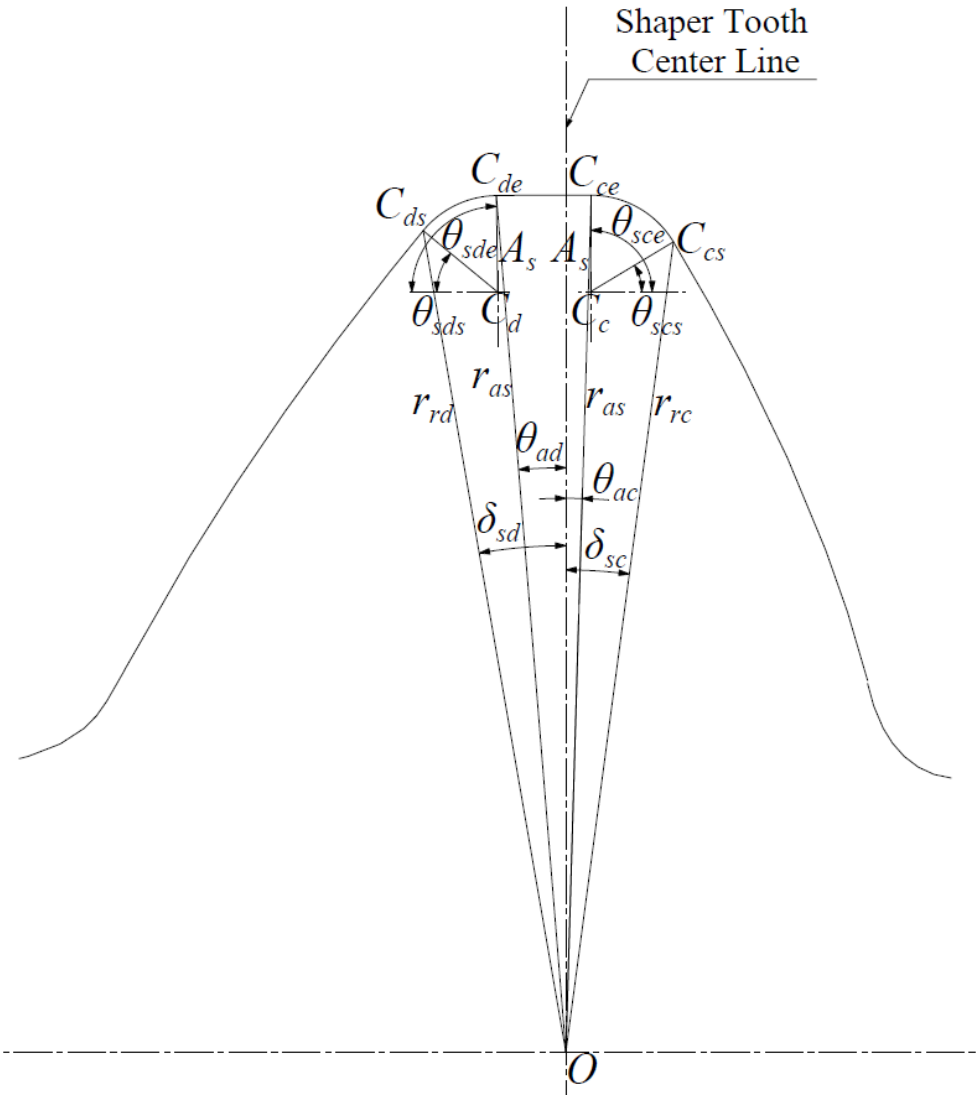

Fig. C.1 The asymmetric shaper cutter rounded surfaces parameters 1

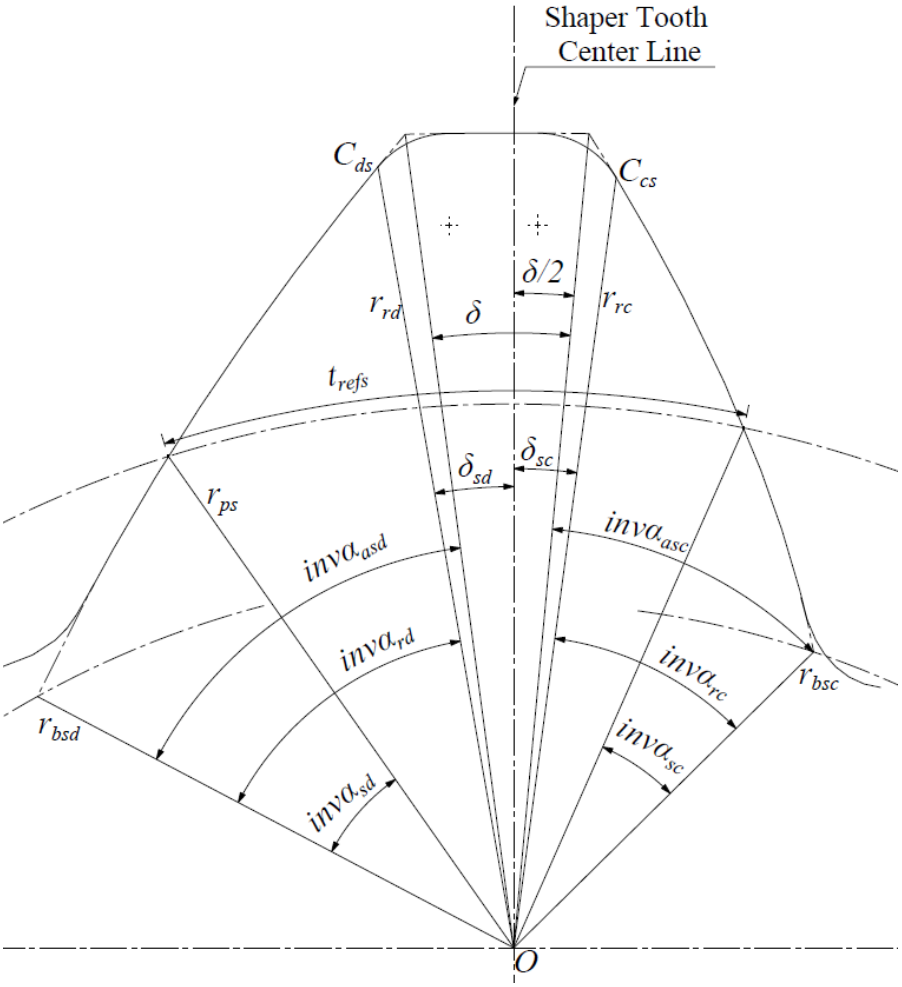

Fig. C.2 The asymmetric shaper cutter rounded surfaces parameters 2

At point C_{cs}, x, y components of drive side involute and radius can be determined as:

$$x_{ccsi} = r_{rc}\sin(\delta_{sc}) \tag{C.1}$$

$$y_{ccsi} = r_{rc}\cos(\delta_{sc}) \tag{C.2}$$

$$r_{rc} = \frac{r_{bsc}}{\cos(\alpha_{rc})} \tag{C.3}$$

$$r_{rc} = \frac{r_{ps}\cos(\alpha_{sc})}{\cos(\alpha_{rc})} \tag{C.4}$$

$$\delta_{sc} = \delta/2 + inv\alpha_{asc} - inv\alpha_{rc} \tag{C.5}$$

$$x_{ccsi} = \frac{r_{ps}\cos(\alpha_{sc})}{\cos(\alpha_{rc})}\sin(\delta/2 + inv\alpha_{asc} - inv\alpha_{rc}) \tag{C.6}$$

$$y_{ccsi} = \frac{r_{ps}\cos(\alpha_{sc})}{\cos(\alpha_{rc})}\cos(\delta/2 + inv\alpha_{asc} - inv\alpha_{rc}) \tag{C.7}$$

$$x_{ccsr} = x_{Cc} + A_s\cos(\theta_{scs}) \tag{C.8}$$

$$y_{ccsr} = y_{Cc} + A_s\sin(\theta_{scs}) \tag{C.9}$$

At point C_{cs}, x, y components and $\frac{\partial y}{\partial x}$ of coast side involute and round must be equal because they are tangent at this point:

$$x_{ccsi} = x_{ccsr} \tag{C.10}$$

$$\frac{r_{ps}\cos(\alpha_{sc})}{\cos(\alpha_{rc})}\sin(\delta/2 + inv\alpha_{asc} - inv\alpha_{rc}) = x_{Cc} + A_s\cos(\theta_{scs}) \tag{C.11}$$

$$y_{ccsi} = y_{ccsr} \tag{C.12}$$

$$\frac{r_{ps}\cos(\alpha_{sc})}{\cos(\alpha_{rc})}\cos(\delta/2 + inv\alpha_{asc} - inv\alpha_{rc}) = y_{Cc} + A_s\sin(\theta_{scs}) \tag{C.13}$$

$$\frac{\partial y_{ccsi}}{\partial x_{ccsi}} = \frac{\partial y_{ccsr}}{\partial x_{ccsr}} \tag{C.14}$$

$$\frac{\frac{\partial y_{ccsi}}{\partial \alpha_{rcs}}}{\frac{\partial x_{ccsi}}{\partial \alpha_{rcs}}} = \frac{\frac{\partial y_{ccsr}}{\partial \theta_{css}}}{\frac{\partial x_{ccsr}}{\partial \theta_{css}}} \tag{C.15}$$

At point C_{ce}, x, y components of coast side radius and tip circle can be determined as:

$$x_{ccer} = x_{Cc} + A_s \cos(\theta_{sce}) \tag{C.16}$$

$$y_{ccer} = y_{Cc} + A_s \sin(\theta_{sce}) \tag{C.17}$$

$$x_{ccet} = r_{as} \sin(\theta_{ac}) \tag{C.18}$$

$$y_{ccet} = r_{as} \cos(\theta_{ad}) \tag{C.19}$$

At point C_{ce}, x, y components and $\frac{\partial y}{\partial x}$ of coast side radius and tip circle must also be equal because they are tangent at this point:

$$x_{ccer} = x_{ccet} \tag{C.20}$$

$$x_{Cc} + A_s \cos(\theta_{sce}) = r_{as} \sin(\theta_{ac}) \tag{C.21}$$

$$y_{ccer} = y_{ccet} \tag{C.22}$$

$$y_{Cc} + A_s \sin(\theta_{sce}) = r_{as} \cos(\theta_{ac}) \tag{C.23}$$

$$\frac{\partial y_{ccer}}{\partial x_{ccer}} = \frac{\partial y_{ccet}}{\partial x_{ccet}} \tag{C.24}$$

$$\frac{\frac{\partial y_{ccer}}{\partial \theta_{cse}}}{\frac{\partial x_{ccer}}{\partial \theta_{cse}}} = \frac{\frac{\partial y_{ccet}}{\partial \theta_{ca}}}{\frac{\partial x_{ccet}}{\partial \theta_{ca}}} \tag{C.25}$$

Now there are six unknowns $\alpha_{rc}, \theta_{scs}, x_{Cc}, y_{Cc}, \theta_{sce}$ and θ_{ac} and six Equations (C.11), (C.13), (C.15), (C.21), (C.23) and (C.25). Therefore all six unknowns can be determined.

The drive side unknowns $\alpha_{rd}, \theta_{sds}, x_{Cd}, y_{Cd}, \theta_{sde}$ and θ_{ad} can be determined same with the coast side procedure. At point C_{ds}, the equalities of x, y components and $\frac{\partial y}{\partial x}$ of drive side involute and radius can be determined by modifying Equations (C.10) to (C.15) respectively as:

$$x_{cdsi} = x_{cdsr} \tag{C.26}$$

$$-\frac{r_{ps}\cos(\alpha_{sd})}{\cos(\alpha_{rd})}\sin(\delta/2 + inv\alpha_{asd} - inv\alpha_{rd}) = x_{Cd} - A_s\cos(\theta_{sds}) \tag{C.27}$$

$$y_{cdsi} = y_{cdsr} \tag{C.28}$$

$$\frac{r_{ps}\cos(\alpha_{sd})}{\cos(\alpha_{rd})}\cos(\delta/2 + inv\alpha_{asd} - inv\alpha_{rd}) = y_{Cd} + A_s\sin(\theta_{sds}) \tag{C.29}$$

$$\frac{\partial y_{cdsi}}{\partial x_{cdsi}} = \frac{\partial y_{cdsr}}{\partial x_{cdsr}} \tag{C.30}$$

$$\frac{\frac{\partial y_{cdsi}}{\partial \alpha_{rds}}}{\frac{\partial x_{cdsi}}{\partial \alpha_{rds}}} = \frac{\frac{\partial y_{cdsr}}{\partial \theta_{dss}}}{\frac{\partial x_{cdsr}}{\partial \theta_{dss}}} \tag{C.31}$$

At point C_{de}, the equalities of x, y components and $\frac{\partial y}{\partial x}$ of the drive side radius and tip circle can be determined by modifying Equations (C.20) to (C.25) respectively as:

$$x_{cder} = x_{cdet} \tag{C.32}$$

$$x_{Cd} - A_s \cos(\theta_{sde}) = r_{as} \sin(\theta_{ad}) \tag{C.33}$$

$$y_{cder} = y_{cdet} \tag{C.34}$$

$$y_{Cd} + A_s \sin(\theta_{sde}) = r_{as} \cos(\theta_{ad}) \tag{C.35}$$

$$\frac{\partial y_{cder}}{\partial x_{cder}} = \frac{\partial y_{cdet}}{\partial x_{cdet}} \tag{C.36}$$

$$\frac{\frac{\partial y_{cder}}{\partial \theta_{dse}}}{\frac{\partial x_{cder}}{\partial \theta_{dse}}} = \frac{\frac{\partial y_{cdet}}{\partial \theta_{da}}}{\frac{\partial x_{cdet}}{\partial \theta_{da}}} \tag{C.37}$$

Now there are six unknowns α_{rd}, θ_{sds}, x_{Cd}, y_{Cd}, θ_{sde} and θ_{ad} and six Equations (C.27), (C.29), (C.31), (C.33), (C.35) and (C.37). Therefore all six unknowns can be determined.

C.2. The Case of Maximum Value for Shaper Cutter Tip Radius

At point C_{cs}, the equalities of x, y components and $\frac{\partial y}{\partial x}$ of coast side involute and radius can be determined by modifying Equations (C.10) to (C.15) respectively as:

$$x_{ccsi} = x_{ccsr} \tag{C.38}$$

$$\frac{r_{ps}\cos(\alpha_{sc})}{\cos(\alpha_{rc})}\sin(\delta/2 + inv\alpha_{asc} - inv\alpha_{rc}) = x_C + A_{smax}\cos(\theta_{scs}) \tag{C.39}$$

$$y_{ccsi} = y_{ccsr} \tag{C.40}$$

$$\frac{r_{ps}\cos(\alpha_{sc})}{\cos(\alpha_{rc})}\cos(\delta/2 + inv\alpha_{asc} - inv\alpha_{rc}) = y_C + A_{smax}\sin(\theta_{scs}) \tag{C.41}$$

$$\frac{\partial y_{ccsi}}{\partial x_{ccsi}} = \frac{\partial y_{ccsr}}{\partial x_{ccsr}} \tag{C.42}$$

$$\frac{\frac{\partial y_{ccsi}}{\partial \alpha_{rcs}}}{\frac{\partial x_{ccsi}}{\partial \alpha_{rcs}}} = \frac{\frac{\partial y_{ccsr}}{\partial \theta_{css}}}{\frac{\partial x_{ccsr}}{\partial \theta_{css}}} \tag{C.43}$$

At point C_e, x, y components and $\frac{\partial y}{\partial x}$ of coast side radius, drive side radius and tip circle must all be equal since they are tangent. Here the drive and coast side parameters are totally same. Then the equalities of x, y components and $\frac{\partial y}{\partial x}$ of drive/coast side radius and tip circle can be determined by modifying Equations (C.20) to (C.25) respectively as:

$$x_{cer} = x_{cet} \tag{C.44}$$

$$x_C + A_{maxs}\cos(\theta_{se}) = r_{as}\sin(\theta_a) \tag{C.45}$$

$$y_{cer} = y_{cet} \tag{C.46}$$

$$y_C + A_{maxs}\sin(\theta_{se}) = r_{as}\cos(\theta_a) \tag{C.47}$$

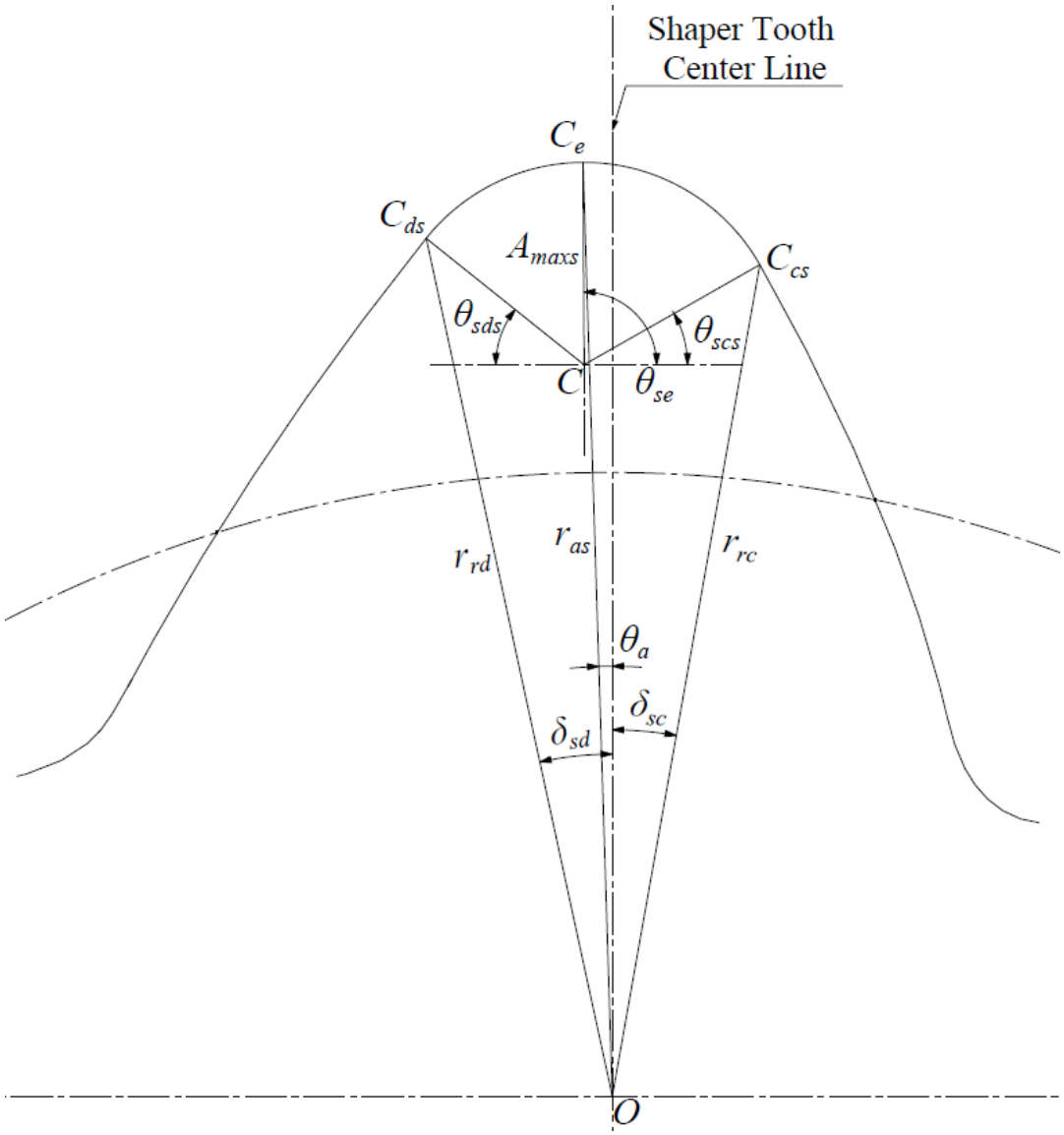

Fig. C.3 The maximum asymmetric shaper cutter radius

$$\frac{\partial y_{cer}}{\partial x_{cer}} = \frac{\partial y_{cet}}{\partial x_{cet}} \tag{C.48}$$

$$\frac{\frac{\partial y_{cer}}{\partial \theta_{se}}}{\frac{\partial x_{cer}}{\partial \theta_{se}}} = \frac{\frac{\partial y_{cet}}{\partial \theta_a}}{\frac{\partial x_{cet}}{\partial \theta_a}} \tag{C.49}$$

Now there are seven unknowns $\alpha_{rc}, \theta_{scs}, A_{maxs}, x_C, y_C, \theta_{se}$ and θ_a but six Equations (C.39), (C.41), (C.43), (C.45), (C.47) and (C.49). Therefore the coast side parameters of the shaper cannot be solved alone. The drive side analysis shall also be done.

At point C_{ds}, the equalities of x, y components and $\frac{\partial y}{\partial x}$ of drive side involute and radius can be determined by modifying Equations (C.10) to (C.15) respectively as:

$$x_{cdsi} = x_{cdsr} \tag{C.50}$$

$$-\frac{r_{ps}\cos(\alpha_{sd})}{\cos(\alpha_{rd})}\sin(\delta/2 + inv\alpha_{asd} - inv\alpha_{rd}) = x_C - A_{maxs}\cos(\theta_{sds}) \tag{C.51}$$

$$y_{cdsi} = y_{cdsr} \tag{C.52}$$

$$\frac{r_{ps}\cos(\alpha_{sd})}{\cos(\alpha_{rd})}\cos(\delta/2 + inv\alpha_{asd} - inv\alpha_{rd}) = y_C + A_{maxs}\sin(\theta_{sds}) \tag{C.53}$$

$$\frac{\partial y_{cdsi}}{\partial x_{cdsi}} = \frac{\partial y_{cdsr}}{\partial x_{cdsr}} \tag{C.54}$$

$$\frac{\frac{\partial y_{cdsi}}{\partial \alpha_{rds}}}{\frac{\partial x_{cdsi}}{\partial \alpha_{rds}}} = \frac{\frac{\partial y_{cdsr}}{\partial \theta_{dss}}}{\frac{\partial x_{cdsr}}{\partial \theta_{dss}}} \tag{C.55}$$

The extra equation comes from the drive side since there are three equations but only two unknowns $\alpha_{rd}, \theta_{sds}$ different from the seven unknowns mentioned above. Now there are nine unknowns α_{rc}, $\alpha_{rd}, \theta_{scs}$, θ_{sds}, A_{maxs}, x_C, y_C, θ_{se} and θ_a and nine Equations (C.39), (C.41), (C.43), (C.45), (C.47), (C.49), (C.51), (C.53), (C.55). Therefore all nine unknowns can be determined, A_{maxs} too.

APPENDIX D

DETERMINATION OF INTERNAL ASYMMETRIC SPUR GEAR TOOTH AND GEAR PAIR MESH PARAMETERS

D.1. Determination of Internal Asymmetric Spur Gear Tooth Pointed Tip Radius, Drive and Coast Sides Tooth Thicknesses

$$\alpha_{tid} = \cos^{-1}\left(\frac{r_{bid}}{r_{ti}}\right) \tag{D.1}$$

$$t_{gid} = r_{gpi}\left(inv\alpha_g - inv\alpha_{tid}\right) \tag{D.2}$$

$$t_{gid} = r_{gpi}\left(inv\alpha_g - tan\alpha_{tid} + \alpha_{tid}\right) \tag{D.3}$$

$$\alpha_{tic} = \cos^{-1}\left(\frac{r_{bic}}{r_{ti}}\right) \tag{D.4}$$

$$t_{gic} = r_{gpi}\left(inv\alpha_{gsc} - inv\alpha_{tic}\right) \tag{D.5}$$

$$t_{gic} = r_{gpi}\left(inv\alpha_{gsc} - tan\alpha_{tic} + \alpha_{tic}\right) \tag{D.6}$$

$$t_{gi} = t_{gic} + t_{gid} \tag{D.7}$$

$$t_{gi} = r_{gpi}\left(inv\alpha_{gsc} - tan\alpha_{tic} + \alpha_{tic}\right) + r_{gpi}\left(inv\alpha_g - tan\alpha_{tid} + \alpha_{tid}\right) \tag{D.8}$$

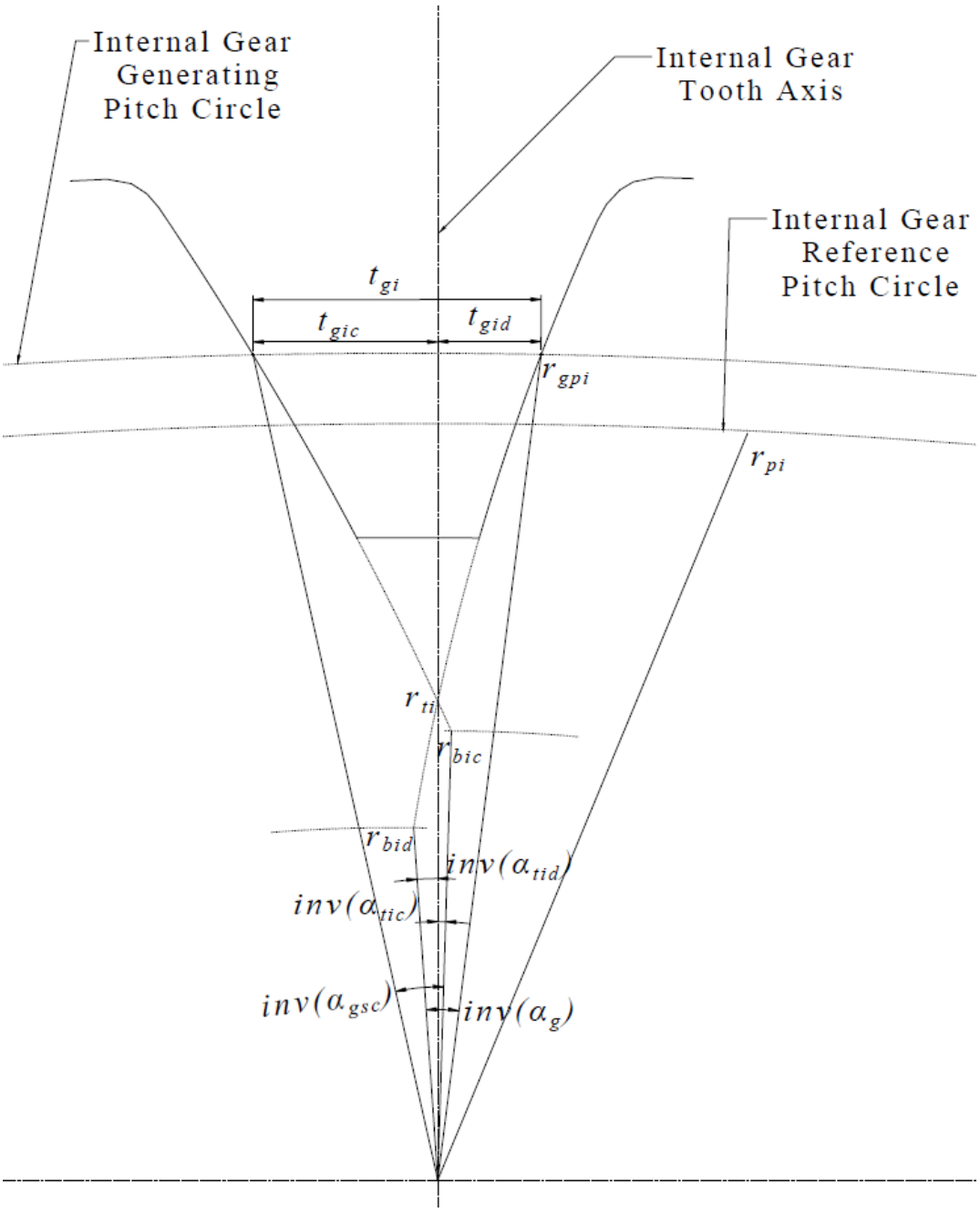

Fig. D.1 The asymmetric internal gear tooth pointed tip radius

Since t_{gi} is already known by Equation (3.56), then in Equation (D.8) all parameters are known except r_{ti}. In order to find r_{ti} Newton-Raphson method is used to solve the Equation (D.8). In Matlab, fsolve function uses this method and can be used to find r_{ti}.

D.2. Determination of Lowest Point Single Tooth Contact Radius

$$B_2B_1 = IB_1 - IB_2 \tag{D.9}$$

$$B_2B_1 = r_{opi}\sin(\alpha_{oi}) - r_{ope}\sin(\alpha_{oi}) \tag{D.10}$$

Here subscript "e" represents the external gear which is in mesh with the internal gear.

$$E_c = r_{pi} - r_{pe} + x_e \tag{D.11}$$

$$r_{pe} = m\frac{Z_e}{2} \tag{D.12}$$

$$r_{ope} = \frac{E_c}{\frac{Z_i}{Z_e} - 1} \tag{D.13}$$

$$r_{opi} = r_{ope} + E_c \tag{D.14}$$

$$\alpha_{oi} = \cos^{-1}\left(\frac{r_{bid}}{r_{opi}}\right) \tag{D.15}$$

$$C_1B_2 = C_1B_1 - B_2B_1 \tag{D.16}$$

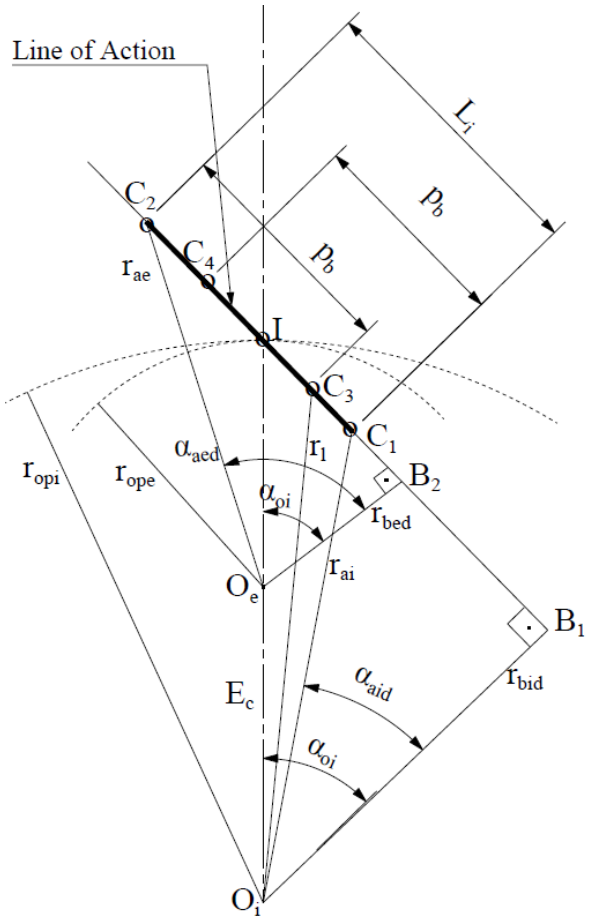

Fig. D.2 The line of action of internal asymmetric gear mesh

$$C_1B_1 = r_{ai}\sin(\alpha_{aid}) \tag{D.17}$$

$$\alpha_{aid} = \cos^{-1}\left(\frac{r_{bid}}{r_{ai}}\right) \tag{D.18}$$

$$C_2B_2 = r_{ae}\sin(\alpha_{aed}) \tag{D.19}$$

$$C_3C_1 = C_2B_2 - C_1B_2 - p_b \tag{D.20}$$

$$C_3B_1 = C_3C_1 + C_1B_1 \tag{D.21}$$

$$r_l = \sqrt{(C_3 B_1)^2 + (r_{bid})^2} \tag{D.22}$$

$$C_{ri} = \frac{L_i}{p_b} \tag{D.23}$$

$$C_{ri} == \frac{C_2 B_2 - C_1 B_2}{p_b} \tag{D.24}$$